UiT The Arctic University of Norway

Faculty of Science and Technology

Department of Geosciences

Origin and Economic Potential of Lithium-mineralized Granitic Pegmatites in Helgeland, North Norway

Reginald Mensah Lomotey

Master's thesis in Geology GEO-3900, August 2023

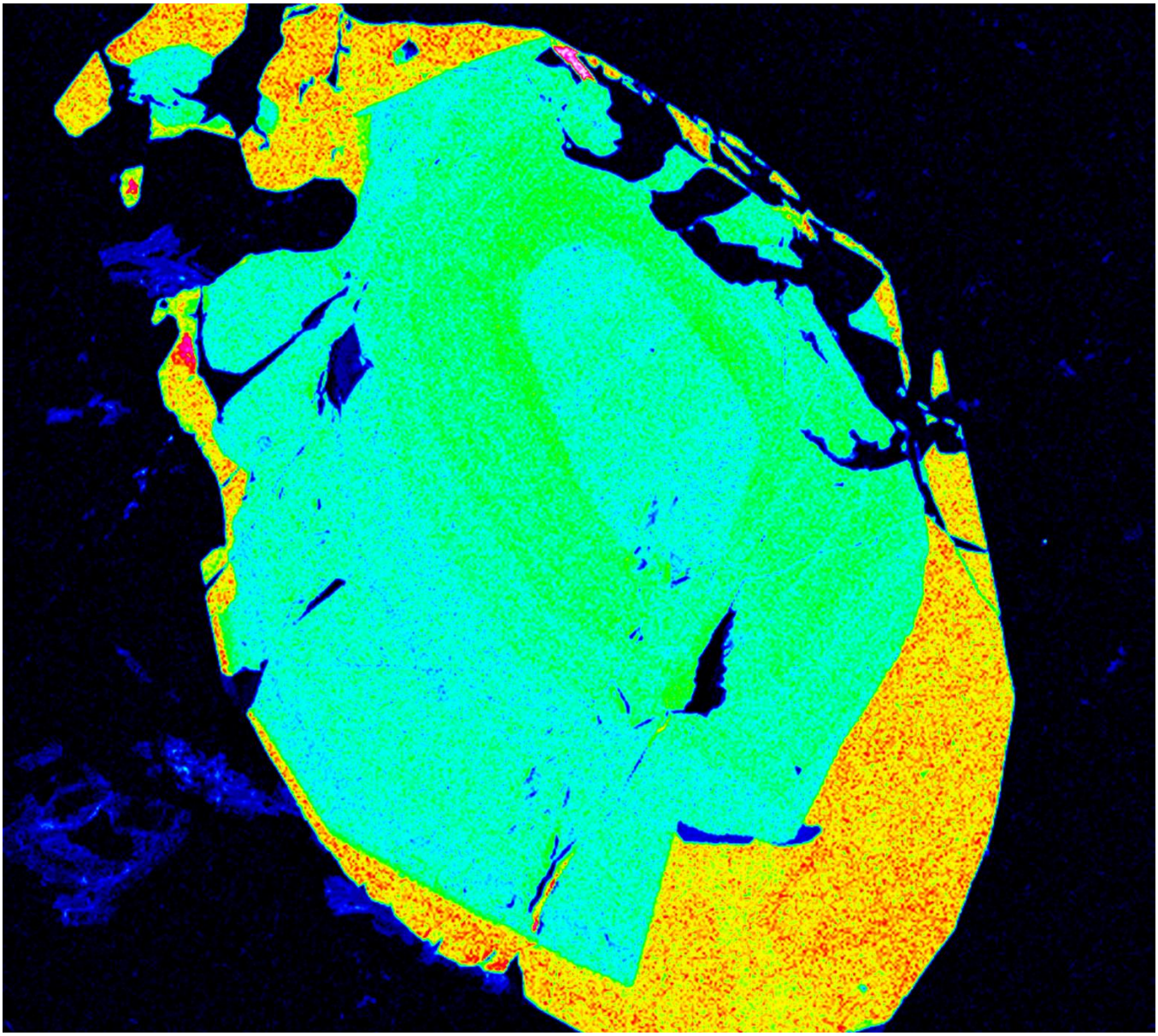

Supervisor: Prof. Sebastian Tappe (Department of Geosciences, UiT The Arctic University of Norway)
Co-supervisors: Dr. Jiří Konopásek (Department of Geosciences, UiT The Arctic University of Norway)
Dr. Christophe Ballouard (University of Lorraine, France)
Dr. Trond Slagstad (Geological Survey of Norway)

Acknowledgements

This MSc project would have been impossible without the generous support by Kuniko Norge AS, who supported our fieldwork in Helgeland and contributed to some of the analytical costs. Antony Beckmand of Kuniko is gratefully acknowledged for his generous help to make this project happen. I would like to express my sincere gratitude to Dr. Benedikt Steiner from the Camborne School of Mines for his invaluable assistance in coordinating the entire fieldwork. My unreserved gratitude also goes to the supervisors of this thesis, namely Dr. Jiří Konopásek, Dr. Trond Slagstsad, Dr. Christophe Ballouard, and especially Prof. Sebastian Tappe, for their invaluable direction and guidance throughout the duration of this project. In addition, I appreciate the help I received from Trine Merete Dahl and Karina Monsen of the Department of Geosciences laboratory throughout the laboratory work.

Lastly, my sincerest gratitude goes to my dearest wife, family and friends for their consistent presence, and unwavering support and motivation throughout the course of this work.

Reginald M. Lomotey,

August 2023.

ABSTRACT

A comprehensive set of analytical techniques, encompassing geological, petrographic, mineralogical, and zircon U-Pb-Hf isotopic compositions, was employed to investigate a relatively poorly known pegmatite field located in Helgeland, North Norway. The Paleoproterozoic basement gneisses in the area have U-Pb zircon crystallization ages between 1870 ± 12 and 1811 ± 6 Ma, meaning that they belong to the Transscandinavian Igneous Belt (TIB) of the Fennoscandian Shield. The Paleoproterozoic basement in the study area has been overprinted by metamorphism during late stages of the Caledonian orogenic event.

The U-Pb zircon age determinations for granitic pegmatite magma emplacement define two discrete pegmatite generations during the late stage of the Caledonian collisional event. An older generation of pegmatites, with ages between 422 ± 5 and 412 ± 5 Ma, that formed by partial melting related to collision and thrusting during the Caledonian orogenic event. The younger generation of pegmatites has ages between 403 ± 6 and 387 ± 6 Ma, and these magmas formed during decompression in the latest stages of the Caledonian orogeny. Using fractionation indicators such as K/Rb and Nb/Ta in micas, the study identified a correlation between the U-Pb ages of the Caledonian pegmatites and their degree of magmatic differentiation; the younger pegmatites are more evolved. The Helgeland pegmatites form a cluster of highly evolved and more primitive granitic magmas with some minor rare metal enrichment such as Li-Cs-Ta in the younger and more evolved pegmatites. Hafnium isotopic data for zircons reveal slightly subchondritic to firmly juvenile εHf_i values between -3.3 and +5 for the Paleoproterozoic gneisses, whereas the Caledonian pegmatites show a spread between -32 and -8. For the pegmatites, significant within-sample variations of up to 24 epsilon-units are recorded, which indicates magma derivation from an isotopically heterogeneous crustal source region that may have contained metasedimentary rock packages. The zircon Hf isotopic compositions reveal that the pegmatites formed by partial melting of the Paleoproterozoic basement during the latest stages of the Caledonian

orogeny. The study demonstrates that partial melting of a ca. 1.8 Ga old metasedimentary rock from the Neverdalen locality can yield similar Hf isotopic compositions to the ca. 0.4 Ga old Helgeland pegmatites after its isotopic evolution for more than one billion years.

Contents

1 Introduction

1.1 Granitic Pegmatites

Granitic plutons often contain lenses of a markedly coarser grained facies referred to as granitic pegmatites (London, 2008; London & Kontak, 2012). Pegmatites comprise the major granite forming minerals (quartz, feldspar, biotite, muscovite), but they differ from granites mainly in the crystal size > 2 cm, which may reach several meters (London, 2008; Anderson, 2012). The very large crystal sizes of pegmatites cannot be attributed to slow cooling but must reflect low degree of nucleation of crystals combined with very fast crystal growth from flux-rich melts (London & Kontak, 2012).

The fluxing agents together with water alter the behavior of the residual melt in the magmatic system significantly. Contributions by Jahns and Burnham (1969) and London and Morgan (2012) explain that H_2O, B, P and F present in the melt, lower melt viscosity and increase diffusivity of Al and Si, thereby promoting the growth of silicate minerals. According to Anderson (2012), another role of these fluxing agents in the melt is to suppress mineral nucleation, resulting in a metastable and supersaturated melt referred to as undercooling (London et al., 1989). Further cooling of the supersaturated, undercooled melt then causes rapid crystal growth, from the margins inward, enhancing large crystal growth and resulting in the oriented textures typically observed in pegmatites (Anderson, 2012; London & Kontak, 2012). In their review of the principal models for the internal evolution of pegmatites, London and Morgan (2012) define a graphic texture that is unique to pegmatites. Fenn (1986) also describes this texture to represent first evidence of the conditions of extended undercooling below the liquidus temperature and supersaturation of viscous melt in quartz- and feldspar-forming components. These features, together with the common concentric layering of pegmatite bodies including quartz cores, give pegmatites the appearance of both igneous and hydrothermal rocks or mineralization (London & Kontak, 2012).

Based on isotope, thermometry, and fluid inclusion studies, pegmatitic melts crystallize at temperatures below the wet solidus of granite in the range of 500–600 °C, or even lower (Thomas et al., 1988; Morgan & London, 1999; Anderson, 2012).

The distinctive textures of granitic pegmatites reflect the same factors that lead to their exceptional ability to concentrate trace elements such as Li, B, Cs, Ta, Bi, and REEs to levels that surpass concentrations of typical continental crustal rocks by several orders of magnitude (Anderson, 2012; London & Kontak, 2012). Element pairs with similar geochemical properties, such as Zr–Hf and Nb–Ta, are extensively fractionated in individual pegmatite bodies (Ballouard et al., 2020b). This may exceptionally lead to the formation of unusual minerals such as hafnon ($HfSiO_4$) and tantite (Ta_2O_5) (London & Kontak, 2012).

Gem-quality crystals may be found in pegmatites and are termed miarolitic, referring to the presence of clay-filled or open crystal-lined cavities (Černý & Ercit 2005; London & Kontak, 2012). Several pegmatites are mined nowadays worldwide for rare metals and minerals they contain, which find uses in batteries, electronics, nuclear power generation, aircraft, automobiles, and other niche sectors (Glover et al., 2012; Bradley et al., 2017a).

1.2 Structure of Pegmatites

Granitic pegmatite bodies occur in variable shapes and forms, from lenticular, ellipsoidal, fracture-filling dykes to facial pods (London, 2008; London & Kontak, 2012). These forms are controlled to a large extent by the competency of the host rocks, depth of magma emplacement, and the tectonic and metamorphic setting during emplacement (Černý, 1991a). The shape and form can significantly influence the internal structure and modal mineral distribution. Sizes may be less than 1 m thick, or a few tens of meters across and hundreds of meters in length, as for some of the most economic pegmatites (Černý, 1991a). Internally, rare element pegmatites are typically heterogeneous and complex (Černý, 1991a). This can result in zoned and unzoned varieties, based on the internal zoning or lack thereof (London, 2008). In unzoned pegmatites, grain size distribution is homogeneous but there may be subtle oriented fabrics (London, 2008). Elongated megacrysts of quartz predominate, with minor compositional and textural zoning at the contacts, occasional layered aplitic assemblages, and rare pods of blocky texture in their central regions (Černý, 1991a). These unzoned pegmatites mostly occur in metamorphic host rocks (London, 2008).

Cameron et al. (1949) described the zoning of pegmatites based on variations in the spatial distribution of grain size, mineral assemblage, crystal habit or rock fabric. Zoned pegmatites

(Figure 1) form the majority of occurrences and typically displays a progressive crystallization from the margins inward, showing increasing crystal size, decreasing number of rock-forming minerals, and textural changes from granitic through graphic in intermediate zones to a blocky coarse-grained monomineralic quartz core (Černý, 1991a; London & Morgan, 2012). Jahns (1982) postulated that discoidal lenses of quartz formed in the monomineralic quartz core, whereas fractionation of alkali elements created zones rich in Na-plagioclase and K-feldspar along the opposite borders of a pegmatite body. London (2008) described the structure of zoned pegmatites to consist of (see Figure 1):

- **The border zone** comprises thin cooling margins of less coarse granitic rocks in contact with the host rocks of a pegmatite body. The grains are ∼2-5 mm across and the texture can be described as granitic or bimodal if the fine-grained portion constitutes a groundmass to larger (∼1-3 mm) crystals.
- **The wall zone** is a thicker (∼1 m), coarser-grained (∼1-3 cm) variation of the border zone in most pegmatite bodies. An anisotropic orientation of inward-pointing minerals such as tourmaline, micas, and feldspars is common in the wall zone.
- **The intermediate zone** is marked by a sharp increase in crystal size up to an order of magnitude compared to the outer zones (Jans, 1953). Single mineral phases dominate, typically perthitic microcline, plagioclase and quartz. In Li-rich pegmatites, the intermediate zone commonly concentrates Li-aluminosilicates or phosphates such as spodumene, petalite, or montebrasite. This is the most prominently developed part in the pegmatite body, and such an intermediate zone may be symmetrically or asymmetrically distributed within the igneous body.
- **The core zone** is the innermost unit of a pegmatite body and predominantly consists of monomineralic quartz, but may contain various minor proportions of perthite, albite, aluminosilicates, and phosphates (London, 2008; Bowell et al., 2020).

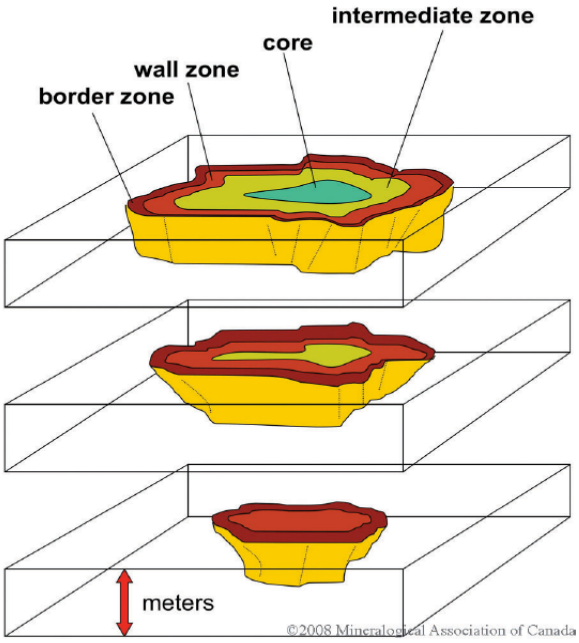

Figure 1. Generalized block diagram of a zoned pegmatite body, displaying concentric zoning in a steeply dipping, irregular and lens shaped intrusion. Vertical and lateral scales are in meters (modified from Cameron et al.,1949) (London, 2008).

Generally, most ore minerals of Li, Rb and Cs occur in the intermediate and central zones (Černý, 1991a). Pegmatite bodies may display fracture fillings mainly consisting of quartz but may also contain migrated material from other zones (Černý, 1991a). Metasomatic reactions can also lead to the formation of replacement bodies in pegmatites. This ranges from selective replacement of individual mineral species (e.g., micas after beryl or topaz), through pervasive, but diffuse assemblages replacing primary mineral assemblages (e.g., albite + Li-mica after K-feldspar), to bulk replacement of primary assemblages in pre-existing units (Černý, 1991a). Clear evidence of replacement zones is pseudomorphism, which is defined as recognizable morphologic properties of crystals in the original mass despite total compositional modification (London, 2008). The pseudomorphic assemblage may preserve host phase textural features including cleavage and twinning (London, 2008), even when replacement is very selective in petrographic thin sections.

1.3 Classification of Granitic Pegmatites

Černý and Ercit (2005) developed a classification scheme for granitic pegmatites, which is presently the most popular. In Table 1, five pegmatite classes, ten subclasses, thirteen types, and seven subtypes are distinguished by this classification. The five pegmatite classes

determined by pressure-temperature conditions of magma emplacement are 'abyssal', 'muscovite', 'muscovite-rare-element', 'rare-element', and 'miarolitic' pegmatites (Černý & Ercit, 2005). The majority of pegmatite classes are associated with a connotation that implies their specific environment of formation, which is generally correlated with their depth of emplacement (Černý & Ercit, 2005). However, the chemical or textural characteristics of the pegmatites do not provide strong constraints on the pressures (depths) at which they crystallized, hence such models are generally based on the P-T condition records of their host rocks (Černý et al., 2012). These factors make the application of the pegmatite classes rather confusing and contradictory (Tkachev, 2011).

Geochemical characteristics, however, guide the further classification of classes into subclasses. Pegmatite types, which make up the third level of classification hierarchy, are based on mineral assemblages (Černý & Ercit, 2005).

Class	Subclass	Type	Subtype	Family
Abyssal	HREE			NYF
	LREE			
	U			NYF
	BBe			LCT
Muscovite				
Muscovite–rare element	REE			NYF
	Li			LCT
Rare element	REE	allanite–monazite euxenite gadolinite		NYF
	Li	beryl	beryl–columbite beryl–columbite–phosphate	LCT
		complex	spodumene petalite lepidolite elbaite amblygonite	
		albite–spodumene albite		
Miarolitic	REE	topaz–beryl gadolinite–fergusonite		NYF
	Li	beryl–topaz spodumene petalite lepidolite		LCT

Table 1. The pegmatite classification scheme of Černý & Ercit (2005), modified to show the correlation between pegmatite classes and families. NYF = niobium–yttrium–fluorine family (green); LCT = lithium–cesium–tantalum family (yellow); HREE = heavy rare earth elements; LREE = light rare earth elements (London, 2008).

Černý (1991a) further classified pegmatites into two main families denoted by the fingerprints of ordinary trace elements that have been concentrated to high levels in

pegmatites due to differentiation of their parental granitic magmas: the LCT (Li-Cs-Ta) and NYF (Nb-Y-F) pegmatite families, which differ in their characteristic metal enrichment and the nature of the melt source in the deeper crust. A third pegmatite type, the mixed NYF and LCT family, derived from a variety of sources, has also been recognized (Černý & Ercit, 2005).

1.3.1 The LCT family

The LCT pegmatite suite is typically associated with peraluminous (S-type) granites derived from partial melts of metamorphosed sedimentary rocks in overthickened continental crust (Chappell & White, 2001; Martin & De Vito, 2005; Černý et al., 2012). The most common Li minerals are the silicates spodumene, petalite, lepidolite and elbaite, as well as the phosphate series amblygonite – montebrasite [$LiAlPO_4(F,OH)$] and lithiophilite–triphylite [$Li(Mn,Fe)PO_4$] (Černý et al., 2012). Regardless of the tectonic regime in which partial melting occurred, the primary properties of LCT pegmatites are derived from mica-rich metasedimentary rocks (London, 2008; Černý et al., 2012). Phosphorous is a key component of the feldspars in many LCT pegmatites, and its high abundance is manifested by the presence of apatite as a major mineral phase (London et al., 1999, London, 2008). The high P abundance in LCT pegmatites points to a metapelitic source, such as metamorphosed marine black shales (London, 2008 and references therein). Pegmatites bearing the LCT signature significantly outnumber those bearing the NYF signature. Among the LCT family, the Be- and Li-rich subclasses and types are by far the most prevalent of the rare-element pegmatites (Černý et al., 2012).

1.3.2 The NYF family

The NYF suite is mostly associated with more alkaline A-type granites (Černý & Ercit, 2005; Martin & De Vito, 2005). A-type granites are derived from mixtures of lower continental crustal pyroxene-bearing quartzo-feldspathic rocks with varying quantities of mantle components added (King et al., 1997). These magmas are believed to be poor in H_2O, but F is incorporated by the decomposition of micas and amphiboles to pyroxene (Skjerlie & Johnston, 1992). Pegmatites in the NYF family contain chemically complex oxide and silicate minerals enriched in heavy rare earth elements (HREEs), Ti, U, Th and Nb > Ta, among others

(Černý et al., 2012). Fluorine enrichment is visible in NYF pegmatites that contain modal fluorite or topaz. The most common mafic minerals are ferruginous biotite, aegirine and riebeckite, the latter two denoting peralkaline compositions of these granitic pegmatites (Černý *et al.*, 2012). In contrast to LCT pegmatites, NYF pegmatites lack P, have low Ca contents, and tourmaline is uncommon (Černý et al., 2012).

1.4 Genesis of Granitic Pegmatites

Many compositional characteristics and genetic aspects relating to the petrology of granitic pegmatites remain poorly understood and lack a unifying model. For example, whether LCT pegmatites originate from S-type granites by magmatic differentiation (i.e., a magmatic origin) or whether they represent the direct partial melting products of flux-rich metasedimentary rocks (i.e., an anatectic origin) has been debated during the past decade (e.g., Černý et al., 2012; Dill, 2015; Müller et al., 2017; Steiner, 2019; Ballouard et al., 2020a; Bonzi et al., 2021; Zhao et al., 2022; Knoll et al., 2023). Below, these two main models for the origins of granitic pegmatites are briefly reviewed.

1.4.1 Magmatic Origin

Most pegmatites are believed to form from parental granitic melts that rise through the continental crust and presumably undergo fractional crystallization (Cameron et al., 1949; Černý, 1991, 2012; Martin & De Vito, 2005; London, 2008; Hulsboch et al., 2014; Roda-Robles et al., 2018). Two not mutually exclusive processes may occur during cooling and crystallization of the magma: (i) progressive fractional crystallization, which enriches the residual melt in incompatible elements including fluxing components (B, Li, F, H_2O) that are likely to affect the magma's rheology, including its ability to fractionate efficiently, and (ii) fluid exsolution (Martin & De Vito, 2005). This process can generate and concentrate rare minerals in the cooling pegmatites if exotic fluids are involved (Martin & De Vito, 2005). The resultant pegmatite rocks are classified as magmatic or granite-related. Figure 2 depicts the conventional and generally accepted model for the development of pegmatites from a parent pluton, including mineralogical-geochemical zonation of the pegmatite bodies (Černý, 1991b; Müller et al., 2017).

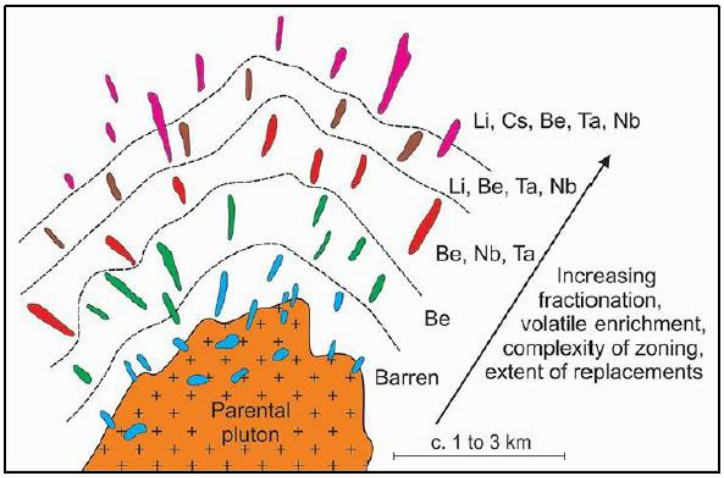

Figure 2. An idealized model of regional zonation and fractionation trend from a parental pluton source to barren and to evolved pegmatites (modified from Černý, 1991b) (Müller et al. (2017). The schematic drawing illustrates rare metal enrichment with increasing distance from the parental granite.

1.4.2 Anatectic Origin

Pegmatite generation and the mobility of elements in peraluminous melts are not restricted to fractional crystallization. Rather than requiring fractional crystallization of a parent granitic magma, some studies propose that felsic pegmatites can form directly by partial melting of metamorphic rocks (anatexis) deep in the continental crust (Martin & De Vito, 2005; Müller et al., 2022). This process involves low-degree partial melting of thickened continental crust where there is an increase in heat generation as a result of mechanical and/ or radiogenic decay processes (Tkachev, 2011). A rise increase in heat generation facilitates partial melting of regionally heated greywackes- and shale-bearing metasedimentary rock sequences in the continental crust (e.g., Puziewicz & Johannes, 1988; Sylvester, 1998). This results in redistribution and enrichment of elements that prefer to enter the granitic melt (London, 2008). With progressive fractionation of such an anatectic melt, incompatible elements including those that are known as fluxing-agents (B, P, F and H_2O) are concentrated in the residual melt. This concentration of incompatible elements and fluxing-agents results in lower viscosity and liquidus temperature, thereby effecting crustal migration of the melts away from the source area (Roda-Robles et al., 2018 and references therein). These melts may eventually crystallize as discrete pegmatite bodies into the upper continental crust (Simmons & Webber, 2008). It is possible that a pluton-size mass of magma can also result from the coalescence of several batches of anatectic melt (Martin & De Vito, 2005). There are several lines of geophysical, geochronological, geochemical and

mineralogical evidence from large pegmatite fields in northern Norway (e.g., Tysfjord) and southern Norway (e.g., Froland) against a genetic link between the pegmatites and nearby S-type granite plutons (Müller et al., 2015, 2022).

1.5 The Mineralogy of LCT pegmatites and Li-mineralization

Li is the lightest alkali metal and third-lightest chemical element. It is a trace element typically found in silicate rocks, with an average concentration of 1.39 ± 0.10 (2-sigma) µg/g or ppm in the primitive mantle (Pogge von Strandmann et al., 2020). Due to its strong incompatibility, Li is significantly enriched in the oceanic crust (mean = 5.5 ± 3.8 µg/g in mid-ocean ridge basalts) (Marschall et al., 2017) and continental crust (mean = 18 µg/g in the bulk continental crust; Sauzéat et al., 2015) compared to the mantle. Lithium concentrations can reach higher levels up to 7,000 µg/g in the continental crust thereby forming Li minerals (London, 2017).

With Li brines from salar, "Hard-rock" Li hosted in LCT pegmatites or some volcanic clays, represents among the most important geological resources of Li (Bradley et al., 2017b). Grew (2020) lists 124 known Li-bearing minerals, nine of which are deemed economically significant (Table 2). In LCT pegmatites, Li mostly occurs in spodumene (α-$LiAlSi_2O_6$), petalite ($LiAlSi_4O_{10}$), and Li-micas (e.g., zinnwaldite, lepidolite), and less commonly Li-Al-phosphates (amblygonite-montebrasite), Li-tourmaline (elbaite), and Li-Mn-Fe phosphates (Grew, 2020). The strong enrichment of Li comes from the involvement of micas in melting reactions within the metapelitic source, and from the high incompatibility of Li in most other minerals that remain largely unmelted as part of the source residue (London, 1995; London, 2005).

Mineral	Formula	Li_2O, wt%	Comment
Spodumene	$LiAlSi_2O_6$	6–9	Major ore
Petalite	$LiAlSi_4O_{10}$	4.73	Common in African ores
Lepidolite (series polylithionite–trilithionite)	$KLi_2Al(Si_4O_{10})(F,OH)_2$ to $K(Li_{1.5}Al_{1.5})(AlSi_3O_{10})(F,OH)_2$	4.19	Widespread in low-grade ores especially Australia
Zinnwaldite (series siderophyllite–polylithionite)	$KFe^{2+}{}_2Al(Al_2Si_2O_{10})(OH)_2$ to $KLi_2Al(Si_4O_{10})(F,OH)_2$	2–5	Common in European greisen ores
Amblygonite	$Li,Al(F,OH)PO_4$	7.4	Common in African ores e.g., Zimbabwe
Montebrasite	$LiAl(PO_4)(OH)$	7.4	Common in African ores
Eucryptite	$LiAlSiO_4$	9.7	Common in African ores
Triphylite	$Li(Fe,Mn)PO_4$	9.47	Common in African ores
Jadarite	$LiNaSiB_3O_7(OH)$	7.3	Only present at Jadar (Serbia)
Hectorite	$Na_{0.3}(Mg,Li)_3(Si_4O_{10})(F,OH)_2{\cdot}nH_2O$	<1–3	Main ore in volcanic tuff hosted ores

Table 2 Major hard rock lithium minerals. Based on the International Mineralogical Association list of minerals (Garrett, 2004; London, 2008; Evans, 2014)

Spodumene typically forms large to gigantic euhedral tabular or lath-shaped crystals in a variety of colors such as white, beige, light pink or green (London, 2008). It is not uncommon to find meter-sized spodumene crystals (Bowell et al., 2020). Petalite forms large, subhedral, club-shaped crystals often white or light gray in color (London, 2008). Eucryptite (α-$LiAlSiO_4$) is a minor mineral constituent of many petalite- or spodumene-rich pegmatites. Pure eucryptite resembles quartz but is distinguishable from quartz by its bright red fluorescence in short-wave ultraviolet light (London, 2008). All these minerals are anhydrous Li-aluminosilicates and their stability is pressure dependent.

At most locations where all three Li aluminosilicates are found, a clear progression from petalite + quartz → spodumene + quartz → eucryptite + quartz can be observed due to incomplete reactions (London, 2008).

Spodumene is a monoclinic pyroxene and the rotation of silicate tetrahedra chains makes its structure unstable upon cooling (Cameron et al., 1973), leaving it more rapidly exposed to alteration, weathering, and dissolution. Petalite and bikitaite possess an open silicate framework structure, whereas eucryptite is isostructural with α-quartz (Kocman et al., 1974). According to London (2008), the Li aluminosilicates possess distinct crystal habits: petalite has one excellent cleavage direction that distinguishes it from feldspars and spodumene; spodumene has the {1 1 0} cleavage typical for pyroxenes; and eucryptite lacks any cleavage. Phase stability of petalite, spodumene and eucryptite is only dependent on pressure and temperature because reactions among these Li aluminosilicates only involve silica, with silica saturation being maintained by quartz (London, 2008). The experimental findings of London (1984) revealed that the crystallization of Li aluminosilicates is restricted at variable pressure and temperatures below 700˚C due to reactions involving spodumene or petalite to virgilite or β-spodumene, as depicted in Figure 3. Petalite is stable at high temperature, and spodumene at comparatively high pressure. London (2008) in his experiments also found that eucryptite + quartz may form by replacement of either petalite or spodumene due to cooling.

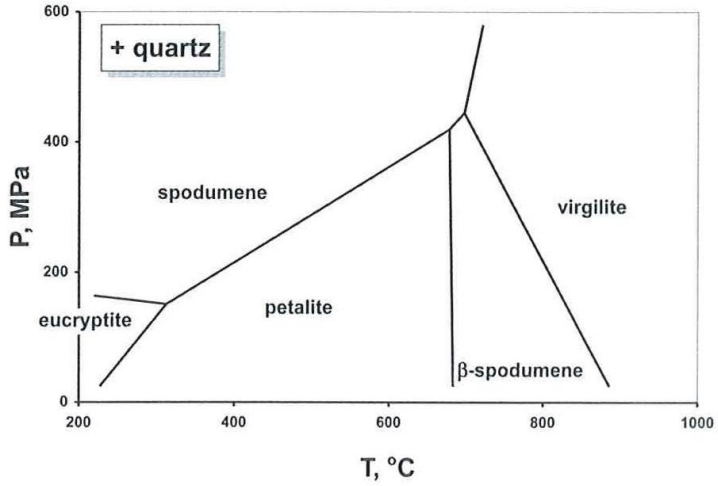

Figure 3. Quartz-saturated stability relations among α-spodumene ($LiAlSi_2O_6$*), eucryptite (*$LiAlSiO_4$*), petalite (*$LiAlSi_4O_{10}$*), β-spodumene (*$LiAlSi_5O_{12}$*), and virgilite (*$LiAlSi_5O_{12}$*) in the system* $LiAlSiO_4$-SiO_2-H_2O. *Modified from London (1984).*

1.6 Research History of Helgeland Pegmatites

Sizeable pegmatite bodies occurring in the Norwegian part of the Caledonian Orogen have since the last world war been mined locally by small-scale entrepreneurs for industrial minerals such as feldspar and quartz. However, the Geological Survey of Norway (NGU) researchers started looking more systematically for pollucite in Helgeland pegmatites in the early 2000s. Pegmatites in Norway, including those in the Helgeland field in the north and those in the Evje-Iveland field in the south, with widths of up to 15 m and strike lengths of up to 50 m, are relatively small in size compared to economic pegmatite deposits worldwide, (Ihlen, 2004; Rosing-Schow et al., 2018). However, larger pegmatite bodies do occur, for example the Ågskardet LCT pegmatite in Helgeland has a width of 35 m and a length of 120-160 m (Ihlen, 2004).

In the Helgeland pegmatite province, there is a lack of compelling evidence for an association of the pegmatite intrusions with larger contemporaneous granitic bodies (Ihlen, 2004; this work). Rather, it has been suggested that the pegmatites were produced by direct partial melting of Paleoproterozoic orthogneisses and Caledonian supracrustal rocks (Larsen et al., 2002; Ihlen, 2004). According to Ihlen (2004), the inspection of 40 pegmatite bodies in Helgeland revealed that they represent at least two discrete Devonian generations, but the geochronological data that led to this model are unpublished and not available to the public.

Interestingly, both Paleoproterozoic and Paleozoic ages were recently reported for a granitic pegmatite field of NYF-character in the Tysfjord region some 200 km northeast of our study region in Helgeland (Müller et al., 2022). Both unzoned and zoned pegmatite bodies have been reported from the Helgeland pegmatite province (Ihlen, 2004). In the Hogtuva area, some 48 km south of our study area, Schilling et al. (2015) reported a U-Pb zircon crystallization age of 434 ± 14 Ma for peraluminous aplites and pegmatites. This was interpreted by these authors to record an imprint of Caledonian metamorphism on Be-mineralised and barren pegmatites.

1.7 Study Hypothesis

The research hypothesis that guided this study is as follows: The granitic pegmatites of the study region (Figure 4) formed by anatexis of Precambrian metasedimentary rocks without involvement of a larger S-type granitic pluton/batholith. The anatectic melting episode that led to granitic pegmatite magmatism occurred during the late stages of the Caledonian orogeny. Given the presence of Li-rich tourmaline, muscovite and garnet in the analysed samples, it is hypothesized that Li- and B-rich metasediments provided the source to this granitic pegmatite swarm in Helgeland. The Helgeland pegmatites form a genetically related cluster, with highly evolved and more primitive granitic magmas coexisting in space and time.

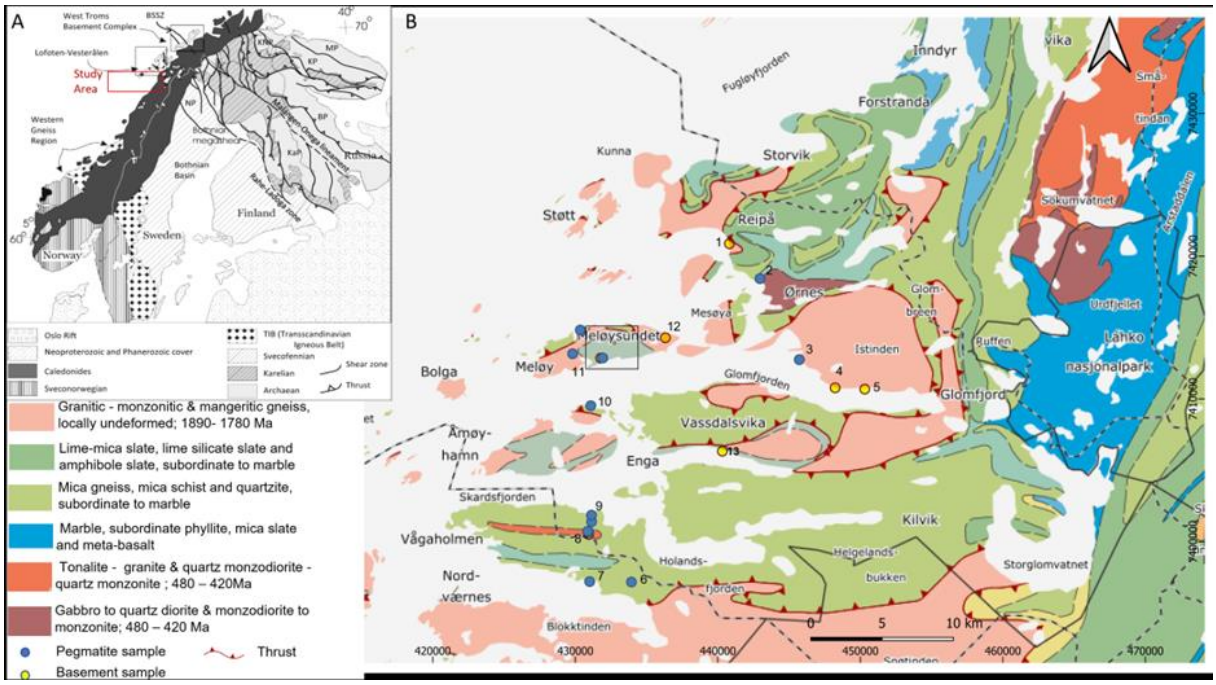

Figure 4. Inset (A). Geological overview map of the Fennoscandian Shield with location (frames) of the West Troms Basement Complex and the Lofoten-Vesterålen area representing tectonic outliers to the west of the Scandinavian Caledonides. Archean and younger provinces and major ductile shear zones are included for the Fennoscandian Shield to the east of the Caledonides. The map is modified from Bergh et al. (2014), Corfu et al. (2003) and Hölttä et al. (2008). Abbreviations are: BP = Belomorian province, BSSZ = Bothnian-Senja shear zone, MP = Murmansk province, KaP = Karelian province, KNP = Kola-Norwegian province, KP = Kola province, NP = Norrbotten province. (B) An outline of the bedrock geology in the coastal area of North Helgeland. Sampled sites:1= Kleiva Quarry,2= Ørnes, 3 = Neverdalen,4 = Selstad,5 = Ytre Holten,6 = 2906R- Rismålstinden, 7= Ågskardet-S,8 = Ågskardet UB,9 = Ågskardet,10 = Grønnøya,11&12 = Meløy,13 = Åsjord. Map base from NGU's bedrock geology of Norway 1:1 350 000 (2023).

1.8 Aims and Objectives

This MSc thesis study aims to investigate a poorly known regional swarm of granitic pegmatites in North Helgeland (Figure 4b, 5) in the vicinity of the town of Ørnes for its field relationships, magma emplacement ages, mineralogy, and geochemistry to address the nature and origin of these potentially economic magmatic bodies.

To achieve these goals, the following research methods were applied:

A. Determination of pegmatite emplacement styles (e.g., cross-cutting relationships to diverse country rock units) and collection of pegmatite plus country rock samples for analytical work.
B. Mineral separation (e.g., zircon, monazite, apatite) and U-Pb age determinations by LA-MC-ICP-MS analysis.

C. Optical petrography and electron microscopy on polished rock thin sections to determine the crystallization sequence.

D. Determining the major element compositions of rock-forming and accessory minerals by electron probe micro-analysis (EPMA) (e.g., feldspar, mica, tourmaline, garnet, apatite).

E. Determining trace element compositions of rock-forming minerals by LA-SF-ICP-MS analysis (e.g., feldspar, mica, tourmaline, garnet).

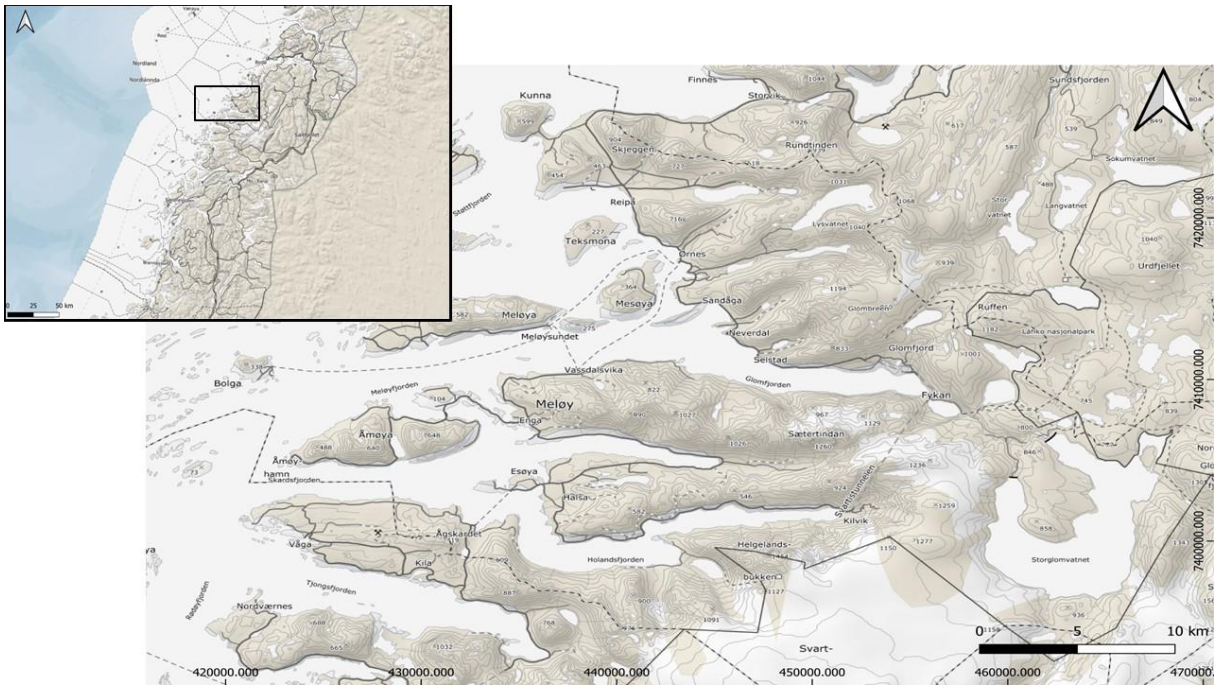

Figure 5. Study area in North Helgeland, central Nordland county, northern Norway. Map base from NGU's topographic map of Norway (1:250,000), 2023.

2 Geological Background

2.1 Fennoscandian Shield

The Fennoscandian Shield (inset Figure 4) is known for its concentric growth during the Archaean and Proterozoic (Gaál & Gorbatschev, 1987). The shield is composed of gradually younger units from the northeast to the southwest (Figure 5). In the northeast of the shield is a Late Archean Domain (3.1–2.6 Ga); in the central portion is an Early Proterozoic (Svecofennian) Domain (2.0–1.75 Ga); and in the southwest is a Mesoproterozoic Sveconorwegian Domain (1.14–0.90 Ga) (Skår, 2002; Åhäll & Connelly, 2008). A major magmatic belt, the Trans-Scandinavian Igneous Belt (TIB), occurs in between the Svecofennian and the Sveconorwegian domains (Gorbatschev, 1985; Högdahl et al., 2004). According to Skår (2002), all four domains were accreted to the Fennoscandian Shield during various orogenic events and were collectively overprinted by the Caledonian orogeny (490-390 Ma) along the western margin of the shield (Müller et al., 2022).

The Archean Domain consists of greenstone belts and trondhjemite-tonalite-granodiorite (TTG) intrusions (Nironen, 1997; Müller et al., 2022), which form the northeastern Fennoscandian basement in NW Russia, Finland, and northern Sweden (Gaál & Gorbatchev, 1987). Two basement outliers, the West Troms Basement Complex (Bergh et al., 2010) and a basement suite in the Lofoten-Vesterålen area (Corfu, 2004), located west of the Scandinavian Caledonides in northern Norway, were previously thought to be exotic tectonostratigraphic units (Hölttä et al., 2008). However, recent studies by Bergh et al. (2010, 2014) developed a sound correlation with the Fennoscandian Shield based on geological and geodynamic evidence.

The Svecofennian Domain consists of several ca. 1.9 Ga magmatic arcs that were accreted to the Archean craton before 1.82 Ga (Müller et al., 2022). The oldest rocks are calcic and calc - alkaline, I-type granitoids ranging from gabbro to granite (Wilson, 1982). The Svecofennian Domain also consists of volcanic rocks that were generated from 1.90 to 1.87 Ga, followed by a younger group of anatectic high-K granites emplaced between 1.85 and 1.82 Ga. Nironen (1997) interpreted the high-K granites as anatectic melts of Svecofennian

metasedimentary units. The youngest group of Svecofennian granitoids was emplaced at 1.80 – 1.77 Ga (Nironen, 1997).

2.2 The Trans-Scandinavian Igneous Belt (TIB)

The TIB forms a giant, elongated array of batholiths stretching along the Scandinavian Peninsula for about 1400 kilometers from southeastern Sweden to Troms in northwestern Norway (Gorbatschev, 1985; Högdahl et al., 2004). It is understood to represent the result of microcontinent–microcontinent and island-arc–microcontinent collisions at the margin of Baltica (Högdahl et al., 2004). Geochemical investigations of TIB plutons to the east and south of the Caledonides reveal subalkaline to alkaline, and metaluminous to peraluminous compositions. In the TIB granite complexes, monzonitic, syenitic and peralkaline granitic rocks dominate, whereas trachytes and rhyolites dominate in the volcanic complexes (Högdahl et al., 2004). Due to their relatively high U (4 ppm) and Th (10 ppm) concentrations, a few of the TIB plutons are classified as high heat production (HHP) granites (Wilson & Åkerblom, 1980).

The TIB is divided into sections by Paleoproterozoic shear zones that strike N-S and extend into the Svecofennian Domain. This results in different ages of the magmatic rocks along the belt (Müller et al., 2022).

TIB magmatism can be divided into two distinct episodes on the basis of age distributions and chemical compositions. The northern part of the belt consists of TIB-1 rocks formed during 1.85 to 1.76 Ga magmatism that was coeval with post-kinematic granites within the Svecofennian Domain (Högdahl et al., 2004). For example, in the northern TIB, the meta-monzonites and meta-syenites of the Sjona and Høgtuva basement windows show ages of 1797 ± 3 Ma and 1800 ± 2 Ma, respectively (Skår, 2002). In contrast, the TIB-2 rocks have ages between 1.72 and 1.65 Ga, and they dominate the central and southern belt, coeval with Rapakivi granite magmatism in southern Finland (Vaasjoki et al., 1991). In many locations within the TIB, mafic rocks are prevalent, and structures of magma mixing are common (Müller et al., 2022). Based on isotopic evidence, it appears that the TIB originated partly by reworking of juvenile Svecofennian crust (2.1 to 1.87 Ga), with the addition of mantle-derived components in a continental arc setting (Müller et al., 2022).

The Precambrian crystalline rocks of Nordland county are exposed west of the Caledonian nappes and in tectonic windows (Figure 7) (Skår, 2002). There are four main tectonic basement windows within the Caledonian nappes of central Nordland: The Svartisen, Glomfjord, Høgtuva and Sjona windows (Skår, 2002). The Helgeland granite gneisses, which host the pegmatites of this study, are located in the Glomfjord tectonic window that is part of the TIB (Skår, 2002). The N-S oriented basement windows are affected by the former continental margin, the regularly reactivated NW-SE striking shear zones, and to an extent by the Caledonian orogeny (Romer & Bax, 1992; Klein et al., 1999). Except for the Høgtuva Be-REE-U-Sn mineralization (Lindahl & Grauch, 1988; Schilling et al., 2015) and the meta-pegmatites of the Tysfjord-Hamarøy area, which are mined for high-purity quartz since the late 1990s, significant economic mineral deposits are unknown from TIB plutons and the regions where they occur.

2.3 Caledonian Orogen

The Caledonian orogen is the product of the Silurian collision between Laurentia and Baltica, marking the final phase of the closure of the Iapetus Ocean, which began in the Ordovician (Gee & Sturt, 1985; Kroner et al., 2021). The orogen comprises several nappe complexes (Figure 6) that are grouped into the Lower, Middle, Upper, and Uppermost Allochthons, characterized by contrasting provenance, tectonic and metamorphic history (Gee & Sturt, 1985; Roberts & Gee, 1985; Gee et al., 2008). The Lower and Middle Allochthon nappes are related to the Baltic craton (Gee & Sturt, 1985; Roberts & Gee, 1985), whereas the Upper Allochthon nappes formed at the continent-ocean transition zone (Andréasson, 1994) and in the Iapetus Ocean (Stephens et al., 1985). The Uppermost Allochthon is thought to have formed in a continental margin setting (Roberts et al., 2007).

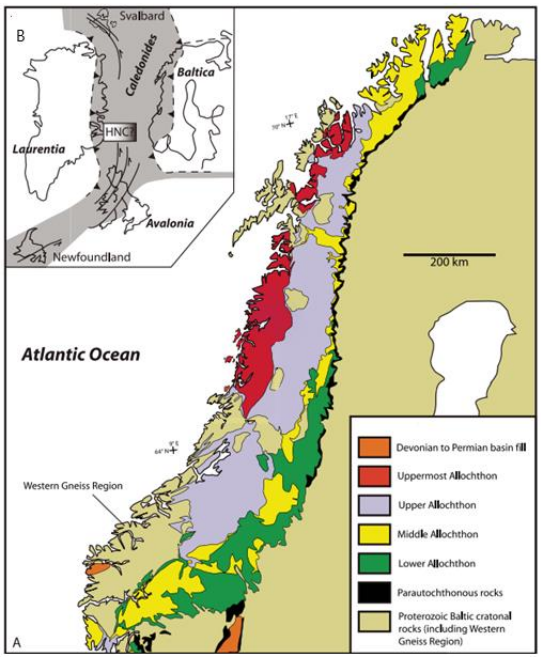

Figure 6. (A) Tectonostratigraphic map displaying the major units within the Scandinavian Caledonides (after Gee & Sturt, 1985). (B) Speculative Ordovician–Silurian reconstruction of the Caledonides and possible location of rocks within the Helgeland Nappe Complex (HNC). After Greiling & Garfunkel (2007).

The Fennoscandian Shield basement was reworked during collisions to varying degrees of intensity in different regions. There is evidence of the western basement windows, including the Helgeland window, being reworked at higher metamorphic grade with more intense granitic rock deformation compared to the central basement windows (Greiling et al., 1993). Folds, fold-trains, lineations, and S–C fabrics in these basement windows indicate early thrusting and nappe emplacement, possibly near continental collision (Larsen et al., 2002; Osmundsen et al., 2003). Numerous N-S striking faults at the margins of the basement-sedimentary cover contact exhibit slight offset, providing evidence for basement reworking during the Caledonian orogeny (Müller et al., 2002).

In Helgeland, the exposed nappes are part of the Uppermost Allochthon comprising two nappe complexes, the structurally higher and lower Helgeland and Röddingsfjell nappe complexes, respectively (Barnes et al., 2007). Both nappe complexes comprise multiple deformed nappes with varying proportions of psammitic, pelitic and calcareous schists, as well as marbles, amphibolites, and gabbroic to granitic intrusions (Gustavson & Gjelle, 1991). The metamorphism of these rocks ranged from low-grade amphibolite facies to high-grade greenschist facies. Mafic, intermediate, and felsic magmatism of various forms and phases

accompanied the Caledonian orogeny (Stephens et al., 1985). The Uppermost Allochthon contains various Caledonian granitic and granodioritic plutons that have not yet been thoroughly investigated. These plutons are located south and northeast of Bodø (Husdal et al., 2017).

2.4 Geology of the study area in North Helgeland

2.4.1 The Basement Gneisses

The Glomfjord basement window (Figure 7) exposes four sub-areas in the study region: Skjeggen, Bjellåtind, Fykan and Glomfjord (Skår, 2002). The granitic gneisses in the region, like in other tectonic windows in central Nordland, occur structurally beneath the Caledonian nappes (Larsen et al., 2002; Skår, 2002). They are part of the TIB (Romer et al., 1992), which formed during the late-stage of the Svecofennian orogeny (1.92 – 1.79 Ga; Lahtinen et al., 2008, 2009). Gustavson and Gjelle (1991) described the Paleoproterozoic rock suites (1795 – 1800 Ma) as granites, tonalites and gabbros, as well as pre-schistose and migmatitic equivalents. They are coarse-grained, foliated meta-granites containing biotite, amphibole, quartz, K-feldspar and albite ranging in color from pale grey to pale red.

At Skjeggen, pink to red microcline gneisses and grey gneisses yielded a Rb–Sr whole-rock isochron age of 1822 ± 70 Ma (Cribb, 1981). To the east at Bjellåtind, pale to grey foliated microcline granite yielded a Rb-Sr age of 1749 ± 53 Ma (Cribb, 1981). Rutland et al. (1960) reported that the southern Glomfjord window, including the Fykan and outer Glomfjord zone, consists of granite – monzonite gneisses, whereas the central area consists of grey granodioritic gneisses. Whole-rock Rb-Sr analyses from different rock types in the Glomfjord area yielded ages of 1694 ± 73 Ma (Wilson & Nicholson, 1973) and 1747 ± 86 Ma (Cribb, 1981).

The Glomfjord basement window, like others in central Nordland, contains strongly deformed rocks at the margins to the overlying Caledonian nappes, but remained relatively undeformed within the window (Skår, 2002). In the Tysfjord area northeast of the Glomfjord window, Andresen and Tull (1986) found that the foliation and re-crystallization of the

granites go down by at least 2500 m from the top (now eroded) Caledonian nappes. Northrup (1997) suggested that the foliation developed under amphibolite-facies conditions during the Caledonian orogeny at ca. 432 Ma.

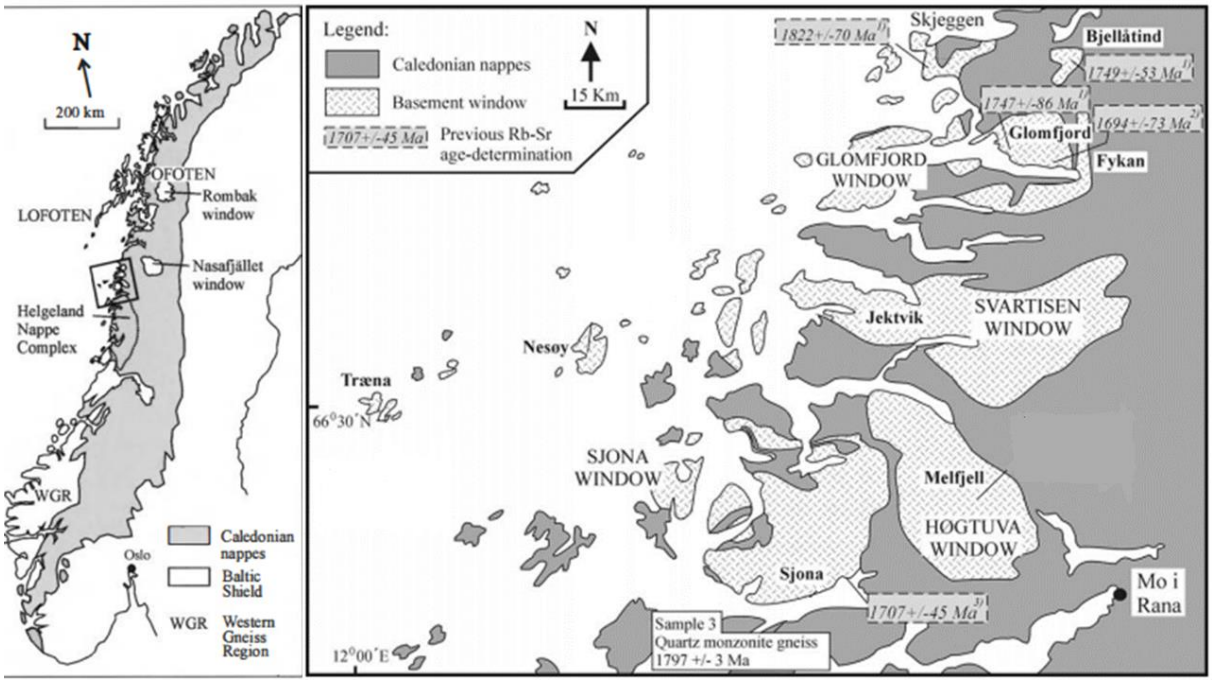

Figure 7. Central Nordland Basement Windows. Interpreted isotopic ages are shown together with the U–Pb sample locations. Modified from Skår (2002) and Larsen et al. (2002). Previous age determinations are from: (1) Cribb (1981); (2) Wilson and Nicholson (1973); (3) Wilberg (1987).

The Caledonian and post-Caledonian deformation are best documented in the Sjona basement window. Pegmatite emplacement and local migmatization from 425 to 407 Ma were the result of a contractional phase, whereas partial melting from 402 to 398 Ma at Træna defines an extensional phase during the late-stage of the Caledonian orogeny (Larsen et al., 2002). Bugge (1963) reports Mo mineralization from the basement and overlying Caledonian schists north of Glomfjord.

2.4.2 The North Helgeland Pegmatites

Professional geologists have not conducted much research on the pegmatites in North Helgeland, hence, knowledge about them is limited. In the early 2000s, a group of geologists from NGU led by Peter Ihlen identified close to 600 pegmatite bodies and conduit systems (>2 m thick) in North Helgeland (Figure 8). Ihlen (2004) identified that the Caledonian cover rocks include more pegmatites than the underlying Paleoproterozoic basement. Tourmaline

is present in pegmatites found in the Caledonian cover but absent in the basement pegmatites (see also Müller et al., 2022). The largest pegmatite bodies in the area have dimensions between 50 and 100 meters in width, and between 400 and 1000 meters in length (e.g., Lysvatn, Bjerangsdalskardet, Rismålstind, Solstrand and Kvina (Ihlen, 2004).

Limited studies have classified most of the pegmatites to be relatively simple and unzoned (Ihlen, 2004; Steiner, personal communication in 2022). Out of the few zoned pegmatites, including Ågskardet, only those at Grønøya show the classic pegmatite structure consisting of a massive quartz core surrounded by a blocky zone of alkali feldspar, albite and muscovite. This also includes an oligoclase-quartz-dominated contact zone with the ultramafic host rocks (Ihlen, 2004). The pegmatites comprise K-feldspar and quartz as main components, with minor but significant amounts of plagioclase, muscovite, biotite, garnet and tourmaline (Ihlen, 2004). Pegmatitic granites occur across the district on a regional scale, but they are most common in the western parts of the region, which also exhibits the highest degree of regional metamorphism (Figure 8). Ihlen (2004) attributes the apparently unsystematic distribution of different pegmatite types on a regional scale to different pulses of magma injections and isolated granitic magma centers. This resulted in the older pegmatites having been overprinted by a younger phase of more fractionated pegmatites with rare-metal enrichment (Be, Li, Ta-Nb and Sn).

Müller (2010) reports beryl or aquamarine occurring in pegmatites in contact zones with the basement windows at Fykavannet and Storglomvann. However, the pegmatites at Ågskardet are the most promising in the area (Ihlen, 2004; Müller, 2010), with over 30 reported minerals including microlite, helvite, beryl, cassiterite, monazite, alkali-rich tourmaline, and apatite. These and other minerals occur together with spodumene in a cleavelandite-rich zone of K-feldspar-quartz-dominant pegmatite (Oftedal, 1950; Neumann, 1985; Ihlen, 2004).

In the Tysfjord tectonic window northeast of the study area, undeformed amazonite-tourmaline pegmatites yielded columbite and zircon U–Pb ages of 400 to 379 Ma (Müller et al., 2022). Schilling et al. (2015) also report crystallization ages of texturally distinct zircons in peraluminous aplites and pegmatites of 434 ± 14 Ma, believed to be the imprint of the Caledonian metamorphism on Be-mineralized and barren pegmatites. Zircon U-Pb analyses

from weakly deformed pegmatites in the Sjona window (southwest of the Glomfjord window) and the Træna window (further west) yielded ages of 409 ± 5 Ma and 403 ± 3 Ma, respectively (Larsen et al., 2002). These early Devonian pegmatites are interpreted to have formed by decompression melting during uplift of the basement gneisses after the Caledonian thrusting from SW to NE (Larsen et al., 2002; Müller et al., 2022).

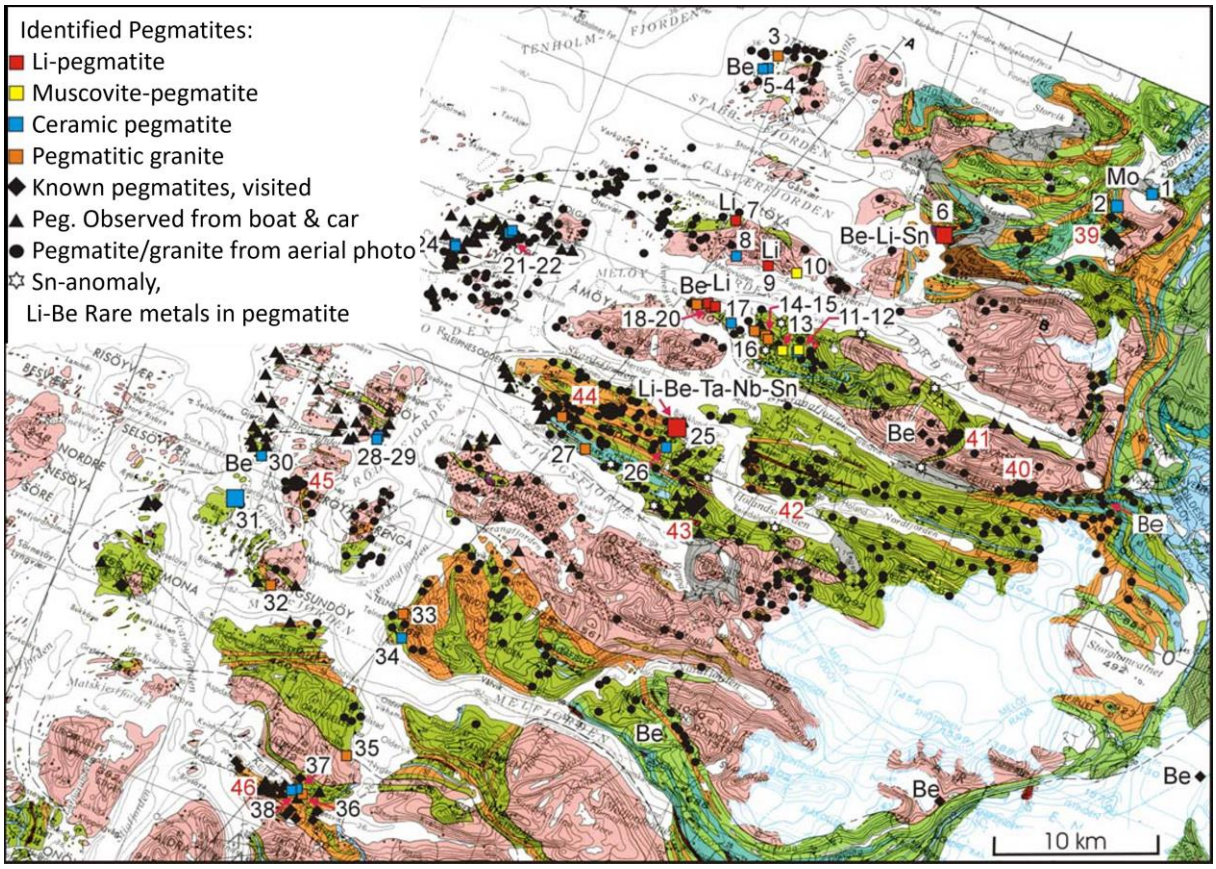

Figure 8. Map showing the distribution of pegmatites and associated mineralization in the southern part of the North Helgeland pegmatite district (Ihlen, 2004). Large symbol sizes indicate large occurrences. The geological base map is from Gustavson and Gjelle (1991).

3 Materials and Methods

3.1 Fieldwork and Sampling

The fieldwork took place from May 28th till June 24th, 2022, in selected areas around Grønnøya, Meløy, Ørnes, Rismålstinden, Glomfjord and Ågskardet, all located in North Helgeland. Focus was set on confirmed pegmatite occurrences earlier identified in the study area by Kuniko Norge AS using remote sensing techniques. Structural data (e.g., strike and dip of foliation planes) of exposed pegmatite bodies and immediate country rocks were collected for documentation purposes and further analysis.

For this study, a total of 89 rock samples consisting of 59 pegmatites, 9 granitic gneisses, 14 mafic gneisses, and 7 paragneiss/metasediments were collected with Prof. Sebastian Tappe. Part of this sample collection was collected by other hired staff of Kuniko Norge AS who explored for Li pegmatites in the region. The rock samples, which typically weighed 2 to 3 kg each, were delivered to the Department of Geosciences at UiT in Tromsø for detailed investigations. Each sample location was documented with field photographs, GPS coordinates (WGS 84), field description, and structural data.

3.2 Sample Preparation

3.2.1 Thin Sections

To reduce the risk of contamination, the first step in processing the rock samples was to wash them clean with a metal scrub. Thin slabs were cut from a variety of basement rock and pegmatite samples. This was done in the Emilbua Lab at the Department of Geosciences at UiT where a diamond rotary saw was used to strategically cut the acquired rock samples (either for representative mineralogy or specific minerals). After that, the samples were sent to the Institute of Mineralogy at the University of Münster in Germany, where polished thick and thin sections were prepared (at a thickness of 100 µm). Table 3 and Appendix 8.1 list selected samples for which thin sections were prepared. Readers should refer to Appendix 8.2 for complete scans of thin sections used in this study.

3.2.2 Carbon Coating

To carry out EPMA analysis, the sample mounts and thin sections required carbon coating. The coating is prepared from 5-50 nm, adequate to generate conductivity on the sample surface, dissipate charge, avoid overcharge, heat, and beam damage on the sample without altering the surface morphology. The coating process was carried out on an "AGAR auto carbon coater" (with glove protection) and involved the placing of the sample on the sample holder after any necessary sharpening of the carbon sources. The top-plate was closed, and the machine was turned on, then the chamber pump was activated (for about 30 seconds). It was essential to verify that the chamber pressure was less than 0.05 mbar (Vacuum Check) and that the following settings were selected: Auto mode, 5.0 V voltage, and a 10 s timer. Carbon evaporation is harmful to the eyes; hence the machine was started without anyone watching. The procedure was repeated as required. This procedure was facilitated by Prof. Sebastian Tappe and Beate Schmitte at the Institute of Mineralogy, University of Münster, Germany. Table 3 contains selected samples used for thin-section-based optical microscopy and EPMA analysis.

Table 3. Selected samples used for thin-section-based optical microscopy and EPMA analysis.

Sample ID	E	N	Locality	Rock Type
RL22-01 A	431085	7409524	Grønnøya	Pegmatite
RL22-01 B	431085	7409524	Grønnøya	Pegmatite
RL22-01 C	431085	7409524	Grønnøya	Pegmatite
RL22-04 I	442956	7418430	Ørnes	Pegmatite
RL22-04 J	442956	7418430	Ørnes	Pegmatite
RL22-05 D	445718	7412753	Neverdalen - road section exposure	Metasedimentary rock
RL22-05 J	445718	7412753	Neverdalen - road section exposure	Pegmatite
RL22-05 F	445718	7412753	Neverdalen - road section exposure	Mafic gneiss
RL22-06 A	430960	7400672	Ågskardet Upper Body	Pegmatite
RL22-16	430865	7400726	Ågskardet Upper Body	Pegmatite
RL22-07 E	431138	7401858	Ågskardet Old Quarry	Pegmatite
RL22-08 C	431138	7401858	Ågskardet Old Quarry	Pegmatite
RL22-08F	431138	7401858	Ågskardet Old Quarry	Pegmatite
RL22-22	430350	7414829	Meløy	Pegmatite
RL22-23C	430350	7414829	Meløy	Pegmatite
RL22-25 A	429811	7413165	Meløy	Pegmatite
2904R	431011	7397201	Ågskardet-South	Pegmatite
2906R	433940	7397169	Rismålstinden	Pegmatite

RL22-02	440319.3	7406336	Åsjord north of Bjærangenfjord	Granitic gneiss
RL22-03 E	440814.4	7420880	Kleiva Quarry, Reipå	Granitic gneiss
RL22-05 D	445717.6	7412753	Neverdalen - road section exposure	Metasediment
RL22-05 F	445717.6	7412753	Neverdalen - road section exposure	Mafic gneiss
RL22-12	448232	7410780	Selstad- road section exposure	Granitic gneiss
RL22-13	450309.6	7410688	Ytre Holten - road section exposure	Granitic gneiss
RL22-18	436323	7414287	Meløy	Granitic gneiss
RL22-24	431784.6	7412865	Meløy	Mafic gneiss

3.2.3 Heavy Mineral Separation

Part of the remaining rock piece was then cut into 3 cm thick slabs totaling about 1.0 to 1.2 kg, which were then reduced into smaller pieces using a hammer and a metal plate. This procedure reduced the rock slabs to chips <10 mm across. After crushing of each sample, the metal plate was thoroughly cleaned under running water with a metal brush and allowed to dry before crushing of the next sample. In the next step, a Retsch hammer mill with a 0.45 mm aperture was used at UiT. This further reduced the grain size for the next step in preparing the samples for heavy mineral separation. For country rock basement samples, only grain sizes <355 µm were collected, whereas three separate grain size fractions were collected for pegmatite samples: >1.18 mm, 500 µm to 1.18 mm, and <500 µm. However, heavy mineral separation using the Wilfley Table at UiT was done exclusively on the <500 µm grain size fraction (and <355 µm fraction for country rocks).

To avoid any sample contamination, the method required a strict cleaning procedure during crushing which included: a well-functioning dust fume extractor, opening up and blowing out all machine parts exposed to sample material using compressed air, alcohol wipe down of all exposed machine parts, cleaning meshes under running water with a plastic brush and further cleaning in an ultra-sonic bath for 5 minutes, cleaning all work benches before and after each sample run while having only one sample at a time in the designated work space.

After obtaining size fractions of <355 µm and <500 µm, separating the heavy and light weight mineral components became the main objective. The heaviest grains in each sample were concentrated using the Wilfley gravity shaking table at UiT. The sample cuts were divided into three grain fractions — heavy, middle and light — by automatic shaking of the

table while it was submerged in flowing water. A grain feeder speed of 12% was used for sample flow onto the Wilfley Table, which ensured effective separation by mitigating sample overload. Considering that zircon crystals (prime target) are among the densest minerals in granitic rocks, only the heaviest portion of each sample underwent further processing. The intermediate and light grain fractions are stored in case they will be needed in the future. Following gravity separation, the samples included heavy mineral concentrate containing zircon, tourmaline, apatite, and opaque minerals such as magnetite, but low-density minerals such as feldspar, quartz and micas were still present in significant quantities.

The samples were then loaded onto lithium heteropolytungstate (LST; density of 2.91 g/cm^3) to further concentrate heavy minerals such as zircon and monazite. Pegmatite samples rich in Fe-garnet (almandine) were not fed into the LST, but rather were directly considered for magnetic separation using a Frantz isodynamic separator at UiT. As zircon has a greater density of 4.65 g/cm^3 than LST, liberated zircon crystals will sink to the bottom of the LST reservoir, while lighter minerals float. The majority of samples does not contain paramagnetic minerals and hence could not be further separated by use of a strong neodymium hand magnet (provided by S. Tappe). The weakly magnetic minerals of the heavy mineral fractions (e.g., zircon) were concentrated further by using a Frantz isodynamic separator. This process was overseen by Prof. Jiří Konopásek.

3.2.4 Preparation for whole-rock analysis

The sample preparation for whole-rock analysis required the rock samples to be pulverized into a homogeneous powder of <20 µm grain size. To obtain such powders of representative rock samples from the study area, crushing and milling of cleaned samples was required. The process was carried out by manually crushing about 300 g of each cleaned sample to a size of <6 mm using a metal plate and a hammer. A Retsch PM 100 agate ball mill was used to pulverize the rock chips into powder employing 13 agate balls in an agate jar. Program 7 (550 rpm at 8 minutes) was used for milling of all samples.

To avoid any sample contamination, the same strict cleaning procedure as during mineral separation work was applied. In addition, special care was taken to fully clean the agate mill after each sample run, which included washing of the agate balls in an ultra-sonic bath for

ca. 5 minutes. The whole process was meticulously executed following the instructions of Prof. Sebastian Tappe.

After dividing the rock powder for each sample into three vials of approximately 50 g each, one batch was submitted to the University of the Witwatersrand in South Africa for trace element analysis by inductively coupled plasma mass spectrometry (ICP-MS), and a second batch to NGU for major element quantification by X-ray fluorescence analysis (XRF). Currently, both facilities experience unforeseen analytical problems, so that these data will only be available during Q4 later in 2023. The remainder of the sample powders is stored at UiT for reference keeping and for different types of analyses to be performed in the near future.

3.3 Petrological Methods

3.3.1 Optical Thin Section Microscopy

The prepared rock thin sections (see Table 3) were analyzed for their petrographic properties using a Zeiss Axio Lab A1 microscope at UiT. Mineralogy and textures, including the paragenetic relationships of the different minerals, were investigated. A Leica DM4500 polarization microscope with an attached Leica DMC4500 camera was used to capture images of up to 20-times magnification. Thin sections of both pegmatites and basement rocks (see Appendix 8.1-2) were analyzed in plane-polarized light (PPL) and cross-polarized light (XPL).

3.3.2 Mineral major element analysis by EPMA

To determine the major and minor element compositions of rock-forming and accessory minerals of the pegmatites (e.g., feldspar, mica, tourmaline, apatite, garnet), electron microprobe analyses were performed on 9 representative granitic pegmatite samples. The complete results of the studied samples are shown in Appendix 8.4.

Analyses were carried out with a JEOL JXA 8530F field-emission electron microprobe on thin sections at the University of Münster, Germany, with the help of Dr. Jasper Berndt-Gerdes. Seventeen elements in total were analyzed, including Si, Ti, Al, Cr, Fe, Mg, Mn, Ca, Ba, Sr, Na, K, Rb, Cs, F, Cl and P. For tourmaline, B was added to the elemental list to be analyzed.

Matrix-matched natural and synthetic reference materials were used for standardization before elemental analyses (Table 4). The accelerating voltage and current were set to 15 kV and 10 nA respectively, and the electron beam diameter was set to of 5 µm, following the procedure of Berndt & Klemme (2022).

All F concentrations were subsequently corrected based on the sample Fe concentrations that were previously determined. The two analyses were merged using the Offline-matrix correction feature of the JEOL instrument software in the final step.

Table 4. Electron microprobe analytical conditions at 15kV and 10nA and 5 µm spot size.

Element	Channel	Diff. crystal	X-ray line	Beam current	Peak/Bkg. Counting time (s)	Reference material
F	1	LDE1	Kα	15	30/15	Ast_Topas
Na	2	TAP	Kα	10	5/2.5	H_Jadeit
Mg	2	TAP	Kα	10	10/5	U_OlivineSanCarlos
Al	2	TAP	Kα	10	10/5	H_DistheneR8
Si	2	PETJ	Kα	10	10/5	U_Hypersthene
K	3	PETJ	Kα	10	5/2.5	H_SanidineP14
Ca	3	PETJ	Kα	10	10/5	H_DiopsideST48
Cl	4	PETJ	Kα	15	30/15	Ast_Tugtupite
S	4	PETJ	Kα	10	10/5	Ast_Celestite
P	4	LIFH	Kα	10	10/5	U_Apatite_P
Ti	5	LIFH	Kα	10	10/5	Ast_Rutile
Fe	5	LIFH	Kα	10	10/5	U_Fayalite
Cr	5	LIFH	Kα	10	10/5	Ast_Cr2O3
Mn	5	LIFH	Kα	10	10/5	Ast_Rhodonite

3.3.3 Mineral trace element analysis by LA-SF-ICP-MS

The polished thin sections of the pegmatite samples were used for the LA-SF-ICP-MS procedure. The analyses were conducted at the Institute of Mineralogy, University of Münster. Minerals were analyzed for trace elements using a 193 nm Photon Machine excimer laser coupled to a ThermoFisher Scientific Element-2 ICP-MS instrument with Sector Field Technology. The analyzed isotopes and the relevant detection limits are available in Appendix 8.5. Helium was used as a carrier gas. The beam diameter, energy density, and repetition rate of the laser were 35 µm, 5.9 J/cm^2, and 10 Hz, respectively. Mass ^{29}Si was used for internal standardization of the LA-ICP-MS data, calibrated against the SiO_2 contents

of the respective minerals as independently determined by EPMA. Signals were collected for every 20 s and 40 s on gas background and unknown samples, respectively. The software Glitter version 4.4.4 was used for ICP-MS data reduction. For calibration of elemental concentrations, the NIST SRM 612 glass was used as the primary standard, whereas BHVO-2G and BIR-1G were used as the secondary standards. Appendix 8.5 contains the complete analytical dataset. For further information regarding accuracy and precision of the trace element concentration data, readers are referred to Appendix 8.5.5.

3.4 Geochronological Methods

3.4.1 Grain mount preparation and SEM imaging

3.4.1.1 Mount Preparation

The first step in preparing the mount is to pour the mineral concentrate into a petri dish and examine it with a binocular microscope. Four samples were found to neither contain zircon, apatite nor monazite; and they were not processed any further. The datable minerals were then handpicked using tweezers. The mount's circular size was traced onto a double-sided tape attached to a glass plate, and the zircon grains were transferred onto the tape using a pipette. The crystals collected for each sample were arranged in a recognizable pattern and documented. Each sample is represented by approximately 70 grains; however, some grains were lost during the polishing process at UiT.

In the next step, the zircon grains were mounted in epoxy resin enclosed in plastic cast support cups of diameter 2.5 cm and labelled with sample number and a reference N point. The epoxy resin was prepared using a mixing ratio of 4:1 of the epoxy resin (Buehler - Epoxy cure 2) and Epofix hardener, respectively. Due to the toxicity of the chemicals, mixing was done using a rod in a fume chamber with rubber glove protection. The mixture was warmed up in an oven for about 5 minutes at 50˚C to release any remaining air bubbles before pouring it carefully over the zircon grains enclosed by a plastic ring and glass plate. The mounts were cured in open air for about 24 hours before separating them from the glass plate. The remaining glue on the mount surface was carefully removed under warm running water before grinding. To ensure that none of the sides protrude with the dried epoxy, the sides of the mount were ground on a rotating sandpaper.

For grinding of mineral grains, the silicon carbide powder Grit 600 (suitable for minerals more prone to breakage) was mixed with a tiny amount of water on a glass plate. The top face of the epoxy cast was then ground against the table in the silicon powder mixture until it was flat. This step was repeated for each of the selected samples. The epoxy casts were polished with Struers Tegramin 30 using a pan cloth and 6 µm synthethic diamond paste for progressive exposure of the mineral grain surface. Before polishing, the samples were cleaned in an ultrasonic device, and then the pan cloth was lubricated with DP lubricant to reduce friction between the sample and cloth. The grain mounts were periodically checked under a reflected light microscope to monitor the level of exposure of the mineral grains. Finally, 3 and 1 µm diamond pastes were used until adequate exposure of the mineral grains was attained.

3.4.2 SEM Imaging

Prior to zircon geochronology work, SEM imaging of the polished grains was carried out at UiT to further characterize grain morphology and internal structure. The mounts did not require carbon coating before the imaging as most of the samples have low charging potential, hence charging effects were minimal. The obtained BSE images of the zircons are contained in Appendix 8.3.

The Hitachi HM3030 Tabletop Microscope SEM at UiT was used for the BSE imaging. The machine allows for highly magnified thin section imaging with enlargements of up to 300,000 times, which provided another level of detail of mineral grains compared to the optical microscope. Attached to the SEM is a Bruker XFlash MIN SVE energy dispersive spectrometer (EDS), which operates on a four segment BSE. Since sample mounts did not require carbon coating before SEM analyses, a low-vacuum mode was employed in the sample chamber. Each sample mount was wiped with ethanol before insertion into the instrument. A working distance of 8.5 mm between the stage and the EDS detector was employed. The use of both the SEM and EDS detectors allowed simultaneous imaging of elemental analysis of the samples.

BSE images that are produced when the electron beam interacts with the sample surface depend on the composition of the sample. This produces various shades of grey in the

resulting images. On BSE images, heavy elements like Fe and those with high atomic numbers appear brighter and offer some insights into compositional variation and distribution.

Using the EDS detector, targeted locations around cores of less metamict zircon grains were identified and characterized chemically in a semi-quantitative manner with the EDS software Quantax 70. The X-ray spectrum obtained from EDS analysis typically consists of peaks corresponding to the characteristic X-rays of various elements. A typical EDS spectrum shows an X-ray count vs. energy (in keV) plot. The peaks are determined by the X-ray energy, and their intensities (peak heights) indicate the elemental abundances. The EDS method can identify elements in concentrations as low as 1.0 wt%, ranging from C to U.

3.4.3 Zircon U-Pb and Lu-Hf isotope analyses by LA-MC-ICP-MS

The U-Pb isotope ratio measurements on zircon crystals from 17 samples were performed on a Nu Plasma-3 MC-ICP-MS instrument at MiMaC/NGU, with sample introduction via a Photon Machines Analyte Excite 193 nm excimer laser system. The samples were subsequently re-oriented and compared with the BSE images to identify the optimal spots for analysis. The laser tuning parameters were a frequency of 6 Hz, a fluence of 2 J/cm^2, and a spot size of 15 µm. Gas blanks were measured for 20 seconds before 20 seconds of laser ablation, followed by a 5 second wash-out period. Ablations were carried out in a He atmosphere and sample aerosol was transported to the ICP-MS instrument by a He carrier gas, with Ar added to the He carrier gas before entering the plasma torch. The isotopic masses 202, 204, 206, 207, 208, 232 and 238 were measured. Identical laser parameters were used for all standard and sample measurements in each analytical sequence. The GJ-1 zircon standard (608.5 ± 1.5 Ma; Jackson et al., 2004) was analyzed at the beginning and end of each run, and between every 10 analyses, as the primary calibration standard. The secondary reference material 91500 (1065.4 ± 0.3 Ma; Wiedenbeck et al., 1995), Z-6412 (1160 ± 2 Ma; unpublished, GSC Ottawa), Plesovice (337.13 ± 0.37; Sláma et al., 2008), Temora-2 (416.8 ± 1.3 Ma; Black et al., 2004), and Sjona (1797 ± 3Ma; Skår, 2002) were analyzed repeatedly to monitor accuracy and precision. The complete U-Pb zircon dataset is

available in Appendix 8.6. Results obtained for the secondary standards are reported in Appendix 8.6.1 and are generally in good agreement with the recommended ages.

U-Pb Data Processing

Results were processed using the 'U-Pb Geochronology' data reduction scheme (DRS) in Iolite v. 4. The calculated U-Pb ages were displayed in concordia and discordia diagrams using the online open-source platform IsoplotR (Vermeesch, 2018). On-peak gas-blank baselines were fit with an 'automatic spline' and subtracted from each channel. Approximately 1 second of collected sample data was discarded from the beginning and end of each analysis. The GJ-1 zircon was used as the primary standard to correct for drift and downhole fractionation, and to normalize $^{238}U/^{206}Pb$ and $^{207}Pb/^{206}Pb$. Exponential fits to the downhole fractionation trends were used for data correction.

Lu-Hf

Hafnium isotope compositions of 146 zircons distributed in the 17 samples were measured by multicollector LA-ICP-MS at the Norwegian Laboratory for Mineral and Materials Characterisation (MiMaC) at the Geological Survey of Norway. The polished zircons in epoxy rounds were ablated with a Teledyne-Cetac Analyte Excite 193 nm excimer laser equipped with a HelEx II two-volume cell. A laser beam diameter of 40 µm was used to ablate the previously dated zircon domains, either covering the spots ablated for U-Pb determinations or placed in similar BSE textural domains. A laser fluence of 4 J/cm^2 and a repetition rate of 9 Hz ablated the grains for 45 s. Each ablation was preceded by 35 s gas-blank baselines and followed by 5 s washouts. A He and Ar gas mixture transported the ablated aerosols to the MC-ICP-MS. Adjacent faraday cups with 10^{11} Ω resistors with an integration period of 0.1 s measured isotopes with masses between 171 and 180.

To normalise the $^{176}Hf/^{177}Hf$ and calculate a scaling factor between Yb and Hf mass bias, the standards Plešovice (Sláma et al., 2008) and MUNZirc4 (Fisher et al., 2011) were used, respectively. These standards were analysed at the beginning and end of each run and bracketing every 8-10 analyses of unknowns and two quality-control ("secondary") standards, including MUNZirc3 and MUNZirc4.

Data were processed with Iolite v. 4 using a customised data reduction scheme. A summary of the calculations performed by the data reduction scheme is as follows:

1) On-peak baselines are fit with an "automatic spline" and subtracted from each channel.
2) Hafnium mass bias (βHf) is calculated relative to $^{179}Hf/^{177}Hf = 0.7325$[1,2] (Patchett and Tatsumoto, 1980, 1981). A standard with relatively high Yb/Hf (MUNZirc 4) is used to calculate a scaling factor between βHf and βYb ("Xbeta" = βYb/βHf). Reference ratios for $^{173}Yb/^{171}Yb$ and $^{176}Yb/^{173}Yb$ from Segal et al. (2003) were used, respectively, to calculate Yb mass bias and correct the interference of ^{176}Yb on ^{176}Hf. Throughout, we used the exponential mass-bias law.
3) Ytterbium-176 is subtracted from the total ^{176}(Hf+Lu+Yb) signal in each measurement in two different ways: (*a*) By using the measured ^{173}Yb signal, a canonical $^{176}Yb/^{173}Yb$ ratio, and measured βHf scaled by Xbeta (determined using the bracketing measurements of MUNZirc4). The same scaled mass-bias factor (βHf*Xbeta), measured ^{175}Lu signal, and a canonical $^{176}Lu/^{175}Lu = 0.02656$[4] (Chu et al., 2002) are used to subtract ^{176}Lu from the residual ^{176}(Hf+Lu) signal; (*b*) By using the βYb and βHf determined internally for each measurement for Yb (and Lu) and Hf isotope ratios, respectively.
4) The residual ^{176}Lu and ^{177}Hf signals and the average of βHf and βHf*Xbeta are used to calculate the interference- and mass-bias-corrected $^{176}Lu/^{177}Hf$.
5) The residual ^{176}Hf and ^{177}Hf signals and βHf is used to calculate the interference- and mass-bias-corrected $^{176}Hf/^{177}Hf$.
6) The final $^{176}Hf/^{177}Hf$ is normalised relative to $^{176}Hf/^{177}Hf = 0.282482$ for Plešovice (Sláma et al., 2008).
7) Internal uncertainties on all results are calculated as 2 SE of the individual measurements ("integrations") during analysis with 3 SD outlier rejection.

The $^{176}Hf/^{177}Hf$ calculated by either method *a* or *b* outlined in step 3 of the data reduction was selected based on the following criteria: If the measured $^{176}Yb/^{177}Hf$ was greater than 0.055 and the difference between $^{176}Hf/^{177}Hf$ determined by methods *a* and *b* was greater

than 0.8 ε-units (80 ppm), then the $^{176}Hf/^{177}Hf$ from method *b* was selected. Otherwise, the $^{176}Hf/^{177}Hf$ from the method *a* was selected.

Initial $^{176}Hf/^{177}Hf$ ($^{176}Hf/^{177}Hf_i$) for each spot analysis was calculated using the corrected $^{176}Hf/^{177}Hf$ and $^{176}Lu/^{177}Hf$, $\lambda^{176}Lu=1.867 \times 10^{-11}$ yr^{-1} (Scherer et al., 2001; Söderlund et al., 2004) and the U-Pb date of the corresponding zircon domain. Initial εHf (εHf_i) was calculated from $^{176}Hf/^{177}Hf_i$ relative to CHUR (at the age of the zircon domain) with present-day $^{176}Hf/^{177}Hf = 0.282785$ and $^{176}Lu/^{177}Hf= 0.0336$[7] (Bouvier et al., 2008). Two-stage depleted-mantle model ages (T_{DM}) were calculated relative to a depleted mantle model reservoir with present-day $^{176}Hf/^{177}Hf = 0.28325$[8,9,10] (Griffin et al., 2000; Griffin et al., 2002; Nowell et al., 1998) and $^{176}Lu/^{177}Hf= 0.0384$[10] (Griffin et al., 2002), and the crustal average $^{176}Lu/^{177}Hf = 0.015$[10] (Griffin et al., 2002) for the Hf isotopic evolution of crustal magma sources after separation from the depleted mantle.

The $^{176}Hf/^{177}Hf$ determined for the secondary reference zircons are as follows (average $^{176}Hf/^{177}Hf$ ± 2 SD, n): Mud Tank: 0.282517 ± 2.5 x 10^{-5}, 9 (reference: 0.282507 ± 3; Woodhead and Hergt, 2005); 91500: 0.282313 ± 2.7 x 10^{-5}, 9 (reference: 0.282308 ± 3; Blichert-Toft, 2008); MUNZirc 1,3, and 4: 0.282136 ± 4.2 x 10^{-5}, 27 (reference: 0.282140 ± 8 [from solution MC-ICP-MS]; Fisher et al., 2011). Hf analyses were excluded based on a selection duration shorter than 15 s or had propagated εHf uncertainties >2 ε-units following final data reduction. For the complete analytical data for Lu-Hf isotopic compositions in zircons, readers should refer to Appendix 8.7.

4 Results

4.1 Field Description and Petrographic Analysis

Most of the investigated pegmatites showed simple mineralogy of quartz-K-feldspar-biotite and quartz-K-feldspar-plagioclase-tourmaline-muscovite-biotite, with either simple or no internal zonation, indicative of limited internal evolution within most of the pegmatites. The descriptions from field observations are combined with BSE images and optical microscopy of thin sections for a more complete understanding of mineralogy as well as the

crystallization sequence and relationships. Appendix 8.2.1-2 contains thin sections scans and a summary of further petrographic analyses of thin sections from this study.

4.1.1 Granitic Pegmatites

4.1.1.1 Ørnes

The Ørnes pegmatite was surveyed because it was identified as a high-priority Be-Li rare metal pegmatite by Ihlen (2004). The pegmatite can be reached from the town of Ørnes via a steep scree slope and a dense forest. The pegmatite body essentially creates a cliff face that is about 40 m high and 30 m wide, with a forested top (Figure 9a). As a result, only the cliff face and several rolled over boulders at the base of the cliff are within reach. The pegmatite has a general trend of 030˚NE and occurs in contact with an amphibolite gneiss that shows evidence of migmatization. The pegmatite samples are coarse-grained with feldspar/albite, quartz and minor amounts of muscovite, schorl, garnet, tourmaline and opaque minerals. Apatite, zircon, monazite and beryl occur as accessory minerals. The coarse-grained texture displays graphic intergrowth of quartz and K-feldspar, and it is not uncommon to find unidirectional crystallization texture in feldspar with quartz-tourmaline pockets forming at the crystallization front of the feldspar (Figure 9b). This could possibly reflect the formation of a boundary layer liquid rich in water and boron after feldspar crystallization. A less common finer grained variety show tourmaline formed in miarolitic cavities (Figure 9c). Generally, the accessible pegmatite portions show no evidence of internal mineral zonation except for the contact zone with the host rocks, which is characterized by a fine-grained mosaic texture in the wall zone. A smaller pegmatite vein about 10 cm wide and 5 m long occurs below the main pegmatite outcrop and cuts the foliation of the host rock obliquely. The mafic host rock is rich in garnet, and some parts have been metamorphosed into garnetites after the felsic components were melt mobilized.

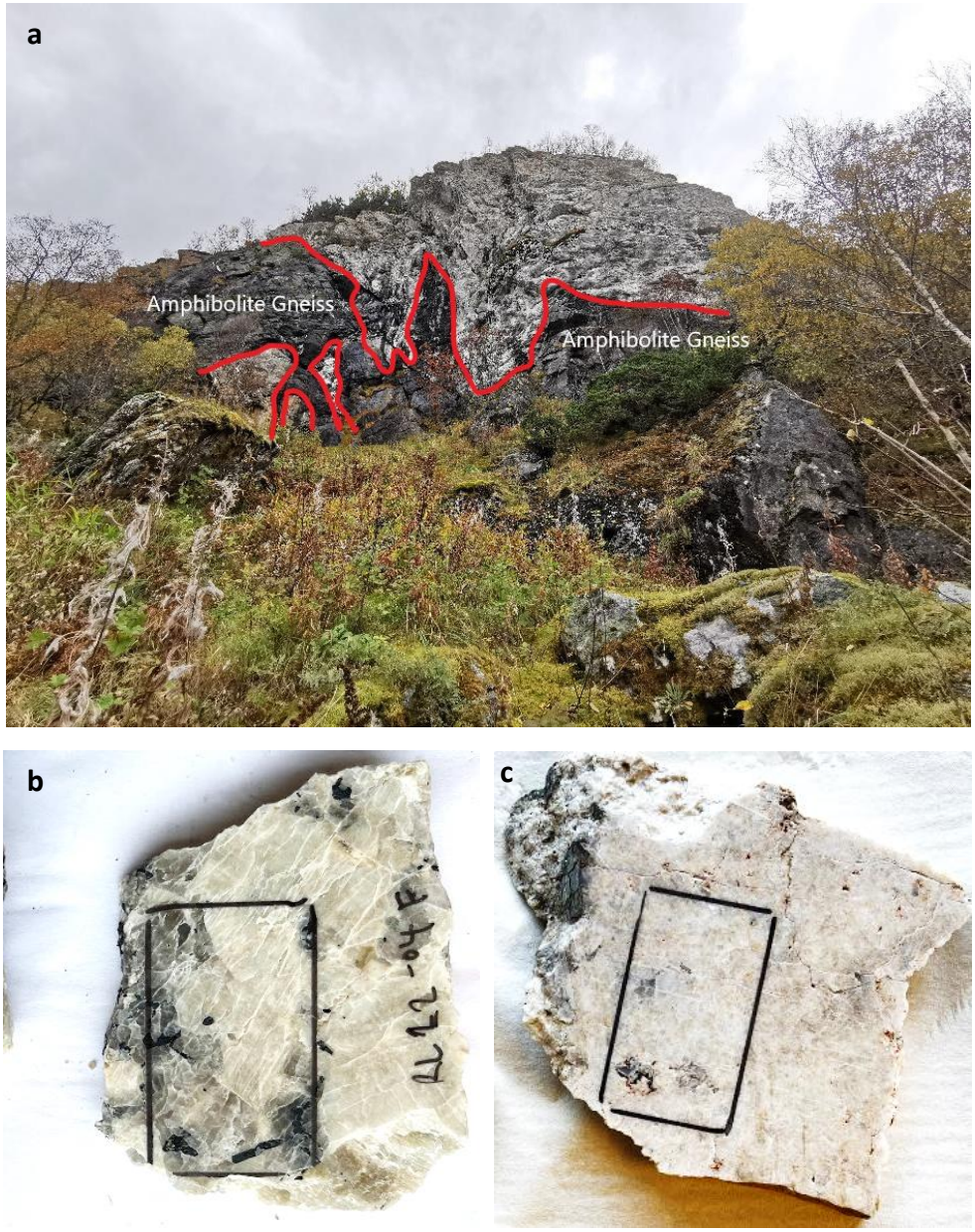

Figure 9.(a) Ørnes pegmatites showing rafts of host amphibolite gneiss in the border zone, (b) unidirectional growth of feldspar from top-right to bottom-left, with quartz-tourmaline pockets forming at the crystallization front of the feldspar, (c) fine grained recrystallized pegmatite with tourmaline forming in miarolitic cavity. Scale is outline of thin section on hand samples.

Thin Section

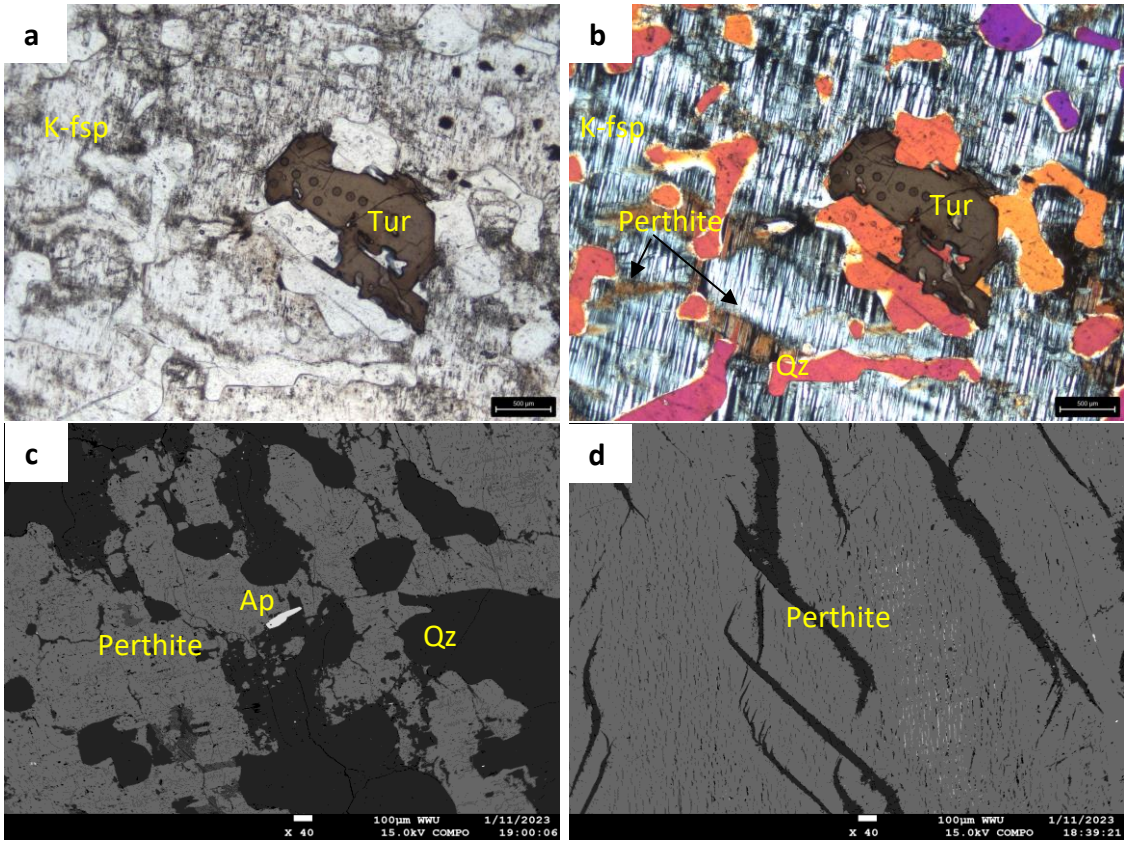

Figure 10. Photomicrographs of sample RL22-04J1 from Ørnes in thin section. (a) in ppl, (b) in xpl, (c, d) BSE images. (a,b) quartz forms spheroidal blebs and precipitates in deformed tourmaline, apatite crystal (white) precipitating in perthite-quartz pockets, (d) perthite showing albite exsolution lamellae(dark grey) in K-feldspar. Ap = apatite, K-fsp = K-feldspar, Tur = tourmaline, Qz = quartz.

Sample RL22-04J1 is a deformed pegmatite with the following mineral assemblage: quartz (25%), K-feldspar (40%) plagioclase (15%), chlorite (3%), garnet (5%), tourmaline (5%), and opaque minerals (7%). Quartz has highly a variable grain size from < 0.10 mm to 3 mm, and crystals form irregular to spheroidal shaped blebs (Figures 10a, b). Deformation in the rock is expressed as undulose extinction in few quartz crystals. K-feldspar forms perthite with a colorless and a grainy appearance in plane polars (Figures 10c, d). Crystals can be up to 3mm in size and display an intergrowth with quartz in a graphic texture. Plagioclase mostly forms exsolved albite in K-felspars, but a few altered discrete plagioclase crystals also occur. They display the characteristic polysynthetic twinning, apart from a few that pinch out. Biotites are altered into chlorite that form subhedral lathlike crystals with well-developed cleavages and display weak green to grey interference colors. Garnet is subhedral and ~5 mm in size with several irregular fractures. It contains inclusions of chlorite, quartz and opaque minerals

which infers a late-stage formation. Tourmaline occurs as 1.5 to 2 mm euhedral crystals (Figures 10a, b) that have partially been deformed and disfigured by micro-faulting in the rock. They display slight compositional zoning with a light brown core and dark brown rim and often associated with quartz and perthite. Anhedral dark opaque minerals (0.5 - 3 mm) occur mostly as irregular replacement minerals in quartz. BSE images confirmed the presence of apatite as an accessory mineral ~0.2mm in size forming in quartz and K-feldspar (Figure 10c).

4.1.1.2 Grønnøya

The Grønnøya Island pegmatite field is located west of Jektvika, near the shoreline and a small settlement. Ihlen (2004) described three N-S trending pegmatites that were mined locally for feldspar during WWII. For our study, six N-S trending pegmatite bodies were delineated, however, only one site provided good exposure free of vegetation. The visited outcrop was previously mined for minerals and hence offers a good exposure for study. The pegmatite body has a strike of 010˚N and is ~20 m wide and 70 m long. It occurs as a discordant body in an amphibolite at the coast of Grønnøya. The pegmatite samples contain smoky quartz, K-feldspars, albite, tourmaline (schorl), green Fe-rich muscovite, biotite and minor amounts of garnets (almandine-rich). Although it lacked clarity due to quarry excavations, it was possible to identify some local evidence of internal mineral zonation in the pegmatite body. It consists of a thin border zone made up of mosaic textures of quartz, K-feldspar, albite; a relatively coarser grained wall zone consisting of quartz, K-feldspar, albite, almandine, and 30 by 10 cm large biotite and tourmaline crystals with inward perpendicular growth from the contact into the pegmatite (Figure 11a). The intermediate zone contains coarser grained quartz, muscovite, increased amounts of K-feldspar and less albite, whereas the core zone contains predominantly quartz including the rose quartz variety (Figure 11b). In some pegmatite boulders, garnet occurs mostly together with tourmaline veins that cut the rock at a late stage (Figure 11c). In these veins, tourmaline does not show crystal faces and appears rather massive.

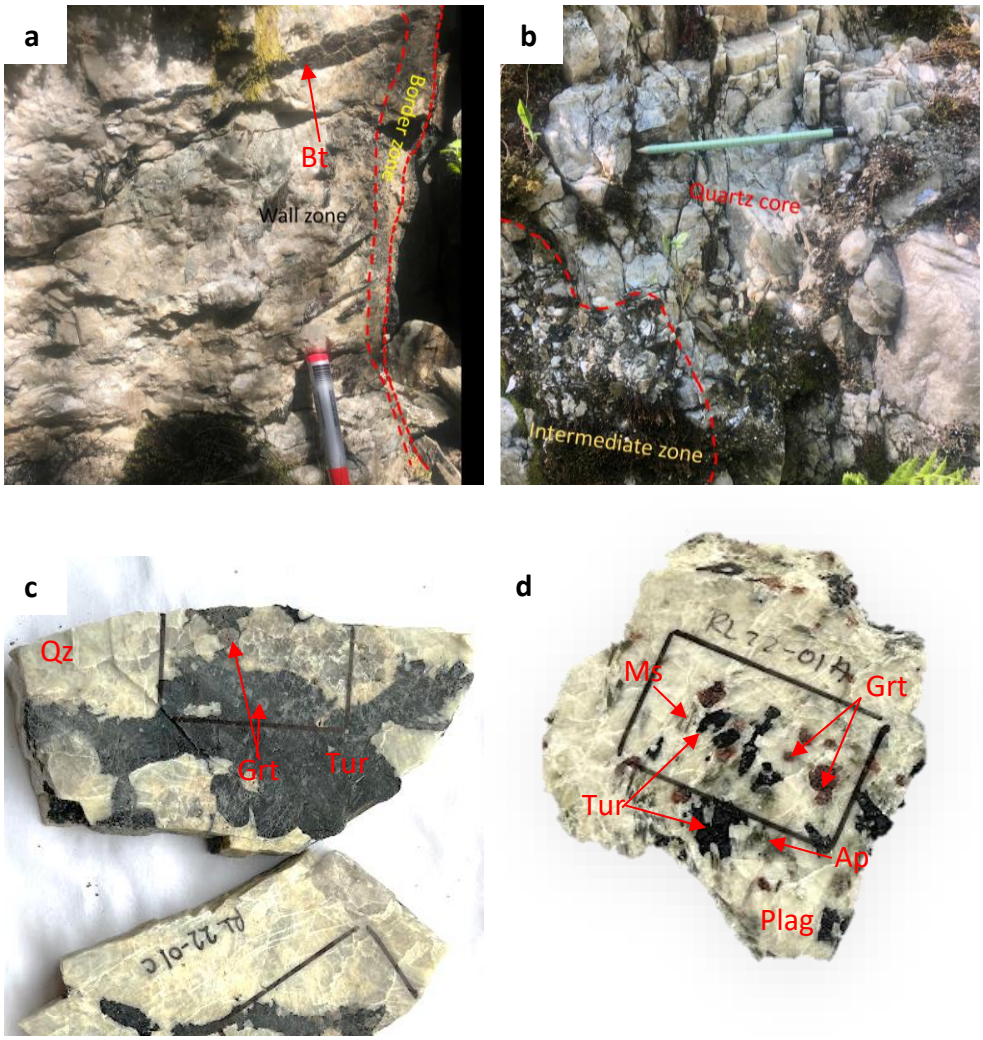

Figure 11. (a) 30 cm long biotite crystal displaying inward perpendicular growth within the border zone in the Grønnøya pegmatite. (b) monomineralic quartz core and an intermediate zone consisting of coarse crystals of muscovite, quartz and K-feldspar, (c) euhedral garnet crystals (red) that form in black tourmaline veins, (d) tourmaline (black), euhedral garnet (red), muscovite (grey), and green apatite. Scale is the outline of thin sections on hand samples. Ap = apatite, Bt =biotite, Grt = garnet, Ms = muscovite, Plag = plagioclase, Tur = tourmaline, Qz = quartz.

Thin Section

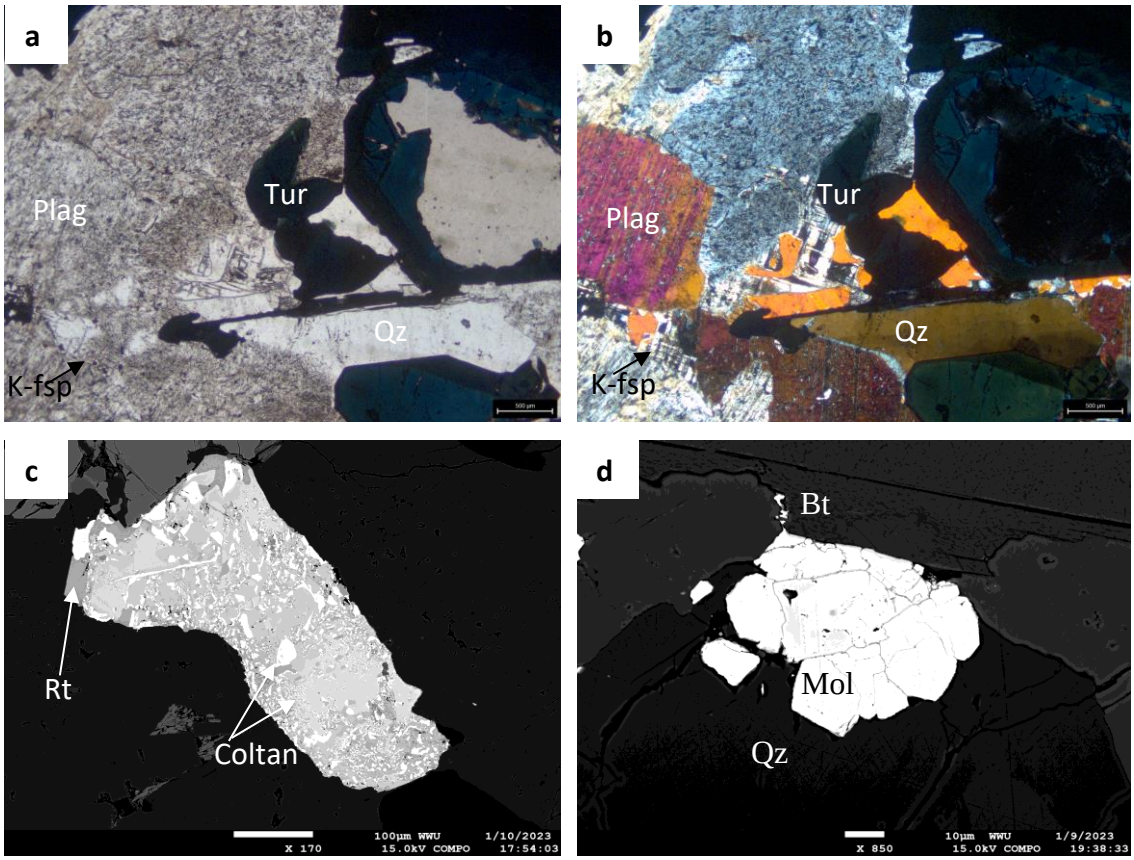

Figure 12. Photomicrographs of sample RL22-O1A from Grønnøya in thin section. (a) in ppl, (b) in xpl, (c, d) BSE images. (a, b) tourmaline crystal with resorbed core and euhedral overgrowth in a matrix of quartz, plagioclase and K-feldspar, (c) replacement of rutile (grey) by coltan (white) crystals, (d) molybdenite precipitating in pockets of quartz and biotite. Bt = biotite, K-fsp = K-feldspar, Mol = molybdenite, Plag = plagioclase, Rt = rutile, Tur = tourmaline, Qz = quartz.

The pegmatite thin section (RL22-01A) shows some deformation zones of stretched minerals with preferred alignment. The mineral assemblage consists of 30% K-feldspar, 25% plagioclase, 15% quartz, 15% tourmaline, 5% garnet, 5% muscovite, 5% apatite, and < 1% zircon. Quartz consists of crystals of up to 3 mm in size with rounded edges and fills the interstices between interlocking feldspar crystals. K-feldspar is mostly microcline and can occur as perthite with albitic exsolution. Cleaner looking patches of feldspar are surrounded by a greyish film of fine-grained altered feldspar. Muscovite occurs as big platy colorless crystals with a mottled extinction and hosts opaque minerals. A film of clean looking tiny flakes of muscovite recrystallizes on the edges of larger muscovite flakes, and a secondary generation of larger aligned muscovite crystals also cross-cut tourmaline and feldspar crystals. Biotite is present as brown tabular crystals with strong pleochroism and contains

small inclusions of muscovite and tourmaline. Tourmaline is present as up to ~ 18 mm long crystals that show strong blue to brown pleochroism, with dark opaque cores and transparent brown rims. They may have resorbed cores with euhedral overgrowth (Figures 12a, b), and some appear more diffuse and patchier. Tourmaline and garnet often show sharp magmatic contact. The garnets are subhedral, have irregular fractures and often contain inclusions that can reach 1mm. Some garnet crystals also form in interstices between tourmaline crystals. Apatites are ~ 0.6 mm size crystals and form a magmatic contact with tourmaline and plagioclase. EPMA analyses revealed that rutile, coltan, and molybdenite also occur as accessory minerals (Figures 12 c, d).

4.1.1.3 Ågskardet Old Quarry

The pegmatite deposit is located close to the beach about 2 km NW of the ferry berth at Ågskardet. Ihlen (2004) reports previous mining of coarse-grained muscovite in five small quarries on the pegmatite stretch. Pegmatite outcrops are scarce and only minimally exposed outside the quarries, hence the walls of the old muscovite quarries provide the best pegmatite exposures (Ihlen, 2004). However, at the time of visit in May-June 2023, the pegmatites had been blasted off into a muckpile. Despite this, boulders from the blast exposed a wide variety of minerals, which were sampled for our study. According to Ihlen (2004), the Ågskardet pegmatite body strikes WSW-ENE and forms a steep lens-shaped body with thickness and length of up to ~36 m and 160 m respectively flanked to the east and west by gneisses along well-exposed escarpments. The pegmatite samples are coarse grained containing plagioclase, K-feldspar, quartz and muscovite, with tourmaline, garnet and biotite as minor minerals. Accessory minerals include green apatite, zircon, cookeite, coltan, and spodumene. The pegmatite displays a graphic intergrowth between quartz and K-feldspar. Quartz transitions from milky to rose quartz varieties and occurs as interstitial crystals within unidirectionally crystallized feldspar that also contain garnet, tourmaline and 1-4 cm large books of biotite and muscovite. At the old quarry, the host rocks are polydeformed, strongly foliated metasedimentary rocks that exhibit isoclinal folds (Figure 13a). The pegmatites have a crosscutting relationship with the foliation of the metasedimentary host rocks. The presence of discrete brecciated zones of garnet and tourmaline in cut rock sections suggests brittle deformation of the main pegmatite body

(Figure 13b). It is also common to find olive green muscovites (Figure 13c) and pink Li chlorite (cookeite) (Figure 13d) inside fractures within large albite crystals interpreted as secondary hydrothermal mineralization (Figure 13d) (e.g., Ihlen 2004).

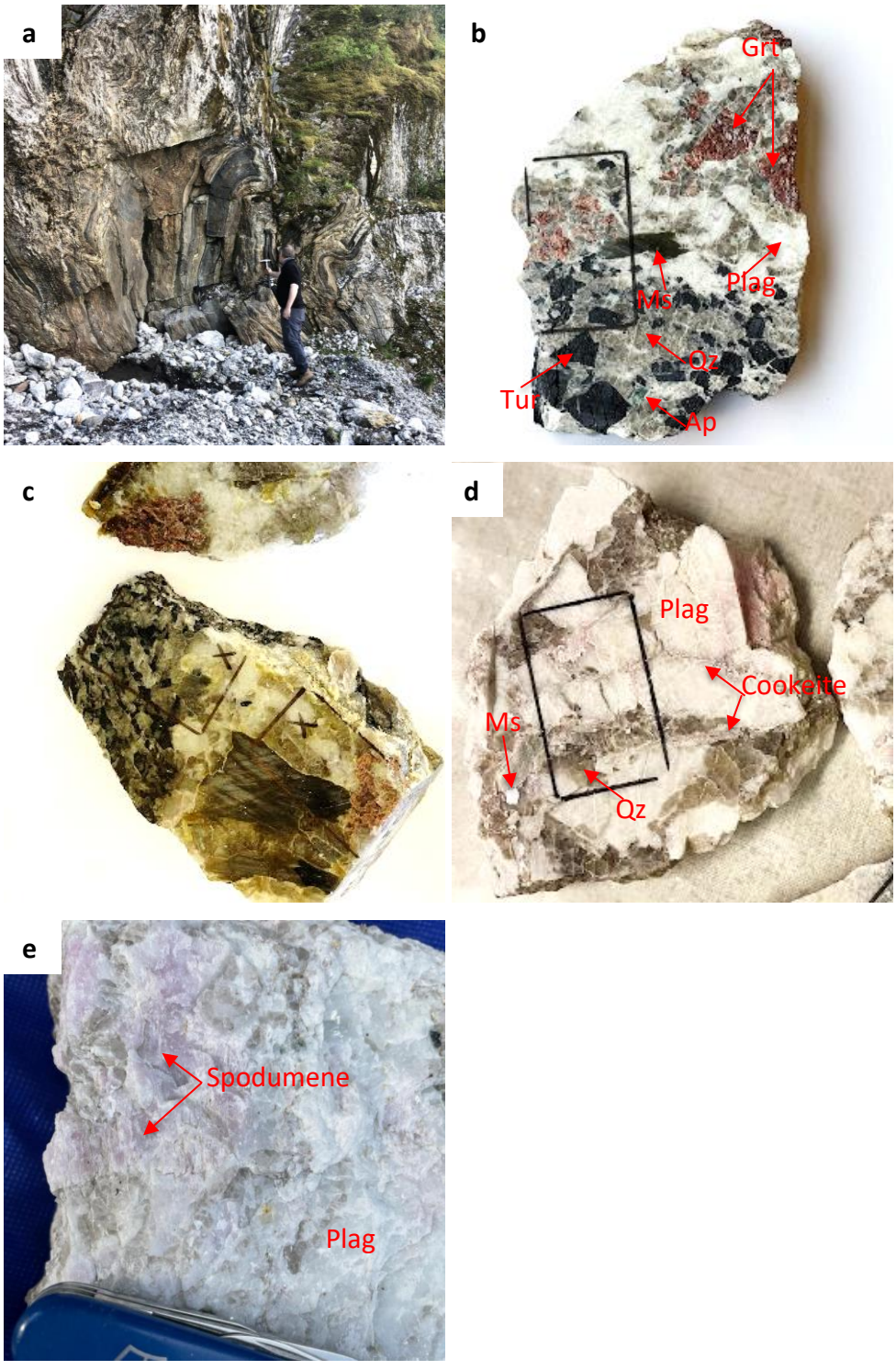

Figure 13. (a) Poly-deformed metasedimentary rocks showing isoclinal folds exposed in in the Ågskardet OQ. (b) K-feldspar-quartz crystal intergrowths and garnet crosscut by quartz-tourmaline breccia along a network of cracks. (c) association of olive-green muscovite, tourmaline, garnet and quartz in a strongly hydrothermally overprinted pegmatite sample, (d) interstitial quartz crystals in albite with pink cookeite (Li chlorite) and muscovite precipitating in feldspar cracks (e) pink spodumene crystal in a plagioclase matrix. Scale is outline of thin section on hand samples. Ap = apatite, , Grt = garnet, Ms = muscovite, Plag = plagioclase, Tur = tourmaline, Qz = quartz.

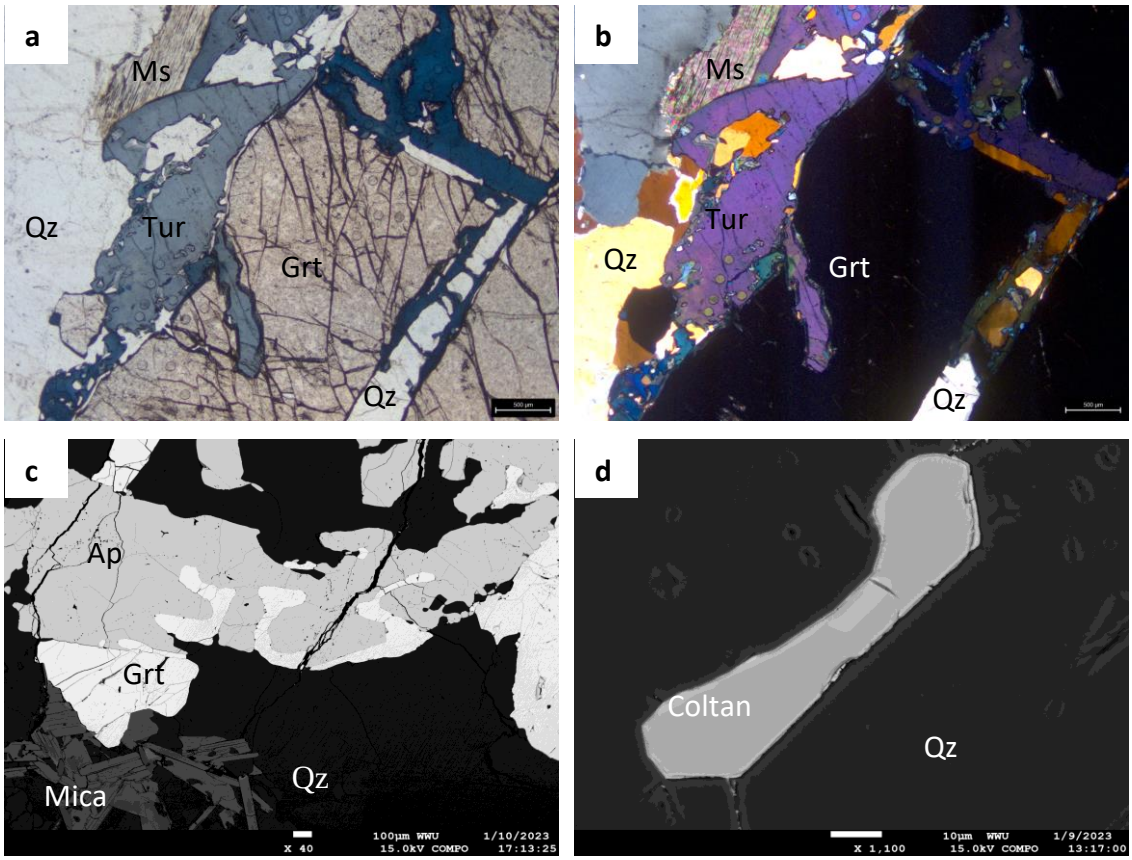

Figure 14. Photomicrographs of sample RL22-08C from Ågskardet OQ in thin section. (a) in ppl, (b) in xpl. (c, d) BSE images. (a, b) quartz-tourmaline ingrowth in garnet cracks, (c) garnet-apatite crystal intergrowths, (d) interstitial coltan crystal in quartz crystal boundary. Ap = apatite, Grt = garnet, Ms = muscovite, Tur = tourmaline, Qz = quartz.

The mineral assemblage of the Agskardet OQ pegmatite (RL22-08C) consists of quartz (20%), plagioclase (20%), garnet (30 %), muscovite (10%), apatite (8%), K-feldspar (10%), and tourmaline (5%). Quartz forms clear anhedral crystals up to 3 mm with some crystals displaying grain boundary migration. Deformation in the rock has developed subgrains in quartz that show undulose extinction. Plagioclase dominates in feldspar composition mostly as tabular crystals that can reach 5 mm in size. About 50% of the plagioclase has been altered into sericite. The crystals display subgrain aggregates with wavey and discontinuous lamellae twinning. Garnets form large euhedral crystals up to 20 mm with several irregular fractures. These fractures are filled with anhedral tourmaline, apatite, and quartz crystals inferring a relatively earlier crystallization of garnet (Figures 14a, b). The patchy anhedral tourmalines display some compositional zoning with dark purple cores and lighter rims. Muscovite occurs as colorless, elongated laths between 0.2 and 1 mm with bright interference colors, and is often associated with tourmaline, quartz, and plagioclase. Apatite

forms colorless anhedral crystals of up to 3 mm and often occurs as inclusions or intergrowths with garnet (Figure 14c). BSE images reveal coltan precipitating in quartz interstices (Figure 14d) as well as compositional zoning in euhedral mica crystals with dark cores and lighter rims.

4.1.1.4 Ågskardet- Upper Body

A similar lenticular pegmatite body occurs on a steep cliff just about 1 km south of the Ågskardet Quarry. The field photo (Figure 15a) shows a large white pegmatite body that sticks out of the forest at a ~20˚ angle to the main foliation of the basement. The pegmatite body has a thickness and length of up to 50 m and 150 m, respectively. It trends NW-SE. The internal structure of the pegmatite is mostly homogenous across the body. The pegmatite contains quartz, large K-feldspar crystals up to 40 cm across, plagioclase and biotite, plus minor amounts of garnet, apatite and tourmaline. Muscovite, zircon and monazite are present as accessory components. There is no visible zonation, but it is noted that the outcrop conditions are relatively poor. Graphic intergrowth between quartz and feldspar was observed in some of our pegmatite samples. Quartz is well developed in the feldspar cleavage planes where it occurs as smoky quartz, whereas rose quartz is observed in other parts of the pegmatite samples. The feldspars appear murky in hand sample due to secondary hydrothermal alteration. Cut sections through the pegmatite samples show that minerals have been weakly sheared in places (Figure 15c), with development of porphyroblastic garnet, quartz and feldspar crystals along the pegmatite margins. No contact was observed between the pegmatite body and its host rocks, but paragneisses of the basement were observed in ~200 m distance from the inferred pegmatite margins.

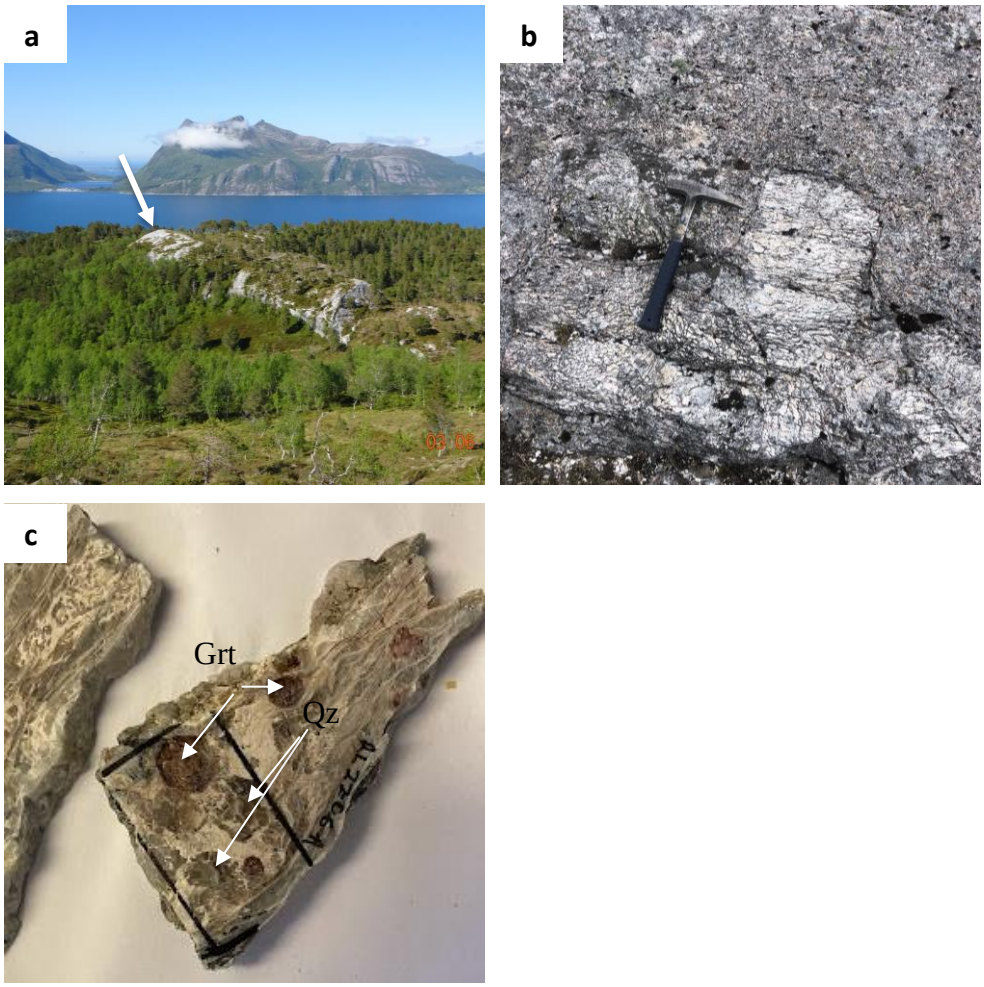

Figure 15. (a) the arrow points to the deformed pegmatite body occurring close to the fjord at Ågskardet-S, (b) large feldspar crystals up to 40cm in size in pegmatite, (c) garnet and quartz porphyroblasts in a quartz-plagioclase matrix. Scale is the outline of thin sections on hand samples. Grt = garnet, Qz = quartz.

Thin Section

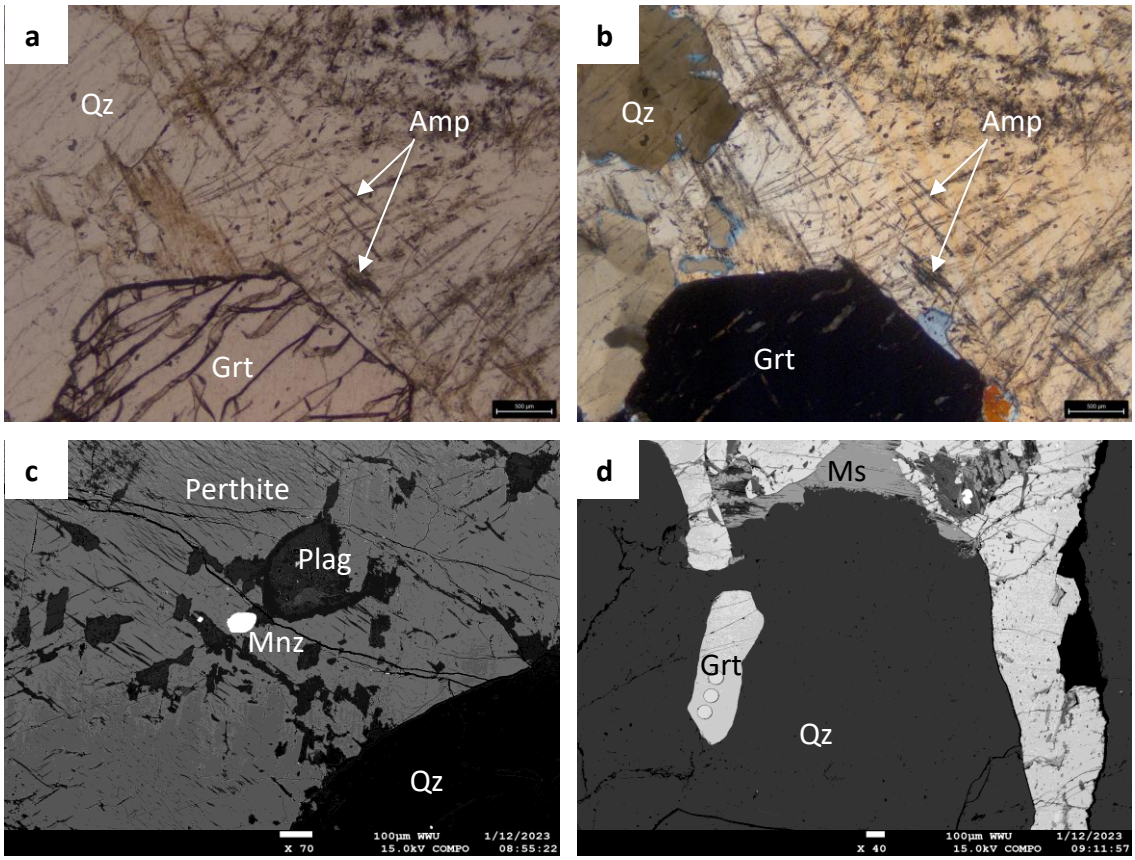

Figure 16. Photomicrographs of sample RL22-06A from Ågskardet UB in thin section. (a) in ppl, (b) in xpl. (c, d) BSE images. (a, b) Altered feldspar associated with euhedral garnet and quartz. Amphiboles are acicular crystals scattered throughout the matrix and defines a foliation in thin section, (c) monazite precipitating in pockets of perthite-plagioclase matrix, (d) anhedral garnet crystals intergrown with quartz and muscovite. Amp = amphibole, Grt = garnet, Mnz = monazite, Plag = plagioclase, Qz = quartz.

The entire mineral assemblage of this thin section (RL22-06A) is heavily overprinted by deformation reflecting observations in hand samples. All minerals have been sheared and metamorphosed and are littered with several small acicular amphiboles (15%) that define a foliation in thin section (Figure 16a, b). Quartz (25%) consists of several subgrains with grain boundary migration, exhibits undulose extinction and forms crystals up to 12 mm with blastic shape and a tail. All feldspars (40%) are highly altered into sericite, and they occur as stretched crystals in between large quartz crystals. Muscovites are < 0.1 mm crystals with straight extinction. Garnets constitute ~5% of the thin section and forms anhedral to euhedral crystals ~ 5 mm with several quartz inclusions. Monazite forms sub-rounded crystals of < 0.08 mm commonly as inclusions in K-feldspar and garnet (Figure 16c). Tourmaline (15%) occurs as high relief, patchy anhedral crystals defining aligned patterns in

interstices of quartz grains. It sometimes forms an envelope around large garnet and quartz crystals. Zircon occurs as elongated prismatic crystals up to 0.4 mm long with terminating ends and bright interference colors. Opaque crystals with size < 0.03 mm form anhedral patches in the fine-grained matrix.

4.1.1.5 Meløy

In the Meløy area, pegmatites occur as homogenous concordant and discordant veins or lenses in biotite gneisses and in metasedimentary rocks along the coast. In a road section exposure, a sub-vertical pegmatite dyke cuts the foliation of the gneiss basement with a sharp contact; the dyke strikes 160˚ and dip 30˚ SW. This homogenous pegmatite dyke is about 5 m wide and contains quartz, K-feldspar, plagioclase and muscovite. Quartz and feldspar are intergrown forming a graphic texture.

Several small pegmatite veins or lenses form a swarm parallel to the headland in western Meløy. The first group of pegmatites occurs as low-dipping veins or lenses that have a general NE-SW trend parallel to the foliation of the strongly deformed Caledonian metasedimentary host rocks (Figure 17a). In some places, the deformation has led to the development of boudins and shear planes in the pegmatites (Figure 17b). They are medium to coarse grained and contain quartz, feldspar and biotite with minor amounts of muscovite, apatite, tourmaline and garnet. A second group of younger pegmatites appears as lenses discordant to the steep foliation of the host metasedimentary rocks, especially along the northwestern part of Meløy beach. They are medium- to coarse-grained and contain quartz, feldspar and biotite with minor amounts of muscovite, apatite, tourmaline and garnet. Graphic intergrowth is observed between quartz and feldspar. The host rock is a strongly deformed garnet-rich metasediment bearing a foliation that strikes NW-SE and dips to the northeast. The orientation of the folds and the low dipping nature of the pegmatites may suggest magma emplacement along sub-horizontal compression-related structures, which most likely developed during Silurian thrust tectonics (Ihlen, 2004).

About 300 m east of the headland in the western part of Meløy, away from the flat-lying pegmatites, occurs a pegmatite body that is up to 30 m thick and 150 m long, with a NE-SW trend. It is coarse grained and consists of quartz, feldspar, muscovite and biotite with garnet,

green apatite and schorl as accessory minerals. The coarse-grained texture displays graphic intergrowth between quartz and feldspar. The host rock is a highly deformed garnet-rich metasediment containing quartz, plagioclase and biotite. The wall zone of the pegmatite body contains 0.2-2.5 m large rafts of the host rock (Figure 17d), rich in biotite with some plagioclase and quartz. In general, the pegmatites from Meløy appear to be more 'granitic' and contain fewer garnets compared with their counterparts from Agskardet.

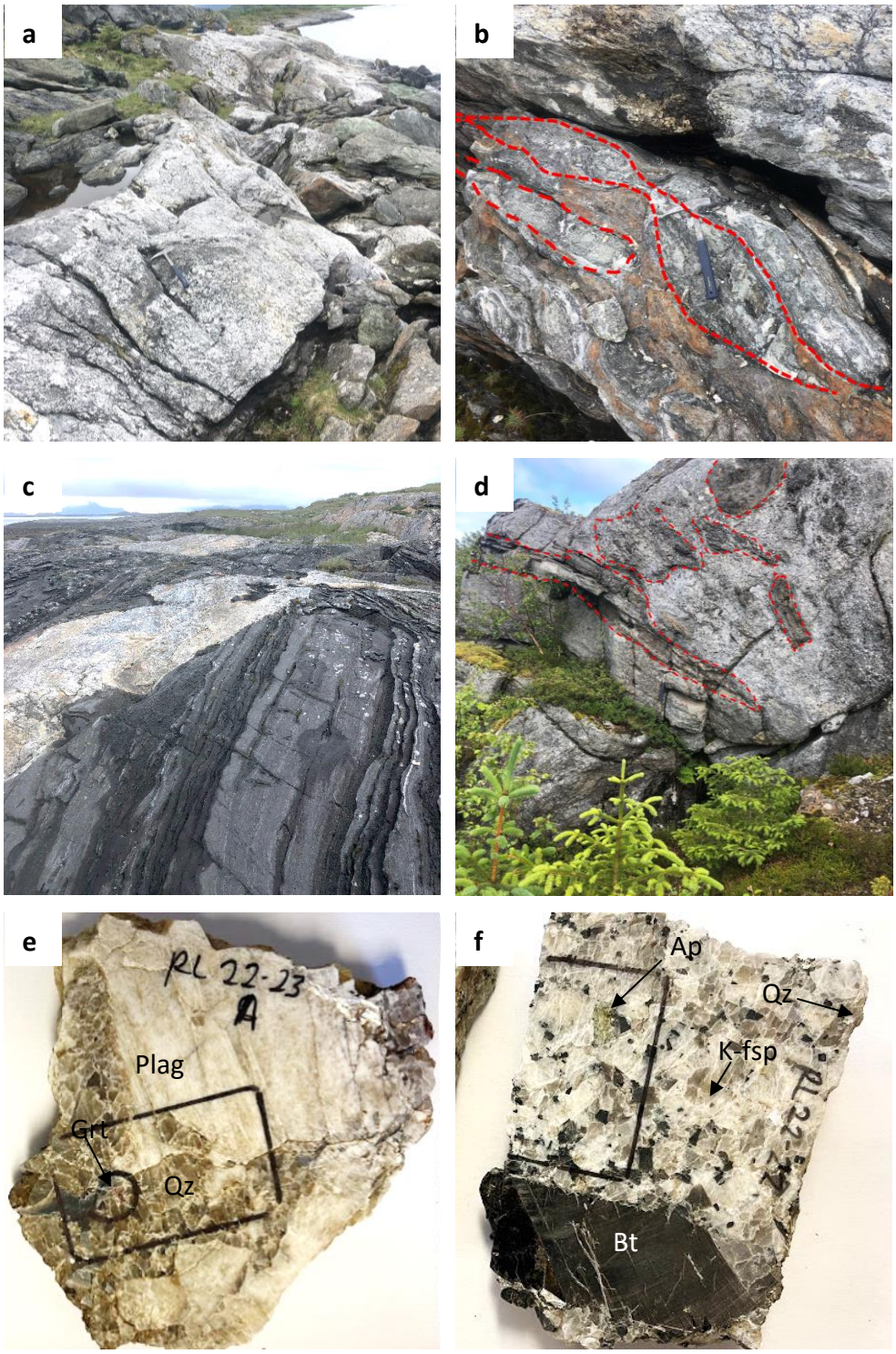

Figure 17.(a) Low dipping pegmatite lenses concordant to the foliation of metasediment host, (b) boudinage structures in pegmatite, (c) vertical pegmatite vein discordant to steep foliation of metasediments, (d) rafts of host rock embedded in the border zone of a pegmatite, (e) quartz forming in interstices of large unidirectional crystallizing feldspar crystals, (f) green apatite forming with quartz, feldspar and muscovite with large biotite crystal below. Scale is the outline of thin sections on hand samples. Ap = apatite, Bt = biotite, Grt = garnet, K-fsp = K-feldspar, Plag = plagioclase, Qz = quartz.

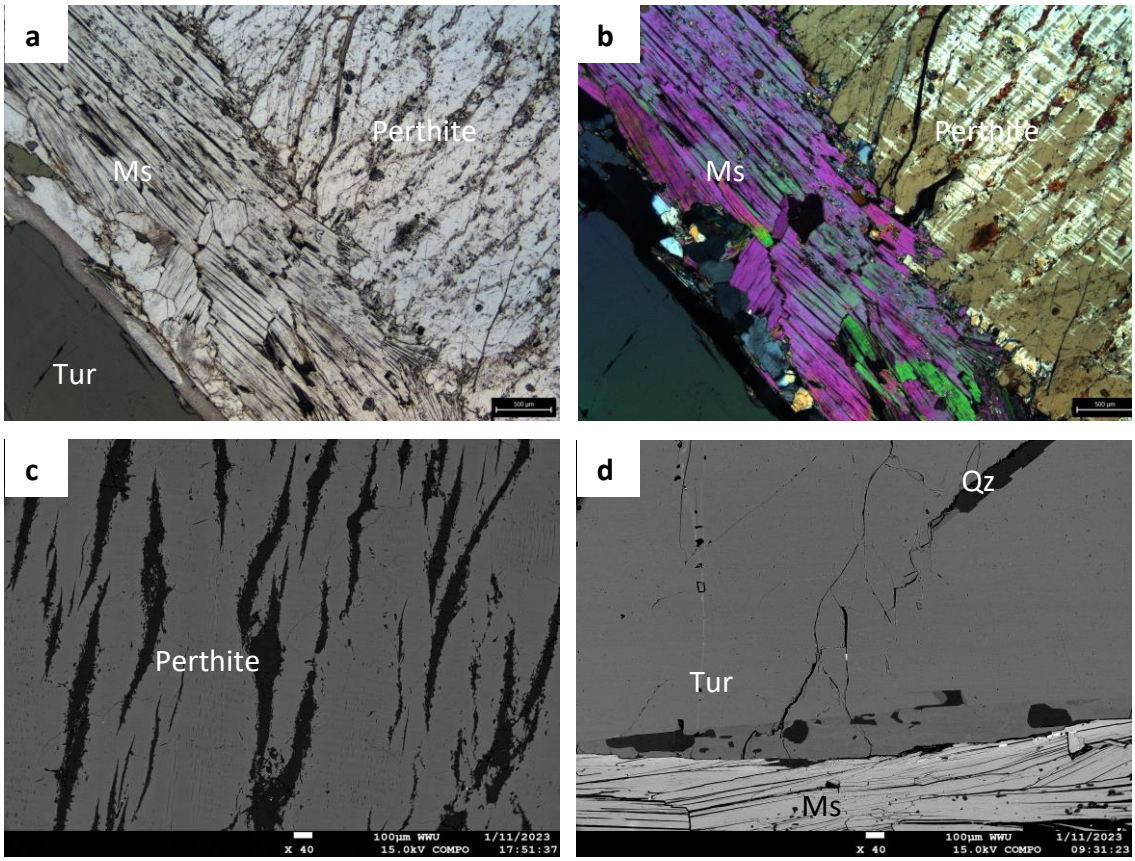

Figure 18. Photomicrographs of sample RL22-23C from Meløy in thin section. (a) in ppl, (b) in xpl, (c, d) BSE images. (a, b) fine zone of muscovite flakes aligned parallel to quartz tourmaline-K-feldspar interface. (c) Perthite showing albitic exsolution of K-feldspar, (d) quartz crystals precipitating in tourmaline cracks. Ms = muscovite, Tur = tourmaline, Qz = quartz.

The feldspar in the pegmatite (RL22-23C) is predominantly microcline that shows perthitic exsolution of albite across the entire grain of ~30 mm (Figures 18a, b, c). In between feldspar and tourmaline there is a fine zone that consists of several tiny flakes of muscovite (~10%) aligned parallel to the interface that can reach 0.4 mm in length (Figures 18a, b, d). Tourmaline is euhedral green to blue and hosts quartz and tiny muscovite flakes that form in cracks within the ~20 mm crystal. The tourmaline displays patchy compositional zoning. Opaque minerals constitute ~3% and occur as < 0.1 mm grains irregularly distributed in the sample.

4.1.1.6 Rismålstinden

The pegmatite field sits on the southern flank of the NNW-SSE trending Rismålstinden mountain range, separated by the E-W trending Bjorntindalen stream. The river and northern valley flanks expose pegmatites of variable strike length and thickness. According

to an NGU (2013) airborne magnetic survey in Holandsfjorden, the Rismålstinden pegmatites have a distinct structural control and occur along the E-W trending fold axis and nose closure of a large-scale regional fold, which provided favorable conditions for pegmatite magma emplacement. The pegmatite swarm forms dykes and lenses in marble host rocks. They have a variable thickness and length of up to 2 m and 50 m, respectively, and are E-W striking. The internal structures of the pegmatites are mostly homogenous across strike, and they contain quartz and murky feldspar, plus minor biotite, muscovite, garnet, tourmaline, apatite and zircon. They contain domains with large crystals up to 10 cm in length, and the coarse-grained domains display graphic intergrowth between quartz and K-feldspar.

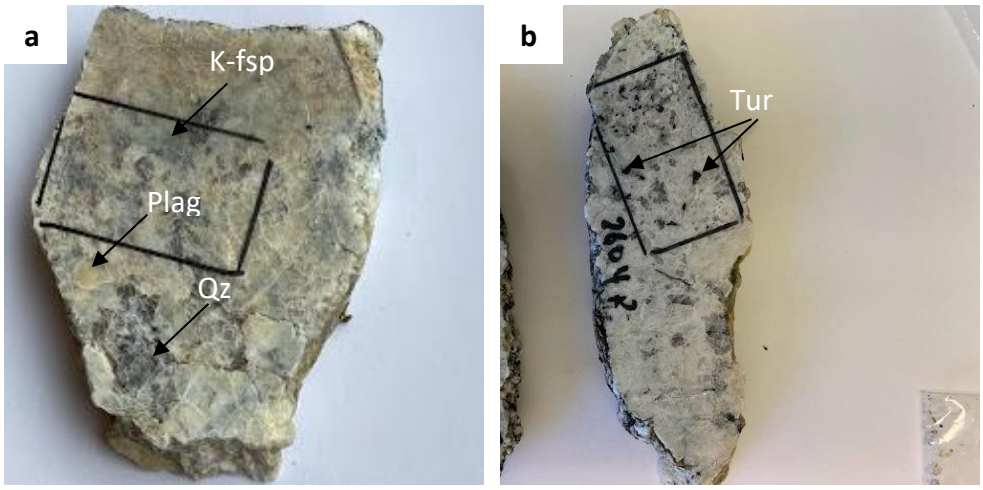

Figure 19. Hand samples showing (a) murky feldspars and quartz due to deformation in rock, (b) small tourmaline crystals within feldspar and quartz. Scale is outline of thin section on hand samples.

Thin Section

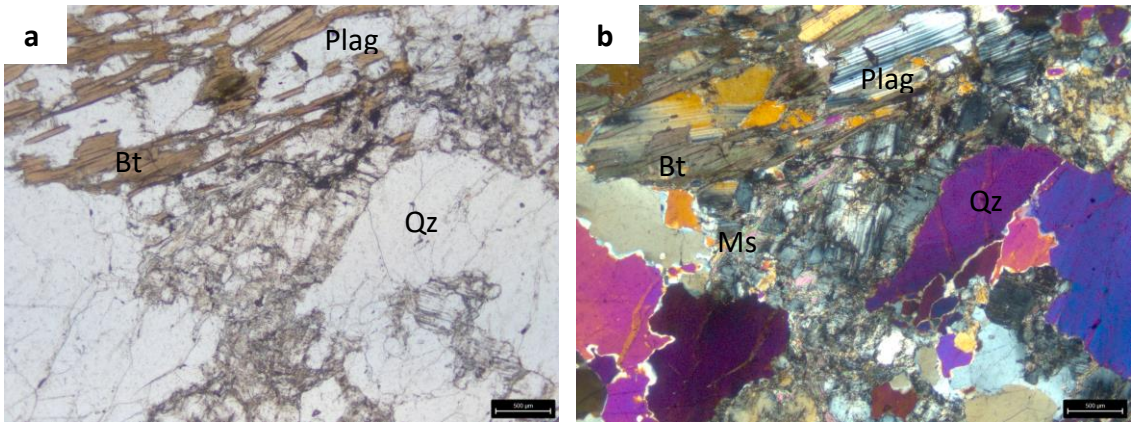

Figure 20. Photomicrographs of sample 2906R from Rismålstinden in thin section. (a) in ppl, (b) in xpl. (a, b) Deformed pegmatite showing large quartz, plagioclase and biotite crystals in a matrix of smaller recrystallized

crystals. Quartz displays grain boundary migration and the preferential alignment of biotite and plagioclase define a foliation in thin section. Bt = biotite, Plag = plagioclase, Ms = muscovite, Qz = quartz.

The pegmatite (2906R) is highly deformed, and the entire thin section shows porphyritic texture with larger phenocrysts in a matrix of small, recrystallized crystals. Quartz (25%) forms subgrains that range in size from 0.2 – 5 mm and show interfingering with undulose extinction. The feldspar content is predominantly plagioclase with polysynthetic twinning and ∼30% of plagioclase has altered into sericite. Two cleavage systems are present in the plagioclase with one more commonly developed in the crystals. Some plagioclase crystals also display oscillatory twinning. Reactions within feldspars form tiny films of muscovite that makes up ∼ 3% of the minerals in the thin section. K- feldspar makes up about 10% and is also weakly weathered. A narrow zone of aligned lathlike biotite, muscovite and plagioclase form a weak foliation in the rock (Figure 20a, b). Biotite (8%) forms euhedral crystals, have high relief with brown pleochroic colors.

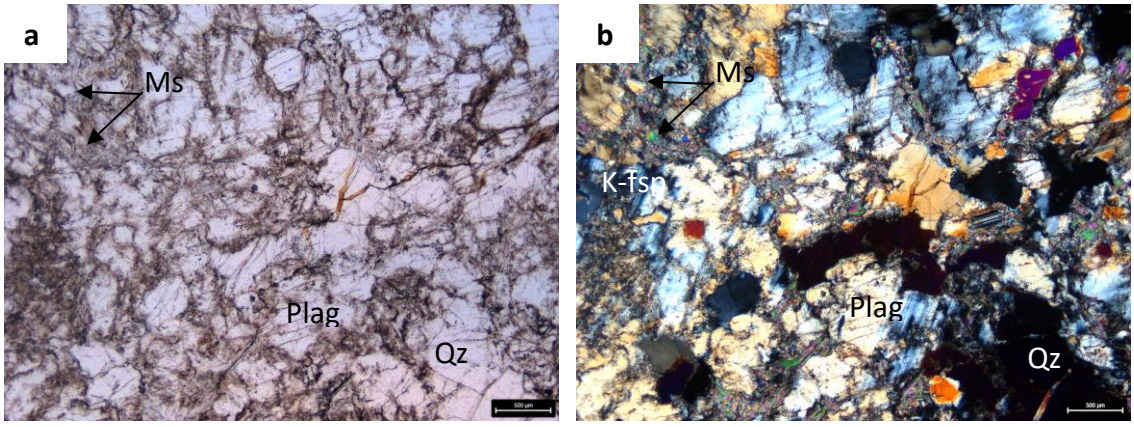

Figure 21. Photomicrographs of sample 2904R from Ågskardet-South in thin section. (a) in ppl, (b) in xpl. (c, d) BSE images. (a, b) deformed pegmatite showing reactions in feldspar crystals precipitating tiny films of muscovite. Ms = muscovite, Plag = plagioclase, K-fsp = K-feldspar, Qz = quartz.

The mineral assemblage of the pegmatite (2904R) consists of quartz (30%), plagioclase (35%), K-feldspar (20%), biotite (7), tourmaline (4%), muscovite (3%), and accessory amounts of zircon and monazite (Figures 21a, b). The sample is albite rich with polysynthetic twinning. Microcline is subhedral and tabular forms crystals up to 1.2 mm that display crosshatch twinning. Zircons are present in the feldspars as prismatic crystals with darker rims, high relief and strong birefringence. About 50-60 % of the K-feldspars show albite exsolution exsolution lamellae. The micas are mostly very fine dark brown biotite with minor

muscovite. Muscovites are colorless and non-pleochroic with very colorful 2nd order green to blue birefringence. Some muscovites form by replacement reactions of K-feldspar (Figure 21b) and myrmekite < 0.1 mm occurs in the rims of K-feldspar. Tourmaline are subhedral with light to dark brown pleochroic colors and high birefringence. They display compositional zoning with dark green core and light green rim. The entire crystal length is cut by several irregular fractures.

4.1.2 Basement rocks

4.1.2.1 Granitic Gneisses

The study area is underlain by gneissic basement units with varying degrees of deformation. The granitic gneiss basement is of Paleoproterozoic age (1.80 – 1.65 Ga) (Wilson & Nicholson, 1973; Cribb, 1981), and it is exposed in the Glomfjord window such as in the eastern, northern and central parts of the study area. The granitic gneisses occur as mostly pink, weakly foliated basement units. They are composed of K-feldspar, quartz, plagioclase, biotite, and hornblende amphibole. Apatite, zircon, titanite and some opaque minerals typically occur as accessory minerals. Generally, the gneisses are more deformed towards the western part of the area.

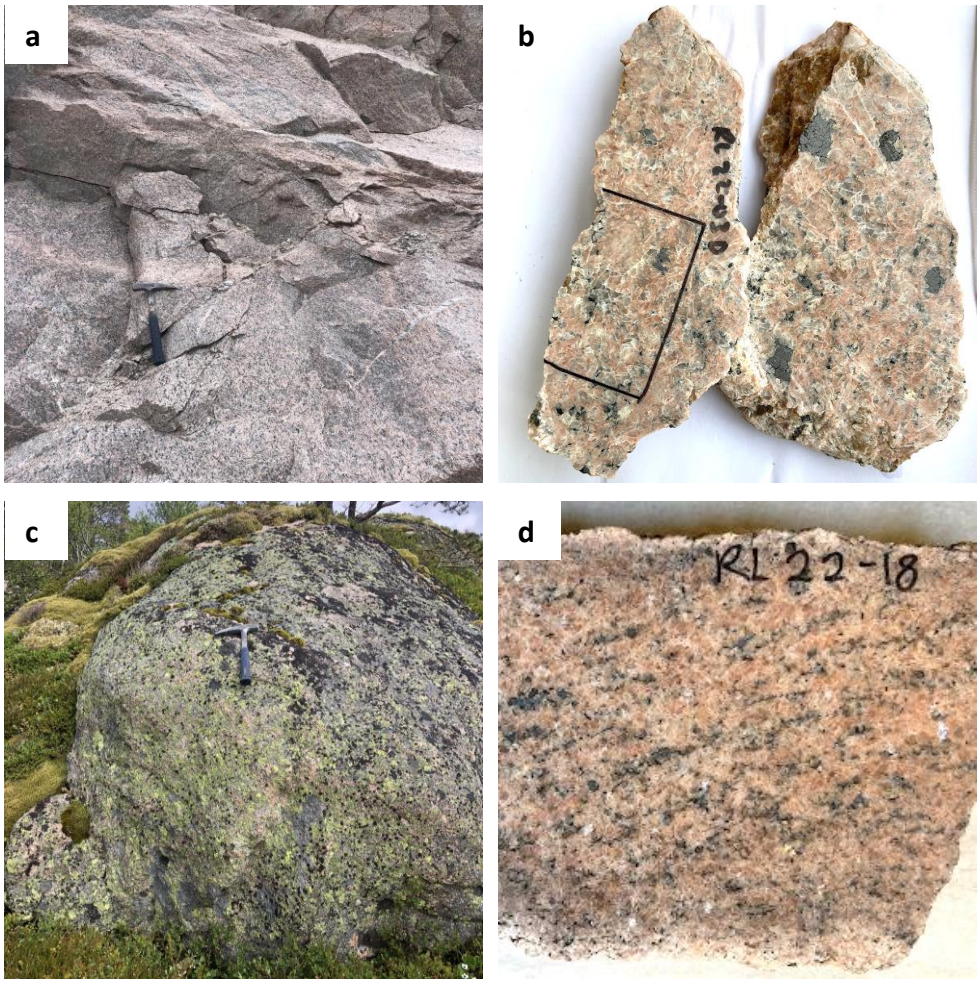

Figure 22. (a) Localized strain zone in granitic gneiss wall rocks at Kleiva Quarry, Reipå; (b) titanite crystals (shiny black) in K-feldspar rich rock from Kleiva Quarry; (c) granitic gneiss outcrop at Meløy; (d) amphibole and biotite defining weak foliation in granitic gneiss at Meløy.

A weakly deformed granitic gneiss is exposed in the wall rocks of Kleiva Quarry, located at the county road 17 in Reipå, 6 km north of Ørnes (Figure 22a). The granitic gneisses are light pink and contain K-feldspar, biotite, quartz, euhedral amphiboles, titanite, and minor amounts of pyrite and zircon (Figure 22b). The rocks are medium- to coarse-grained and sections show amphibole crystals set in coarser grained feldspar. In hand samples, zircon is conspicuous as small brown prismatic crystals closely associated with biotite. The rocks have undergone low strain only with no clear orientation of the foliation in some investigated sections. Where foliation is developed, it tends to change direction, which may indicate magmatic rather than tectonic foliation. The predominant foliation strikes ~110° ESE-WNW with a dip of ~20° to the SSW. There is a localized strain zone in the granitic gneisses where

quartz veins form close to the shear zone and around which the foliation also bends. A small pegmatite vein, ~7 cm wide, cuts the foliation obliquely.

A road section along the main county road 17 at Selstad, 6 km west of Glomfjord, exposes a similar type of medium to coarse grained granitic gneiss as was observed at the Kleiva Quarry. These gneisses contain K-feldspar, quartz, biotite, plagioclase, amphibole and minor amounts of titanite and zircon. The granitic gneisses have a weak foliation that trends E-W along the fjord.

Similar outcrops of medium to coarse grained granitic gneisses were observed at Åsjord north of Bjærangenfjord and on Meløy island (Figure 22c). They are also weakly foliated and contain K-feldspar, quartz, biotite and amphibole, with zircon and titanite as accessory minerals (Figure 22d). Overall, the fieldwork did not identify any major pegmatite lenses or dykes within the granitic gneiss basement.

Thin section

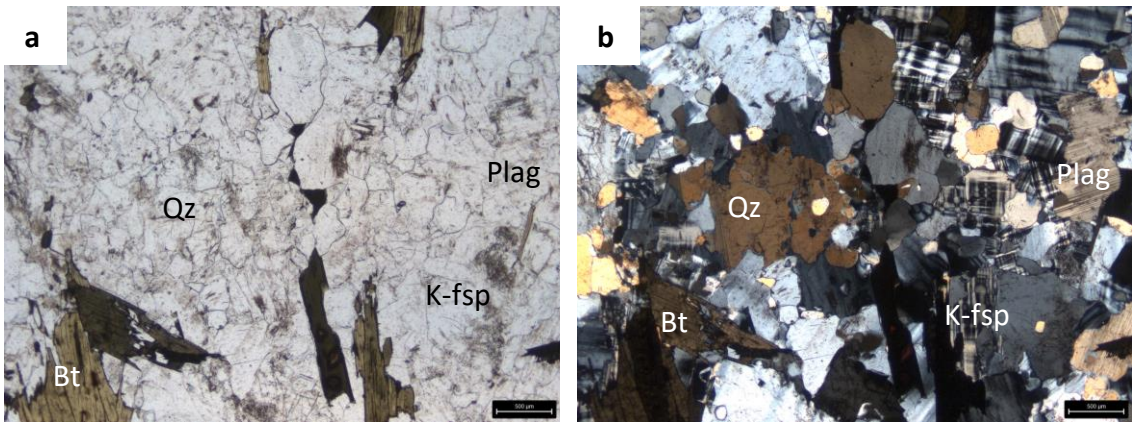

Figure 23. Photomicrographs of sample RL22-03E from Kleiva Quarry, Reipå in thin section. (a) in ppl, (b) in xpl. (a, b) biotite crystals showing preferred orientation in a matrix of quartz, K-felspar and plagioclase. Bt = biotite, K-fsp = K-feldspar, Plag = plagioclase, Qz = quartz.

The sample is a weakly deformed granitic gneiss that consists of quartz (30%), K-feldspar (25%), amphibole (15%), plagioclase (10%) and 10% opaque minerals. Quartz is present as anhedral crystals ranging from 0.1 mm to 1.5 mm and often interfinger with K-feldspar (Figure 23a, b). Feldspars are mostly subhedral microcline with cross hatch twinning and minor albite that show the characteristic polysynthetic twinning. Titanite displays no

difference in color in ppl and xpl due to its higher order birefringence. It has a high relief with a pale brown color and is often associated with biotite and other smaller grains in feldspar. Zircons are prismatic, display green interference colors and have high birefringence different from the titanite. Biotite is present as euhedral lathlike grains, and some are slightly chloritized. Radiation damage forms pleochroic halos in micas when titanite is included and gives it a slightly altered appearance. Monazite is present as transparent oval shaped chips in plane-polarized light but displays bright interference colors in cross-polarized light.

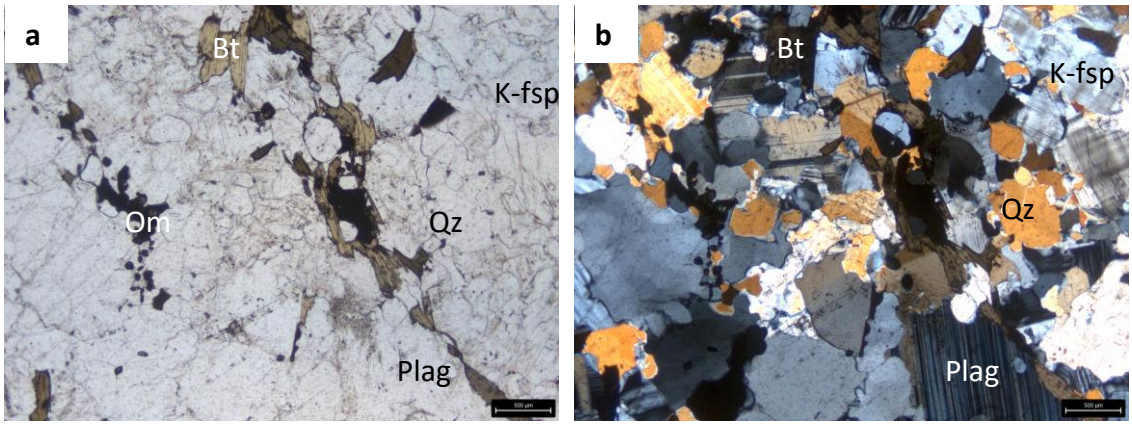

Figure 24. Photomicrographs of sample RL22-02 from Åsjord in thin section. (a) in ppl, (b) in xpl. (a, b) biotite crystals showing preferred orientation in a matrix of quartz, K-feldspar and plagioclase. Opaque minerals (dark) often occur as replacement minerals in biotite. Bt = biotite, K-fsp = K-feldspar, Om = opaque minerals, Plag = plagioclase, Qz = quartz.

Analyses of the granitic gneiss (RL22-02) showed that it contains less K-feldspar compared to that of the Kleiva Quarry. The sample contains quartz (27%), microcline (25%), plagioclase (25%), biotite (15%), and amphibole (5%). The minerals in the sample are undeformed and texturally similar to the granites at Kleiva Quarry. Quartz displays clear rounded anhedral shapes that range in size from < 0.1 to 1.6 mm. K-feldspar occurs as tabular subhedral crystals of microcline ranging from < 0.1 to 1.2 mm with cross-hatched twinning. The larger crytals > 0.7 mm contain small inclusions of apatite and orthoclase that shows carlsbad twinning. The plagioclase crystals are colorless with subhedral tabular shapes that contain inclusions of biotite and microcline. Polysynthetic twinning is well developed in plagioclase, but it is weak and terminates in a few crystals. Biotite occurs as < 0.1 to 0.6 mm well cleaved crystals with high relief and brown pleochroic colors. They display a weak but recognizable

orientation fabric compared to the other major constituents (Figures 24a, b). Amphiboles are usually < 0.2 mm in size with a pleochroic brown color and high relief. The crystals show two developed cleavage systems at a 120˚ angle. They mostly occur with biotite, quartz, k-feldspar, and some opaque minerals. Opaque minerals in the rock constitute about 3% and appear as dark anhedral minerals < 0.2 mm in size. Prismatic zircons in accessory occur in amounts as < 0.07 mm size crystals included in K-feldspar.

4.1.2.2 Mafic Gneiss

Mafic gneisses occur as a minor lithology in the peripheries of the granitic gneisses as part of the basement window. They are medium to coarse grained and consist of quartz, amphibole, biotite and plagioclase. Muscovite and garnet are usually absent, which gives an indication of the low Al content and rules out a possible sedimentary protolith. The mafic gneisses show varying degrees of deformation defined by two distinct sets of foliation: one set strikes 100˚ E-W and dips 35˚ N, and the other strikes 250˚ WSW-ENE and dips 35˚ SSE. Along the lake at Spilderdalsvatnet, ~6.2 km northeast of Ørnes, outcrops show varying degrees of partial melting marked by formation of leucosomes (Figure 25a). Leucosomes sit within the foliation planes indicating syn-kinematic development. In contrast, thin quartz veins crosscut the foliation at low angles.

At a road section in Neverdalen, about 7 km southeast of Ørnes, a migmatitic mafic gneiss occurs in contact with a 'fertile' metasedimentary unit, and a coarse-grained granitic or pegmatitic dyke (~15 cm wide) emplaced into the shear zone between the two contrasting basement rock units (Figure 25a, b). The pegmatite contains muscovite, quartz, K-feldspar and biotite, and zircon as accessory minerals. The pegmatite dyke intruded into a deformation zone and appear to be syn-kinematic with the second foliation of the migmatitic gneiss.

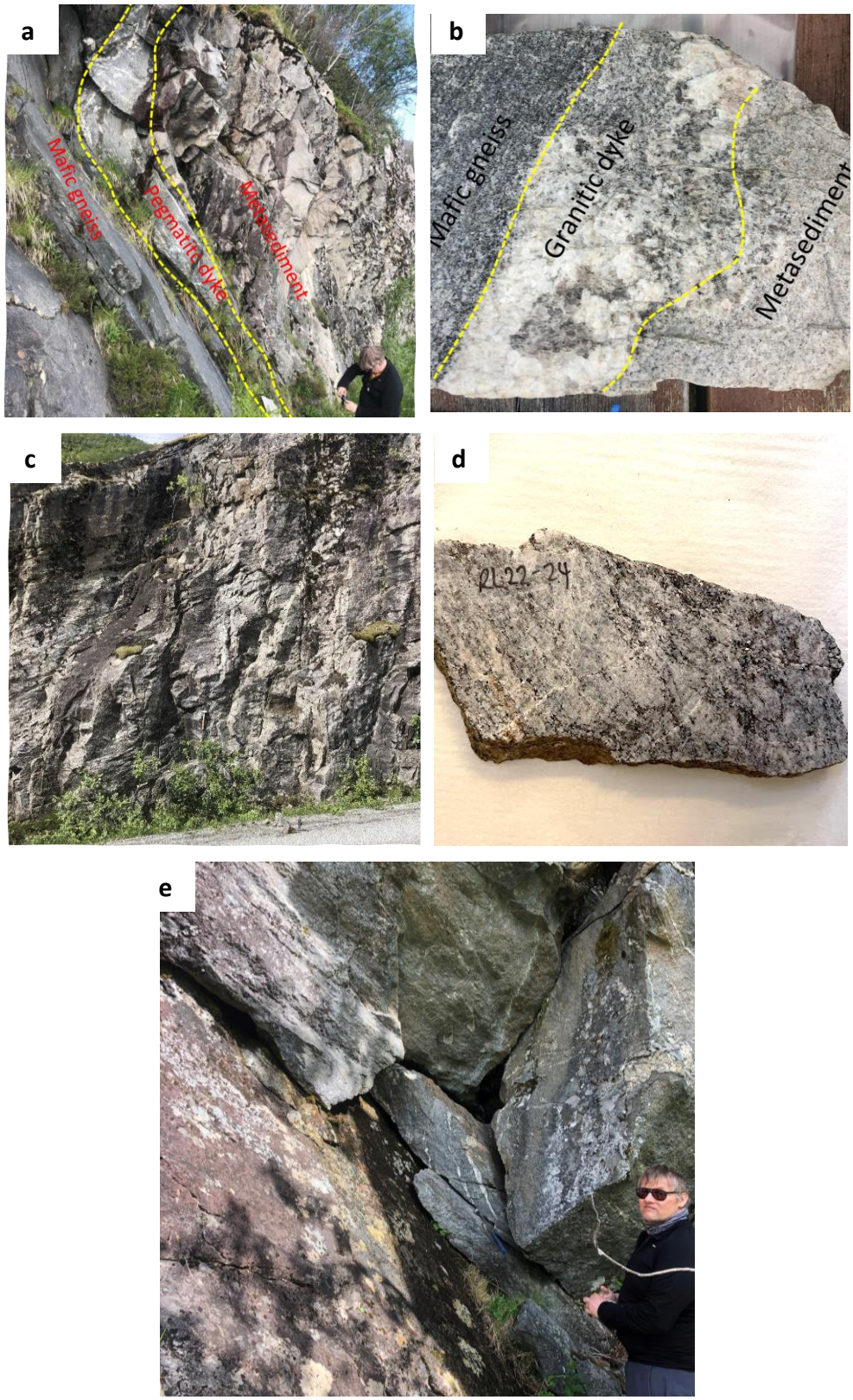

Figure 25. (a) Pegmatitic dyke in between a migmatitic mafic gneiss to the left and a metasedimentary rock to the right, (b) hand sample of thin pegmatitic dyke in between the mafic gneiss and metasedimentary rock, (c) and (d) road section outcrop and hand sample of mafic gneiss from Meløy, (e) Syn-kinematic development of leucosome within foliation plane at Spilderdalsvatnet, Ørnes.

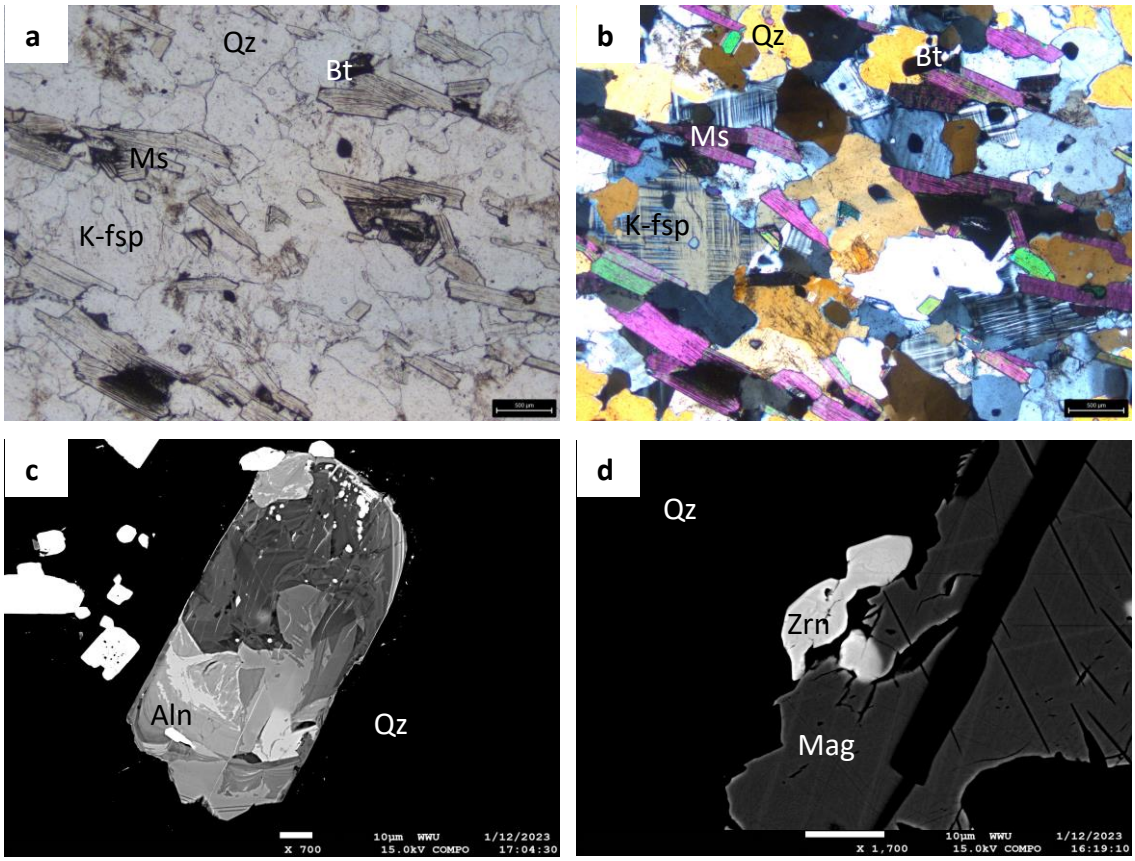

Figure 26. Photomicrographs of sample RL22-05D from Neverdalen in thin section. (a) in ppl, (b) in xpl. (c, d) BSE images from sample RL22-5J. (a,b) muscovite and biotite crystals showing preferred orientation in a matrix of quartz, K-feldspar and plagioclase, (c) an allanite crystal showing compositional zonation, (d) an anhedral zircon crystal precipitating close to a magnetite crystal. Aln = Allanite, K-fsp = K-feldspar, Ms = muscovite, Qz = quartz, Zrn = zircon, Mag = magnetite.

The sample (RL22-05D) is a metasedimentary rock that consists of quartz (35%), K-feldspar (30%), muscovite (18%), plagioclase (10%), opaque minerals (4%), and amphibole (2%). Quartz is present as subhedral crystals up to 1.5 mm in size that hosts several zircon inclusions. Feldspar is predominantly microcline and ~30% are altered into sericite. The large feldspar grains >1 mm contain inclusions of quartz and zircon. Plagioclase is present as colorless subhedral crystals with weak polysynthetic twinning due to sericitization. Muscovite has medium relief, and forms elongated platy minerals with 2nd order interference colors. The muscovite grains are aligned and define a foliation in the rock (Figure 26a, b). Opaque minerals range in size from < 0.1 to 0.4 mm and are randomly distributed in the rock. Small aggregates of euhedral amphiboles with brown to green interference colors are associated with muscovite and opaque minerals. Zircons form prismatic crystals < 0.2 mm with high relief and display bright 2nd order interference colors.

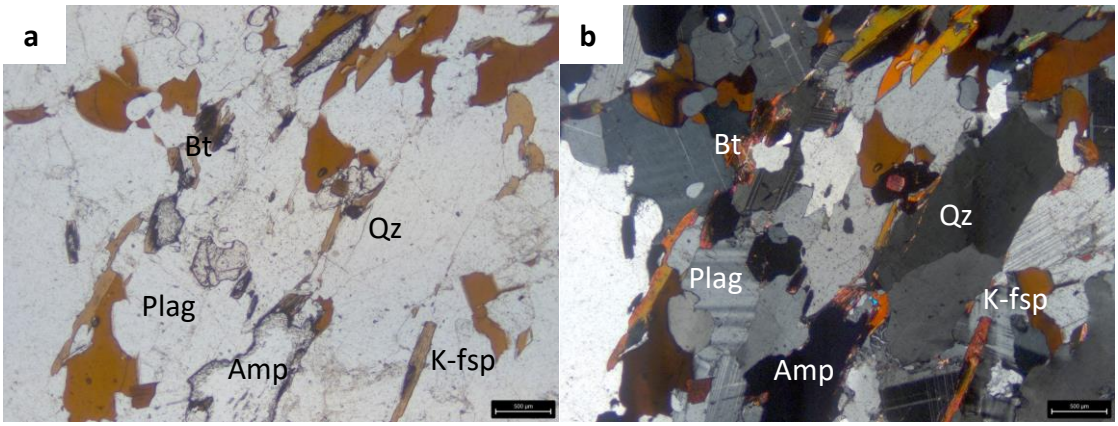

Figure 27. Photomicrograph of sample RL22-24 from Meløy in thin section. (a) ppl and (b) xpl. (a, b) preferred orientation of biotite, quartz, K-feldspar, plagioclase and amphibole crystals defining a foliation in the rock. Amp = amphibole, Bt = biotite, K-fsp = K-feldspar, Plag = plagioclase, Qz = quartz.

The sample (RL22-24) is a amphibole gneiss made up of quartz (20%), albite (20%), K-feldspar (25%), biotite (15%), amphibole (10%), muscovite (5%), opaque minerals (2%) with zircon, garnet and apatite as accessory minerals. Muscovite occurs as lathlike flakes and biotite mostly displays a stronger preferred orientation compared to the other crystals (Figure 27a, b). About 5% of mica grains are replaced by elongated isotropic grains with high relief.

4.2 Mineral Compositions

4.2.1 Feldspar

Feldspar group minerals are abundant and diverse, and they predominate in igneous rocks. Their wide range in chemical compositions makes them the main tool for classifying felsic and intermediate igneous rocks (Deer et al., 2013). Common feldspars consist of ternary solid solutions of three components (Figure 28): $NaAlSi_3O_8$, albite (Ab) and $CaAl_2Si_2O_8$, anorthite (An), both referred to as plagioclase feldspars, and orthoclase (Or), $KAlSi_3O_8$, referred to as potassium feldspars or simply K-feldspar. Feldspar relationships among solid solutions must be characterized by their chemical compositions and crystal structure, which depends on the crystallization temperature and thermal history (Deer et al., 2013).

Feldspar data for the North Helgeland pegmatites were acquired by EPMA, converted to apfu and then plotted in the An-Ab-Or classification diagram (Figure 28). From this ternary diagram, most pegmatite samples contain plagioclase and orthoclase in varying amounts, except for the Neverdalen dyke where plagioclase (oligoclase) is the only feldspar. The Ab-rich samples display great variability, with plagioclase feldspars from Ågskardet UB exhibiting the widest compositional range between $An_{1.16}$-Ab-$_{98.30}$-$Or_{0.57}$ and $An_{15.70}$-Ab-$_{83.36}$-$Or_{0.95}$. Plagioclase from Ågskardet OQ display the lowest variability between $An_{0.6}$-Ab-$_{99.82}$-$Or_{0.59}$ and An_{0}-Ab-$_{99.72}$-$Or_{0.27}$; i.e., pure albite. Orthoclase ranges between An_{0}-Ab-$_{2}$-Or_{98} and An_{0}-Ab_{24}-Or_{76}. Table 5 contains a summary of the EPMA analyses of feldspars from this study. For the complete analytical dataset, readers are referred to Appendix 8.4.1.

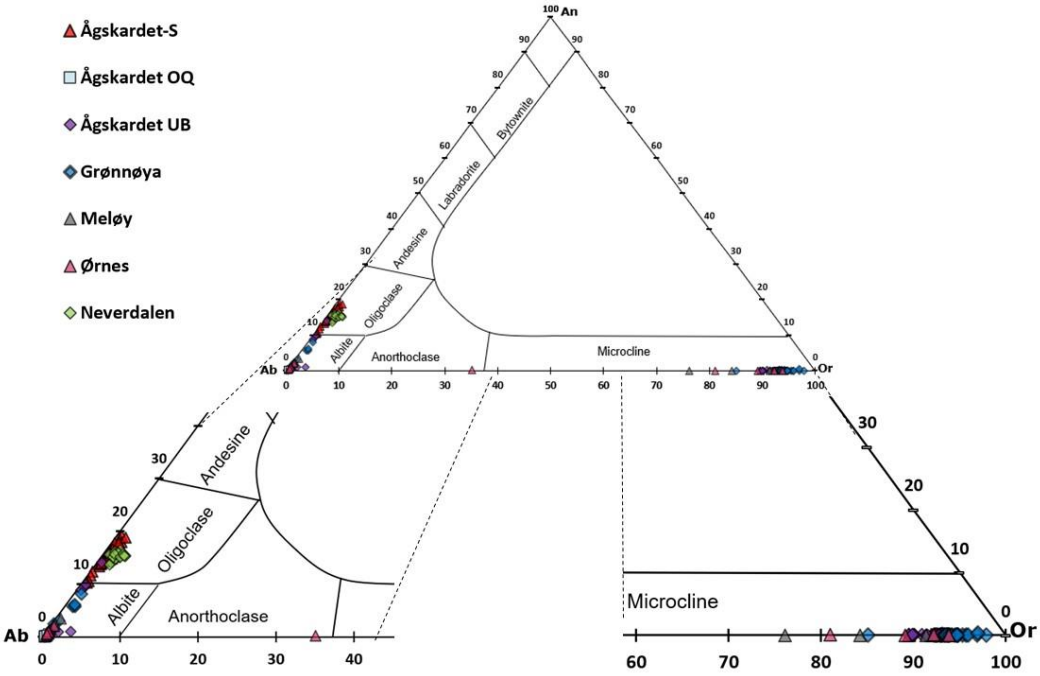

Figure 28. Ternary diagram classifying feldspars in the North Helgeland pegmatites.

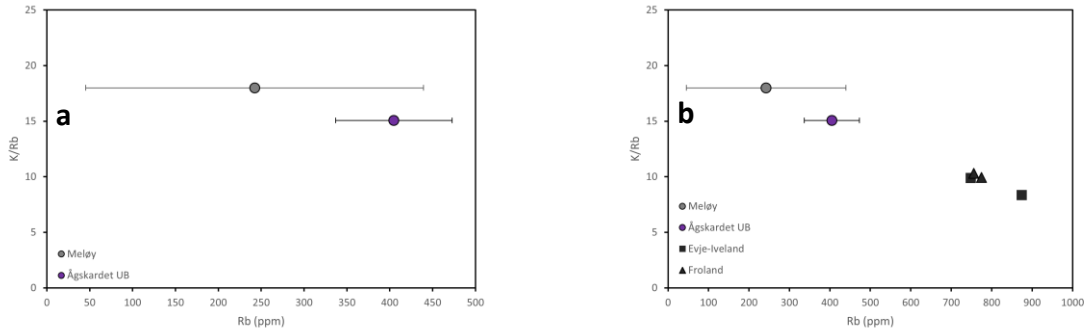

Figure 29. (a) K/Rb ratio vs Rb in k-feldspars from the North Helgeland pegmatites, (b) comparison to literature data of K-feldspars in Evje-Iveland and Froland pegmatites, southern Norway (Larsen, 2002). Granitic pegmatites in North Helgeland have a less evolved signature compared to these pegmatites.

To understand the evolution of the studied pegmatites in North Helgeland, the K/Rb vs Rb plot was used to evaluate the degree of fractionation in K-feldspars. Our dataset for trace elements in K-feldspar is smaller compared to that of plagioclase, hence only K-felspars from Ågskardet UB and Meløy were used for the K/Rb vs Rb plots. Average values of K ppm calculated from K_2O wt% EPMA data and Rb in ppm were used to calculate the K/Rb ratio of feldspar from our study data and that from literature (Larsen, 2002). From Figure 29a, K-feldspars in the Ågskardet UB pegmatites are more fractionated with lower K/Rb and high Rb content but when considering Rb concentration within error are similar to the Meløy K-feldspars. However, compared to literature data for K-feldspar from the Evje-Iveland pegmatites in southern Norway (Larsen, 2002), the North Helgeland feldspars are relatively primitive (Figure 29b).

Table 5. Summary of EPMA analyses of feldspars from the North Helgeland pegmatites.

Locality	Rismålstinden		Ågskardet-Upper Body		Ågskardet OQ		Grønnøya	
Sample ID	2904R		RL-22-16		RL-22-8C		RL-22-1A	
Lithology	Pegmatite		Pegmatite		Pegmatite		Pegmatite	
	ave. (44)	s.d.	ave. (27)	s.d	ave. (9)	s.d	ave. (31)	s.d
SiO_2	64.16	1.25	65.51	2.75	68.44	0.47	65.71	3.34
TiO_2	0.02	0.04	0.02	0.05	0.03	0.05	0.01	0.03
Al_2O_3	21.21	3.32	19.49	2.54	19.58	0.22	18.88	1.10
FeO	0.02	0.04	0.01	0.03	0.01	0.01	0.01	0.03
BaO	0.12	0.17	0.13	0.21	0.07	0.13	0.08	0.12
MnO	0.01	0.02	0.01	0.02	0.01	0.02	0.01	0.01
MgO	0.00	0.01	0.00	0.01	0.01	0.02	0.00	0.01
CaO	2.32	2.98	0.62	2.17	0.04	0.07	0.06	0.26
Na_2O	7.24	8.02	4.82	9.78	11.55	0.24	4.21	10.29
K_2O	4.36	13.93	9.25	15.35	0.07	0.04	10.65	14.83
SrO	0.03	0.06	0.03	0.07	0.02	0.05	0.01	0.04
Cr_2O_3	0.01	0.02	0.01	0.02	0.02	0.02	0.01	0.01
P_2O_5	0.04	0.05	0.09	0.10	0.10	0.06	0.07	0.11
F	0.02	0.08	0.03	0.09	0.02	0.07	0.04	0.13
Cl	0.00	0.00	0.00	0.01	0.00	0.01	0.00	0.01
Cs_2O	0.01	0.02	0.01	0.03	0.00	0.01	0.02	0.03
Total	99.58	0.99	100.03	0.76	99.96	0.61	99.78	0.96
apfu based on 8 oxygen atoms								
Si	2.88	0.14	2.96	0.10	2.99	0.01	2.99	0.02
Ti	0.00	0.00	0.00	0.00	0.00	0.00	0.00	0.00
Al	1.12	0.14	1.04	0.10	1.01	0.01	1.01	0.01
Fe^{2+}	0.00	0.00	0.00	0.00	0.00	0.00	0.00	0.00
Fe^{3+}	0.00	0.00	0.00	0.00	0.00	0.00	0.00	0.00
Ba	0.00	0.00	0.00	0.00	0.00	0.00	0.00	0.00
Mn	0.00	0.00	0.00	0.00	0.00	0.00	0.00	0.00
Mg	0.00	0.00	0.00	0.00	0.00	0.00	0.00	0.00
Ca	0.11	0.14	0.03	0.10	0.00	0.00	0.00	0.01
Na	0.62	0.69	0.41	0.83	0.98	0.02	0.36	0.87
K	0.26	0.82	0.54	0.90	0.00	0.00	0.63	0.88
Sr	0.00	0.00	0.00	0.00	0.00	0.00	0.00	0.00
Cr	0.00	0.00	0.00	0.00	0.00	0.00	0.00	0.00
P	0.00	0.00	0.00	0.00	0.00	0.00	0.00	0.00
F	0.00	0.01	0.00	0.01	0.00	0.01	0.01	0.02
Cl	0.00	0.00	0.00	0.00	0.00	0.00	0.00	0.00
Cs	0.00	0.00	0.00	0.00	0.00	0.00	0.00	0.00
Total	5.00	0.02	5.00	0.02	4.99	0.02	5.00	0.02
Endmembers (%)								
An	11.14	14.28	2.98	10.48	0.20	0.33	0.30	1.24
Ab	62.93	69.33	42.02	84.48	99.41	0.52	36.20	87.57
Or	25.93	82.98	55.00	91.34	0.39	0.24	63.49	88.43

Table 5 continued.

Locality	Grønnøya		Meløy		Ørnes		Neverdalen	
Sample ID	RL-22-1B		RL22-23C		RL22-4J1		RL22-5J	
Lithology	Pegmatite		Pegmatite		Pegmatite		Pegmatite	
	ave. (13)	s.d	ave. (12)	s.d	ave. (14)	s.d	ave. (26)	s.d
SiO_2	65.42	2.58	66.12	3.65	66.81	3.40	63.98	0.65
TiO_2	0.01	0.02	0.02	0.06	0.01	0.04	0.02	0.04
Al_2O_3	19.14	1.96	19.30	1.21	19.33	0.83	22.06	0.38
FeO_{tot}	0.02	0.03	0.01	0.02	0.01	0.03	0.08	0.05
BaO	0.07	0.11	0.25	0.40	0.09	0.15	0.10	0.16
MnO	0.01	0.02	0.00	0.01	0.01	0.02	0.01	0.02
MgO	0.00	0.01	0.01	0.02	0.01	0.01	0.00	0.01
CaO	0.46	1.28	0.23	0.51	0.13	0.24	3.23	0.29
Na_2O	4.50	10.30	6.31	10.59	8.27	9.55	9.54	0.30
K_2O	9.95	16.10	7.39	15.43	4.75	13.81	0.33	0.20
SrO	0.01	0.02	0.02	0.05	0.00	0.01	0.04	0.08
Cr_2O_3	0.01	0.02	0.01	0.02	0.01	0.02	0.01	0.02
P_2O_5	0.05	0.07	0.07	0.07	0.11	0.12	0.01	0.02
F	0.03	0.07	0.03	0.08	0.03	0.09	0.03	0.09
Cl	0.00	0.02	0.00	0.01	0.00	0.01	0.00	0.01
Cs_2O	0.00	0.01	0.01	0.02	0.00	0.02	0.01	0.03
Total	99.66	0.82	99.77	0.94	99.57	1.16	99.46	0.96
apfu based on 8 oxygen atoms								
Si	2.97	0.05	2.98	0.01	2.98	0.01	2.84	0.02
Ti	0.00	0.00	0.00	0.00	0.00	0.00	0.00	0.00
Al	1.02	0.05	1.02	0.01	1.02	0.02	1.15	0.02
Fe^{2+}	0.00	0.00	0.00	0.00	0.00	0.00	0.00	0.00
Fe^{3+}	0.00	0.00	0.00	0.00	0.00	0.00	0.00	0.00
Ba	0.00	0.00	0.00	0.01	0.00	0.00	0.00	0.00
Mn	0.00	0.00	0.00	0.00	0.00	0.00	0.00	0.00
Mg	0.00	0.00	0.00	0.00	0.00	0.00	0.00	0.00
Ca	0.02	0.06	0.01	0.02	0.01	0.01	0.15	0.01
Na	0.39	0.88	0.54	0.89	0.71	0.81	0.82	0.02
K	0.59	0.95	0.44	0.91	0.28	0.82	0.02	0.01
Sr	0.00	0.00	0.00	0.00	0.00	0.00	0.00	0.00
Cr	0.00	0.00	0.00	0.00	0.00	0.00	0.00	0.00
P	0.00	0.00	0.00	0.00	0.00	0.00	0.00	0.00
F	0.00	0.01	0.01	0.01	0.00	0.01	0.00	0.01
Cl	0.00	0.00	0.00	0.00	0.00	0.00	0.00	0.00
Cs	0.00	0.00	0.00	0.00	0.00	0.00	0.00	0.00
Total	5.00	0.02	5.00	0.05	5.00	0.02	5.00	0.02
Endmembers (%)								
An	2.22	6.12	1.08	2.45	0.60	1.13	15.48	1.31
Ab	39.15	89.32	54.56	90.06	71.23	81.31	82.62	1.46
Or	58.63	94.93	44.36	92.24	28.17	82.09	1.89	1.13

Numbers in parenthesis represent the number of analyses; ave. = average; s.d = 2* standard deviation; An = anorthite; Ab = albite; Or = orthoclase.

4.2.2 Mica

Micas constitute the third most abundant mineral group in granitic pegmatites after quartz and feldspar. They are characterized by their platy habit and perfect cleavage, which is due to their layered atomic structure (Černý & Burt, 1984; Deer et al., 2013).

Micas have a wide chemical variability due to the complex nature of their trioctahedral crystal structure which can fit a large number of ionic sizes and charges by isomorphic substitutions (Tischendorf et al., 2001, 2007). According to Rieder et al. (1998), the general formula for micas is written as:

$I_2M_{4-6}\square_2$-$0T_8O_{20}A_4$, where:

I represents K or Na, but Cs, NH_4, Rb, Ca, Ba, and other cations may fit;

M is commonly Mg, Fe^{2+}, Fe^{3+}, Al, Ti, Mn, Li, Zn, Cr, V and other cations.

□ is a vacancy.

T is Si, Al, and Fe^{3+}.

A is commonly F, Cl, OH, O and S.

The most common micas are the lighter colored muscovite (octahedral site occupied by Al) and the darker biotite (octahedral site occupied by Fe, and Mg), but also Mg-rich phlogopite, Fe-rich annite and siderophyllite, and Li micas where Li substitutes for Mg plus Si (Deer et al., 2013). Pegmatites contain a highly diverse mica population, and individual mica compositions represent distinct stages of pegmatite evolution. The minor and trace elements, including F, Rb, Li, Cs, Zn, Sc, Nb, Ta and Sn, contained in micas are used in classifications and serve as indicators for pegmatite genesis and economic potential (Černý & Burt, 1984; Deer et al., 2013).

Muscovite and biotite are the two most common micas present throughout the pegmatite fields in North Helgeland. Mica aggregates can reach ~30 cm in diameter (see Figure 11a), with varied coloration from olive green, grey, pink, silver, and brown to black. Several mica aggregates occur in association with quartz, feldspar, garnet and tourmaline in the coarse-grained pegmatites. During fieldwork, representative mica samples were collected to aid in characterizing their composition and distribution in the area. Table 6 shows the summary of

major and minor element composition, determined by EPMA. For the entire EPMA dataset for micas, refer to Appendix 8.4.2. All the mineral formula been calculated based on 22 oxygen atoms per unit. The trace element compositions of micas from the pegmatites were determined by LA-ICP-MS Appendix 8.5.2. Figure 30 shows selected BSE images with EPMA analyses of micas in thin section and Figure 31 shows the Fe_{tot} + Mn +Al^{VI} versus Mg-Li classification diagram (feal vs. mgli) of Tischendorf et al. (1997, 2001). For mica classification, EPMA data and mean values of Li from LA-ICP-MS analyses were used. The analyzed micas contain on average 8.2 wt% FeO and 3.7 wt% MgO. About a third of the samples classified as Fe-muscovite and pure muscovite, and the remaining two thirds classified as Fe-biotite (magnesian siderophyllite), Mg-biotite (phlogopite), Li-Fe muscovite and pure muscovite. White to pink micas from Ågskardet OQ are classified as both Li-Fe muscovite and Li-muscovite. Similar white micas without significant Li enrichment at Grønnøya and Ørnes classified as both Fe-muscovite and pure muscovite between -0.03 to 0.09 mgli and -4 to -2.57 feal, respectively. The cores of micas from Ørnes classify either as Fe-muscovite or muscovite, while the rims usually fall at the transition between Fe-muscovite and muscovite. At Ågskardet-S the cores of dark micas in the pegmatite classify as Fe-biotite, whereas the rims of some crystals transition into pure muscovite.

Large micas from Neverdalen also displays core-rim compositional difference with the core classifying as Mg-biotite, whereas the rims are Fe-muscovites.

Micas in the Ågskardet UB and Meløy pegmatites are more homogenous and classify as Fe-biotite and pure muscovite, respectively.

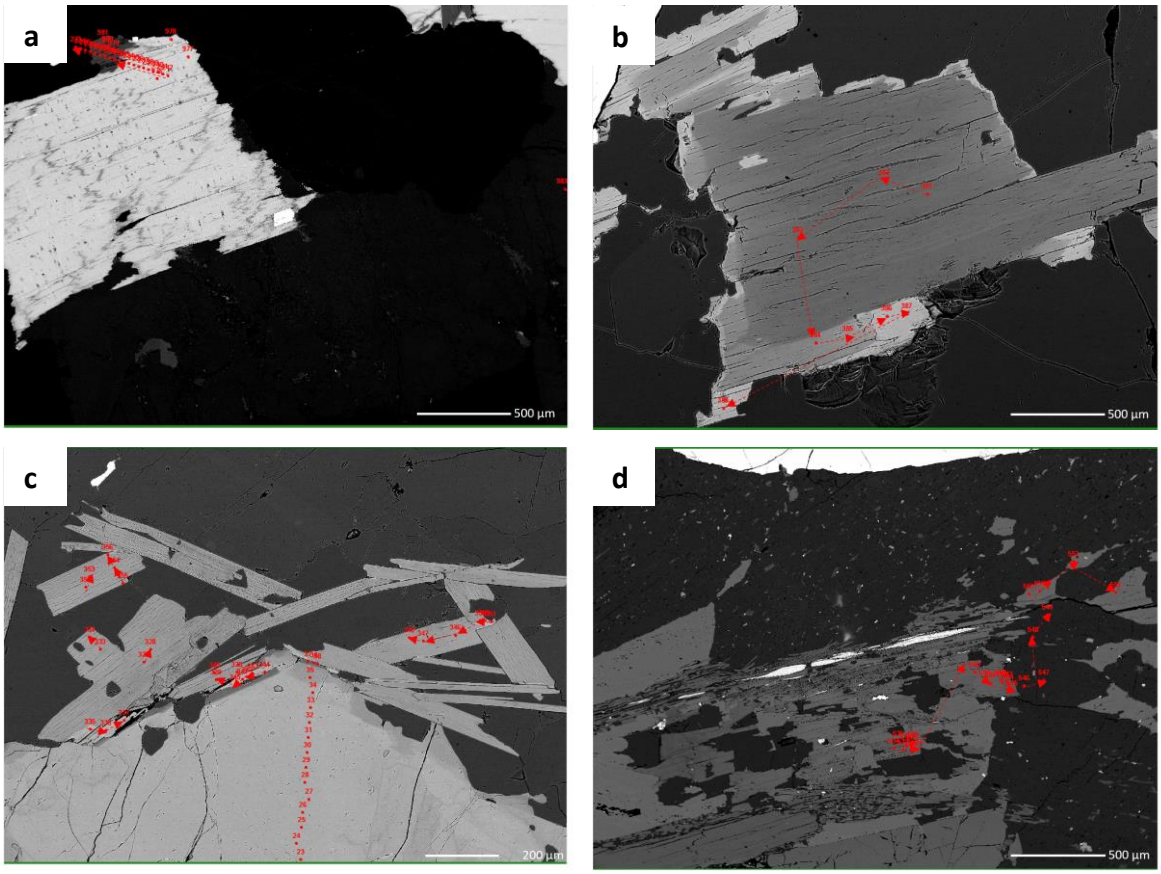

Figure 30. BSE images of mica. (a) Ågskardet-S, (b, c) Ågskardet OQ, (d) Grønnøya. (a) Mica with worm-like zoning and a zircon inclusion (white) in the rim, (b) muscovite showing compositional zoning with Al-Li rich core and Fe-Li rich rim, (c) small lathlike muscovite crystals with quartz replacement. Some crystals also show patchy zonation at the rims. (d) preferred orientation of elongated muscovite, K-feldspar, plagioclase, and garnet (white) in a deformed pegmatite.

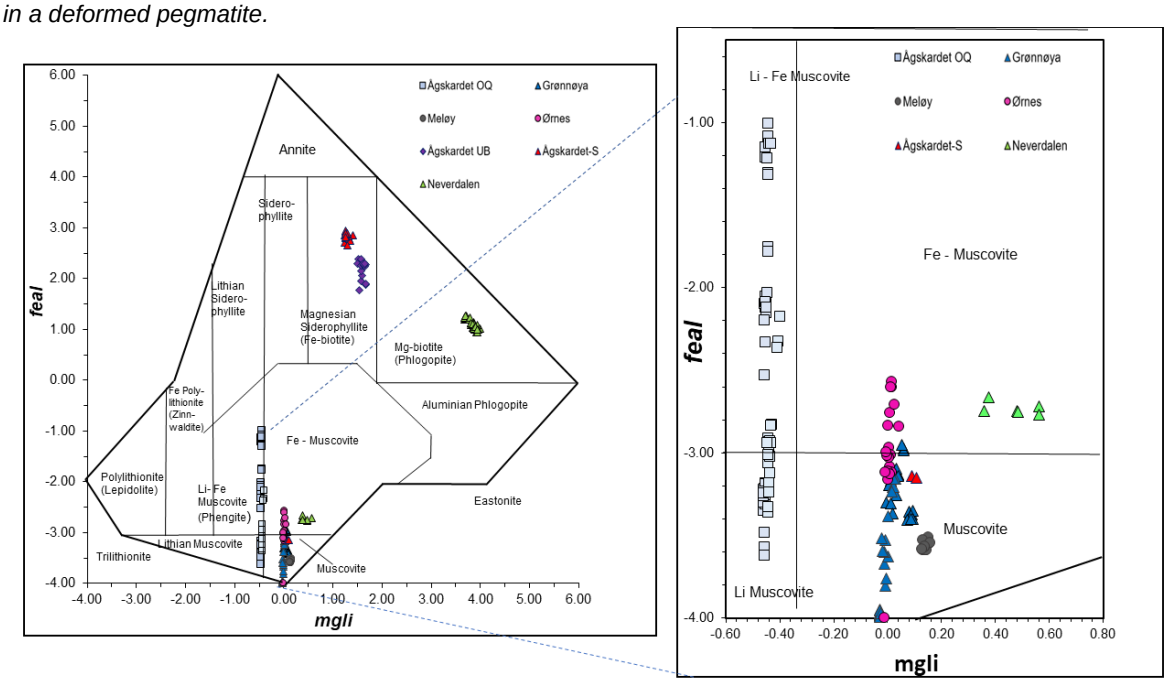

Figure 31. Fe_{tot} + Mn + Ti - Al^{VI} vs. Mg-Li (apfu) classification after Tischendorf et al., (1997, 2001). The plot shows micas classifying as Li-Fe muscovite, Li-muscovite, Fe-muscovite, pure muscovite, and Fe and Mg biotite.

Table 6a. Average EPMA compositions of dioctahedral micas (muscovite) from the Nord Helgeland pegmatites.

Locality	Ågskardet Old Quarry		Ågskardet Old Quarry		Grønnøya		Grønnøya	
Sample ID	RL22-7E		RL22-8C		RL22-1A		RL22-1C	
Lithology	Pegmatite		Pegmatite		Pegmatite		Pegmatite	
	ave. (44)	s.d	ave. (20)	s.d	ave. (24)	s.d	ave. (28)	s.d
SiO_2	46.89	5.19	44.99	0.96	45.50	0.48	45.70	0.93
TiO_2	0.01	0.04	0.01	0.03	0.06	0.15	0.02	0.05
Al_2O_3	26.65	12.72	31.78	2.97	33.23	1.31	35.98	3.52
FeO	5.74	6.33	4.62	2.43	3.35	1.60	1.34	2.81
MnO	1.04	1.16	0.40	0.32	0.03	0.04	0.01	0.04
MgO	0.05	0.06	0.14	0.12	0.38	0.30	0.08	0.19
CaO	0.00	0.01	0.00	0.02	0.00	0.00	0.00	0.01
Na_2O	0.20	0.34	0.30	0.19	0.28	0.24	0.24	0.15
K_2O	10.57	0.55	10.30	0.52	10.52	0.62	10.48	0.67
F	3.37	5.19	0.69	0.52	0.13	0.23	0.03	0.08
Cr_2O_3	0.01	0.02	0.00	0.02	0.01	0.02	0.01	0.02
Cs_2O	0.09	0.13	0.02	0.05	0.02	0.03	0.01	0.03
H_2O	2.67	2.77	4.09	0.33	4.40	0.11	4.51	0.08
-O=F	1.42	2.19	0.29	0.22	0.05	0.10	0.01	0.04
TOTAL - (O=F)	95.88	4.15	97.06	1.30	97.86	1.15	98.39	1.43
apfu based on 22 oxygen atoms								
Si	6.73	1.04	6.28	0.10	6.25	0.07	6.16	0.17
Ti	0.00	0.00	0.00	0.00	0.01	0.02	0.00	0.00
$Al^{(IV)}$	1.27	1.04	1.72	0.10	1.75	0.07	1.84	0.17
$Al^{(VI)}$	3.19	0.87	3.52	0.28	3.62	0.12	3.87	0.29
Fe	0.70	0.82	0.54	0.30	0.39	0.19	0.15	0.32
Mn	0.13	0.15	0.05	0.04	0.00	0.00	0.00	0.00
Mg	0.01	0.01	0.03	0.03	0.08	0.06	0.02	0.04
Ca	0.00	0.00	0.00	0.00	0.00	0.00	0.00	0.00
Li	0.46	0.00	0.46	0.00	0.03	0.00	0.03	0.00
Na	0.05	0.09	0.08	0.05	0.07	0.06	0.06	0.04
K	1.93	0.20	1.84	0.11	1.84	0.11	1.80	0.11
Cr	0.00	0.00	0.00	0.00	0.00	0.00	0.00	0.00
OH	2.43	2.45	3.69	0.24	3.94	0.10	3.99	0.04
F	1.57	2.45	0.31	0.24	0.05	0.10	0.01	0.04
Cl	0.00	0.00	0.00	0.00	0.00	0.00	0.00	0.00
sum	18.49	0.33	18.52	0.13	18.04	0.07	17.94	0.10
mgli	-0.45	0.01	-0.43	0.03	0.05	0.06	-0.01	0.04
feal	-2.36	1.76	-2.93	0.62	-3.23	0.29	-3.72	0.61

Table 6a. continued.

Locality	Meløy		Ørnes		Ågskardet South		Neverdalen	
Sample ID	RL22-23C		RL22-4J1		2904R		RL22-5J	
Lithology	Pegmatite		Pegmatite		Pegmatite		Pegmatite	
	ave.(12)	Std Dev	ave. (25)	s.d	ave. (2)	s.d	ave. (6)	s.d
SiO_2	46.02	0.77	45.16	1.12	45.74	2.49	46.70	0.97
TiO_2	0.12	0.13	0.02	0.05	0.74	0.18	0.29	0.16
Al_2O_3	34.79	0.38	34.04	4.96	32.25	1.20	29.53	0.28

FeO	1.38	0.09	3.69	4.88	2.45	0.00	3.85	0.60
MnO	0.02	0.03	0.06	0.10	0.04	0.00	0.11	0.07
MgO	0.72	0.09	0.08	0.13	1.03	0.06	2.32	0.82
CaO	0.00	0.01	0.00	0.02	0.01	0.04	0.02	0.08
Na_2O	0.36	0.13	0.24	0.15	0.33	0.04	0.22	0.05
K_2O	10.54	0.49	10.51	0.48	10.24	0.59	10.60	0.48
F	0.04	0.11	0.03	0.11	0.30	0.25	0.37	0.32
Cr_2O_3	0.01	0.02	0.01	0.02	0.01	0.00	0.01	0.02
Cs_2O	0.01	0.02	0.01	0.02	0.00	0.00	0.01	0.03
H_2O	4.49	0.06	4.44	0.16	4.34	0.11	4.26	0.16
-O=F	0.02	0.05	0.01	0.04	0.12	0.10	0.16	0.13
TOTAL - (O=F)	98.47	1.02	98.29	1.22	97.35	4.52	98.12	1.48
apfu based on 22 oxygen atoms								
Si	6.21	0.05	6.18	0.15	6.28	0.04	6.43	0.03
Ti	0.01	0.01	0.00	0.00	0.08	0.02	0.03	0.02
$Al^{(IV)}$	1.79	0.05	1.82	0.15	1.72	0.04	1.57	0.03
$Al^{(VI)}$	3.74	0.04	3.67	0.47	3.51	0.02	3.22	0.07
Fe	0.16	0.01	0.43	0.57	0.28	0.01	0.44	0.07
Mn	0.00	0.00	0.01	0.01	0.00	0.00	0.01	0.01
Mg	0.15	0.02	0.02	0.03	0.21	0.02	0.48	0.16
Ca	0.00	0.00	0.00	0.00	0.00	0.01	0.00	0.01
Li	0.00	0.00	0.01	0.00	0.11	0.00	0.04	0.00
Na	0.09	0.03	0.06	0.04	0.09	0.01	0.06	0.01
K	1.81	0.08	1.84	0.14	1.79	0.02	1.86	0.07
Cr	0.00	0.00	0.00	0.00	0.00	0.00	0.00	0.00
OH	3.98	0.05	3.98	0.04	3.87	0.10	3.84	0.14
F	0.02	0.05	0.01	0.05	0.13	0.10	0.16	0.14
Cl	0.00	0.00	0.00	0.01	0.00	0.00	0.00	0.00
sum	17.96	0.05	18.03	0.22	18.08	0.01	18.14	0.06
mgli	0.14	0.02	0.00	0.03	0.10	0.02	0.44	0.16
feal	-3.566	0.052	-3.23	1.05	2.39	0.02	-2.73	0.08

Table 6b. Average EPMA compositions of trioctahedral micas (biotite) from the Nord Helgeland pegmatites continued.

Locality	Ågskardet-Upper Body		Ågskardet South		Neverdalen	
Sample ID	RL22-16		2904R		RL22-5J	
Lithology	Pegmatite		Pegmatite		Pegmatite	
	ave. (22)	s.d	ave. (25)	s.d	ave. (29)	s.d
SiO_2	35.10	0.58	35.03	0.49	38.96	0.73
TiO_2	2.39	2.61	2.94	0.38	1.34	0.17
Al_2O_3	18.62	0.74	17.39	0.51	15.13	0.34
FeO	21.04	1.54	23.54	0.70	9.69	1.26
MnO	0.30	0.09	0.69	0.07	1.28	0.22
MgO	7.44	0.38	6.00	0.28	17.56	0.82
CaO	0.00	0.03	0.00	0.00	0.00	0.01
Na_2O	0.05	0.04	0.04	0.05	0.07	0.03
K_2O	9.52	1.05	9.55	0.43	9.93	0.32
F	0.64	0.35	0.86	0.33	2.28	0.44
Cr_2O_3	0.01	0.02	0.01	0.03	0.01	0.02
Cs_2O	0.01	0.03	0.01	0.03	0.01	0.02

H_2O	3.61	0.18	3.45	0.16	3.01	0.21
-O=F	0.27	0.15	0.36	0.14	0.96	0.19
TOTAL - (O=F)	98.47	2.14	99.15	0.96	98.30	1.15
apfu based on 22 oxygen atoms						
Si	5.44	0.08	5.48	0.06	5.77	0.05
Ti	0.28	0.30	0.35	0.04	0.15	0.02
$Al^{(IV)}$	2.56	0.08	2.52	0.06	2.23	0.05
$Al^{(VI)}$	0.85	0.26	0.69	0.06	0.41	0.04
Fe	2.73	0.26	3.08	0.09	1.20	0.16
Mn	0.04	0.01	0.09	0.01	0.16	0.03
Mg	1.72	0.09	1.40	0.07	3.88	0.17
Ca	0.00	0.01	0.00	0.00	0.00	0.00
Li	0.12	0.00	0.11	0.00	0.04	0.00
Na	0.02	0.01	0.01	0.02	0.02	0.01
K	1.88	0.18	1.91	0.08	1.88	0.06
Cr	0.00	0.00	0.00	0.00	0.00	0.00
OH	3.68	0.18	3.57	0.16	2.92	0.21
F	0.32	0.18	0.42	0.16	1.07	0.21
Cl	0.00	0.00	0.00	0.01	0.01	0.00
sum	19.64	0.11	19.63	0.06	19.73	0.05
mgli	1.60	0.09	1.29	0.07	3.84	0.17
feal	2.20	0.34	2.83	0.13	1.10	0.18

(Mg - Li) = mgli and (Fe_{tot} + Mn + Ti - Al^{VI}) = feal; ave. = average; s.d = 2* standard deviation; H_2O is estimated by full occupancy of the F-OH site.; numbers in parenthesis represent the number of EPMA analyses.

Overall, the dioctahedral micas (muscovite) display high heterogeneity in elemental compositions (Table 6a). TiO_2 is generally low (0 to 0.28 wt%) for most micas except in the muscovite and Fe-muscovite rims of the Ågskardet-S and Neverdalen micas with relatively high values of up to 0.81 and 0.43 wt%, respectively. Conversely, the Li-Fe muscovites from the Ågskardet OQ record the highest FeO content of ~11 wt%, whereas the Grønnøya and Ørnes micas record the lowest FeO contents of <6.7 wt%. Similarly, MnO in dioctahedral micas is elevated in the Ågskardet OQ with a variable range between 0.2 to 1.9 wt%, whereas those from Grønnøya, Meløy, Ågskardet-S, and Neverdalen range from below detection to 0.2 wt%. MgO contents of dioctahedral micas are the lowest in the Ågskardet OQ pegmatites, Grønnøya, and Ørnes pegmatites ranging from below EPMA detection to 0.57 wt%. The dioctahedral mica rims from the Neverdalen pegmatite record the highest MgO content that can reach 3 wt%. Na_2O content in the dioctahedral micas is irregularly distributed with the highest mean value of 0.36 wt% occurring in the Meløy pegmatite. The

F content is generally low in the muscovites and those from the Ågskardet OQ record the highest and most variable concentrations ranging from 0.47 to 7.5 wt%, whereas the lowest F content occurs in micas from Grønnøya, Meløy and Ørnes, with values of <0.3 wt%. K_2O in muscovites is generally consistent in most of the North Helgeland pegmatites with an average value of 10.5 wt%.

The trioctahedral micas (biotite) also show some compositional heterogeneity in the Ågskardet UB, Ågskardet-S and Neverdalen pegmatites (Table 6b). The Mg-biotite cores from the Neverdalen pegmatite contain higher MnO (1.1 to 1.5 wt %), MgO (17 to 18.3 wt%) and F (1.8 to 2.8 wt%) but are low in FeO (9 to 11 wt%) compared to the Ågskardet UB and Ågskardet-S biotites. Comparably the Fe-biotites from the Ågskardet UB pegmatite contain the lowest MnO (< 0.4 wt%) and F (< 0.93 wt%) contents. The FeO content of the Ågskardet-S biotites are the highest in the area ranging between 22.6 and 24.1 wt% but contain lower MnO that rarely exceeds 6.5 wt %. The Na_2O content in the Ågskardet UB and Ågskardet-S are usually low ranging from below detection to 0.08 wt%, whereas the Neverdalen biotites display concentrations between 0.06 and 0.1 wt%. The K_2O content of biotites in the study area is fairly consistent with a mean of 9.6 wt%.

Mn versus Rb diagrams (Figures 32a, b) were plotted for dioctahedral and trioctahedral micas in the study area. For our mica dataset, the Rb values in apfu were calculated from LA-ICP-MS data and averaged for each locality. The diagrams (Figure 32a, b) show that the Ågskardet OQ pegmatite contain the highest Mn (0.02 to 0.25 apfu) contents for dioctahedral micas, whereas the Mg-biotites from the Neverdalen pegmatite contain higher Mn (0.13 to 0.18 apfu) content for trioctahedral micas. Furthermore, data from this study were plotted and compared with literature data from Sveconorwegian pegmatites of southern Norway (Figure 32c) (Rosing-Schow et al., 2018). The plots show that the Helgeland pegmatite micas are significantly low in Rb and Mn compared to micas from the Tørdal and Evje-Iveland pegmatite fields, with up to 2.65 and 0.63, and 2.04 and 0.48 apfu, respectively (Figure 32c).

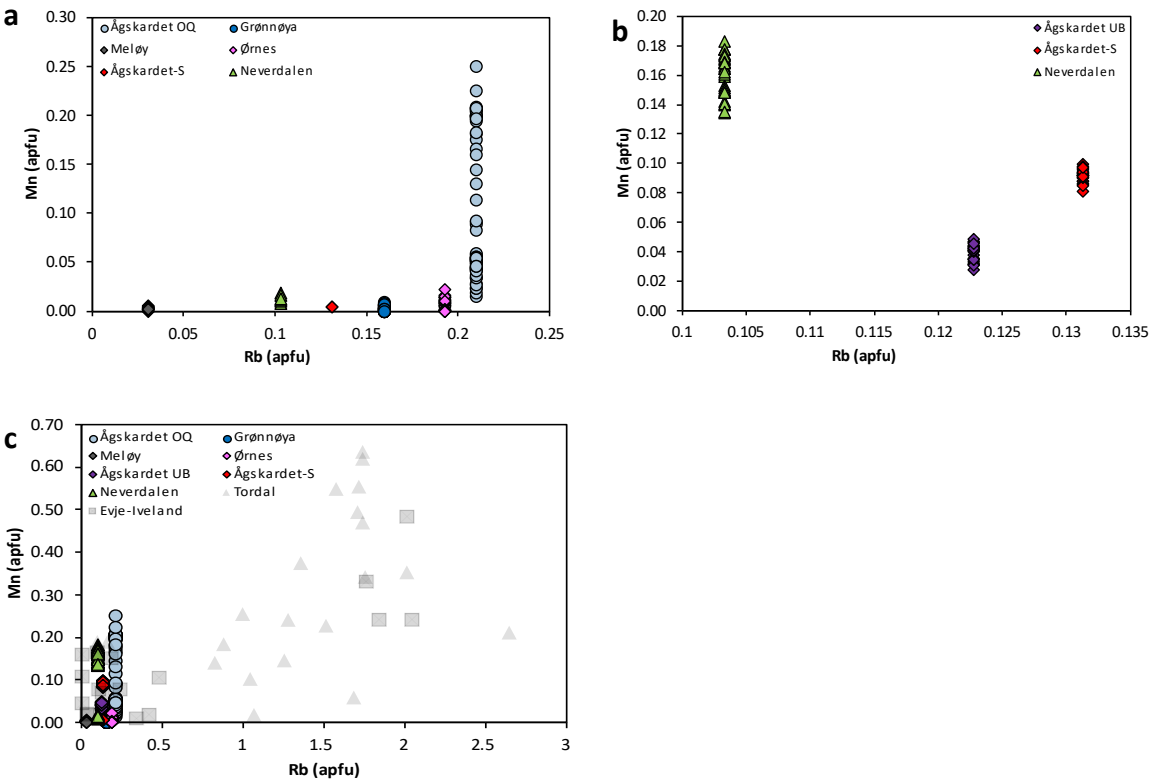

Figure 32. Mn vs Rb diagrams of micas from North Helgeland, (a) trioctahedral micas, (b) dioctahedral micas, (c) comparison to literature data (grey) of micas in pegmatites of southern Norway (Rosing-Schow et al., 2018).

A K/Rb ratio versus Rb plot was used to assess the degree of mica fractionation, similar to the approach taken with feldspars. Average values of K ppm calculated from K_2O wt% EPMA data and Rb were used (Figure 33).

From the plot, micas from Ågskardet and Ørnes display the highest degree of fractionation (within error) with the lowest K/Rb values of 8.75 and 9.52, respectively. Disregarding the K/Rb value for Meløy, which occurs as an outlier in this case, the Neverdalen pegmatite micas are the most primitive with a mean value of 18.14. Only slight differences occur between the K/Rb values for Ågskardet-S and Ågskardet UB (14.45 and 15.35, respectively), but values overlap within error.

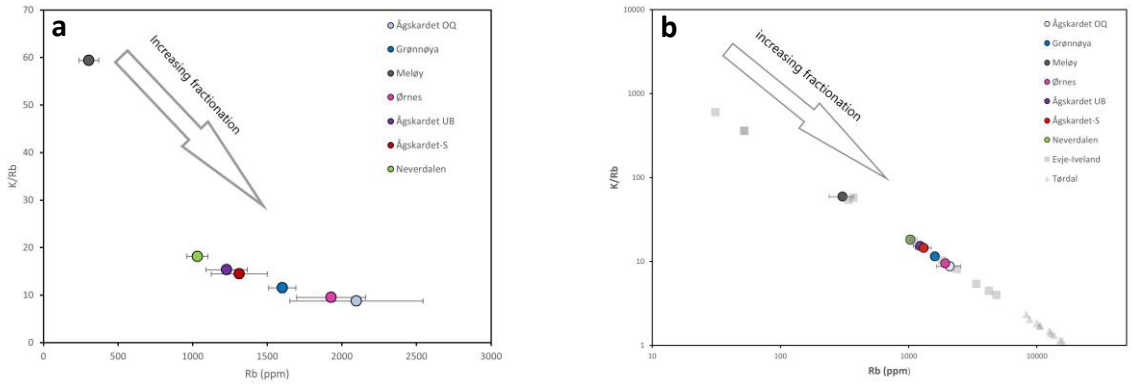

Figure 33. (a) Fractionation trends of the North Helgeland pegmatites showing K/Rb ratios in micas from the different areas, (b) Comparison to literature data of micas from Evje-Iveland and Tørdal in southern Norway (Rosing-Schow et al., 2018).

To further address the level of evolution and the distinctive chemical characteristics of the North Helgeland micas, our data were compared to data from the literature on Sveconorwegian pegmatites of Tørdal and Evje-Iveland in southern Norway (Rosing-Schow et al., 2018).

The Evje-Iveland micas display the highest variability in K/Rb, ranging from primitive pegmatite values with K/Rb of ~600 and 31 ppm Rb to highly fractionated pegmatite values with K/Rb of 4.5 and 4232 ppm Rb (Figure 33b). The Tørdal micas show lower variability but high degrees of fractionation with consistently low K/Rb <17.8. Compared to the pegmatite fields of southern Norway, even the most evolved pegmatite body in Helgeland (the Ågskardet OQ) is relatively primitive.

4.2.1 Trace Element

A total of one hundred and eight trace element analyses were obtained for mica from the Helgeland pegmatites using LA-SF-ICP-MS. Figures 34 and 35 display the results together with relevant literature data.

The white and pink micas from the Ågskardet UQ pegmatites have the highest Ta, Li, Cs and Rb contents with low Nb contents and Nb/Ta values (Figures 34a, c, e). They also have a low average K/Rb ratio of 8.75. The Ågskardet micas display two distinct trace element compositions. The pink micas are more enriched in Li (9008 to 11770 ppm), Cs (694 to 864 ppm), Ta (83 to 104 ppm), with lower Nb/Ta values <0.7. By contrast, the white micas have

relatively high Nb/Ta value between 2.30 and 3.61 but are low in Nb (<164 ppm), Ta (<59 ppm), Li (< 1684 ppm) and Cs (<89 ppm).

Muscovites from the Meløy and Ørnes pegmatites have overlapping Nb/Ta ratios between 2.62 and 10.38, but the Ta and Cs contents are higher at Ørnes (Figures 34a, c, e). However, the Li and Rb contents in micas are slightly higher at Meløy of up to 682 ppm and 4504 ppm, respectively. Two compositionally distinct muscovite types occur in the Ørnes pegmatite: type 1 is high in Li (110 to 178 ppm), Cs (105 to 181 ppm), Nb (80 to 157 ppm), Ta (15 to 31 ppm), Rb (1805 to 2085 ppm), and Nb/Ta is often <5.5; type 2 Fe-biotite is relatively low in Li (<33.2 ppm), Cs (<52 ppm), Nb (<7.6 ppm), Ta (<0.64 ppm) and Rb (<484 ppm) with Nb/Ta values of up to 10.4.

Meløy muscovites also display two distinct trace element compositions: type 1 has higher Nb (47 to 66 ppm), Ta (5 to 16 ppm), Li (404 to 682 ppm), Cs (9.7 to 79.7 ppm) and Rb (up to 619 ppm) contents, whereas type 2 has relatively low Nb (<20.8 ppm), Ta (<7.9 ppm), Li (<54.8 ppm), Cs (<21.8 ppm) and Rb (<348.6 ppm) contents (Figures 34a, c, e) . Futhermore, the Nb/Ta values are lower for type 2 muscovites (<3.5). The muscovite compositions of the Grønnøya and Neverdalen pegmatites are similar, with relatively low Li and Cs contents, but high Nb/Ta values >16.7. However, the Grønnøya micas have higher Ta (21 to 26.5 ppm), Nb (401 to 460 ppm) and Rb (1522 to 1667 ppm) contents compared to the Neverdalen Fe-muscovite rims.

Fe-biotites from the Ågskardet-S pegmatite have elevated Ta and Cs contents, compared to the Ågskardet UB and Neverdalen biotites. In addition, the Ågskardet-S Fe-biotites have Nb/Ta ratios <10, with average K/Rb ratio of 14.5, and relatively higher Nb contents ranging from 573 to 627 ppm (Figures 34b, d, f).

In comparison, the Ågskardet UB biotites have slightly overlapping Li, Cs and Rb contents and K/Rb ratio (within error) with the Ågskardet-S biotites, but with lower Nb (324 to 377 ppm) and Ta (27 to 34 ppm) contents. Mg-biotite cores from the Neverdalen pegmatite have the lowest Li (<359 ppm), Cs (<32.6 ppm), Ta (<6 ppm) and Nb (<113.6 ppm) contents with a higher mean Nb/Ta ratio of 19.

In general, only micas from Neverdalen, Ågskardet UB and mica cores from Grønnøya have Nb/Ta values above the average bulk continental crust value of 11.4 according to Rudnick & Gao (2003). A positive correlation is observed between Li and Rb (Figure 35). Again, our data were compared to literature data for the southern Norwegian pegmatite micas to assess the level of Li enrichment (Figure 35). In our study, the highest Li and Rb contents are recorded by mica cores from pegmatites of the Ågskardet OQ reaching 11769 and 2517 ppm, with average concentrations of 4629 ppm Li and 2098 ppm Rb, respectively. Compared to micas from the Sveconorwegian pegmatites in southern Norway, the Helgeland pegmatites of North Norway contain significantly less Li and Rb.

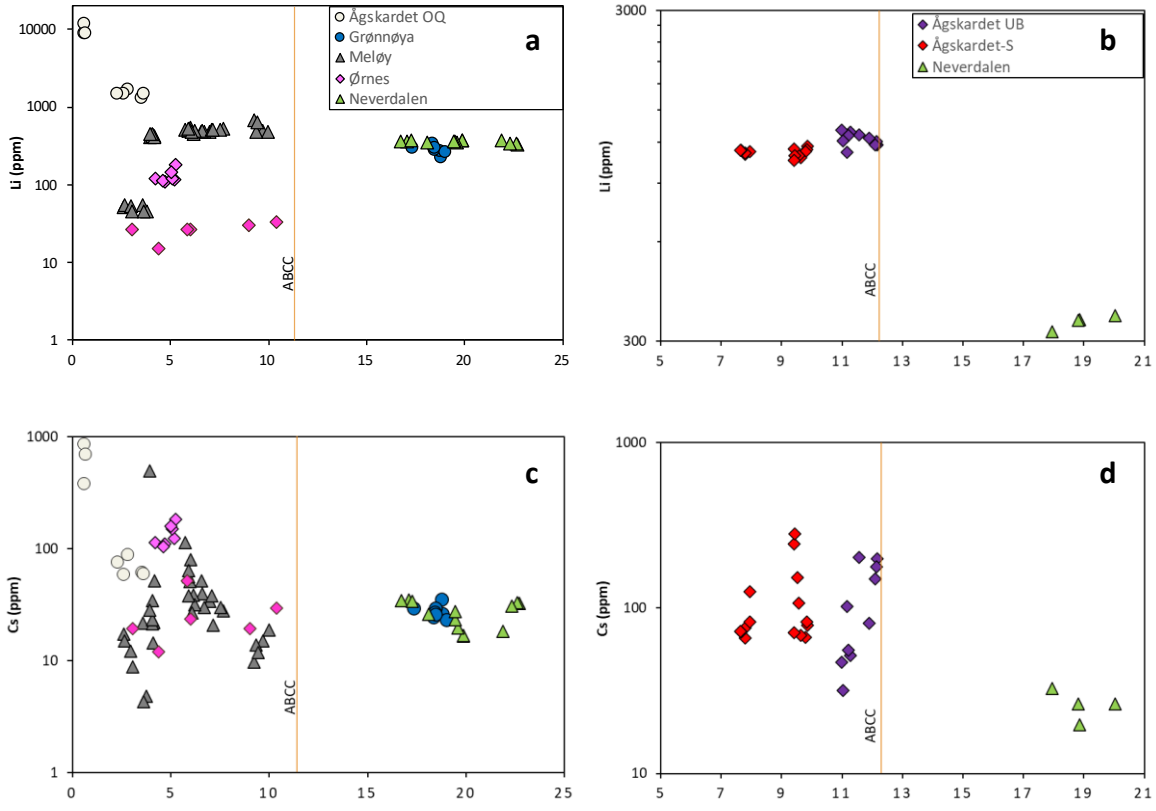

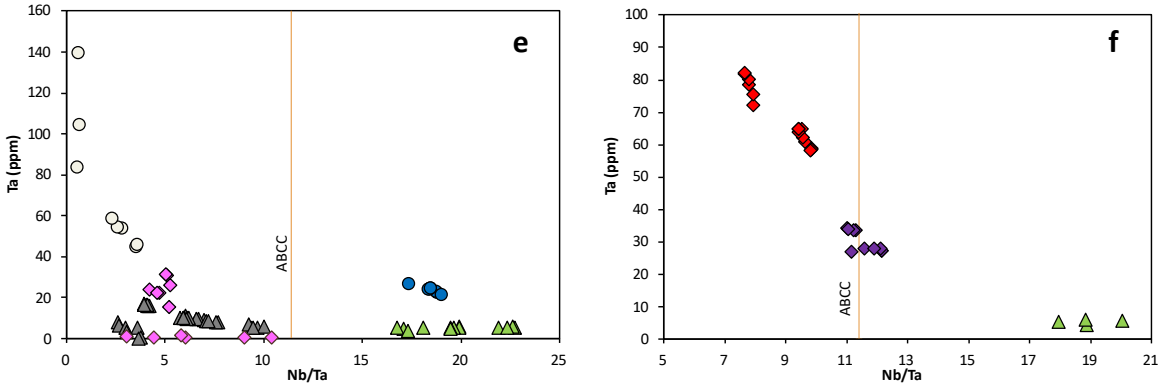

Figure 34. (a, b) Li, (c, d) Cs, (e, f) Ta vs Nb/Ta diagrams comparing the composition of micas. ABCC = average bulk continental crust composition of Rudnick & Gao (2003). Diagrams (a,c,d) are for dioctahedral micas; (b, d, f) are for trioctahedral micas.

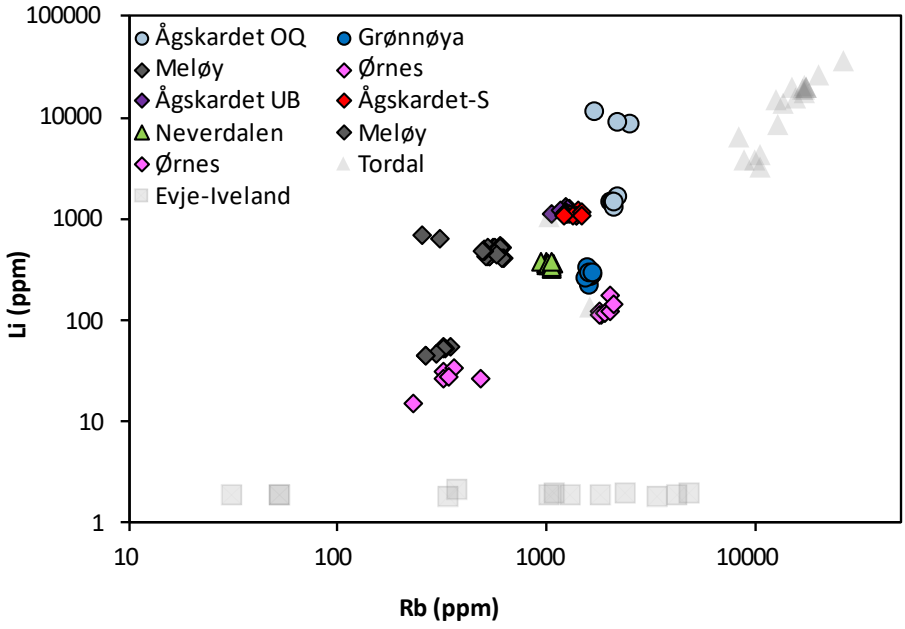

Figure 35. The Li versus Rb content of mica from North Helgeland compared to literature data (grey) of micas from Tørdal and Evje-Iveland (Rosing-Schow et al., 2018).

4.2.2 Garnet

Garnets are mostly found in metamorphic rocks but also occur in some igneous rocks, specifically granites and granitic pegmatites. They have a general formula of (X3)(Y2)(Z3)ϕ12, where X, Y and Z refer to dodecahedral, octahedral, and tetrahedral sites, respectively, and ϕ is O, OH, or F (Grew et al., 2013). X and Y are sites for divalent (Ca, Mg,

Fe and Mn) and trivalent (Al, Fe^{3+}, Mn^{3+}, and Cr) cations with dominant Si in the tetrahedral position respectively. The principal endmembers are subdivided into two series: the Mg (pyrope), Fe (almandine) and Mn (spessartine) garnets; and the Ca garnets andradite and grossular as well as the Cr garnet uvarovite (Deer et al., 2013). Recent attention has been drawn to garnets from granitic pegmatites because of their potential for elucidating pegmatite petrogenesis and their ore potential (e.g., Müller et al., 2012; Feng et al., 2017).

4.2.2.1 Major Elements

A total of 159 spots on garnets from pegmatites in Helgeland were analyzed by EPMA. A summary of the EPMA analyses is provided in Table 7. For the complete dataset, readers are referred to Appendix 8.4.3. The garnets are dominated by almandine and spessartine, with little pyrope component (0.05 to 12.41 mol.%), grossular (0.81 to 2.80 mol.%), and almost no andradite or uvarovite (Table 7). The Na_2O, K_2O, SrO, TiO_2, Cr_2O_3 and P_2O_5 contents are mostly below 0.1 mol.%. Garnets within the pegmatites at Ågskardet UB contain > 70 mol.% almandine and ~11 to 15.9 mol.% spessartine. Pyrope content is ~10.7 to 14.54 mol.% with grossular ~ 2.08 to 3.60 mol.%. By contrast, garnets from Ågskardet UQ, Grønnøya and Ørnes are relatively high in spessartine component (31.3 – 58.8 mol.%) with almandine contents at ~40 to 65 mol.%. These garnets also record lower pyrope of ~0.05 to 2.94 mol.% and grossular of ~0.81 – 2.80 mol.%.

The major element or component profiles show that garnets from Grønnøya display increased almandine contents but decreased spessartine contents from core to rim (Figure 36a). Conversely, garnets from Ørnes and Ågskardet OQ show a significant increase in spessartine content but decrease in almandine content from core to rim (Figures 36b, c). In sample RL22-08C from Ågskardet OQ, the almandine rich core consistently decreases toward the rim, whereas spessartine content increases toward the rims (Figure 36d). The garnets from the Ågskardet UB have fairly consistent almandine, spessartine, grossular and pyrope contents (Figure 36e).

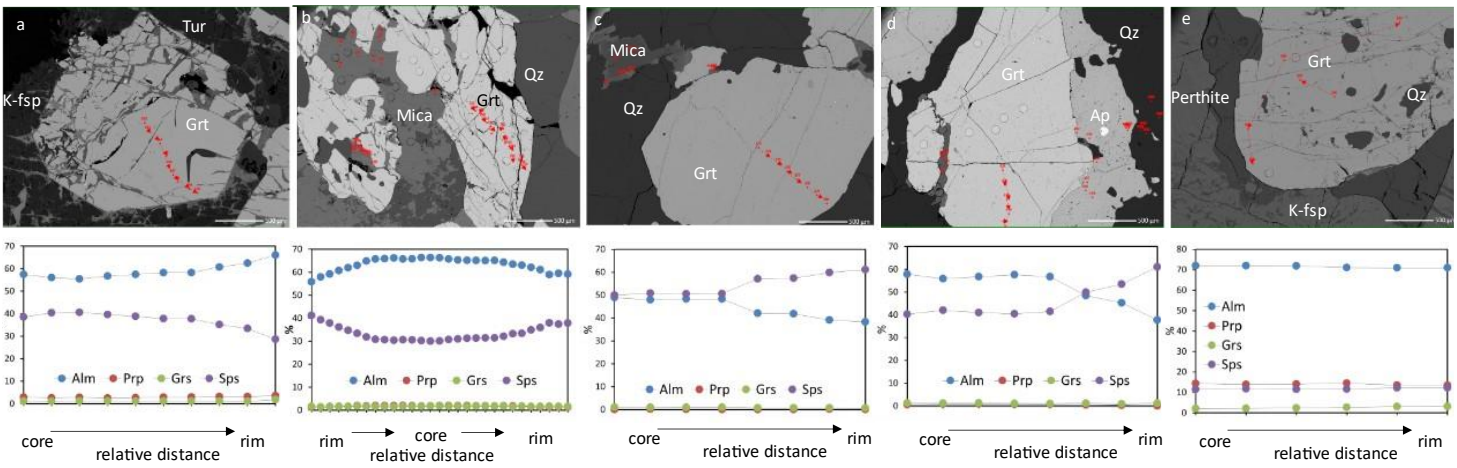

Figure 36. Major element profiles of garnets from the North Helgeland pegmatites. (a) Grønnøya, (b) Ørnes, (c, d) Ågskardet OQ, (e) Ågskardet UB. Alm = almandine, Grs = grossular, Prp = pyrope, Sps = spessartine.

4.2.2.2 Trace Elements

All the analyzed garnets from the North Helgeland pegmatite field contain detectable Li, Na, Y, P, HREE, Sc and Ti (see Appendix 8.5.3). The Li concentrations of the garnets are highly variable, ranging from 22.5 ppm at Neverdalen to 205 ppm at Ågskardet OQ. Garnets from Ørnes are highly variable in Na (below detection to 102 ppm) compared to garnets from other areas. They also contain the highest Ti concentrations (435 to 1220 ppm). At Neverdalen, garnets have the highest Y (2703 to 4592 ppm) and REE (2043 to 3349 ppm total REE) concentrations. In general, the Sc concentrations of the analyzed garnets range from below detection for Ågskardet OQ to up to 306 ppm for Ågskardet UB.

Figure 37 shows the trace element profiles for garnets from our study area. Ågskardet OQ garnets show enrichment in Li, but depletion in Ti from core to rim. The Nb concentration and Nb/Ta ratio slightly decrease from core to rim and become enriched towards the outermost rims. In contrast, garnets from Grønnøya show enrichment in Li and Ti from core to rim. The Nb and Ta concentrations of the garnets show a sharp decrease from crystal core to rim, and then slightly increase towards the outermost rim. At Meløy, the Li correlates positively with the Nb and Ta contents, which exhibit enrichment spikes from core to rim, but sharp depletion towards the outermost rim. Ti content and the Nb/Ta ratio are irregular in the rims and sharply decrease towards the outermost rim. Garnets from the Neverdalen pegmatite show identical patterns of Li, Ti, and Nb depletion from core to rim. These garnets are generally very depleted in Ta. At Ørnes, there is a concentration spike for Ti, Nb, Ta and the Nb/Ta ratio in the core, which sharply decreases in the rim and does not show any significant change towards the outermost rim, with the exception of very depleted Nb content. Li is moderately

enriched from core to rim in the garnets from the Ørnes pegmatite. At the Ågskardet UB, the Li and Ti contents of the garnets decrease from core to rim, and they increase towards the outermost rim. Nb is completely depleted in the garnet rims, whereas Ta generally decreases from core to rim.

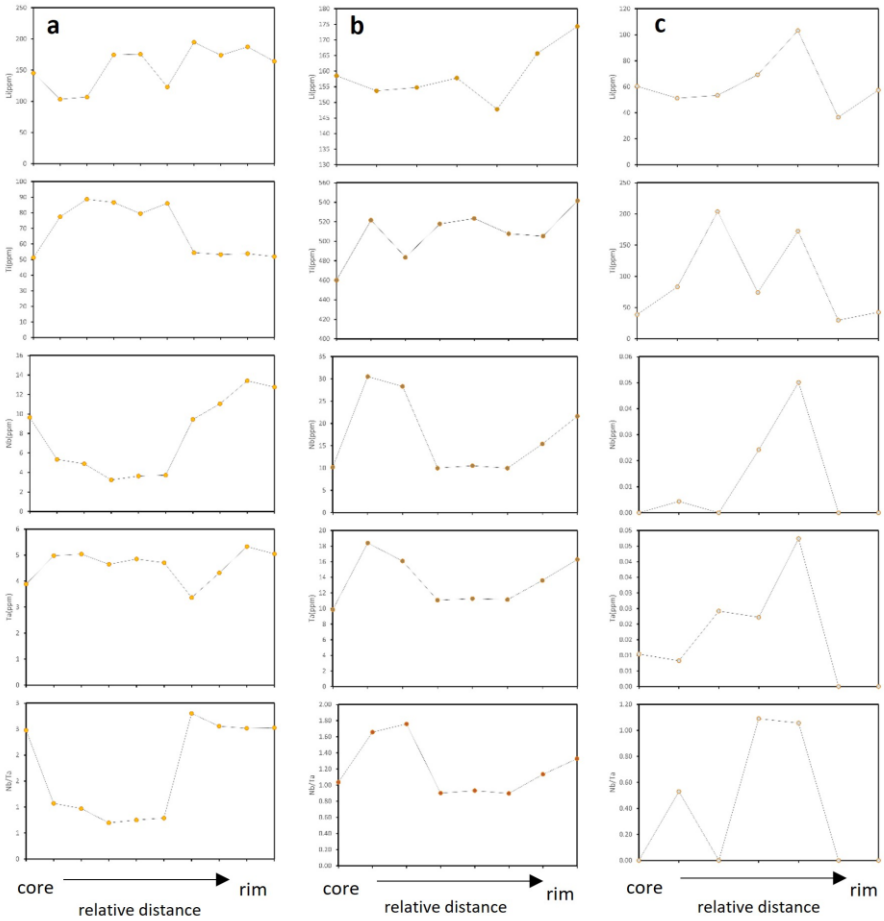

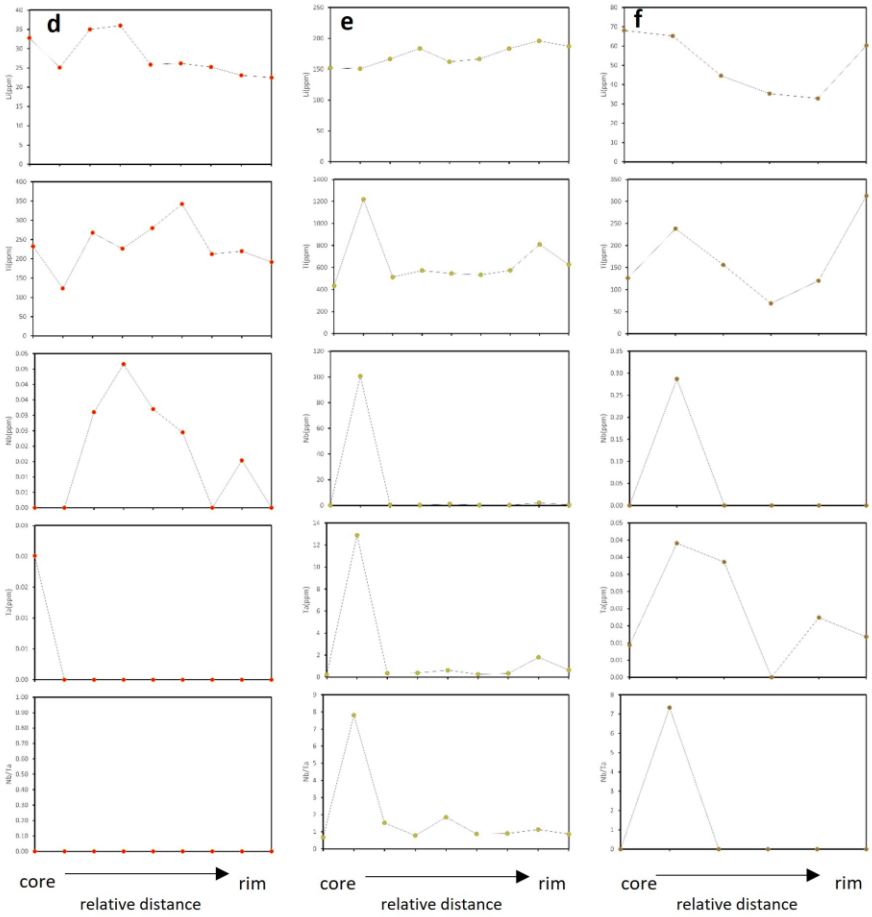

Figure 37. Trace element profiles of garnets from the North Helgeland pegmatites. (a) Ågskardet OQ, (b) Grønnøya, (c) Meløy, (d) Neverdalen, (e) Ørnes, (f) Ågskardet UB.

Table 7. Summary of EPMA analyses of garnets from the North Helgeland pegmatites.

Locality	Ågskardet-Upper Body		Ågskardet Old Quarry		Ågskardet Old Quarry	
Sample ID	RL22-16		RL-22-7E		RL-22-8C	
Lithology	Pegmatite		Pegmatite		Pegmatite	
	ave. (27)	s.d	ave. (26)	s.d	ave. (22)	s.d.
SiO_2	37.05	0.51	36.16	0.56	36.03	0.60
TiO_2	0.02	0.05	0.02	0.05	0.02	0.04
Al_2O_3	20.92	0.28	20.32	0.27	20.21	0.39
FeO_{tot}	32.43	0.39	18.27	5.26	22.64	5.94
BaO	0.07	0.13	0.06	0.09	0.09	0.13
MnO	6.00	1.55	25.06	5.20	20.25	6.12
MgO	3.08	0.62	0.01	0.03	0.12	0.13
CaO	1.00	0.35	0.28	0.14	0.40	0.08
Na_2O	0.02	0.03	0.01	0.02	0.01	0.03
K_2O	0.00	0.00	0.00	0.00	0.00	0.00
SrO	0.01	0.03	0.01	0.04	0.01	0.04
Cr_2O_3	0.01	0.02	0.01	0.02	0.01	0.02
P_2O_5	0.03	0.06	0.09	0.13	0.15	0.09
F	0.03	0.09	0.03	0.11	0.01	0.05
Cl	0.00	0.01	0.00	0.01	0.00	0.01
Total	97.07	38.06	100.33	1.16	99.95	1.08
apfu based on 12 oxygen atoms						
Si	2.97	0.02	2.98	0.03	2.98	0.03
Ti	0.00	0.00	0.00	0.00	0.00	0.00
Al	1.98	0.02	1.97	0.02	1.97	0.02
Fe^{2+}	2.10	0.05	1.20	0.35	1.51	0.41
Fe^{3+}	0.07	0.04	0.06	0.07	0.06	0.06
Ba	0.00	0.00	0.00	0.00	0.00	0.00
Mn	0.41	0.11	1.75	0.36	1.42	0.43
Mg	0.37	0.07	0.00	0.00	0.01	0.02
Ca	0.09	0.03	0.02	0.01	0.04	0.01
Na	0.00	0.00	0.00	0.00	0.00	0.00
K	0.00	0.00	0.00	0.00	0.00	0.00
Sr	0.00	0.00	0.00	0.00	0.00	0.00
Cr	0.00	0.00	0.00	0.00	0.00	0.00
Endmembers (%)						
almandine	70.93	1.25	40.33	11.77	50.62	13.79
pyrope	12.41	2.36	0.05	0.11	0.50	0.55
grossular	2.80	0.99	0.81	0.39	1.16	0.22
spessartine	13.76	3.67	58.78	12.15	47.68	14.32
uvarovite	0.00	0.00	0.00	0.00	0.00	0.00
andradite	0.10	0.06	0.02	0.03	0.04	0.04
Ca-Ti garnet	0.00	0.00	0.00	0.00	0.00	0.00

Table 7 continued.

Locality	Grønnøya		Grønnøya		Ørnes	
Sample ID	RL-22-1A		RL-22-1C		RL-22-4J1	
Lithology	Pegmatite		Pegmatite		Pegmatite	
	ave. (20)	s.d.	ave. (20)	s.d.	ave. (44)	s.d
SiO_2	36.18	0.37	36.19	0.61	36.18	0.52
TiO_2	0.10	0.08	0.05	0.07	0.08	0.10
Al_2O_3	20.12	0.29	20.13	0.35	20.33	0.26
FeO_{tot}	24.76	3.80	25.09	1.69	29.35	3.30
BaO	0.08	0.16	0.09	0.21	0.08	0.15
MnO	17.43	3.96	17.64	2.04	13.35	3.90
MgO	0.65	0.16	0.71	0.23	0.46	0.18
CaO	0.41	0.12	0.34	0.12	0.60	0.11
Na_2O	0.01	0.03	0.02	0.03	0.02	0.03
K_2O	0.00	0.00	0.00	0.01	0.00	0.00
SrO	0.01	0.05	0.01	0.03	0.01	0.03
Cr_2O_3	0.01	0.02	0.01	0.02	0.01	0.02
P_2O_5	0.13	0.12	0.09		0.05	0.07
F	0.03	0.11	0.02	0.11	0.01	0.08
Cl	0.00	0.01	0.00	0.01	0.00	0.01
Total	99.93	0.78	100.40	1.44	100.52	0.97
apfu based on 12 oxygen atoms						
Si	2.99	0.02	2.97	0.03	2.97	0.02
Ti	0.01	0.01	0.00	0.00	0.00	0.01
Al	1.96	0.02	1.95	0.02	1.97	0.02
Fe^{2+}	1.65	0.26	1.62	0.15	1.93	0.24
Fe^{3+}	0.06	0.04	0.10	0.07	0.09	0.04
Ba	0.00	0.01	0.00	0.01	0.00	0.00
Mn	1.22	0.28	1.23	0.14	0.93	0.27
Mg	0.08	0.02	0.09	0.03	0.06	0.02
Ca	0.04	0.01	0.03	0.01	0.05	0.01
Na	0.00	0.01	0.00	0.00	0.00	0.01
K	0.00	0.00	0.00	0.00	0.00	0.00
Sr	0.00	0.00	0.00	0.00	0.00	0.00
Cr	0.00	0.00	0.00	0.00	0.00	0.00
Endmembers (%)						
almandine	55.24	8.84	54.67	4.68	65.03	8.15
pyrope	2.69	0.63	2.94	0.90	1.90	0.77
grossular	1.18	0.35	0.96	0.32	1.69	0.32
spessartine	40.84	9.51	41.37	5.08	31.30	9.09
uvarovite	0.00	0.00	0.00	0.00	0.00	0.00
andradite	0.04	0.02	0.05	0.04	0.07	0.04
Ca-Ti garnet	0.00	0.00	0.00	0.00	0.00	0.01

Numbers in parenthesis represent the number of EPMA analyses; ave. = average; s.d = 2* standard deviation.

Normalized REE patterns

The garnets from the North Helgeland pegmatites display HREE enrichment (from Gd to Lu) and a negative Eu anomaly in the chondrite normalized REE patterns (Figure 38). Chondrite REE concentrations for normalization are taken from Palme and Jones (2003). The garnets from Ågskardet UB, Grønnøya, Neverdalen, Ørnes and Meløy display consistent normalized REE patterns with $(Gd/Yb)_N$ values between 0.01 to 0.80. The garnets from the Ågskardet OQ, however, exhibit strong depletion in LREE and variation in the fourth tetrad (Er to Lu). From core to rim, the REE patterns generally display increasing depletion in Er to Lu with $(Gd/Yb)_N$ increasing from 2.2 to 18.1. Sample RL22-8C from Ågskardet OQ shows alternating enrichment and depletion from core to rim in the fourth tetrad with highly variable $(Gd/Yb)_N$ values between 26 and 79. Similarly, the garnet patterns from Grønnøya exhibit decreasing enrichment of HREE (Tb to Lu) from core to rim with $(Gd/Yb)_N$ increasing slightly from 0.06 to 0.18. The REE patterns for garnet cores from Ørnes exhibit slight variability with $(Gd/Yb)_N$ between 0.05 and 0.11. The Meløy and Ågskardet UB garnets display alternating patterns of enrichment and depletion in HREE with $(Gd/Yb)_N$ values between 0.04 and 0.21 and 0.01 and 0.18, respectively.

The Eu/Eu* ($Eu^* = [(Sm_N * Gd_N)^{0.5}]$ ratios were calculated for all analyzed garnets to assess the size of the negative Eu anomaly (Figure 39). Garnets from Meløy display the highest Eu/Eu* ratios (i.e., the weakest negative Eu anomaly) ranging from 0.41 to 0.6. Neverdalen garnets have moderately low Eu/Eu* ratios ranging from 0.14 to 0.22. Garnets from pegmatites of the other occurrences studied have characteristically strong negative Eu anomalies, with the lowest Eu/Eu* values recorded by the Ågskardet OQ sample.

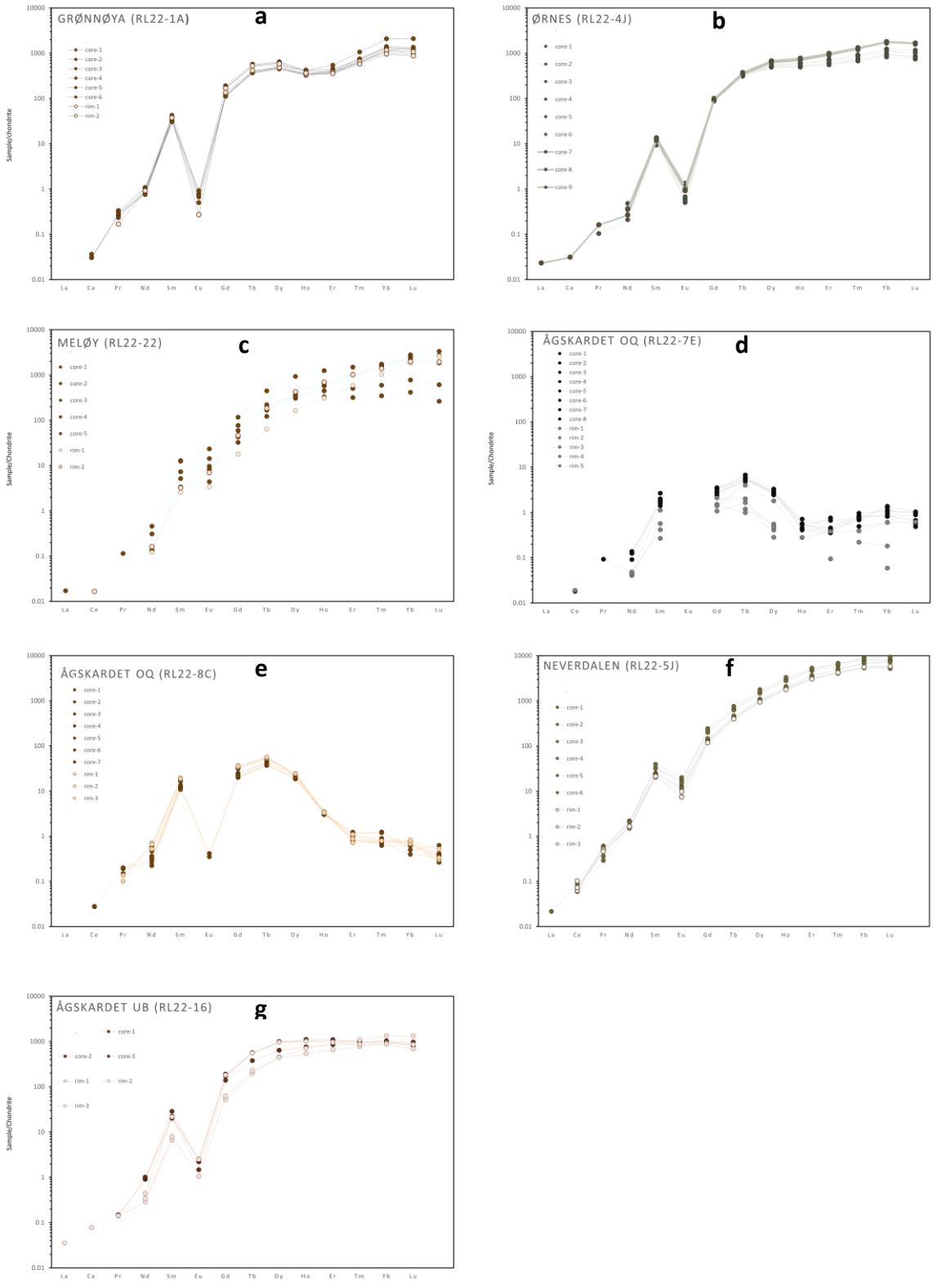

Figure 38. Chondrite-normalized REE patterns for garnets in granitic pegmatites from North Helgeland. REE patterns for representative garnets from (a) Grønnøya, (b) Ørnes, (c) Meløy, (d, e) Ågskardet OQ, (f) Neverdalen, and (g) Ågskardet UB. The values for chondrite REE concentrations are cited from Palme & Jones (2003).

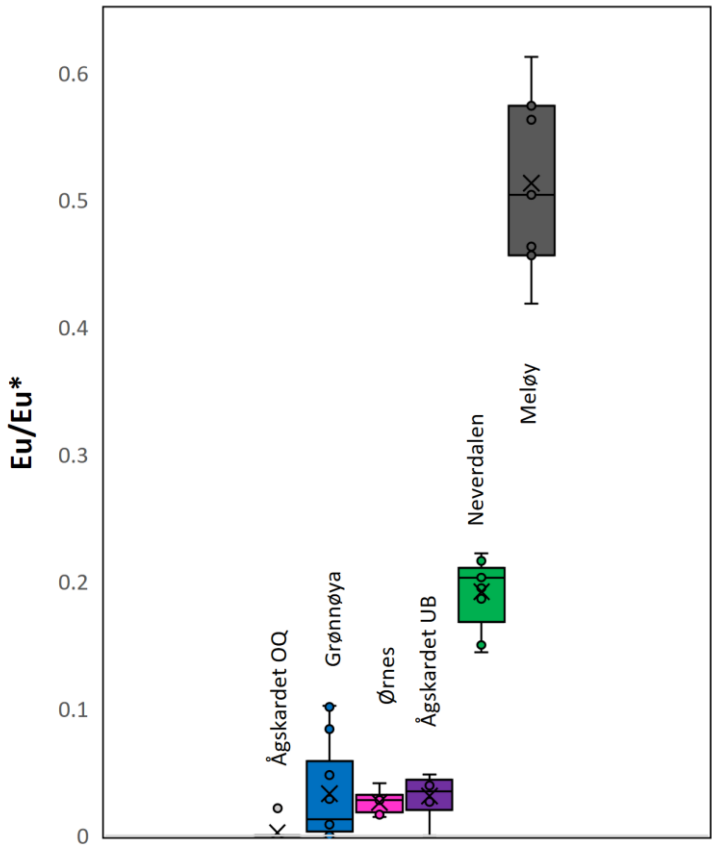

Figure 39. Box and whisker plots showing the Eu/Eu ratios of garnets in the North Helgeland pegmatites. The boxes represent the 1st to 3rd quartile of data; whiskers represent the maximum and minimum values, and the median values are the bars inside the boxes. Meløy records the highest Eu/Eu* ratios of garnets in our study area.*

4.2.3 Tourmaline

Tourmaline has traditionally been regarded as a mineral of interest for collectors, a gemstone of moderate value, or an intriguing accessory mineral found in certain rock formations. The latest developments in the complex and diverse chemistry of tourmaline, along with its limited diffusivity, make it a dependable gauge of its host environment in a broad range of rocks, such as granitic pegmatites (Dutrow & Henry, 2011). According to Henry et al. (2011), the tourmaline supergroup has a general formula of $XY_3Z_6T_6O_{18}(BO_3)_3V_3W$ and comprises 18 species. The site preferences are expressed as follows:

X = □ (vacancy), Na, K, Ca, Pb^{2+},

Y = Li, Mg, Fe^{2+}, Mn^{2+}, Cu^{2+}, Al, V^{3+}, Cr^{3+}, Fe^{3+},

Mn^{3+}, Ti^{4+},

Z = Mg, Fe^{2+}, Al, V^{3+}, Cr^{3+}, Fe^{3+},

T = Si, B, Al,

B = B,

V = OH, O, and

W = OH, F, O.

The letters represent groups of cations and anions that occupy similar sites in the tourmaline structure. Hawthorne and Dirlam (2011) show that the structural setup of tourmalines enables it to attain the trigonal symmetry that is distinct for its crystal morphology. Hawthorne and Henry (1999) subdivided three primary groups for classification of tourmalines according to extensive compositional variations at the X, Y, Z and W sites. They include the X-site vacant, alkali and calcic groups (Figure 40a).

The most common species are schorl [$NaFe_3Al_6Si_6O_{18}(BO_3)_3(OH)_3(OH)$], dravite [$NaMg_3Al_6Si_6O_{18}(BO_3)_3(OH)_3(OH)$] and elbaite [$Na\ (Li_{1.5}Al_{1.5})_3Al_6Si_6O_{18}(BO_3)_3(OH)_3(OH)$]. The tourmaline structure accepts a complex mix of elements including mono-, di-, tri and tetravalent cations together with mono- and divalent anions (Dutrow & Henry, 2011). The stability of tourmaline is attributed to its structural flexibility, which enables it to adapt its composition to varying chemical environments and temperature-pressure conditions (Dutrow & Henry, 2011). Despite its extensive P-T stability range, tourmaline is sensitive to highly acidic to neutral solutions (e.g., Henry & Dutrow, 1996). This enables tourmaline crystals to preserve discrete compositional zones that signify distinct phases of dissolution and growth resulting from changes in fluid composition. Due to its robustness, tourmaline can serve as a geochemical recorder of highly evolved magmatic rocks including granitic pegmatites (Marschall & Jiang, 2011).

In North Helgeland, tourmaline occurs as black crystals, with variable morphology and textures. It forms euhedral to subhedral crystals in some pegmatites such as at Ågskardet

OQ, Meløy, Grønnøya and Ørnes, very often in contact with garnet and quartz, but also with K-feldspar, biotite, muscovite and apatite. For example, at the Ågskardet OQ, parallel zones of brecciated tourmalines occur with interstitial quartz and feldspar matrices. The crystals mostly contain fractures that run perpendicular to the long axes and display compositional zoning from core to rim. However, tourmaline can also form anhedral and vein-like structures that crosscut other minerals or occur in the interstices and cracks of other phases. The entire sections of the late-stage tourmalines are cut by irregular fractures, are patchy and may show less defined compositional zoning. They vary in size from < 0.5 mm to euhedral crystals up to 20 cm in length. Both textural types can host inclusions of other minerals. Figure 40 shows BSE images of representative tourmaline crystals from the North Helgeland pegmatites.

A summary of EPMA analyses of representative tourmaline samples in thin sections is provided in Table 8. The complete results from the tourmaline analyses are provided in Appendix 8.4.4. The structural formulae and site allocation of tourmaline were calculated using the software WinTcac, by Yavuz et al., (2014) from the Department of Geological Engineering, Istanbul Technical University, Turkey based on the current International Mineralogical Association (IMA-2011) nomenclature scheme (Henry et al., 2011). The program calculates H_2O and Li_2O_3 stoichiometrically, including occupancy in the octahedral and tetrahedral (Y+Z+T) sites respectively. This is based on a OH + F + Cl = 4, 15 cations and 31 anions normalization scheme.

Most tourmalines in the study area are of schorl composition and plot in the alkali field (Figures 41a, b). However, a few tourmalines including those from Meløy and Grønnøya (rims) are of dravite composition. The schorl display some variability in elemental composition highlighted by samples from Ågskardet OQ with Mg/Mg+Fe (Mg#) below 0.09 to higher Mg# (0.42 to 0.48) in the Ågskardet-S tourmalines. Ågskardet-S tourmalines also contain variable but high Ti (0.03 to 0.21 apfu) with low Na/Na+Ca (Na#) rarely exceeding 0.91 (Figures 42b, c). The highest Fe contents are found in the Ågskardet OQ and Ørnes tourmalines ranging from 1.24 to 2.19 apfu and 2.18 to 1.72 apfu, respectively. However, Ørnes tourmalines show the highest variability in schorl composition together with variable

Ti content. The Ågskardet OQ tourmalines are relatively homogenous in composition exhibiting the lowest Ti contents with a high degree of clustering (Figure 42b). The highest Mg contents in tourmalines is found in Meløy ranging from 1.22 to 1.48 apfu but with low Ti (< 0.06 apfu) and Na# similar to Ågskardet-S. In general, Fe and Mg contents are inversely correlated whereas Ti and Mg show a positive correlation (Figures 42a, b).

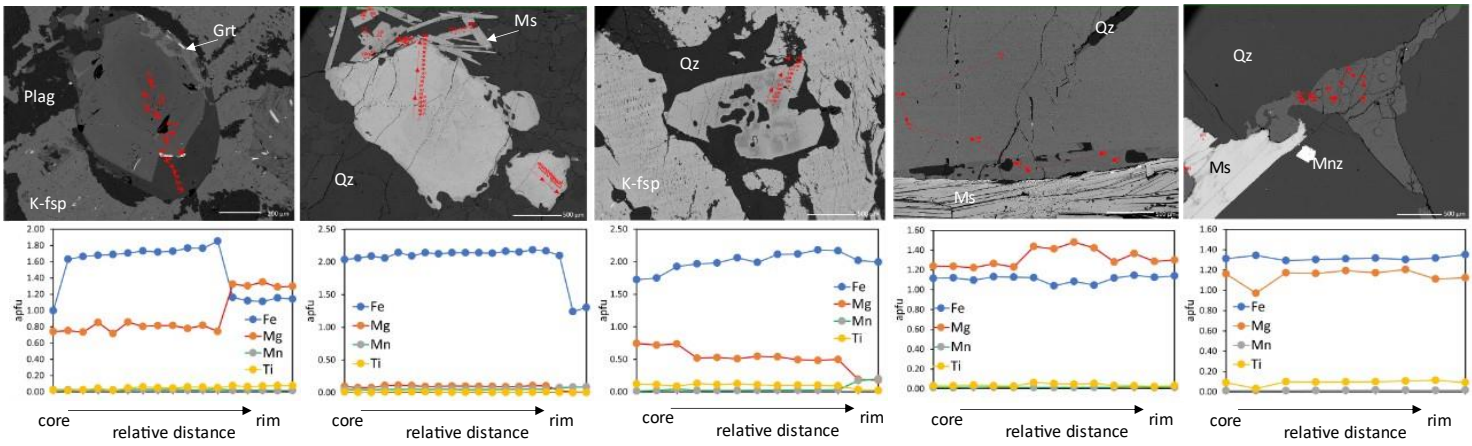

Figure 40. Figure 42. BSE images of tourmalines showing major element core to rim patterns (a) Grønnøya, (b) Ågskardet OQ, (c) Ørnes, (d) Meløy, (e) Ågskardet-S. (a) oscillatory zoning in tourmaline reflecting variations in Fe and Mg compositions from core to mantle. The rim is Mg-rich and the white crystals on the mantle-rim boundary are garnets. (b) Resorbed rims of euhedral tourmalines with quartz replacement. (c) resorbed tourmaline crystal with quartz replacement. (d) euhedral tourmaline with muscovite alignment perpendicular to interface. Quartz forms in cracks of the tourmaline crystal. Anhedral tourmaline forming in quartz interstices. Red arrows indicate direction of EPMA analyses. Grt = garnet, k-fsp = k-feldspar, Mnz = monazite, Ms = muscovite, Plag = plagioclase, Qz = quartz.

Table 8. Summary of EPMA analyses on tourmalines from the North Helgeland pegmatites.

Locality	Ågskardet Old Quarry		Ågskardet Old Quarry		Grønnøya		Grønnøya	
Sample ID	RL22-7E		RL22-8C		RL22-1A		RL22-1C	
Lithology	Pegmatite		Pegmatite		Pegmatite		Pegmatite	
	ave. (116)	s.d	ave. (105)	s.d	ave. (80)	s.d	ave. (44)	s.d
SiO_2	34.04	1.26	34.29	0.97	34.52	0.79	34.89	0.62
TiO_2	0.03	0.05	0.02	0.04	0.32	0.29	0.37	0.34
Al_2O_3	33.47	0.76	33.95	1.16	32.21	1.23	32.59	1.20
Cr_2O_3	0.01	0.02	0.01	0.02	0.01	0.02	0.01	0.03
FeO	14.32	1.96	13.31	0.73	12.72	1.29	11.34	3.25
MnO	0.48	0.21	0.65	0.12	0.14	0.11	0.17	0.07
MgO	0.17	0.21	0.25	0.13	2.77	0.64	3.49	1.85
CaO	0.06	0.05	0.07	0.06	0.13	0.14	0.13	0.13
BaO	0.08	0.16	0.06	0.13	0.07	0.14	0.07	0.14
Na_2O	1.95	0.28	2.04	0.20	2.04	0.30	2.04	0.27
K_2O	0.04	0.02	0.04	0.03	0.05	0.03	0.05	0.03
Cs_2O	0.01	0.02	0.01	0.02	0.01	0.02	0.01	0.02
F	0.58	0.32	0.67	0.22	0.28	0.19	0.24	0.17
Cl	0.00	0.00	0.00	0.01	0.00	0.01	0.00	0.00
B_2O_3	11.65	2.31	11.64	2.63	11.57	2.36	11.55	2.38
Total	96.88	2.68	97.00	2.48	96.82	2.41	96.95	2.19
F	0.31	0.18	0.36	0.12	0.15	0.10	0.13	0.09
Cl	0.00	0.00	0.00	0.00	0.00	0.00	0.00	0.00
OH	3.20	0.63	3.22	0.61	3.35	0.56	3.33	0.61
B	3.00	0.00	3.00	0.00	3.00	0.00	3.00	0.00
Si(T)	5.87	0.12	5.88	0.06	5.89	0.06	5.90	0.06
Al(T)	0.01	0.08	0.02	0.08	0.02	0.08	0.02	0.06
Al(Z)	6.00	0.00	6.00	0.00	6.00	0.00	6.00	0.00
Fe^{3+}(Z)	0.00	0.00	0.00	0.00	0.00	0.00	0.00	0.00
Al(Y)	0.79	0.19	0.85	0.14	0.46	0.21	0.47	0.19
Mg(Y)	0.04	0.05	0.06	0.04	0.70	0.16	0.88	0.45
Fe^{2+}(Y)	2.07	0.28	1.91	0.12	1.82	0.21	1.60	0.48
Mn^{2+}(Y)	0.07	0.03	0.09	0.02	0.02	0.02	0.02	0.01
Ti(Y)	0.00	0.01	0.00	0.01	0.04	0.04	0.05	0.04
Li(Y)	0.05	0.18	0.08	0.12	0.01	0.04	0.01	0.04
Cr(Y)	0.00	0.00	0.00	0.00	0.00	0.00	0.00	0.00
Ca(X)	0.01	0.01	0.01	0.01	0.02	0.03	0.02	0.02
Na(X)	0.65	0.09	0.68	0.07	0.67	0.11	0.67	0.09
K(X)	0.01	0.00	0.01	0.01	0.01	0.01	0.01	0.01
Ba(X)	0.01	0.01	0.00	0.01	0.00	0.01	0.00	0.01
Cs(X)	0.00	0.00	0.00	0.00	0.00	0.00	0.00	0.00
X-vacancy	0.32	0.10	0.30	0.08	0.29	0.13	0.29	0.11
Cation charge	49.05	0.18	49.08	0.12	49.01	0.04	49.01	0.04

Table 8 continued.

Locality	Meløy		Ørnes		Ågskardet South	
Sample ID	RL22-23C		RL22-4J1		2904R	
Lithology	Pegmatite		Pegmatite		Pegmatite	
	ave. (13)	s.d	ave. (37)	s.d	ave. (33)	s.d
SiO_2	35.16	1.25	33.84	0.54	34.69	0.55
TiO_2	0.30	0.20	0.68	0.47	1.02	0.63
$Al2O_3$	33.29	1.19	32.31	1.28	32.13	1.23
Cr_2O_3	0.01	0.03	0.01	0.02	0.01	0.02
FeO	7.94	0.43	13.71	1.89	9.72	0.59
MnO	0.10	0.03	0.32	0.72	0.11	0.04
MgO	5.31	0.71	1.89	1.41	4.76	0.47
CaO	0.40	0.08	0.24	0.11	0.47	0.15
BaO	0.05	0.10	0.08	0.18	0.07	0.16
Na_2O	2.01	0.21	2.10	0.23	2.07	0.17
K_2O	0.04	0.03	0.06	0.03	0.06	0.02
Cs_2O	0.01	0.03	0.01	0.02	0.01	0.02
F	0.08	0.12	0.24	0.22	0.46	0.22
Cl	0.00	0.00	0.00	0.00	0.00	0.00
B_2O_3	12.65	3.16	11.23	2.36	11.16	2.25
Total	97.34	3.30	96.70	2.27	96.74	2.33
F	0.04	0.06	0.13	0.12	0.25	0.11
Cl	0.00	0.00	0.00	0.00	0.00	0.00
OH	3.58	0.46	3.46	0.62	3.28	0.65
B	3.00	0.00	3.00	0.00	3.00	0.00
Si(T)	5.87	0.09	5.81	0.06	5.84	0.07
Al(T)	0.01	0.06	0.05	0.16	0.05	0.13
Al(Z)	6.00	0.00	6.00	0.00	6.00	0.00
$Fe^{3+(}Z)$	0.00	0.00	0.00	0.00	0.00	0.00
Al(Y)	0.54	0.21	0.49	0.23	0.32	0.25
Mg(Y)	1.32	0.18	0.48	0.36	1.19	0.12
$Fe^{2+(}Y)$	1.11	0.07	1.97	0.30	1.37	0.09
$Mn^{2+(}Y)$	0.01	0.00	0.05	0.11	0.02	0.01
Ti(Y)	0.04	0.02	0.09	0.06	0.13	0.08
Li(Y)	0.03	0.09	0.02	0.06	0.03	0.09
Cr(Y)	0.00	0.00	0.00	0.00	0.00	0.00
Ca(X)	0.07	0.01	0.04	0.02	0.08	0.03
Na(X)	0.65	0.07	0.70	0.08	0.68	0.06
K(X)	0.01	0.01	0.01	0.01	0.01	0.00
Ba(X)	0.00	0.01	0.01	0.01	0.00	0.01
Cs(X)	0.00	0.00	0.00	0.00	0.00	0.00
X-vacancy	0.26	0.08	0.24	0.09	0.22	0.08
Cation charge	49.03	0.09	49.02	0.06	49.03	0.09

Numbers in parenthesis represents the number of analyses; ave. = average, s.d = 2* standard deviation.

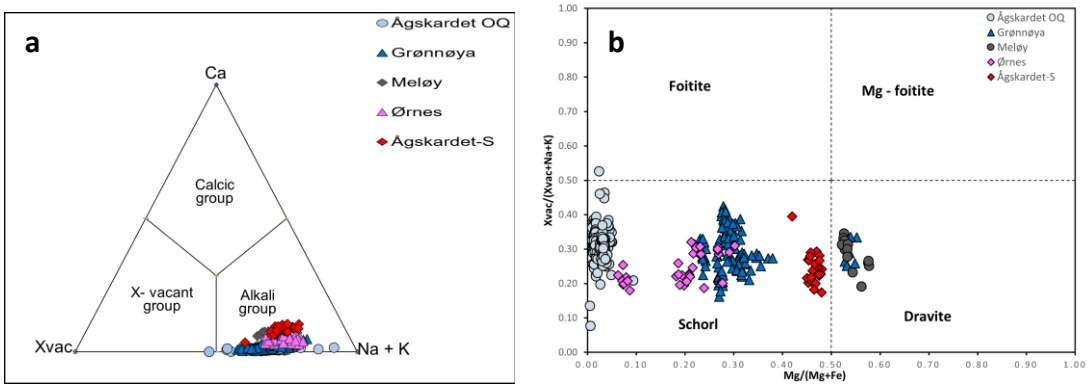

Figure 41. Tourmaline compositions from North Helgeland pegmatites plotted in: (a) ternary system for primary tourmaline groups based on the X site occupancy, (b) classification of tourmaline species based on Xvac/(Xvac+Na+K) vs Mg/(Mg+Fe) after Henry et al.(2011).

The major element patterns of tourmalines from core to rim are distinct for the different pegmatites (Figure 40). Grønnøya tourmalines display an interesting trend with schorl cores and dravite rims i.e., the Fe-rich cores are completely replaced by an Mg-rich rim changing from 1.68 to 1.142 apfu and 0.742 to 1.30 apfu, respectively (Figure 40a). The Ti content correlates positively with the Mg content increasing only slightly towards the rim, while the Mn content remains relatively uniform. At Meløy, the dravite tourmalines increase in Mg from core to mantle and decrease marginally in the rim (Figure 40d). Conversely, Fe is depleted from core to mantle and increases marginally from mantle to rim. The Ti content shows a positive correlation with the Mg content with an increase in the mantle and depletion towards the rim whereas Mn remains relatively uniform. Tourmalines from Ågskardet OQ show a slightly different trend. From core to rim the Fe and Mg contents decrease from 2.19 to 1.88 apfu and 0.09 to 0.05 apfu, whereas the Mn content increases marginally from 0.05 to 0.10 respectively (Figure 40b).

Comparatively, tourmalines in Ørnes have an Fe-rich core similar to those in Meløy, Ågskardet OQ and Grønnøya (Figure 40c). However, unlike these areas, from core to rim the Fe and Mn contents consistently increase from 1.73 to 2.00 apfu and 0.01 to 0.20 apfu, whereas the Mg and Ti contents decrease from 0.75 to 0.18 apfu and 1.21 to 0.02 apfu, respectively. At Ågskardet-S, there is no significant variations in composition of the tourmalines compared to those in other pegmatite areas which is confirmed in the absence of a clear zoning pattern (Figure 40e).

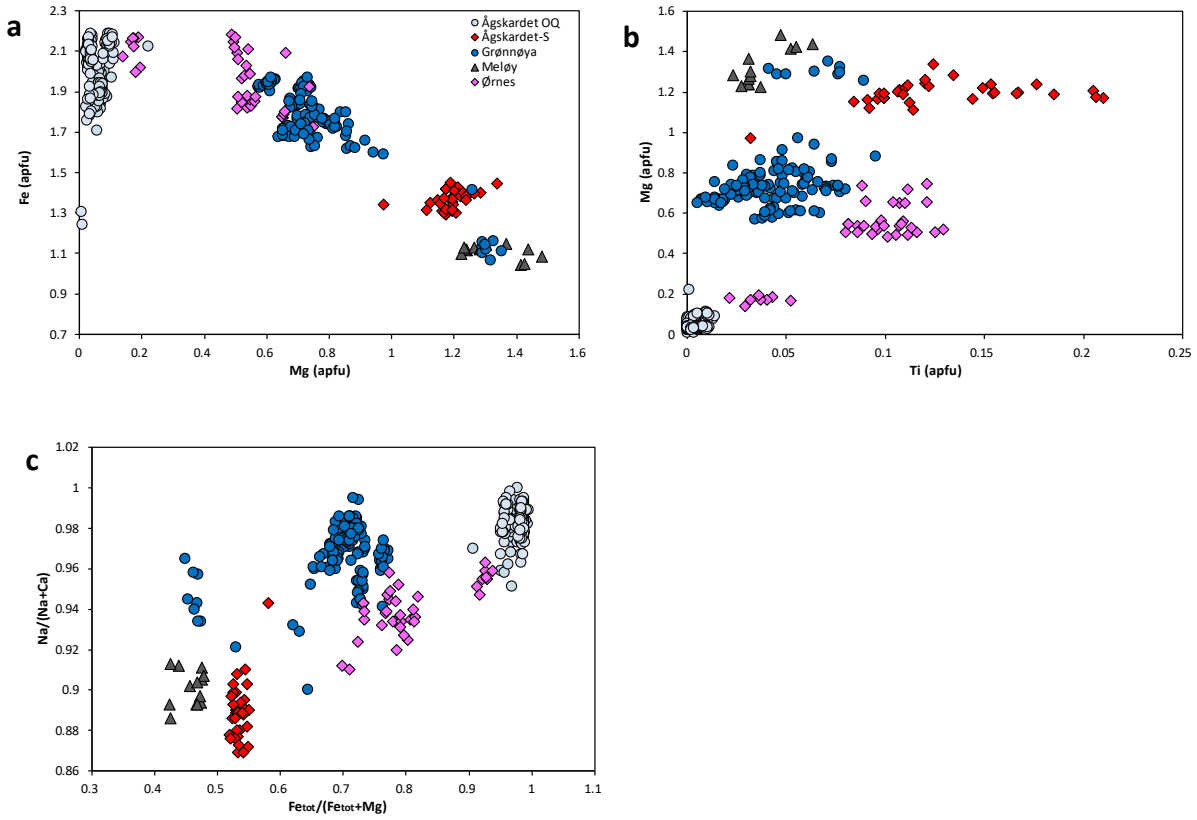

Figure 42. Major element plots for tourmalines in the North Helgeland pegmatites. (a) Fe vs Mg, (b) Mg vs Ti, (c) Na/(Na+Ca) vs Fetot/(Fetot+Mg).

The trace element diagrams (Figure 43) show that the Li content in tourmalines from Ågskardet OQ are highly variable and the highest reaching concentrations of 2138 ppm in the rims . The cores are relatively rich in zinc (Zn) and tin (Sn). The rims of tourmalines from Ågskardet-S are enriched in cobalt (Co) but do not exhibit any clear variation in strontium (Sr), tin (Sn), zinc (Zn), and Li compared to the core. However, similar to the tourmalines at Ågskardet UB and Meløy, they have very low Li and Zn contents.

Cores of Ågskardet UB tourmalines are rich in Co, Sc, Sr, and Ti, compared to the rims. Tourmalines cores from this area record the highest Sc content reaching 60.3 ppm. Sc and Sn content in tourmalines from Ørnes are highly variable and the rims record higher values compared to the core with concentrations of 38 ppm and 88, the latter being the highest in the area. Despite that tourmalines from Meløy exhibit depletion in Li, Zn, and Sn compared to the other pegmatite areas, they have the highest Sr and Co contents of 37.8 and 21.5 ppm

respectively. Readers are referred to Appendix 8.5.4 for the complete analytical data of trace elements in tourmalines.

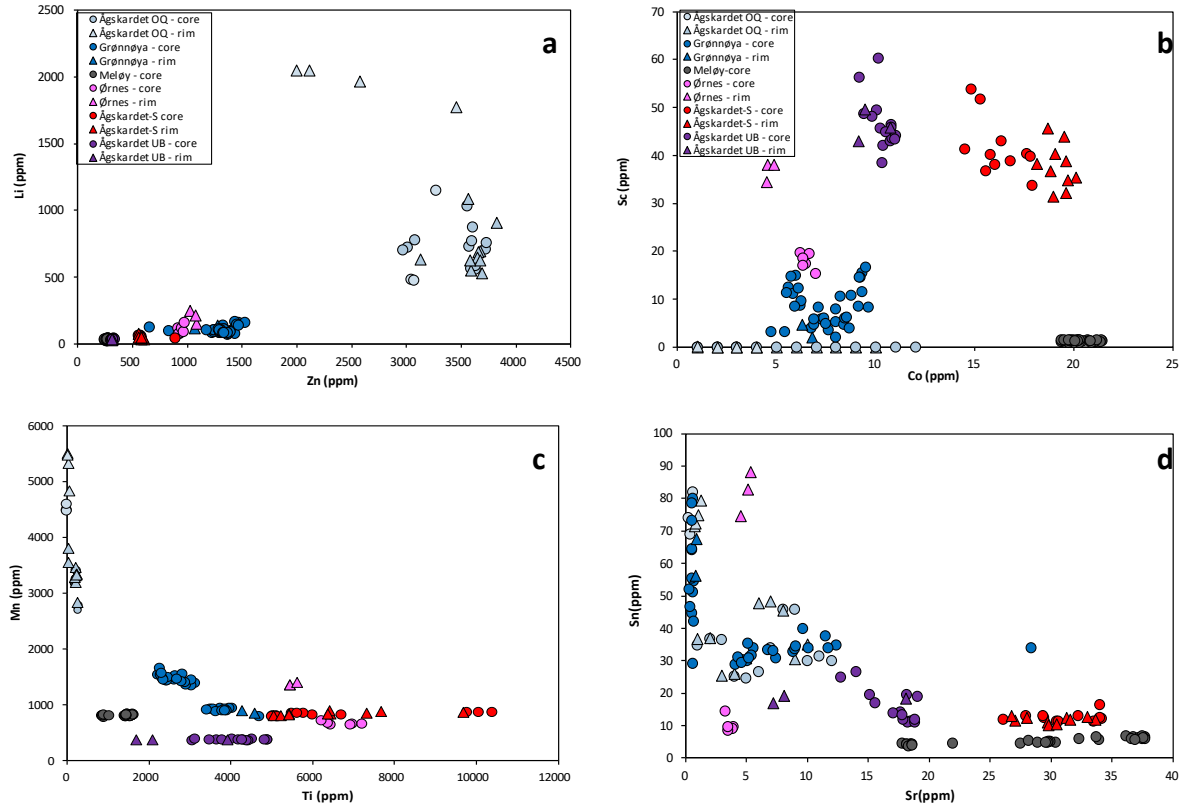

Figure 43. Trace element plots of tourmalines (a) Li vs Zn, (b) Sc vs Co, (c) Mn vs Ti, (d) Sn vs Sr.

4.2.4 Apatite

Apatite is a very common mineral in most rocks, due to the inability of the major rock forming minerals to contain phosphates in large concentrations within their crystal structure (Piccoli & Candela, 2002). The general formula for apatite is $Ca_5(PO_4)_3(OH, F, Cl)$. In igneous rocks, fluoroapatite is the most common even though most natural fluoroapatites contain some Cl and OH, which can be elevated in some cases (Chang et al., 1998). The apatite group consists of three endmembers, F-endmember fluoroapatite, Cl-endmember chloroapatite and OH-group endmember hydroxyapatite. In igneous rocks, apatite may be zoned or unzoned, with zonation occurring from variations in minor and trace elements composition (Piccoli & Candela, 2002 and references therein). Apatite can incorporate a wide spectrum of elements in its lattice including the REE, Y, Mn, Sr, U, and Th, which can individually substitute for Ca; as well as the halogens (F, Cl, Br , and I) and Si, S, Na and V which can

substitute for P. Variations in abundances in these element can be used as tracers for identifying chemical systems during formation of apatite crystals (O'Sullivan et al., 2020).

This study involved a systematic analysis of the textural and compositional properties of apatite using EPMA.

Details of occurrence of apatite in representative rock samples are displayed in BSE images in (Figure 44).

In the North Helgeland pegmatites, apatite occurs mostly as accessory minerals that form subhedral to anhedral aggregates associated with garnet, mica and tourmaline, muscovite and quartz (Figure 44). They range in sizes from 150 µm to 2.2 mm with a few containing monazite and quartz inclusions. In sample RL22-8C from Ågskardet, anhedral apatites are intergrown with garnets (Figure 44b). A different apatite generation also occurs as inclusions in garnets and is predicted to have precipitated earlier than the host minerals. Zoning has not been observed in BSE images for any of the apatites in the area.

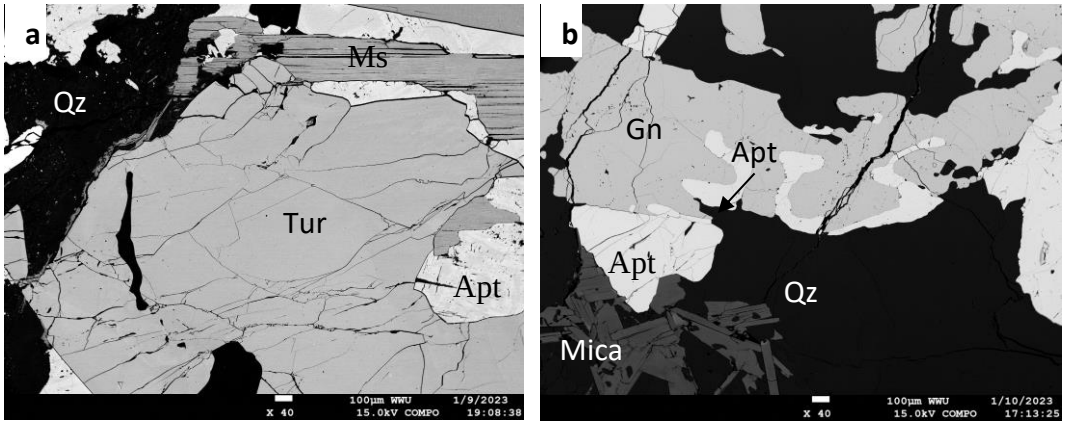

Figure 44. (a) Apatite associated with garnets, muscovite and quartz at Grønnøya, (b) apatite occurs as anhedral aggregates intergrown with garnet at Ågskardet OQ. Some crystals contain garnet inclusions and percolate cracks within garnets.

A total of 57 analyses for major element have been carried on 11 representative apatite crystals in thin section. The structural formulas of the apatite grains were calculated based on (16) cations using a mineral recalculation spreadsheet prepared by Prof. Sebastian Tappe of UiT (2023). The results for the different apatites found in the pegmatites have been summarized in Table 9. Appendix 8.4.5 contains the complete data set for the analyzed

apatites in the study area. The major constituents of apatite, CaO and P_2O_5, show little variations, ranging from 50.05 to 55.71 wt% CaO and from 39.34 to 42.56 wt% P_2O_5 respectively. Al_2O_3 concentrations are typically below 0.03 wt%, and TiO_2, BaO and K_2O concentrations rarely exceed 0.09, 0.4 and 0.2 wt%, respectively (Table 9).

Most of the studied apatites are fluoroapatites, which is characteristic of igneous apatite (2.74 to 6.54 wt% F) where F increases with differentiation (Nash, 1984). Cl is extremely depleted in the Neverdalen, Ågskardet OQ and Ågskardet-S apatites (Figure 45b) and shows complete coupled substitution with F. Cl content in apatite ranges from bdl to 0.62 wt%, and apatites from Ørnes record the highest Cl (0.53 to 0.62 wt%) content but low F/Cl values (4.54 to 7.12). Together, apatites from Neverdalen and Ågskardet OQ record the highest F content and F/Cl values (Figures 45b, c).

The Na_2O and SiO_2 contents generally range from bdl to 0.10 wt% and bdl to 0.24 wt% respectively. The highest Na_2O and SiO_2 concentrations are found in apatites from Neverdalen (Table 9). Al_2O_3, K_2O and TiO_2 are typically below the detection limit and concentrations rarely exceed 0.03, 0.20 and 0.09 wt% respectively (Table 9).

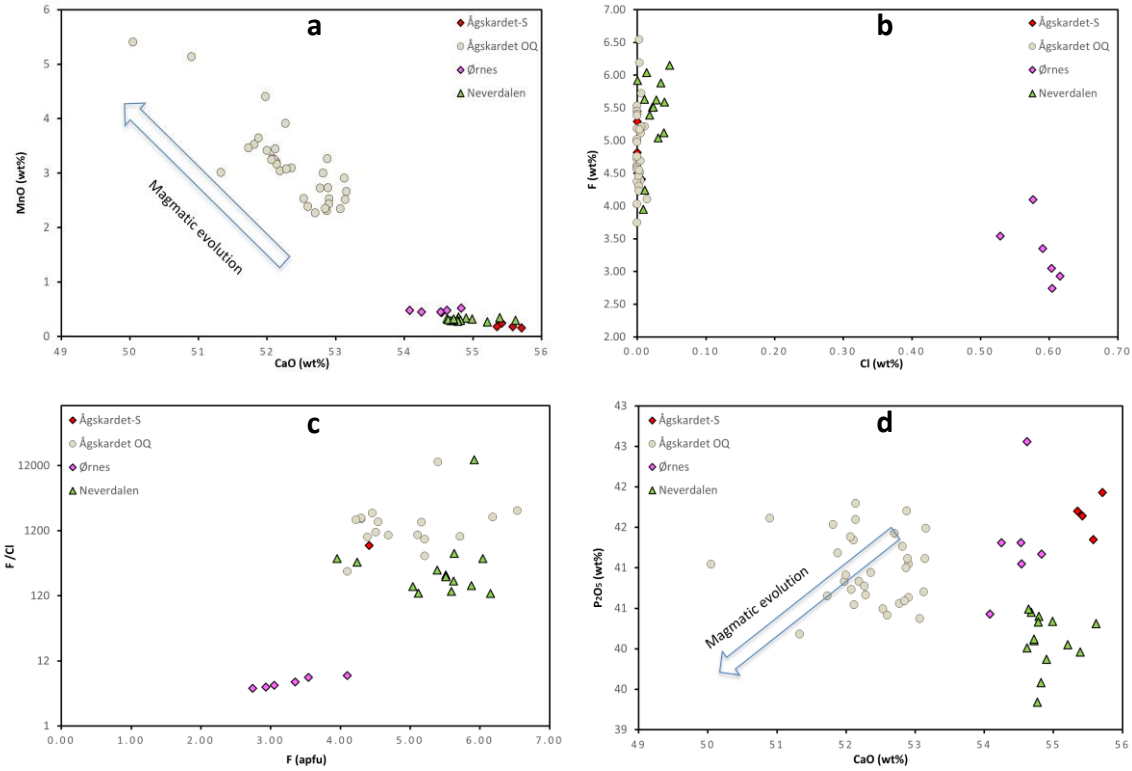

Figure 45. Major element compostions of apatite in the North Helgeland pegmatites. (a) MnO vs CaO, (b) F vs Cl, (c) F/Cl vs F, (d) P_2O_5 vs CaO.

The FeO and MnO contents in apatites are extremely variable in the different pegmatites. Ågskardet-S and Neverdalen record the lowest FeO (< 0.05 wt%), and MnO (< 0.36 wt%) in apatites, whereas Ågskardet OQ apatites contain the highest MnO (2.24 to 5.40 wt%) contents and variable FeO (0.01 to 0.34 wt%) content (Figure 45a, Table 9). By contrast, Ørnes apatites show low MnO concentrations (0.44 to 0.52 wt%) FeO (0.08 to 0.15) similar to the average value at Ågskardet OQ. MgO and SrO in apatite is often below detection limits in all the pegmatites (Table 9).

In general, the CaO and P_2O_5 concentrations decrease and MnO contents increase with magmatic evolution (Figure 45a, d; Cao et al., 2022). The plots show that Ågskardet OQ has the highest magmatic evolution with higher MnO (3.0 to 5.4 wt%), and lower CaO (50 to 53.1 wt%) contents. Apatites from Ågskardet-S record the lowest magmatic evolution with higher CaO (41.4 to 42 wt%) and P_2O_5 (55.4 to 55.7 wt%), respectively.

Table 9. Summary of EPMA analyses of apatites in the North Helgeland pegmatites.

Locality	Ågskardet South		Ørnes		Neverdalen	
Sample ID	2904R		RL22-4J1		RL22-5J	
Lithology	Pegmatite		Pegmatite		Pegmatite	
	ave. (4)	s.d	ave. (6)	s.d	ave. (14)	s.d
K_2O	0.00	0.01	0.05	0.15	0.00	0.01
Na_2O	0.03	0.06	0.02	0.05	0.07	0.05
CaO	55.52	0.32	54.48	0.54	54.90	0.60
SrO	0.01	0.04	0.00	0.00	0.00	0.01
MnO	0.19	0.07	0.47	0.06	0.31	0.05
FeO	0.02	0.04	0.11	0.04	0.01	0.03
Al_2O_3	0.01	0.03	0.01	0.02	0.00	0.00
Cr_2O_3	0.00	0.01	0.00	0.02	0.01	0.02
TiO_2	0.01	0.03	0.01	0.03	0.02	0.04
SiO_2	0.09	0.05	0.05	0.06	0.21	0.05
P_2O_5	41.66	0.48	41.31	1.39	40.10	0.67
Cl	0.00	0.01	0.59	0.06	0.02	0.03
F	4.99	0.94	3.29	0.98	5.40	1.28
Total	102.54	0.37	100.38	2.57	101.05	1.30
apfu based on 25 oxygens						
K	0.00	0.00	0.01	0.03	0.00	0.00
Na	0.01	0.02	0.01	0.02	0.02	0.02
[Ca]	10.07	0.04	10.08	0.10	10.18	0.07
Sr	0.00	0.00	0.00	0.00	0.00	0.00
Mn	0.05	0.02	0.12	0.01	0.08	0.01
Fe^{2+}	0.00	0.00	0.01	0.02	0.00	0.00
Fe^{3+}	0.00	0.01	0.01	0.02	0.00	0.00
Al	0.00	0.01	0.00	0.00	0.00	0.00
Cr	0.00	0.00	0.00	0.00	0.00	0.00
Si	0.02	0.01	0.01	0.01	0.04	0.01
[PO4]	5.96	0.03	5.97	0.10	5.85	0.07
F	2.66	0.52	1.77	0.50	2.93	0.70
Cl	0.00	0.00	0.17	0.02	0.01	0.01
OH	-0.66	0.52	0.06	0.49	-0.93	0.70

Table 9 continued.

Locality	Ågskardet Old Quarry		Ågskardet Old Quarry	
Sample ID	RL22-7E		RL22-8C	
Lithology	Pegmatite		Pegmatite	
	ave. (16)	s.d	ave. (17)	s.d
K_2O	0.00	0.01	0.00	0.01
Na_2O	0.02	0.03	0.05	0.04
CaO	51.96	1.35	52.67	0.96
SrO	0.00	0.00	0.00	0.01
MnO	3.65	1.44	2.65	0.63
FeO	0.17	0.09	0.13	0.18
Al_2O_3	0.00	0.00	0.00	0.01
Cr_2O_3	0.01	0.02	0.00	0.02
TiO_2	0.01	0.04	0.02	0.06
SiO_2	0.03	0.12	0.02	0.03
P_2O_5	41.10	0.79	40.87	0.87
Cl	0.00	0.01	0.00	0.01
F	4.99	1.10	4.75	1.32
Total	101.95	1.63	101.19	1.92
apfu based on 25 oxygens				
K	0.00	0.00	0.00	0.00
Na	0.01	0.01	0.02	0.01
[Ca]	10.46	0.18	10.37	0.09
Sr	0.00	0.00	0.00	0.00
Mn	0.93	0.37	0.68	0.16
Fe^{2+}	0.02	0.01	0.02	0.03
Fe^{3+}	0.00	0.00	0.00	0.00
Al	0.00	0.00	0.00	0.00
Cr	0.00	0.00	0.00	0.00
Si	0.01	0.02	0.00	0.01
[PO4]	5.94	0.08	5.92	0.08
F	2.69	0.60	2.57	0.71
Cl	0.00	0.00	0.00	0.00
OH	-0.69	0.60	-0.57	0.71

Numbers in parenthesis represent number of analyses; ave. = average and s.d. = 2* standard deviation.

4.3 U-Pb ages

4.3.1 U-Pb zircon

A total of 239 U-Pb isotope ratio measurements were made on 211 zircon crystals from 17 samples using the LA-MC-ICP-MS. Table 10 contains a summary of age calculated for the different rock units from concordia diagrams. The complete analytical dataset is listed in Appendix 8.6, together with uncertainties on the ratios and ages at 2 standard error level.

4.3.1.1 Ørnes

The zircons from the Ørnes pegmatite are pale brown and metamict with several fractures bearing the deformation observed in representative hand samples and thin sections. Most of the crystals are fractured and have irregular to prismatic shapes with sizes ranging from 100 to 150 µm (long axes). The crystals do not show any clear zoning or a xenocrystic core and are marked by several irregular cracks and corroded surfaces. Five crystals were analyzed but due to the presence of common Pb, only one was concordant with an age of 400 ± 7 Ma (Figure 46a).

4.3.1.2 Ågskardet OQ

The pegmatites at Ågskardet OQ contain deformed irregular to prismatic zircons in addition to the wide variety of exotic minerals reported there. The crystals have an average size of 200 µm (long axes) with an aspect ratio of 1:2. Crystals with terminated ends are usually absent due to fracturing but one crystal has both pyramids developed. Some crystals show a xenocrystic core with patchy compositional zoning and host inclusions of quartz and apatite. The seven analyzed zircon grains define a lower intercept age of 387 ± 6 Ma (MSWD = 20) in the $^{207}Pb/^{206}Pb$ versus $^{238}U/^{206}Pb$ ratio Tera-Wasserburg diagram that is interpreted as the crystallization age of the pegmatite (Figure 46b).

4.3.1.3 Meløy

Three pegmatite samples (RL22-21, 22 and 25A) and a granitic gneiss basement sample (RL22-18) from Meløy were analyzed. Zircons contained in samples RL22-21 and RL22-25A are very similar and consists of several brown needlelike, metamict zircons with morphology similar to the Ågskardet UB zircons. The zircons have an average aspect ratio of 1:5, host some opaque melt inclusions, and display cracks across the entire crystal

length. When unbroken, zircons can have double terminated ends and do not show distinct compositional zoning except a few that are patchy. Overall, eight and four analyzed zircon crystals defined concordia ages of 420 ± 3 Ma (MSWD = 3.6) and 422 ± 5 Ma (MSWD = 18), for samples RL22-21 and 25A, respectively (Figure 46c, d). Together, these two ages make up the oldest crystallization ages for pegmatites in our study area.

Sample RL22-22 postdates the deformed pegmatites dated above (RL22-21, 25A) and host several yellow trapezoidal shaped monazites in addition to zircons ranging from clear to metamict prismatic crystals. Two distinct aspect ratios are present in the zircon, 1:2 and 1:5. Most zircon crystals in this sample have pitted surfaces with varying degrees of metamictization. Six out of eight analyses defined a concordia age of 396 ± 7 Ma (MSWD = 0.3) (Figure 46e).

The granitic gneisses (RL22-18) range from undeformed to weakly deformed with a more prominent foliation compared to the granites at the Kleiva Quarry. The collected zircons are prismatic with average size of 150 µm and double-terminated ends except for a few that have only one pyramid developed over a sub-rounded core. Some crystals show a ghost xenocrystic core that contains bubbles with oscillatory zoning around it. The eighteen zircon analyses were discordant and define an upper intercept age of 1813 ± 4 Ma in the $^{206}Pb/^{238}U$ versus $^{207}Pb/^{235}U$ Wetherill concordia diagram (MSWD = 6). An age of 280 ± 12 was recorded at the lower intercept, indicating loss of Pb during the Caledonian thermal event (Figure 47e). The upper intercept age of 1813 ± 4 Ma is interpreted as the time of crystallization of the protolith of the granitic gneiss.

4.3.1.4 Rismålstinden

Compared to most of the sampled areas, a relatively low number of zircons were recovered together with apatite crystals. Zircons from this pegmatite are mostly broken, murky and strongly altered similar to observations of the major phases in thin section and hand samples. A significant number of opaque inclusions were observed in the zircon crystals, which also contained cracks, and patchy compositional zoning. Two out of five analyzed zircons yielded a weighted means $^{206}Pb/^{238}U$ age of 416 ± 4 Ma (MSWD = 5.2) (Figure 46f). Within error, this pegmatite with an age of 416 ± 4 Ma forms part of the first-generation of

Caledonian pegmatites in our study area together with the Meløy pegmatites (RL22-21, 25A).

4.3.1.5 Ågskardet-S

The Ågskardet-S pegmatites contain several trapezoid to subrounded monazites in addition to euhedral prismatic zircons with varying degrees of metamictization. The crystals have well developed pyramids at both ends and range in size from 150 to 300 µm. Fourteen analyzed zircons yielded a mean $^{206}Pb/^{238}U$ age of 400 ± 5 Ma (MSWD = 1) defining the age of crystallization of the pegmatite (Figure 46g).

4.3.1.6 Agskardet UB

Zircons contained in two different pegmatite samples from this area were analyzed. Sample RL22-06A is strongly deformed and contains porphyroblasts of garnets and quartz in a sheared rock. The deformed pegmatite contains pale brown elongated prismatic zircons often fractured at one end with several mineral inclusions. Growth zoning is absent in the zircons and crystals have two consistent aspect ratios of 1:9 and 2:7, respectively. Cracks occur parallel to the c-axis of crystals and some show corroded surfaces. Ten zircons define a concordia age of 403 ± 6 Ma (MSWD = 1.5) (Figure 46h). The second sample (RL22-16) is relatively less deformed and consists of quartz and feldspar as the major phases with garnet and tourmaline as minor minerals. The zircons are highly fractured and metamict, have highly variable aspect ratio, and one crystal shows complex twinning. Two out of five analyzed crystals defined a concordia age of 412 ± 5 Ma (MSWD = 12) (Figure 46i).

4.3.1.7 Kleiva Quarry-Reipå

This sample was collected from the granitic gneisses pit-walls at Kleiva Quarry, Reipå. Nineteen clear to murky zircon fractions were analysed. The zircons are less fractured and metamict compared to the more deformed pegmatites bodies in the area. Most of the grains have xenocrystic cores, display radial growth and have only one pyramid formed on a subrounded core which often hosts some melt inclusions. The nineteen zircons that range in size from 100 to 150 µm define a discordia line with upper intercept of 1818 ± 6

Ma and lower intercept of 397 ± 10 Ma (MSWD = 10), respectively, in the Wetherill concordia diagram. The upper intercept age of 1818 ± 6 Ma is interpreted as the crystallization age of the granite protolith, whereas the lower intercept age of 397 ± 10 Ma represents the time of Caledonian deformation and metamorphism (Figure 47a).

4.3.1.8 Selstad

Eighteen zircons were analysed from this granitic gneiss collected in a road section at Selstad, on the main county road to Glomfjord. The zircons are clear prismatic crystals with double-terminated ends and have sizes between 100 and 150 µm with growth zoning. Similar to the granitic gneisses at Ytre Holten, the zircons contain apatite inclusions, and most crystals are free of cracks. The zircon analyses define an upper intercept age of 1811 ± 6 Ma and a lower intercept age of 346 ± 28 Ma (MSWD = 1) in the Wetherill concordia diagram (Figure 47b).

4.3.1.9 Ytre Holten

The granitic gneisses at this location contain less K-feldspar and mafic minerals compared to the Kleiva Quarry granites but both are generally weakly deformed. The sample also contains several clear to murky zircons that range from crystals with one developed pyramid to sub-rounded types. The zircons have sizes between 100 to 200 µm (long axes) and show overgrowth on a xenocrystic core that hosts some apatite inclusions. Both the upper and lower intercept dates of the rock from 16 zircon analyses coincides with that of the Kleiva Quarry granitic gneisses within error. The zircons yield a discordia line with an upper intercept age of 1827 ± 4 Ma and a lower intercept recording an age of 404 ± 17 Ma (MSWD = 5), respectively (Wetherill concordia diagram, Figure 47a). These dates are interpreted to date the time of crystallization of the protolith to the gneiss and the Caledonian metamorphism, respectively. Both upper intercept and lower intercept ages pre-dates the granitic gneisses at Selstad even though they occur less than 2 km apart (Figure 47c).

4.3.1.10 Åsjord

Sample RL22-02 is a granitic gneiss taken from an exposure in road section at Åsjord, ~9.5 km southwest of Grønnøya. The sample contains pale brown broken and metamict

prismatic zircons. Most grains have a metamict core with an overgrowth and marked by cracks. The long axes of grains range from 150 to 200 µm and hosts inclusions of mica and allanite. To date the rock, 19 zircons were analyzed that defined a discordia line with upper intercept of 1870 ± 12 Ma (MSWD = 10) interpreted as the best estimate of crystallization time for the protolith of the granitic gneiss. The lower intercept age of 379 ± 5 Ma defines the date for the Caledonian thermal event (Figure 47d). All the determined U-Pb zircon ages of basement gneisses present in our study area postdate this granitic gneiss.

4.3.1.11 Neverdalen

All three rock types exposed in the contact at Neverdalen contained several zircon grains that were used for U-Pb dating. Sample RL22-05F represents a mafic gneiss and forms part of the basement unit in the study area. The zircons contained in this sample were pale yellow, metamict with small inclusions of apatite. They range from prismatic crystals with double-terminated ends to crystals with only one pyramid developed on sub-rounded to blocky cores. They display some compositional zoning, and some zircons have ghost xenocrystic cores evidenced only by tiny bubble features. The crystals are mostly between 100 to 150 µm sizes with a common aspect ratio of 1:3. A total of 18 zircons define a discordia line with upper and lower intercepts of 1839 ± 7 Ma and 363 ± 7 Ma (MSWD = 20), respectively (Figure 47f). The lower intercept age is interpreted to be date the deformation of the gneiss.

The adjacent muscovite-rich metasedimentary rock (RL22-05D) contains clear to murky prismatic zircons with well-developed pyramids at both ends. The crystals have a ghost xenocrystic core that is recognized by tiny bubble features and host a few quartz inclusions. The long axes of the crystals range between 100 to 200 µm and a few crystals display cracks. All twenty-one analyses yielded a discordia line with upper and lower intercepts of 1864 ± 9 Ma and 388 ± 6 Ma (MSWD = 20). Hence the 1864 ± 9 Ma age, dates the maximum deposition age of the protolith of the metasedimentary rock (Figure 47g).

Sample RL22-05J, the < 1 m pegmatitic dyke locally emplaced in between the mafic gneiss and the metasediment contains clear and less metamict prismatic zircons with sizes ranging from 100 to 200 µm (long axes). Most grains show oscillatory zoning around a

xenocrystic core with very few to no fractures. Twenty-two concordant zircon analysis yielded a mean $^{206}Pb/^{238}U$ age of 413 ± 2 Ma (MSWD = 1700), which defines the date of crystallization (Figure 46j).

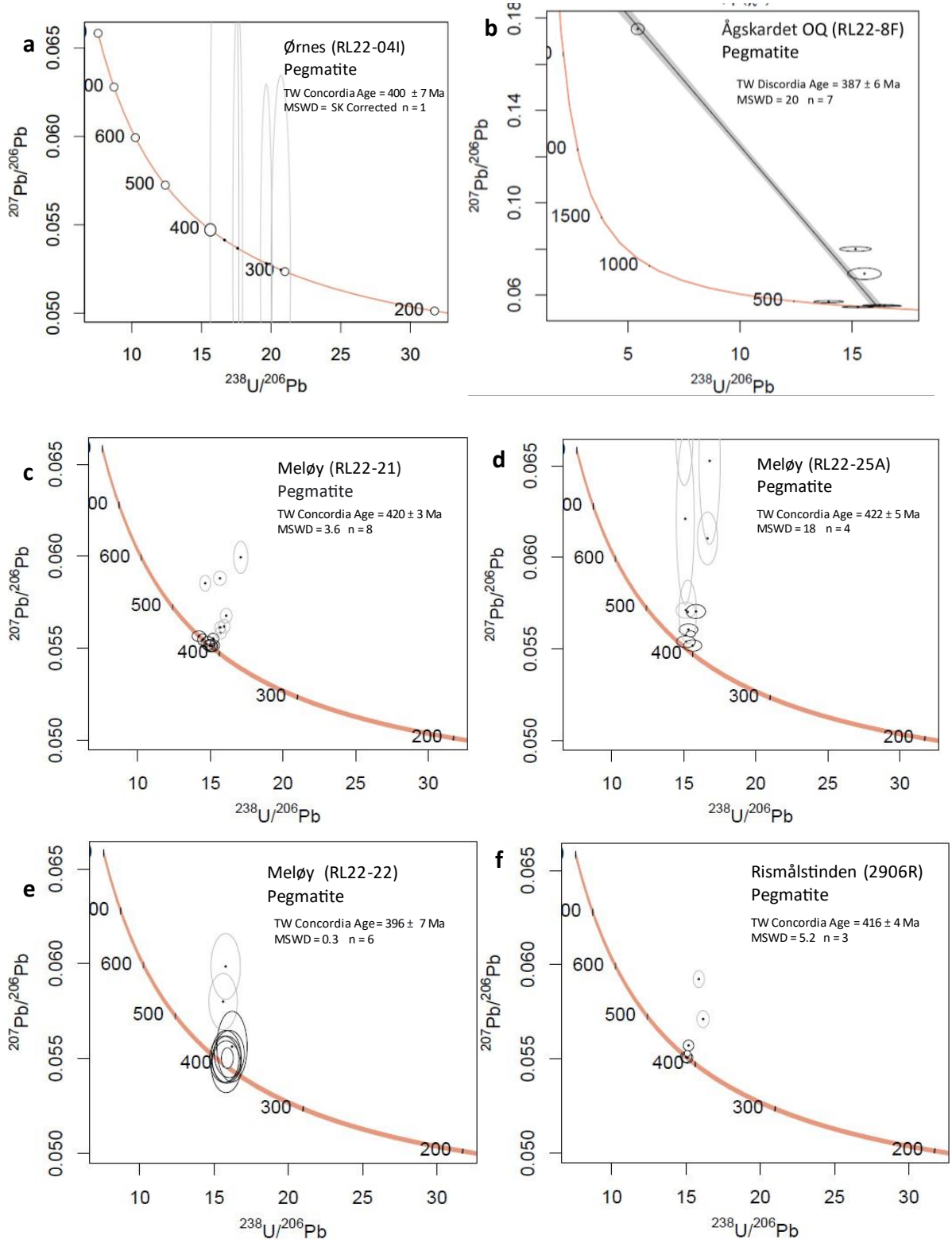

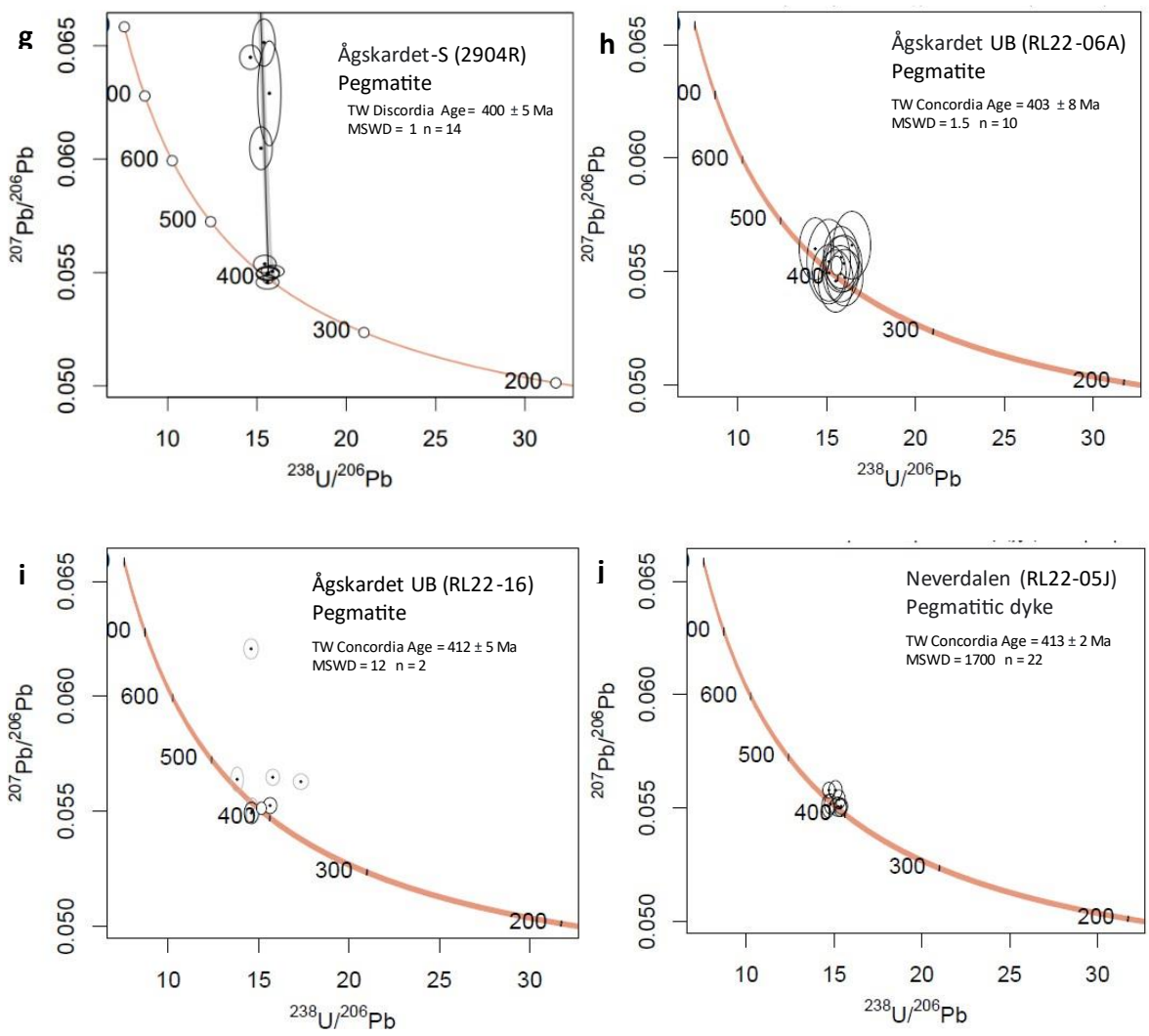

Figure 46. Tera-Wasserburg concordia diagrams for pegmatites samples from North Helgeland. TW = Tera Wasserburg, n = number of analyses used in age calculation. SK = Stacey-Kramers (1975).

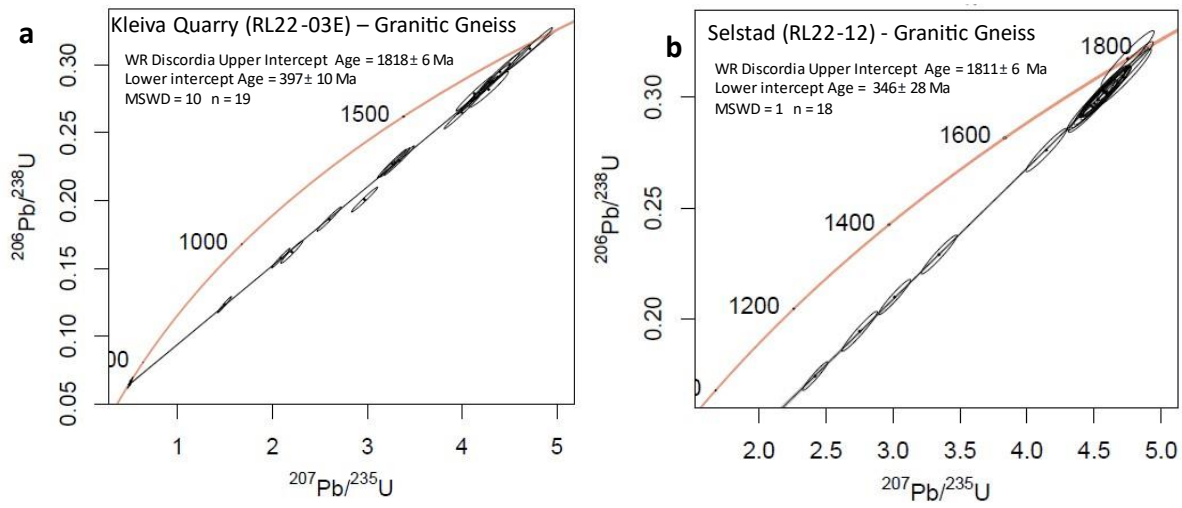

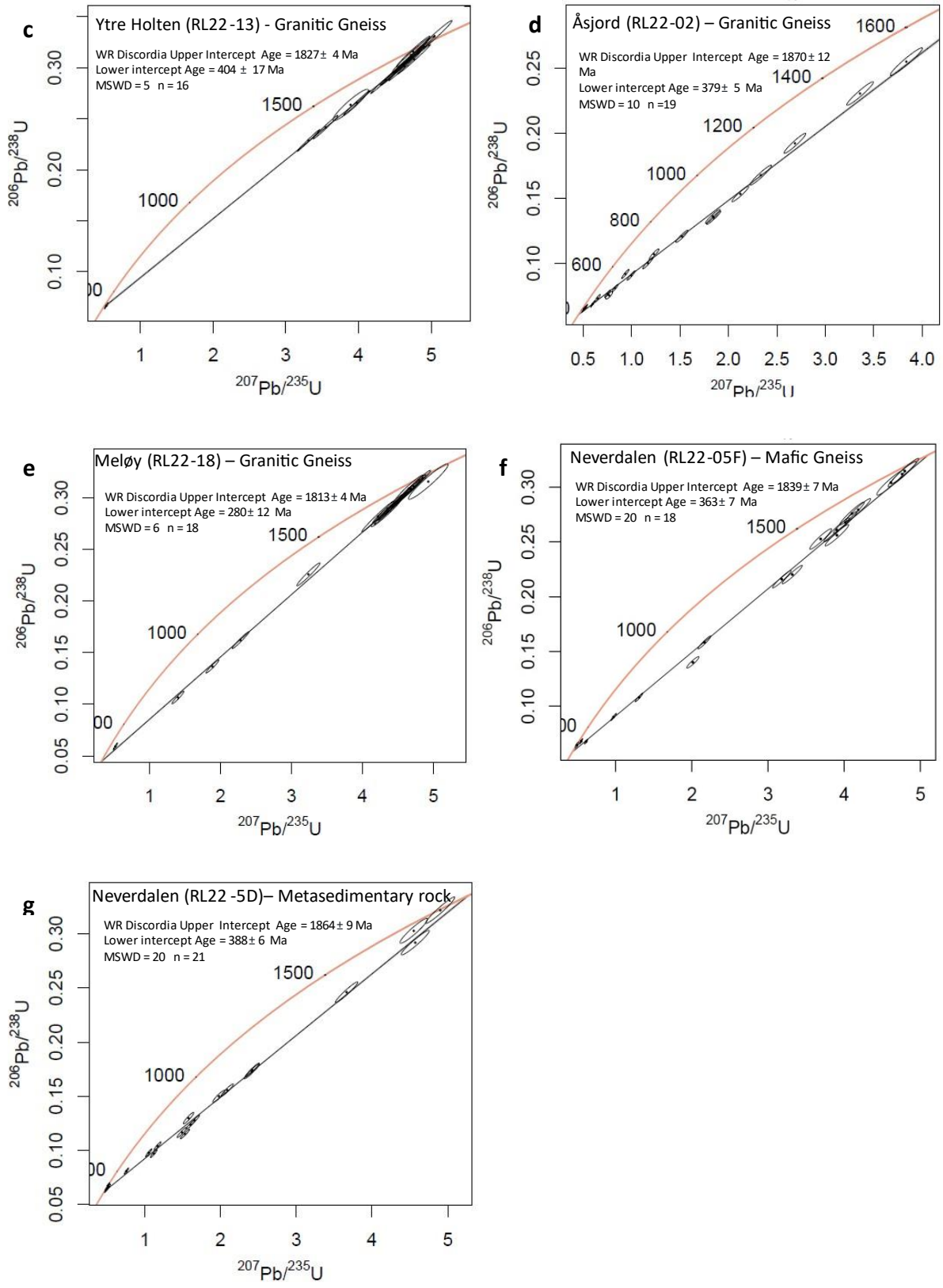

Figure 47. Wetherill concordia diagrams for basement samples from North Helgeland. WR = Wetherill, n = number of analyses used in age calculation.

4.3.2 Hf isotopic compositions of zircon

Before Lu-Hf isotopic compositions analyses, the zircon ages from the pegmatites and basement rocks of the North Helgeland fields were determined by U-Pb (LA-MC-ICP-MS) isotopic analyses as detailed above in Section 3.4.3. Analytic data of $^{176}Hf/^{177}Hf$ ratios and initial εHf (εHf_i) values are summarized in Table 11 and the complete dataset can be found in Appendix 8.7. Results from the analysis show low Lu/Hf ratios, with $^{176}Lu/^{177}Hf$ generally below 7.17 x 10^{-3}. The $^{176}Yb/^{177}Hf$ ratio is variable with values in the range of 0.01 to 0.3 (Appendix 8.7).

Figure 48a gives an overview of the εHf_i compositions versus U-Pb ages of zircon from the rocks in our study area. From the diagram, the Paleoproterozoic basement rock zircon analyses (1811 ± 6 to 1870 ± 12 Ma) plot in the upper right corner around the chondritic uniform reservoir (CHUR, Bouvier et al., 2008). They are characterized by sub- to supra-chondritic εHf_i values (-3.3 to + 5) and have Meso-Archean two-stage model ages (T_{DM}) of 2667 to 2210 Ma. In contrast, zircon from the pegmatite samples with Caledonian ages (387 ± 6 to 422 ± 5 Ma) plot below the CHUR with sub-chondritic εHf_i values between -32 and -8. They have T_{DM} from 3338 to 1854 Ma (see Table 11).

The detailed view (Figures 48c, d) shows distinct zircon isotope composition patterns for the different basement rocks and pegmatites in the area. Within the basement gneisses, zircons from the older meta-igneous rocks (1839 ± 7 to 1870 ± 12 Ma) at Neverdalen (RL22-5F and RL22-5D) and Åsjord (RL22-02) record the widest spread and more juvenile composition with εHf_i values of +2.4 ± 5.2, +1.8 ± 6.8 and +5 ± 6.8, corresponding to T_{DM} = 2336, 2388 and 2210 Ma, respectively (Figure 48c, Table 11). Comparatively, the granitic gneiss from Ytre holten yielded the lowest εHf_i values amongst the basement rocks ranging from -4.1 to -1 and T_{DM} = 2530 to 2714 Ma (Figure 48c, Table 11).

The pegmatites in the area show a wide array in εHf_i values below the CHUR. The pegmatitic dyke sample RL22-05J from Neverdalen recorded the widest spread and the most negative εHf_i values between -33.7 ± 1 and -26.11 ± 0.8, with T_{DM} = 3424 to 2985 Ma (Figure 48d). By contrast, zircons from the Rismålstinden, Meløy, and Ågskardet OQ pegmatites (samples 2906R, RL22-22 and RL22-8F) display some clustering around sub-

chondritic εHf_i values ~-13, -16.3, and -16.5, with T_{DM} of 2189, 2370 and 2380 Ma, respectively (Figure 48d). The εHf_i values between -9.7 and -7.20 are higher in zircons from the Ørnes pegmatite but generally lower than the Paleoproterozoic basement rocks (Figures 48a).

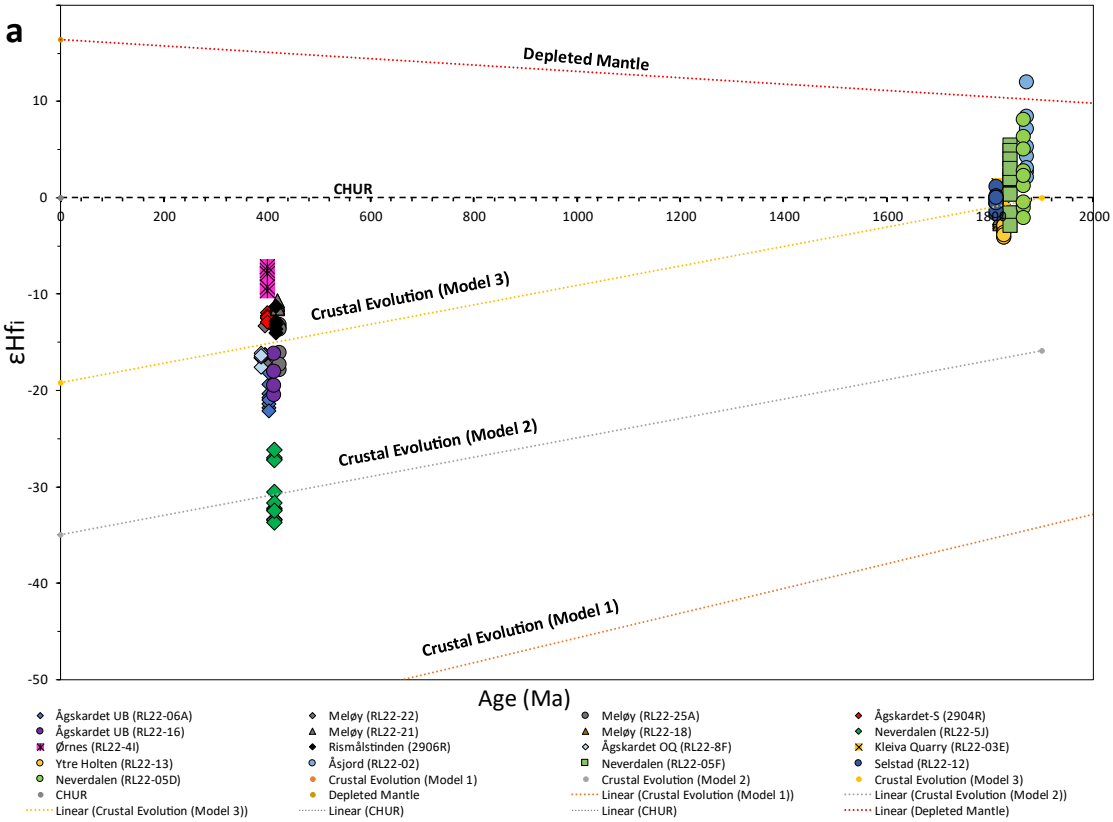

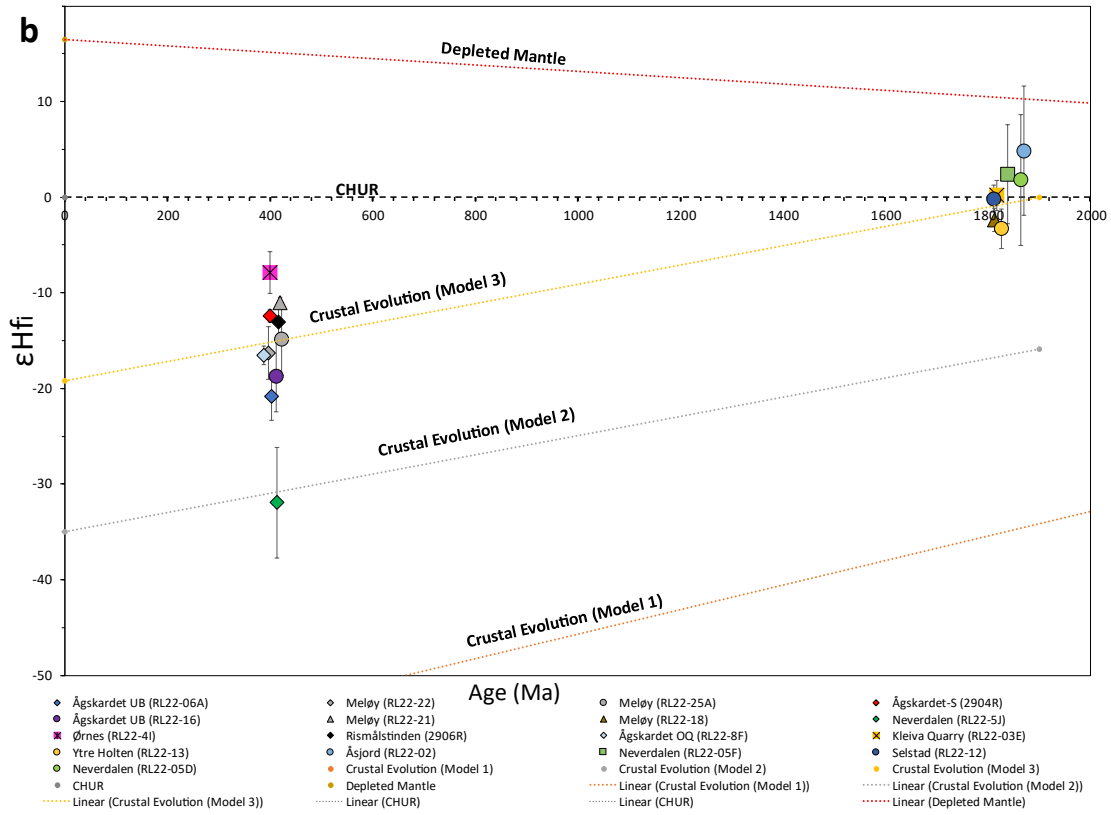
b
Depleted Mantle
CHUR
Crustal Evolution (Model 3)
Crustal Evolution (Model 2)
Crustal Evolution (Model 1)
εHfi
Age (Ma)
Ågskardet UB (RL22-06A)
Ågskardet UB (RL22-16)
Ørnes (RL22-4I)
Ytre Holten (RL22-13)
Neverdalen (RL22-05D)
CHUR
Linear (Crustal Evolution (Model 3))
Meløy (RL22-22)
Meløy (RL22-21)
Rismålstinden (2906R)
Åsjord (RL22-02)
Crustal Evolution (Model 1)
Depleted Mantle
Linear (CHUR)
Meløy (RL22-25A)
Meløy (RL22-18)
Ågskardet OQ (RL22-8F)
Neverdalen (RL22-05F)
Crustal Evolution (Model 2)
Linear (Crustal Evolution (Model 1))
Linear (CHUR)
Ågskardet-S (2904R)
Neverdalen (RL22-5J)
Kleiva Quarry (RL22-03E)
Selstad (RL22-12)
Crustal Evolution (Model 3)
Linear (Crustal Evolution (Model 2))
Linear (Depleted Mantle)

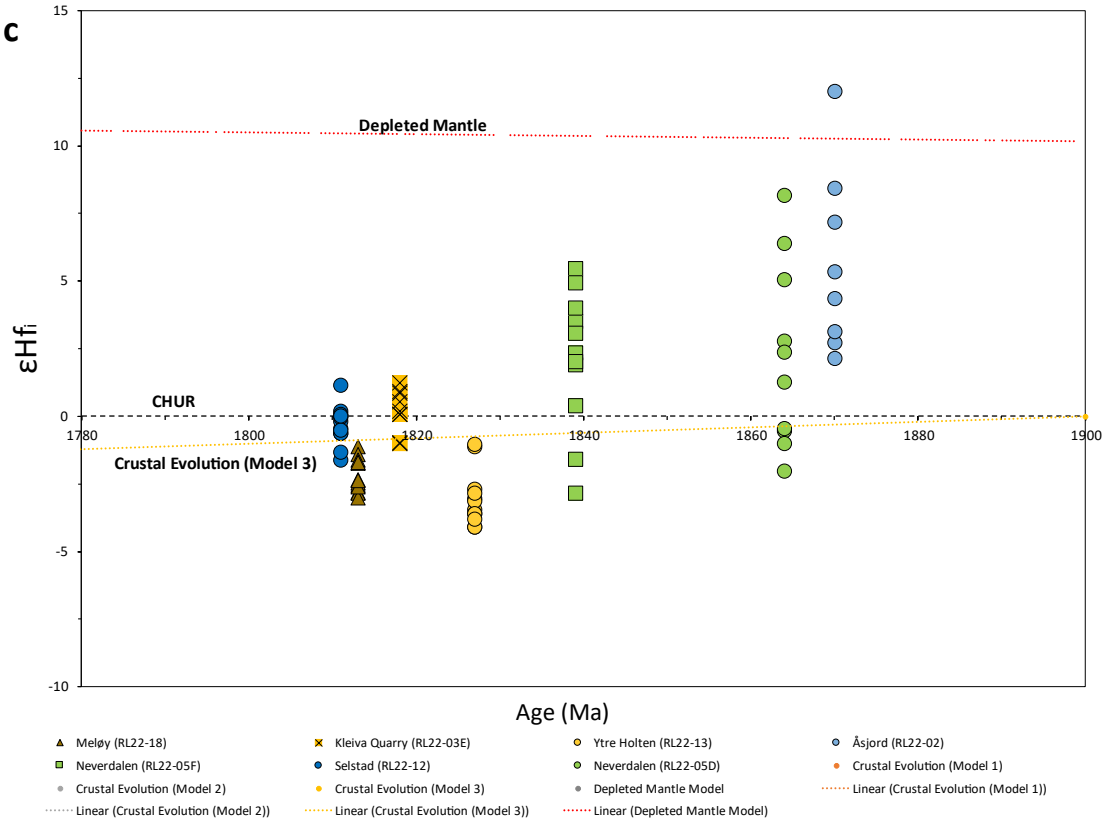
c
Depleted Mantle
CHUR
Crustal Evolution (Model 3)
εHfi
Age (Ma)
Meløy (RL22-18)
Neverdalen (RL22-05F)
Crustal Evolution (Model 2)
Linear (Crustal Evolution (Model 2))
Kleiva Quarry (RL22-03E)
Selstad (RL22-12)
Crustal Evolution (Model 3)
Linear (Crustal Evolution (Model 3))
Ytre Holten (RL22-13)
Neverdalen (RL22-05D)
Depleted Mantle Model
Linear (Depleted Mantle Model)
Åsjord (RL22-02)
Crustal Evolution (Model 1)
Linear (Crustal Evolution (Model 1))

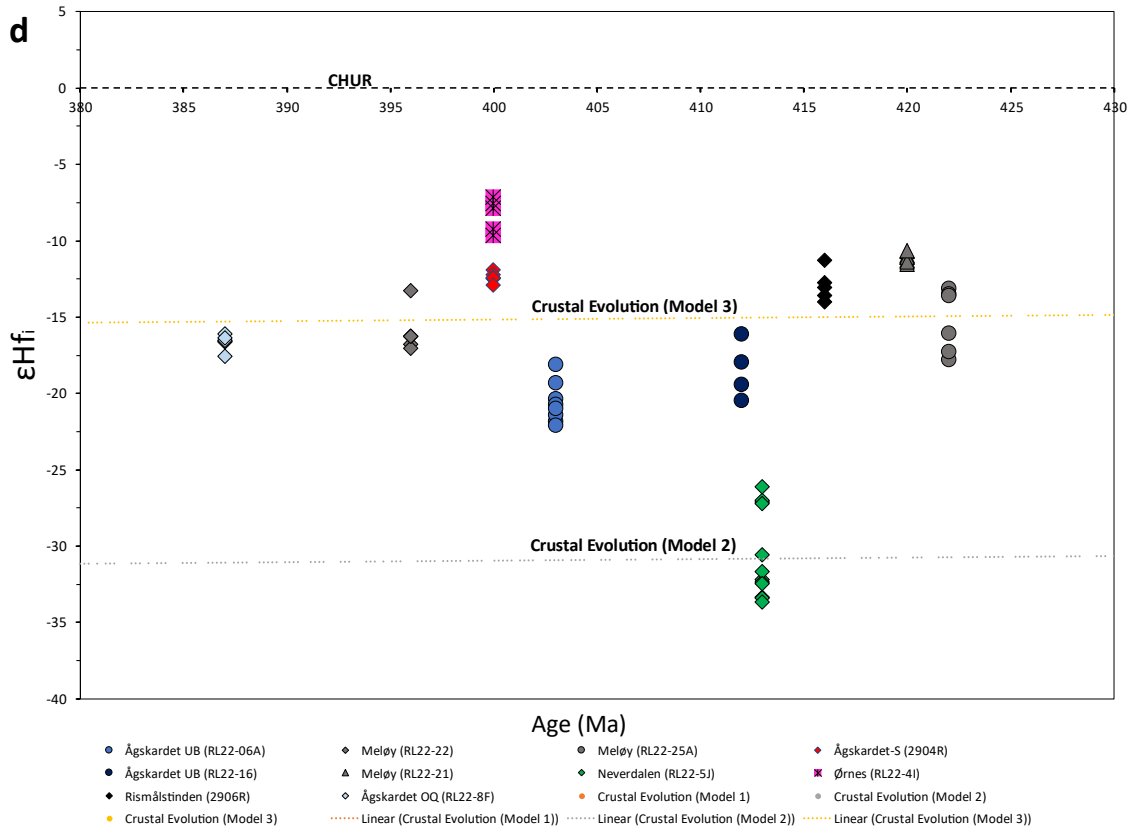

Figure 48. εHfᵢ vs age (Ma) diagrams for zircons from the North Helgeland area. (a) Overview diagram showing all basement rocks and pegmatites, (b) overview diagram with median εHfᵢ values, (c) detailed diagram for basement rocks, (d) detailed diagram of pegmatite samples.

5 Discussion

5.1 Geochronology

5.1.1 Basement rocks

The U-Pb zircon age determinations of Paleoproterozoic basement rocks from the North Helgeland area in northern Norway are correlated with some major magmatic events that affected the geology in the area. Based on previous Rb-Sr whole rock age determinations, it was suggested that there was continuous magmatic activity from 1800 to 1700 Ma (Skår, 2002 and references therein). However, these ages are in question largely due to uncertainties that could have resulted from heterogeneity in the rock Sr isotopic compositions or a possible disturbance in the isotopic system (Skår, 2002). The Paleoproterozoic ages determined in this study reveal that the magmatism leading to the

formation of rocks in the basement windows occurred between the period 1870 to 1811 Ma, contrary to the narrow time period of 1800 to 1795 Ma determined for the central Nordland granitoids (Figure 49) (Skår, 2002). Most of these Paleoproterozoic ages determined in our study, are coeval with the older TIB-1 (1.86 to 1.76 Ga) granites that were emplaced in the wider parts of the northern Fennoscandian Shield during the Late Svecofennian (Figure 4a) (Romer et al. 1992; Gorbatschev, 2004; Andersen et. al, 2009). Ages from this study, largely ranges between 1839 ± 7 and 1811 ± 6 Ma, except for two samples: a metasedimentary rock with maximum deposition age of 1864 ± 9; and a granitic gneiss with age of 1870 ± 12 Ma, that together form the oldest rocks in the area (Figure 49). The magmatism of the granitic gneisses with an age of 1870 ± 12 Ma could be coeval with the early Svecofennian granitoids (1887 ± 9 Ga) from the Horrsjö area in south central Sweden (Andersen et al., 2009). Furthermore, the petrography from the TIB-1 plutons which includes microcline-rich, amphibole- and biotite bearing granitoids, containing titanite and Fe-Ti oxides as accessory phases (Skår, 2002; Gorbatschev, 2004) are in agreement with those of the gneisses that form the North Helgeland basement rocks. Again, similar to greater parts of northern Norway and Sweden, the present granites predominantly have I-type affinity based on the observed mineral assemblages including some positive zircon εHf_i values (e.g., Skår, 2002; Gorbatschev, 2004). Such signatures were developed from melting of mafic to intermediate, continental crust during the Svecofennian accretionary orogeny (ca. 1.9 to 2.1 Ga), including sediments and mantle derived components (e.g., Skår, 2002; Andersen et al., 2009). Notably, all the age determinations from zircons in the North Helgeland Paleoproterozoic gneisses are relatively older than the dominant TIB-1 magmatic ages (1809 to 1781 Ma) reported by Romer et al. (1992) for the northern Tysfjord window.

Overall, the lower intercept U-Pb ages recorded by zircons in all the Paleoproterozoic basement samples in this study define the age of a late ductile deformation and metamorphism that the rocks underwent probably during dome formation in the Caledonian event (e.g., Skår, 2002; Larsen et al., 2002; Schilling et al., 2015; Müller et al., 2022). Although age data are scattered, zircon ages related to the Caledonian metamorphic overprinting in the basement rocks range from 404 ± 17 to 346 ± 28 Ma (Figure 48).

Furthermore, the weak deformation and foliation fabric observed in the granitic gneisses may be due to weak thrusting in the area similar to observations on Træna reported by Larsen et al. (2002).

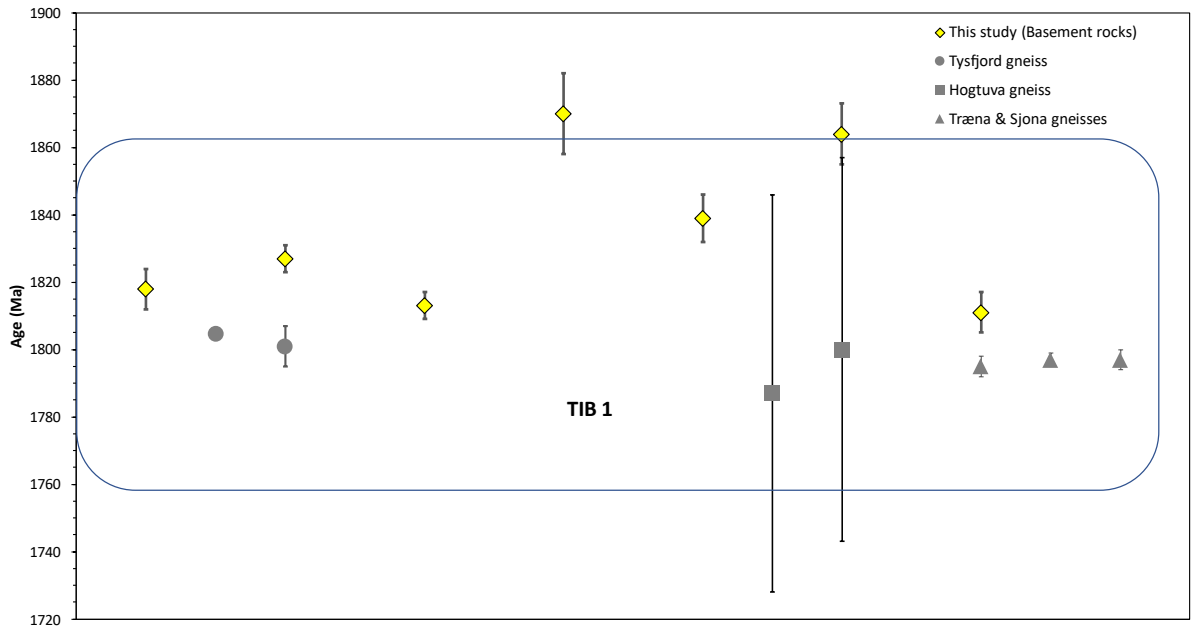

Figure 49. U-Pb zircon age distribution of basement rocks from this study compared with literature data (grey) of other TIB units in northern Norway. The circles represent gneisses from the Tysfjord window (Müller et al., 2022); boxes are gneisses from the Høgtuva window (Skår, 2002; Schilling et al., 2015); triangles are gneisses from Træna and the Sjona window (Skår, 2002).

5.1.2 Granitic pegmatites

U-Pb zircon geochronology has been used extensively in an effort to constrain the ages and origins of the different igneous and metamorphic terranes of the Caledonian orogeny in north-central Norway (e.g., Corfu & Emmett, 1992; Larsen et al., 2002; Skår, 2002; Eide et al., 2002). In this regard, earlier U-Pb geochronology tied with structural geology have revealed an overall top-ENE transport direction, that resulted in crustal uplift and amphibolite metamorphism in the west, and upper greenschist metamorphism to the east (Larsen et al., 2002; Osmundsen et al., 2003). Larsen et al. (2002) determined that pegmatites development mainly occurred during the thrusting related crustal uplift (403-409 Ma). The U-Pb zircon age determinations from this study indicate that all the pegmatites were formed during the Caledonian deformation event with variable

crystallization ages that range from ~422 to 387 Ma (Figure 50). The oldest pegmatite forming events in the North Helgeland area occur at Meløy with ages between 422 ± 5 Ma and 420 ± 3 Ma (Figure 50). A third pegmatite dated from the same area yielded a younger U-Pb zircon age of 396 ± 7 Ma. Previous studies suggested that the North Helgeland pegmatites were formed by two separate batches (e.g., Ihlen, 2004), from magmatism and metamorphism linked to the earlier nappe stacking phase, and the crustal extension phase of the Caledonian deformation event (e.g., Larsen et al., 2002; Müller et al., 2022). However, most age determinations have associated pegmatite formation with the second stage of crustal extension from 400 to 370 Ma (e.g., Larsen et al., 2002; Müller et al., 2022). The U-Pb zircon ages of between 422 and 420 Ma are analytically indistinguishable from local migmatization and granitic gneiss formation during the top-to-the east nappe stacking recorded on Træna and the Sjona window at ~425 Ma (Larsen et al., 2002). Hence, we can assume similar conditions in the Glomfjord window as evidenced by the onset of pegmatite formation at ~422 Ma in the Meløy area including the evidence of migmatite formation in the southern parts of the study area. However, in the North Helgeland area, coeval granite magmatism is absent. The youngest determined zircon U-Pb ages in pegmatites ages range from 403 ± 6 to 387 ± 6 (Figure 50). These ages largely overlap with the second crustal extensional phase (ca. 400 to 370 Ma) associated with extensive magmatism within the Caledonides of Northern Norway (Larsen et al., 2002; Müller et al., 2022). Notably, while pegmatite development was volumetrically minor during this phase, it formed over a large area. Larsen et al (2002) report a U-Pb zircon upper intercept age of 409 ± 5 Ma for a discordant pegmatite in the Sjona gneissic foliation (Figure 50). This age is largely in agreement with most of the pegmatite age determinations in this study, even when considering U-Pb zircon ages between 412 and 416 Ma from the deformed Neverdalen, Rismålstinden and Ågskardet UB pegmatites (Figure 50). Furthermore, a similar age distribution occurs on Træna, some 85 km (straight line distance) southwest of the study area (Figure 50). U-Pb dating of titanite from a discordant pegmatite yielded an age of 403 ± Ma (Larsen et al., 2002). In the Tysfjord basement window northeast of the study area, Müller et al. (2022) reported overlapping columbite and zircon U-Pb ages between 400 and 379 Ma (Figure 50). The fact that this study's data largely coincides with previous reported

ages indicates that all these areas were simultaneously affected by the Caledonian regional metamorphism.

The youngest U-Pb zircon ages from the pegmatites in North Helgeland area are recorded in the Ågskardet OQ with an age of 387 ± 6 Ma. The Ørnes and Ågskardet-S pegmatites yielded very similar U-Pb zircon ages of ∼400 Ma and hence their formation was coeval with the crustal extensional phase. The older ages between 422 to 412 are interpreted to represent crystallization ages of partial melts from the basement gneisses linked to the Silurian-Devonian collision and thrusting (e.g., Larsen et al, 2002). Conversely, the younger ages between 403 and 387 represent the subsequent decompression melting and doming of the gneissic units (e.g., Larsen et al., 2002).

Interestingly, indicators of differentiation and hydrothermal acitivity such as low K/Rb and Nb/Ta (mica) as well as high Li, Cs, Ta, Rb contents used in this study, positively correlate with the determined formation ages of the pegmatites. The youngest pegmatites, such as the Ågskardet OQ and Ørnes pegmatites, exhibit lower K/Rb and Nb/Ta ratios than the oldest pegmatites at Meløy, Rismålstinden and Neverdalen (Figure 33). Further discussions on this are found below in section 5.2.1.

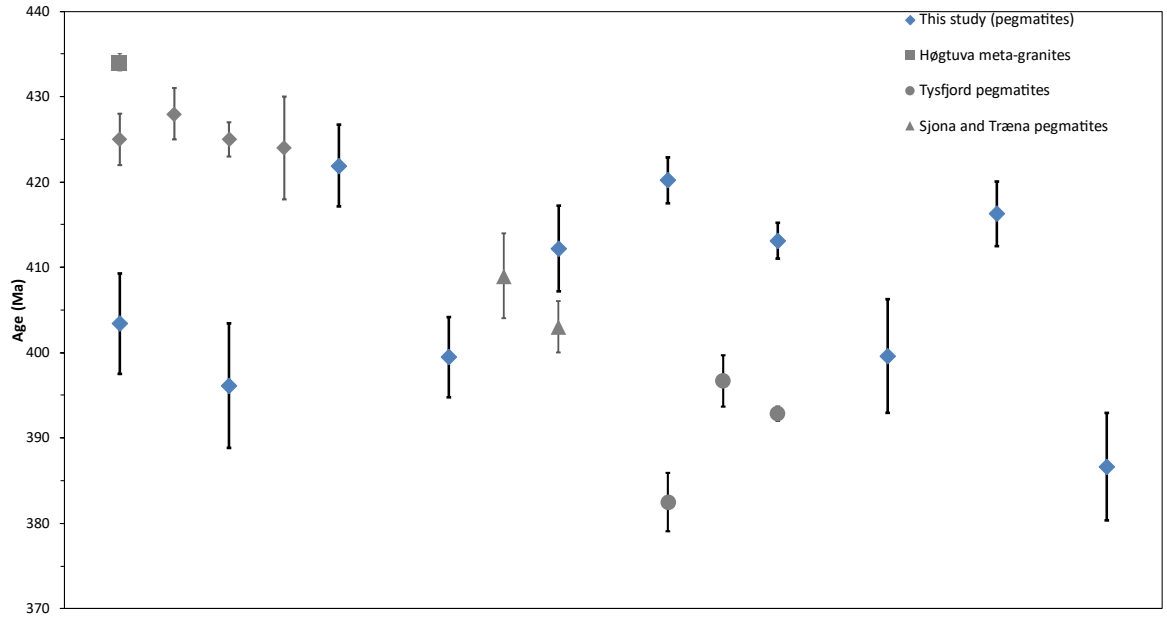

Figure 50. U-Pb zircon age distribution of granitic pegmatites from this study compared with literature data (grey) for granites, migmatites and pegmatites from other Caledonian units in northern Norway. The circles represent pegmatites from the Tysfjord window (Müller et al., 2022); box represents granites from the Høgtuva window (Schilling et al., 2015); triangles are pegmatites from Træna and the Sjona window (Skår, 2002); diamonds are granites and migmatites from the Træna and the Sjona window (Skår, 2002).

5.2 Identification of the pegmatite family in Nord Helgeland

The Helgeland pegmatites were identified as Li-Cs-Ta (LCT) pegmatites by Ihlen (2004) based on the mineral diversity and rare metal enrichment that includes Li (spodumene, cookeite, lepidolite and elbaite), Be (beryl), Cs (pollucite) and Nb-Ta oxide minerals such as columbite and microlite. In general, LCT pegmatites are regarded as products of extreme differentiation of large peraluminous granitic melts (e.g., Černý & Ercit, 2005; London, 2008; Ballouard et al., 2020a). Alternatively, LCT pegmatites could be formed by low degree partial melting of rare metal-rich crustal rocks concentrated in fluxing elements that undergo limited differentiation during movement up the crust (e.g., Černý & Ercit, 2005 and references therein). Most of the LCT pegmatites reported in Norway occur in the Sveconorwegian pegmatite fields (ca. 900 to 1090 Ma) such as Tørdal in southern Norway (Müller et al., 2017 and references therein; Rosing-Schow et al., 2018). The current work uses petrography, mineral chemistry, and field observations to further support the LCT nature of the North Helgeland pegmatites. A characteristic feature of most of the studied

pegmatite is the common occurrence of muscovite and tourmaline within the pegmatites. Tourmaline and muscovite commonly occur in peraluminous granitic pegmatites ultimately derived from melting of aluminous metasediments commonly rich in B (van Hinsberg et al., 2011). Additionally, hydrothermal replacement zones are evident by fine to medium grained albite, olive green muscovites and K-feldspars with partial muscovitization. Furthermore, at the Ågskardet OQ, columbite-group minerals (CGM) present were observed in BSE images as replacement minerals in rutile and further confirmed in thin section. The occurrence of CGM suggests elevated levels of tantalum and/or niobium in the pegmatites, which are frequently found in extensively evolved muscovite-bearing peraluminous granites (MPG), including LCT pegmatites (Barbarin, 1996, Černý & Ercit, 2005).

Feldspar and Micas

In granitic pegmatites, the degree of differentiation of the melt can be evaluated using mineral compositions including the degree of Li, Rb, Cs, Ta enrichment as well as the decrease of K/Rb and Nb/Ta ratios of feldspar, mica, garnet, tourmaline or columbite group minerals. (e.g., Černý, 1989a, b; Ballouard et al., 2020a, b). For this study, we employ mica major and trace element compositions to document the petrogenesis of pegmatites from North Helgeland. Generally, whole-rock analyses are inconclusive for pegmatites because they show diverse textures and coarse crystal size (Ballouard et al., 2020a). Mica is recognized as a highly effective petrogenetic recorder due to its significant ability to accommodate various rare metals and its wide distribution in nearly all pegmatite zones. In comparison to feldspar and quartz, mica has the ability to incorporate significantly higher quantities of Li, Ta, Cs, and Nb. These elements hold considerable economic value in pegmatites (Ballouard et al., 2020a).

About a third of the analyzed micas classified as Fe-muscovite and pure muscovite (Figure 32). White to pink micas from Ågskardet OQ classified as Li-Fe muscovite and muscovite, whereas dark cores and white rims of micas at Ågskardet-S classified as Fe-biotite and pure muscovite, respectively. At Neverdalen, Mg is elevated in most micas exhibited in the form

of Mg-biotite, whereas the rims of some micas are relatively depleted in Mg (and Fe) but enriched in Al, hence classify as Fe-muscovite.

The major element composition of mica shows that in the most evolved pegmatites, muscovite shows Fe-enrichment which correlates with increase in F, Mg, and Mn contents from core to rim. This phenomenon can be explained through two distinct explanations. Firstly, in a peraluminous silica melt, the initial muscovite crystals that form exhibit a purely muscovite composition. This is due to the fact that Fe readily incorporates into the crystal structure of Fe-forming minerals in granitic melts, which tend to crystallize at higher temperatures compared to minerals that form in pegmatites. As the melt temperature decreases, absence of major Fe-rich minerals progressively enriches the melt in Fe, thereby leading to crystallization of Fe-muscovite. The positive correlation of Fe with F contents can be attributed to the increasing flux content during the differentiation of the melt, which occurs due to incompatibility of F. Alternatively, Fe-muscovite may crystallize by a late-stage hydrothermal alteration of primary muscovite as is further discussed in the mineral paragenesis (section 5.3). Notably, from the mica classification diagram (Figure 31), the spread in composition of micas from (Li-) muscovite to (Li-Fe) muscovite at Ågskardet OQ reflects the progressive crystallization from a melt or a late stage-hydrothermal alteration. A similar explanation can be applied to the change in composition from pure muscovite to Fe-muscovite in mica rims at Ørnes and Grønnøya.

The Li-Fe muscovites and Li-muscovites from the Ågskardet OQ show the lowest mean K/Rb value of 8.75 compared to all the micas in the other North Helgeland pegmatites (Figure 33). This value is not far from the average K/Rb value of the Fe-muscovite and pure muscovite of the Ørnes pegmatites with largely overlaps in terms of Rb contents.

The Ågskardet OQ pegmatites exhibit the lowest Nb/Ta values < 3.61 and Nb < 165 ppm reflecting higher Li, Cs and Ta contents compared to micas in the other pegmatites (Figure 35). Additionally, a negative correlation is displayed between Nb/Ta ratios and Li, Cs and Ta contents of micas from the North Helgeland pegmatites. According to Ballouard et al. (2020a), this may be interpreted as the effect of crystallization of feldspar, mica, and oxide minerals from the parent melt. The decrease of Nb/Ta values, reflecting Nb depletion and

Ta enrichment (Figure 35), may indicate crystallization of muscovite and columbite from the melt (Linnen & Keppler, 1997; Stepanov et al., 2014).

When considering Meløy as an outlier, it can be observed that Neverdalen stands out as the most primitive pegmatite in the North Helgeland fields, with a K/Rb value of 18.14 (Figure 34). The logical explanation for this phenomenon is that the Neverdalen pegmatite is observed as a narrow vein, measuring about 15 cm in width (Figure 25a) and formed in contact with a metasedimentary rock and a mafic meta-igneous rock. In contrast, the other pegmatites exhibit larger dimensions and potentially originated from a parent melt that has undergone greater distance of migration, resulting in a higher degree of evolution. In general, many pegmatite fields worldwide exhibit the presence of relatively primitive pegmatites located in close proximity to the assumed source region for the pegmatitic melts (e.g., Larsen, 2002). Importantly, the K/Rb values for the North Helgeland pegmatites are relatively primitive when compared to granitic pegmatites in southern Norway (Figure 34b).

Furthermore, this study identified that the highest Li (11769 ppm) and Rb (2517 ppm) concentrations recorded in mica cores at the Ågskardet OQ are significantly lower compared to the Svecofennian pegmatites in southern Norway.

The analyzed feldspars in section 4.2.1 range in composition from orthoclase to plagioclase (albite and oligoclase, Figure 28). Generally, the feldspars exhibit some variability, and most pegmatites consist of oligoclase and/or albite and microcline. However, feldspar samples from Neverdalen and Ågskardet OQ are more homogenous, with Neverdalen feldspars exclusively consisting of oligoclase and Ågskardet OQ felspars solely of albite. Optical microscopy and BSE images of thin sections also confirm that the Ågskardet OQ feldspars are albite-rich with moderate sericitization, thereby supporting field observations of albite-rich zones in boulders at the quarry. Plagioclase commonly evolves from oligoclase to pure albite with increasing differentiation. Notably, the less evolved pegmatites at Neverdalen, Ågskardet UB, and Ågskardet-S contain plagioclase with oligoclase composition, whereas the more evolved pegmatites at Ågskardet OQ and Ørnes mostly contain albite. In thin sections, perthitic K-feldspar is a common feature in most of

the pegmatites. This further confirms a sub-solidus unmixing reaction of albite from K-feldspar. Ihlen (2004) reports irregular zones of albite and cleavelandite related to late-stage hydrothermal replacement of magmatic minerals in fractures of the Ågskardet OQ pegmatite. However, cleavelandite was not observed in any of the pegmatites during the fieldwork. Notably, the pegmatites at the Ågskardet OQ exhibit the highest evolution with low K/Rb and Nb/Ta values in mica, hence it is not uncommon to find albite rich zones in such an evolved pegmatite body.

Garnet

Our study identified Alm as the predominant garnet endmember in most of the North Helgeland pegmatites. Spessartine-rich garnets were solely observed in the Ågskardet OQ pegmatites often as overgrowths on almandine-rich garnets cores or as individual crystals. Maner et al. (2019) proposed that this phenomenom is mainly due to the tendency of mafic minerals such as tourmaline to incorporate Mg and Fe over Mn in their structure. In an earlier study, Baldwin and von Knorring (1983) proposed that spessartine-rich garnets predominate in Li-rich pegmatites (96.2 to 68.5 mol.%), whereas almandine-rich garnets are more common in low Li pegmatites (65.4 to 72.4 mol.%), suggesting that Li-enriched pegmatites are associated with pure spessartine garnets. Figure 51 emphasizes the association between Mn-rich garnets and Li-pegmatites (Baldwin & von Knorring, 1983). According to Baldwin and Knorring (1983), garnets formed in the replacement zone, or the outer core zone have a higher tendency to be more Mn-rich and Fe-poor. The garnets from the Ågskardet OQ plot within the core and replacement zones, and in the intermediate zones (Figure 51). Similar to Li contents in mica, tourmaline, and feldspar, the Ågskardet OQ pegmatites contain the highest Li-concentrations (204.8 ppm) in the study area. By contrast, the Ågskardet UB which occurs about 1 km south of the Ågskardet OQ pegmatite, has completely opposite composition with < 72.2 ppm Li and predominantly Fe-Mn garnets classifying in the contact zone (Figure 51). Very often, we could not identify specific pegmatite zones in which the samples sit (eg., core, margin or border), but the plot gives a good representation of different zones in the pegmatite. According to Grew et al. (2013), Li incorporation into natural garnets is generally low (< 121 ppm), and presumably occupies

the Z-site. In our study, areas such as Ågskardet OQ, Ørnes and Grønnøya record some elevated Li concentrations up to 204.8 ppm in garnets (Figure 38). The highest Li contents are recorded in the spessartine-rich (39.8 to 69.6 mol.%) and Ti-poor (<89.2 ppm) garnets at the Ågskardet OQ, whereas the almandine-rich garnets from Neverdalen contain very low Li but higher Ti (342.4 ppm) contents.

Earlier studies by Feng et al. (2022) identified that the Y + REE contents of garnets often show a decreasing trend from core to rim similar to observations in this study. This could be attributed to garnet crystallization and increasing H_2O content in the residual melt (e.g., Müller et al. 2012; Feng et al. 2022). Alternatively, this could be a result of crystallization of fergusonite-(Y), xenotime-(Y), and monazite-(Ce) that can take up Y and REE in their structure, thereby resulting in decreasing concentrations outwards in the garnet crystal (e.g., Feng et al., 2022). The highest Y + REE concentration occurs in the Neverdalen almandine-rich garnets with values between 4746 and 7941 ppm (see Appendix 8.5.3). The Y and REE concentrations in the Neverdalen garnets show an abrupt decrease in Y and REE contents from core to rim. The Ågskardet OQ and Grønnøya garnets show two distinct patterns: one type shows a decrease in Y and REE concentrations from core to rim, whereas another generation shows a consistent increase in Y and REE from core to rim similar to the Ørnes garnets. The general decrease in the Y and REE contents could be due to the concomitant crystallization of Y and REE-rich minerals (e.g., xenotime-(Y) and monazite-(Ce) in the pegmatite body, whereas an increase in Y and REE in garnets at the rim can be attributed to diminishing crystallization of xenotime-(Y) and monazite-(Ce) (Feng et al., 2017; Feng et al., 2022).

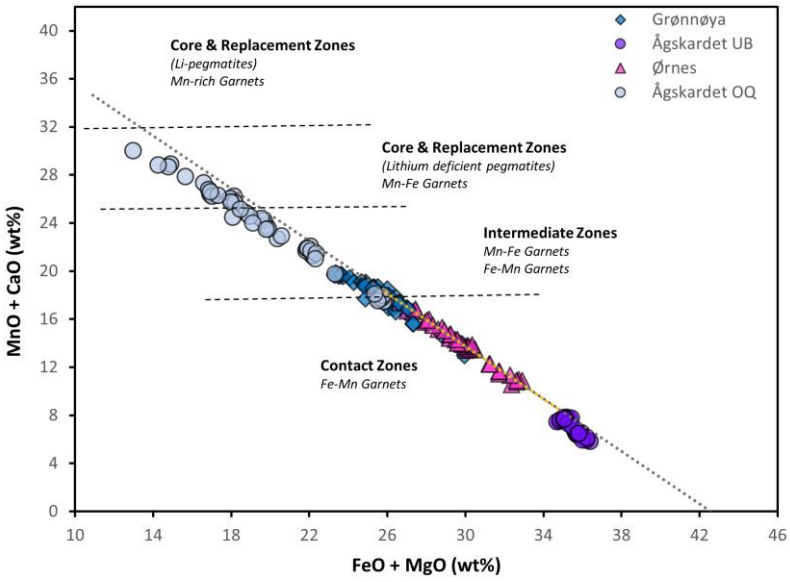

Figure 51. Relationship between garnet chemical composition and pegmatite zones from Baldwin & von Knorring (1983).

Generally, magmatic garnets display decreasing Sc contents towards the rim due to intake by garnets and mica (Stefenssen et al., 2020). This trend was observed in the garnets from Ågskardet OQ and Grønnøya and suggests a competition between Y + REE and Sc for space in the X-site (Westrenen et al., 2003). At Meløy, Sc concentration increases abruptly in the rim which may stem from a late-stage remobilization (Feng et al., 2022). By contrast, garnets from the other pegmatites show increasing Sc concentrations from core to rim which is not clearly understood. Garnet from LCT pegmatites usually contain low Sc concentrations (can reach 306.4 ppm in this study) and are more enriched in NYF pegmatites (e.g., Steffensen et al, 2020). In the Tørdal pegmatites in southern Norway, Sc enrichment of up to 2197 ppm is reported in garnets, hence garnets are used as pathfinders for Sc exploration (Steffensen et al., 2020).

Tourmaline

Tourmaline is a common mineral in LCT pegmatites and more rarely occurs in NYF pegmatites (van Hinsberg et al., 2011). In this study, a variety of pegmatites containing tourmaline were sampled, revealing their frequent occurrence as minor or accessory components within the rocks. All tourmalines belong to the Alkali group and display a range of compositions from schorl (Na–Fe rich) to near dravite (Na–Mg rich) (Figure 41).

This range of composition is interpreted to mainly record subseafloor mixing of Fe-rich hydrothermal fluids and Mg-rich seawater (Slack & Coad, 1989). Recent studies have further demonstrated that in fluids of high salinity, Fe remains attached to Cl, leading to crystallization of Mg-rich tourmalines (Orlando et al., 2017; Chakraborty, 2021). This suggests that Mg-poor cores at Grønnøya may have formed at an early stage when the salinity of granitic melt was low, whereas the Mg-rich rims represent crystallization at a late-stage in higher salininity fluid or melt (e.g., Chakaraborty, 2021). From Figure 43a, the euhedral tourmaline crystal shows concentric zoning in the Fe-rich core followed by a sharp interface of an Mg-rich rim. Compositional zoning in tourmaline reflects in color and sector zoning due to constant changes in the differentiating magmatic system (Hawthorne & Dirlam, 2011). In some crystals, it is displayed as concentric zoning which may also be a result of compositional changes in the melt during primary crystallization of the crystal (Slack & Trumbull, 2011). The episodic growth pattern exhibited by the crystal (Figure 40a) could suggest that the Mg-rich rim most likely crystallized during introduction of highly saline fluids at a late-stage (e.g., Chakraborty, 2021). The near dravite composition of the Meløy tourmalines suggests a single-phase crystallization from a highly saline hydrous melt. The near dravite composition of the Meløy tourmalines closely resembles that of the rims of the Grønnøya tourmalines. It is possible that these crystals have undergone crystallization from identical late-stage highly saline melts or fluids, although they are formed through the nucleation of individual crystals, rather than by forming overgrowths on existing grains. Conversely, tourmaline is predominantly Fe-rich schorl at the Ågskardet OQ, Ørnes and Ågskardet-S. This may suggest that crystallization occurred at a stage of renewed crystallization of tourmaline from low salinity residual melts after demixing of the early stage highly saline fluid from the magma (London, 2005, 2008; Chakraborty, 2021). Tourmalines at the Ågskardet OQ and Ørnes contain very low Mg contents (< 0.22 and < 2.19 apfu), but with higher Fe concentrations and mean values of 2 apfu and 1.97 apfu (n = 211 and 37), respectively. This suggests a positive correlation between the Fe content of the tourmaline and the degree of evolution of the pegmatites. Van Hinsberg et al. (2011) report that the presence of Fe-enrichment in tourmalines can be used as an indicator for moderately fractionated pegmatites. Generally, Li concentrations in tourmalines increase

with magmatic differentiation (Marschall & Jiang, 2011; van Hinsberg et al., 2011) and this is trend is evident in this study's results. The tourmalines in the Ågskardet OQ pegmatites are low in Ti and Sc but significantly enriched in Li, Zn, Sn, Mn, and F compared to the other pegmatites (Figure 43). The higher Zn and fluxes such as Li and F in the Ågskardet OQ tourmalines may suggest crystallization from granite-derived late-stage melts (e.g., Chakraborty, 2021). Conversely, the tourmalines from Ågskardet-S are higher in Sr, Co, Ti and Sc (Figure 43). The Meløy tourmalines, determined to be relatively primitive, often have opposite compositions compared to the Ågskardet OQ tourmalines with depletion in Li, Sn, Sc, Zn, while enriched in Pb, Sr, Co contents. This may suggest a relatively early-stage formation and thus less fractionation compared to the Ågskardet OQ pegmatite, although the source may have changed to form the Ågskardet OQ pegmatite. Based on U-Pb zircon ages determined in this study (section 4.3), the age of the pegmatite formation reflects in the degree of magmatic differentiation.

Apatite

Apatite is a common mineral in granitic pegmatites and can vary significantly in composition even within a single crystal and between grains within a sample (Piccoli & Candela, 2002). This behaviour of apatite may be explained by evolution in the composition of the parental melt during fractionation. Alternatively, this could be due to the late crystallization of apatite from isolated pockets of residual melts, slightly different in composition, and trapped in the interstices between early-crystallizing major minerals such as feldspar (Belousova et al., 2001; O'Sullivan et al., 2020). In this study, apatite from the different pegmatite areas has variable Cl contents and F/Cl values (Figures 45b, c). This could be a result of the difference in fractionation of the pegmatitic melts, that can cause F enrichment and depletion in Cl content, hence a higher F/Cl value signifying a fractionated residual melt (e.g., Pan et al., 2016; Cao et al., 2022). According to the diagram (Figure 46b, c), all apatites, except for those from Ørnes, have overlapping F concentrations but are significantly depleted in Cl, although the Ågskardet OQ apatites have greater F/CL values. Apatites from Ørnes show depletion in F but high Cl concentrations up to 0.61 wt% that rarely exceeds 7.11 F/Cl. Based on this, apatite from the Ågskardet OQ and Neverdalen

show higher fractionation, whereas those from Neverdalen are relatively primitive. This however disagrees with the differentiation indicators such as the K/Rb and Nb/Ta ratios previously discussed in section 5.2 for mica and K-feldspar. Another possible explanation could be the difference in source (e.g., Pan et al., 2016; Cao et al., 2022). Chlorine exhibits strong compatibility with apatite in a Cl-saturated melt, indicating that the concentration of Cl does not undergo significant reduction during the process of magmatic differentiation (Pan et al., 2016; Cao et al., 2022). Consequently, the resulting evolved granites are expected to possess comparable or even elevated levels of chlorine concentration in comparison to the original magma (e.g., Pan et al., 2016; Cao et al., 2022).

Furthermore, earlier studies have demonstrated that Mn enrichment and depletion in Sr (< 100 ppm) can be proxy to a high degree of magmatic differentiation (e.g., Belousova et al., 2001; Cao et al., 2022). In the bivariate plots (Figure 45), the CaO, P_2O_5 and Sr contents decrease, whereas the MnO contents increase. Apatites from the Ågskardet OQ pegmatites contain high MnO contents and relatively low P_2O_5 and CaO contents. This suggests that the Ågskardet OQ pegmatites experienced a higher degree of differentiation than the Ørnes, Ågskardet-S. The Ågskardet-S and Neverdalen pegmatites are relatively primitive with high CaO and low MnO contents. The Sr content is often below detection limits in most of the apatites in the study area (Table 9).

5.3 Mineralization sequence

Previous work on the North Helgeland pegmatites by Ihlen (2004) reported the mineral diversity and rare element enrichment of the rocks. The mineral paragenetic sequence in the pegmatites has been developed by characterization of mineral genesis and general mineralogy. This work further describes the conditions during melt emplacement and crystal growth. The petrographic observations of the mineralogy and crystal relationships in pegmatite thin sections have been summarized in the paragenetic sequence (Table 10). Quartz crystallization is assumed to have occurred in all stages of the paragenetic sequence, hence not included here. A three-stage mineral paragenetic sequence is

proposed for the North-Helgeland pegmatites following the sequence proposed by Kaeter et al. (2018) and Ballouard et al. (2020a):

- The primary stage I marks the end of an exclusively magmatic crystallization from a pegmatitic melt. This stage includes the crystallization of K-feldspar, plagioclase (oligoclase and albite), garnet, tourmaline, muscovite, biotite, Li-muscovite, tourmaline, spodumene, rutile, monazite-(Ce), zircon, allanite, ilmenite, magnetite.
- Stage II represents fine-grained sugary albite replacement of early formed K-feldspar, primary plagioclase and spodumene; replacement of rutile by columbite group minerals CGM; replacement of muscovite with green muscovite; and crystallization of apatite and secondary tourmaline in interstices and cracks.
- Stage III is characterized by the overgrowth of primary formed Li-muscovite and muscovite by Li-Fe muscovite and Fe-muscovite, overgrowth of Fe-biotite or Mg-biotite by (Fe-) muscovite; replacement of K-feldspar by small mica crystals.

The primary stage involved the concomitant crystallization of major pegmatite minerals such as K-feldspar, plagioclase (oligoclase and albite), muscovite and biotite (Table 10). Most of the pegmatites do not display the typical internal zonation and we assume that the Grønnøya and Ågskardet OQ as reported by Ihlen (2004), provide the best scenario for zoned pegmatites in the area. The zonation observed in pegmatites is attributed to chemical potential difference existing between different solid solutions in an undercooled melt. This results in the progressive crystallization of plagioclase, K-feldspar, and quartz from the border to the core of the pegmatites (Ballouard et al., 2020a). The graphic texture between quartz and K-feldspar observed in the pegmatites such as in Meløy and Ågskardet OQ may be an indication of an undercooled melt as proposed by London (2014). In thin section, the accessory minerals zircon and monazite are commonly associated with blades of micas, including crystals of quartz and K-feldspar. This suggests that these minerals crystallized during the early and intermediate stages of crystallization. Minerals such as molybdenite, allanite-(Ce), ilmenite and CGM probably formed from the last portions of pegmatitic melt (e.g., Larsen, 2002). The presence of CGM and rutile may suggest high oxygen fugacity in the saturated melt (van Lichtervelde et al., 2018).

At stage II, metasomatic fluid changes the composition of earlier formed K-feldspar and plagioclase into sugary albite and cleavelandite of higher Ab content. For example, the composition of plagioclase in the Meløy pegmatite has lower Ab contents (Ab_{96-98}) compared to that from the Ågskardet OQ pegmatites (Ab_{98-99}). Based on previous knowledge on the Ågskardet OQ (Ihlen, 2004), metasomatism in the pegmatites was pervasive within fracture zones. Hence, we assume that the high Ab contents of the plagioclase reflects its metasomatic origin. Comparably, Ab contents are low in the Ågskardet-S (Ab_{80-89}) and Neverdalen (Ab_{82-84}) pegmatites. Again, tiny pinkish Li-micas forms veinlets that precipitates in the interstices of albite (Figure 14c) in the Ågskardet OQ pegmatite. This is identical to tiny muscovite flakes that crystallize in feldspars in the other pegmatites, however without significant Li enrichment. The Li source is mostly likely from the metasomatic fluids, whereas K may be derived from breakdown of K-feldspar (eg., Ballouard et al., 2020a). Mg-rich tourmaline is interpreted to have formed after crystallization of the primary tourmaline. It is expected that at this stage, the residual melt is more evolved and coexists with a high saline fluid including an increase in fluxes such as B, F, and Li from the magmatic fluids which could favor further tourmaline crystallization. In thin section and BSE images, stage II tourmalines contain inclusions of the early formed minerals such as quartz, K-feldspar, and micas.

During stage III, late hydrothermal fluids were injected into the magmatic system. The cores of (Li-) muscovite to (Fe-Li) muscovite is either partially resorbed or overgrown by Li-Fe-muscovite. Similarly, Mg-biotite cores from the Neverdalen pegmatites are overgrown by Fe-muscovite rims, whereas Fe-biotite cores from the Ågskardet-S pegmatites are overgrown by pure muscovite. Previous studies by Pichavant et al. (2016) determined that muscovite overgrowth on micas may suggest an increase in oxygen fugacity in the melt. Hence, we can assume similar conditions for muscovite and Fe-muscovite overgrowths on the Ågskardet-S and Neverdalen biotites.

Table 10. Mineral paragenetic sequence for the North Helgeland pegmatites.

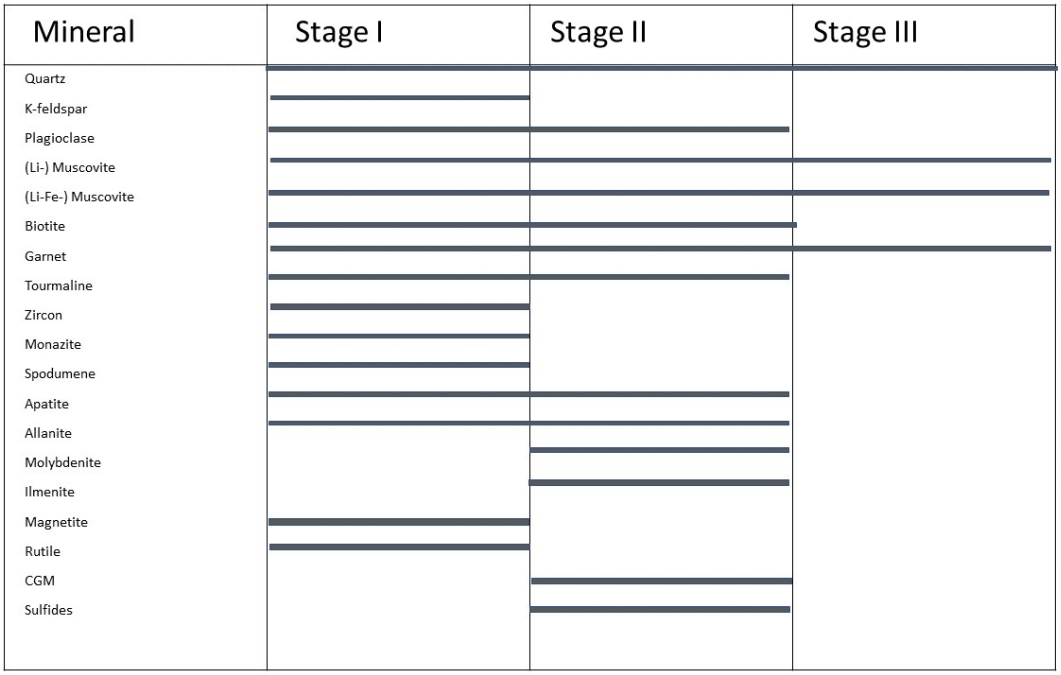

Additionally, at stage III, Mn-rich garnets that occur as replacement bodies in fracture fillings were formed (e.g., Ballouard et al., 2020a). The stage III garnets contain up to ~30 wt% MnO and form overgrowths on the Fe-rich cores. They form subhedral to anhedral crystals and commonly intergrow with apatite (Figure 14c) and exhibit increasing Li content towards the rim. Overall, the magmatic-hydrothermal processes during melt crystallization are assumed to have occurred under undercooled conditions of about 250 ˚C below the solidus temperature of ~650 ˚C for granites (e.g., London, 2014).

5.4 Constraints on pegmatite formation and source evolution

The chondrite normalized REE patterns of garnets from the different pegmatites show distinct patterns although they all show depletion in light REE (LREE) and prominent negative Eu anomaly (Figures 38 and 39). Such patterns cannot be solely attributed to garnet crystallization. Factors such as crystallization of Y and REE-rich minerals, change in H_2O content and even P-T conditions can all influence garnet composition in the pegmatite

(Feng et al., 2022). Müller (2011) interprets the LREE depletion patterns to be a result of crystal fractionation of allanite-(Ce), monazite-(Ce) and fluoroapatite which are the major careers of LREE. Thus, the REE distribution in garnet may be attributed to the degree of differentiation of the pegmatite. In agreement with the mica K/Rb vs Rb diagram (Figure 33), the most primitive pegmatites from Meløy and Neverdalen show the least pronounced negative Eu anomaly in the chondrite normalized REE patterns (Figures 38 and 39).

At the Ågskardet OQ, chondrite normalized REE patterns for garnets show extreme depletion in LREE compared to the other pegmatite areas which all have regular REE patterns expected for garnets (Figure 38). If the pegmatitic melts were derived from a common origin, it is expected that their trace element compositions will be similar. However, this is not observed in the dataset. In addition, it is worth noting that the Ågskardet OQ garnets exhibit notably lower concentrations of Y and REEs in comparison to the pegmatite regions. This may suggest a source melt that was generally low in heavy REE or a high degree of fractionation. REE and Y- bearing phases have low solubility in peraluminous melts, hence these elements behave compatibly in such systems. Therefore, REE depletion in garnet of highly evolved pegmatites is normal and does not reflect a low REE source (Montel, 1993).

Furthermore, the Eu/Eu* ratio measures the extent of the Eu anomaly where values < 1 indicate negative anomaly, whereas values > 1 are positive anomalies. The Eu/Eu* values for garnets, is used to evaluate the presence or absence of plagioclase in the melting residue (Laurent et al., 2019). The strongest Eu anomaly is recorded in the Ågskardet OQ garnets; the least pronounced Eu anomaly in garnets is recorded in the Meløy pegmatites; the Neverdalen garnets also have a relatively low anomaly compared to the other areas which have characteristically strong negative Eu/Eu* values. The interpretation for the negative Eu/Eu* values in garnets is that the melts have undergone plagioclase fractionation or general depletion in Eu from the source melt.

Hafnium Isotopes

For this study we have mostly analyzed Caledonian pegmatites and Paleoproterozoic granitic gneisses that form the basement rocks in the North Helgeland area. Previous studies have suggested that the geochemical and Hf isotopic composition of the granitic gneisses reflect their formation through subduction zone processes during the early Proterozoic, as is well-documented throughout the entire TIB. (Gaál & Gorbatschev, 1987; Nironen, 1997; Skår, 2002). The achievement of their compositions required a combination of mildly depleted mantle sources and a wide range of crustal sources (e.g., Andersen et al., 2009 and references therein). Metasedimentary rocks are associated with the TIB gneisses and contain several heterogenous detrital zircons. In this work, much focus wasn't given to these metasedimentary rocks, however the metasediments at Neverdalen road section were sampled during fieldwork (Figure 25a).

From the diagram (Table 11, Figure 52), the Late Paleoproterozoic rocks in North Helgeland display variable εHf_i values that scatter around CHUR composition with subchondritic to juvenile values (+5 to -3.3, Figure 52). The oldest rocks (1870 ± 12 to 1839 ± 7 Ma) from Neverdalen and Åsjord display more juvenile composition with median εHf_i values between +5 ± 6.8 and +1.8 ± 6.8. The younger basement gneisses (1827 ± 4 to 1811 ± 6 Ma) range in εHf_i values between +0.2 ± 1.6 and -3.3 ± 2. This widespread distribution of εHf_i values among the samples indicate the heterogeneity in Hf isotopes of zircons during formation and further due to slow rate of magma mixing compared to zircon growth (e.g., Andersen et al., 2009). This is different from what we know from the Ersfsjord and Senja granites of the West Troms Basement Complex, in northern Norway. The area contains monzonitic rocks, syeno-granites, and monzo-syenites from the Ersfjord granites with ages ranging between 1790 and 1870 Ma, which have included more Archean (2.6 to 2.8 Ga) basement components that are well exposed in the area (Bergh et al., 2014; Laurent et al., 2019). The Archean basement tends to evolve in the direction of the Ersfjord granites thereby indicating crustal reworking and less juvenile input. The absence of this signature in the North Helgeland granitic gneisses may confirm that Archean basement units are not preserved in the area. However, the data from this study overlaps with published εHf_i data of Late Paleoproterozoic granitoids magmatism in specific areas of the Fennoscandian

shield (Figure 52) (Andersen et al., 2009). This implies that the patterns of Hf isotope composition observed during this study may have relevance to other late Paleoproterozoic granites found in other regions of the shield as well.

Furthermore, the juvenile and sub-chondritic signatures of investigated Paleoproterozoic orthogneiss-hosted zircon, further support the idea that Paleoproterozoic rocks may have formed in a subduction zone where there was mantle wedge melting leading to mantle-like isotopic signatures (e.g, Gaál & Gorbatschev, 1987; Nironen, 1997; Skår, 2002; Andersen et al., 2009). However, mantle melting solely is insufficient to produce a granitic melt, but most likely involved mixing or assimilation of crustal material. In such a setting, the oceanic slab itself may be a source of depleted material. Based on seismic interpretations, Korja and Heikkinen (2005) suggested that large volumes of mafic magma intruded the southern Svecofennian crust during the late Paleoproterozoic. This was suggested to have generated the required heat for the late Paleoproterozoic granitic magmatism (Andersson, 1991; Nironen, 1997).

A total of 66 spot analyses on zircons from the North Helgeland pegmatites define a widespread range of εHf_i values between -32 ± 5.8 and -8 ± 2.2 with a $^{176}Lu/^{177}Hf$ ratio of 0.015 (Table 11). According to Griffin et al. (2002, 2006), zircons derived from magmas with a mix of mantle- and crust-derived sources usually display high within-sample variations in Hf isotopes beyond the range of analytical error. The zircons show single sample variations of up to 7 ε in the Neverdalen pegmatitic dyke, and up to ε 24 units exists between the Neverdalen pegmatite and the Ørnes pegmatite. This highly variable range in εHf_i values may suggest a more heterogenous source for the pegmatites. This is quite significant considering that the pegmatites are assumed to be derived from the partial melting of the basement gneisses during the Caledonian metamorphic event. Zircons from Ørnes contain the least evolved composition with εHf_i values ranging from -9.65 ± 0.7 to -7.15 ± 1.3. When extrapolated back in time, the Hf isotopic composition of the North Helgeland Devonian pegmatites connects with the entire package of Paleoproterozoic basement gneisses (Figure 52). During the Caledonian orogeny, as the crust overthickened and the basement was deeply buried and heated up, the pegmatites were generated. Whether these pegmatites were sourced exclusively from the Paleoproterozoic gneisses or from

metasedimentary rock packages associated with the basement gneisses is currently unclear. However, the largely I-type character of granitic gneisses from the study area suggests that they may not represent an adequate source to generate highly peraluminous magmas with LCT signatures (e.g., Černý and Ercit, 2005; Ballouard et al., 2020a). Indeed, the predominantly LCT character of the North Helgeland pegmatites indicate that they more likely formed by partial melting of a metasedimentary source (i.e., they are S-type granitoids). In the section below, we explore the possibility of generating the North Helgeland LCT pegmatites by partial melting of the Paleoproterozoic metasedimentary rocks during the Caledonian orogenic event.

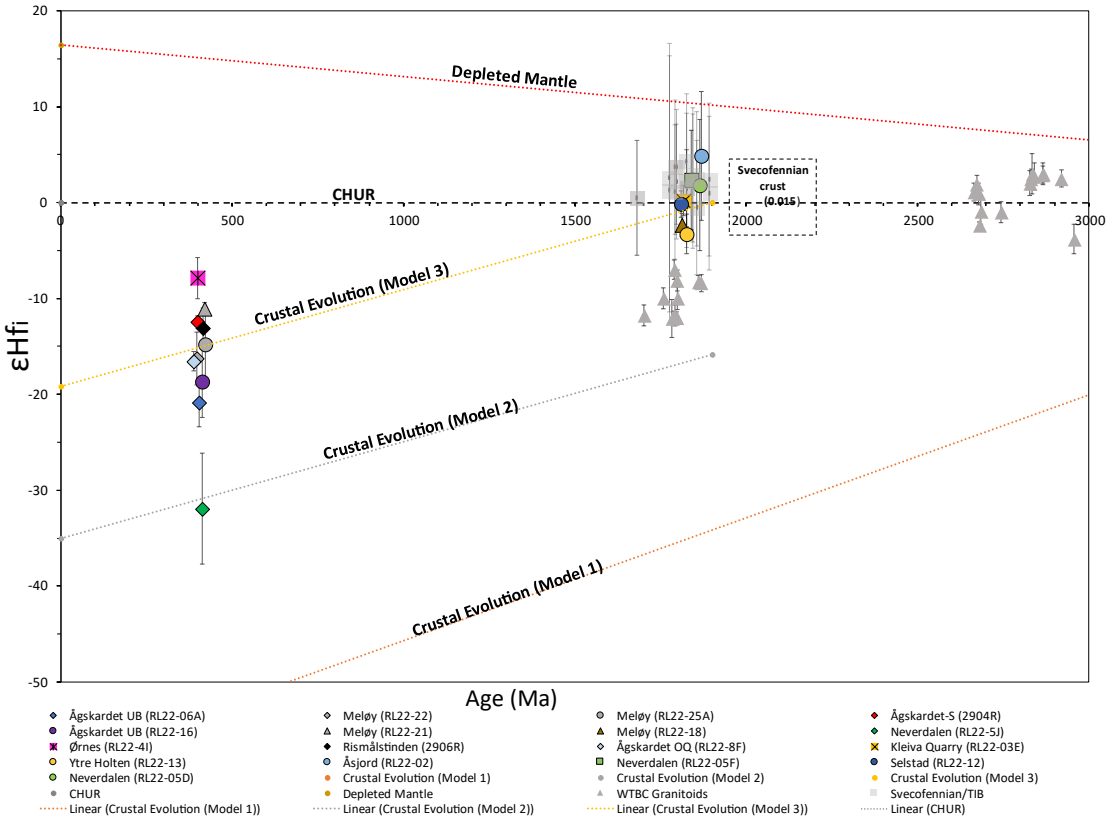

Figure 52. Hf-isotopic evolution of the North Helgeland pegmatites and the Paleoproterozoic basement gneisses. The grey triangles represent literature Hf isotopic data of granitoids from the West Troms Basement Complex (Laurent et al., 2019); the grey triangles are Hf isotopic compositions of granitoids from southern part of the Fennoscandian Shield (Andersen et al., 2009); The colored lines represent the Hf isotopic evolution from the Paleoproterozoic basement rocks; CHUR model is from Bouvier et al. (2008).

5.4.1 The case of the Neverdalen road section.

This present study hypothesized that the granitic pegmatites of North Helgeland formed by anatexis of Precambrian metasedimentary rocks without involvement of a larger S-type granitic pluton/batholith. This hypothesis has been tested through zircon U-Pb geochronology and Hf isotope ratio measurements, and we can show that anatectic melting of a metasedimentary rock easily satisfies the isotopic data. We note that the determined U-Pb age of 1864 ± 9 Ma for the Neverdalen metasedimentary rock is the maximum deposition age for the sedimentary protolith and was overprinted by Caledonian metamorphism similar to other Paleoproterozoic basement gneisses in the area. This provides a constraint for our evolution model (Figure 53) that demonstrates that it is possible to produce pegmatites with similar Hf isotopic compositions by partial melting of such metasedimentary rock. Metasedimentary rocks by their very nature are expected to be heterogeneous, and this is reflected in the highly diverse εHf_i (+8.2 ± 1 and -2 ± 1) values of the zircons analyzed ranging from juvenile to sub-chondritic compositions. In general, one could expect that some of these juvenile components in the metasedimentary rock would evolve into relatively less negative values which could produce a whole range of εHf_i values similar to what we find in the analyzed pegmatites (Figure 53). If the North Helgeland Paleoproterozoic gneisses evolved from a purely subduction zone setting, then the expected pegmatites would have epsilon Hf values scattering around the CHUR value with some juvenile and older inputs. However, it is noteworthy that a diverse array of Hf isotopic compositions is observed in the pegmatites. If there was indeed a single source of granitic gneisses generating pegmatitic melt, it would not account for the significant range of over 30 ε units observed within a relatively confined study area of 20 by 50 km. Additionally, it is possible to 'achieve' εHf_i values as low as -33.5 when the εHf_i values of the Neverdalen metasedimentary rock is projected forward in time from 1864 Ma, when the sediment was deposited and metamorphosed, to 413 Ma when melting occurred under upper amphibolite facies conditions during the Caledonian orogeny (i.e., pegmatite magma formation). In the process of anatexis of metasedimentary rocks, it is typically anticipated to observe greater heterogeneity in the Hf isotopic compositions of the resulting melts. This can be

attributed to the varied nature of the isotopic compositions of the source materials (e.g., Villaros et al., 2012). Notably, this phenomenon is exemplified by the isotopic compositions observed for the North Helgeland pegmatites.

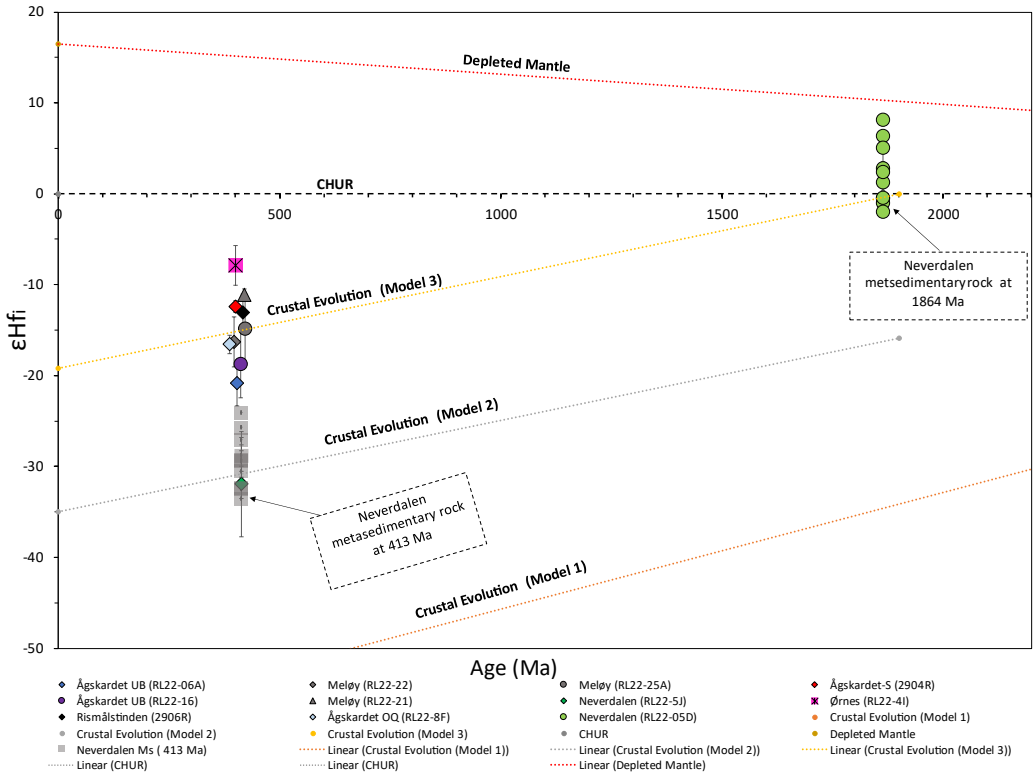

Figure 53. Projected Hf Isotopic evolution of the Neverdalen metasedimentary rock from 1864 Ma to 413 Ma. The sample displays variable εHf_i values similar to the trend displayed by the pegmatites. The diagram illustrates the potential for generating a comparable array of Hf isotopic compositions to those observed in the North Helgeland pegmatites by partial melting of a heterogeneous metasedimentary rock, similar to the one found in Neverdalen.

Table 11.Summary of the U-Pb and Hf-isotopic composition of zircons from the North Helgeland pegmatites and Paleoproterozoic basement gneisses.

Sample ID	Rock Type	Location	Long. E	Lat. N	Age (Ma)	2SE	N U-Pb	$^{176}Lu/^{177}Hf$	2SD	$^{176}Hf/^{177}Hf_i$	2SD	εHf_i	2SD	T_{DM}^{C} 2-stage (Ma)	N Lu-Lf
RL22-06A	Pegmatite	Ågskardet Upper Body	430959.3	7400672	403	5.9	10	0.001376	0.000426	0.281942	0.000071	-20.9	2.5	2657	8
RL22-22	Pegmatite	Meløy	430350	7414829	396	7.3	6	0.000738	0.001182	0.282076	0.000078	-16.3	2.7	2370	6
RL22-25A	Pegmatite	Meløy	429811	7413165	422	4.8	4	0.000849	0.000187	0.282100	0.000108	-14.8	3.8	2300	6
2904R	Pegmatite	Ågskardet-S	431011	7397201	400	4.7	14	0.001731	0.000651	0.282182	0.000018	-12.4	0.6	2136	6
RL22-16	Pegmatite	Ågskardet-UB	430864.5	7400726	412	5	2	0.001198	0.000521	0.281997	0.000106	-18.7	3.7	2531	5
RL22-21	Pegmatite	Meløy	431933.4	7412873	420	2.7	8	0.003270	0.000882	0.282208	0.000018	-11.1	0.6	2067	8
RL22-05J	Pegmatite	Neverdalen	445717.6	7412753	413	2.1	22	0.001027	0.000749	0.281623	0.000163	-31.9	5.8	3338	12
RL22-04I	Pegmatite	Ørnes	442956.2	7418430	400	6.7	1	0.002165	0.004459	0.282310	0.000061	-7.9	2.2	1854	5
2906R	Pegmatite	Rismålstinden	433940	7397169	416	3.8	3	0.003113	0.003031	0.282153	0.000059	-13.1	2.1	2189	5
RL22-08F	Pegmatite	Ågskardet OQ	431137.5	7401858	387	6.3	7	0.001536	0.004822	0.282074	0.000028	-16.5	1	2380	6
RL22-03E	Granitic gneiss	Kleiva Quarry	440814.4	7420880	1818	6	19	0.000586	0.000474	0.281631	0.000044	0.2	1.6	2450	9
RL22-13	Granitic gneiss	Ytre Holten	450309.6	7410688	1827	4	16	0.001308	0.000904	0.281527	0.000058	-3.3	2.0	2667	12
RL22-18	Granitic gneiss	Meløy	436323	7414287	1813	4	18	0.001261	0.000827	0.281562	0.000035	-2.4	1.2	2601	13
RL22-02	Granitic gneiss	Åsjord	440319.3	7406336	1870	12	19	0.001633	0.001005	0.281728	0.000190	4.9	6.8	2210	8
RL22-05F	Mafic gneiss	Neverdalen	445717.6	7412753	1839	7	18	0.000968	0.000555	0.281678	0.000146	2.4	5.2	2336	11
RL22-12	Granitic gneiss	Selstad	448232	7410780	1811	9	21	0.000953	0.000327	0.281625	0.000039	-0.2	1.4	2467	13
RL22-05D	Metasedimentary rock	Neverdalen	445717.6	7412753	1864	6	18	0.001139	0.001579	0.281646	0.000183	1.8	6.8	2388	11

5.5 Comparisons to other granitic pegmatite swarms in Nordland

5.5.1 Tysfjord area

The Tysfjord window is located some 180 km (straight line distance) north-east of the North Helgeland area. Similar to the Glomfjord window, the Tysfjord window is bordered by thrusts faults with the Caledonian nappes. It consists of the Paleoproterozoic Tysfjord granite gneiss and pegmatites that belong to the TIB. These rocks were deformed under amphibolite-facies conditions during the Caledonian orogeny (~430 to 380 Ma; Northrup, 1997). Two distinct pegmatites generations hosted within the Paleoproterozoic basement gneisses: an older deformed metapegmatite generation concordant to the gneiss foliations that forms extremely large bodies (up to 400 m); and a younger undeformed discordant pegmatite generation of Caledonian age (Müller et al., 2022). The mineral assemblage and texture of the foliated Tysfjord granitic rocks, are similar to those from the study area; they consists of coarse-grained, pale red, metagranites with quartz, K-feldspar, biotite, hornblende, and oligoclase albite. They include accessory minerals such as allanite-(Ce), titanite, zircon, magnetite, fluorite, apatite and polycrase (Müller et al., 2022). The younger, undeformed, highly evolved pegmatites show NYF signature and consist of amazonite, cleavelandite, quartz, and minor tourmaline with beryl, fluorite, gadolinite group minerals, columbite, Pb-Bi sulfides and sulfosalts, zircon, thorite, and xenotime-(Y) (Müller et al., 2022). Except for a few identical minerals, the mineral assemblages of the North Helgeland pegmatites rocks differ significantly from the younger undeformed pegmatites of the Tysfjord window. In the Tysfjord area, columbite and U-Pb zircon ages of the younger undeformed pegmatites yielded U-Pb zircon upper intercept ages between 400 and 379 Ma, that overlap within error with zircon U-Pb ages of about half of the North Helgeland pegmatites investigated during this study (Figure 50). Exceptions include ages for pegmatite samples from the older pegmatite samples (i.e., Meløy, Rismålstinden, the Ågskardet UB and Neverdalen) that are relatively older than the Tysfjord younger undeformed pegmatites.

Moreover, the crystallization ages for the TIB-1 granitic gneisses and metapegmatites in the Tysfjord window vary from 1756 to 1809 Ma (Romer et al. 1992; Müller et al., 2022). Contrastingly, most of our basement samples yielded ages older than this age range.

However, the ages of three granitic gneisses from Selstad, Meløy, and the Kleiva Quarry are identical within error (Figure 49). Similar A-type signatures and emplacement ages for both the metapegmatites and the Tysfjord granitic gneisses indicate that the Tysfjord metapegmatites could be residual melts of the TIB granites (Müller et al., 2022). In this study however, we interpret that the Caledonian pegmatites could be sourced from partial melting of metasedimentary rocks that generated highly peraluminous magmas with LCT signatures. Overall, data from this study closely overlaps with previously reported ages including rocks from the basement windows in Høgtuva, Sjona, Tysfjord and on Træna island, suggesting that the Caledonian regional metamorphism affected all these areas concurrently (e.g., Skår, 2002; Larsen et al., 2002; Schilling et al., 2015; Müller et al., 2022)

5.5.2 The Høgtuva area

The Høgtuva window is located ~45 km (straight line distance) south of Glomfjord in central Nordland. The window consists of Precambrian metagranites with subordinate metasedimentary rocks and mafic dykes that were metamorphosed under upper greenschist-facies to lower amphibolite-facies conditions during the Caledonian deformation event (Søvegjarto et al., 1988). Similar to the Glomfjord window, the Høgtuva window belongs to the TIB (Larsen et al., 2002; Skår, 2002) and forms the footwall of a thrust zone below the surrounding Caledonian Allocthon, in this case the Rödingsfjället Nappe Complex (Søvegjarto et al., 1988). The granites are known in Europe to be associated with large Be deposits, constituting 350,000 t with average grade of 0.18 wt% Be (Wilberg & Lindahl, 1991). The upper intercept zircon U-Pb ages between 1870 ± 12 and 1811 ± 6 Ma from the North Helgeland basement granites are interpreted to be their magmatic emplacement ages. All these ages except for the age of 1870 ± 12 Ma recorded for the Åsjord granites are analytically indistinguishable from the 1787 ± 57 Ma age obtained for Be-mineralized granites in the Høgtuva granitic complex (Schilling et al., 2015). The associated deformed Paleoproterozoic pegmatites and aplites in the basement units are peraluminous and characterized by two distinct mineral assemblages: type 1 contains amazonite (green K-feldspar), quartz and minor amphibole without Be-mineralization, whereas type 2 has Be mineralization and includes albite, quartz, biotite and K-feldspar with accessory phases of fergusonite and zircon (Schilling et al., 2015). The study by Schilling et al., (2015) reported a

U-Pb zircon upper intercept age of 1710 ± 59 Ma zircon for Be-bearing peraluminous aplites and pegmatites in the Høgtuva window. This age significantly predates the younger Caledonian pegmatites in this study. However, in our study, U-Pb dating of zircon from the basement granites yielded lower intercept ages between 404 ± 17 Ma and 346 ± 28 Ma (Figure 50), except for a granitic gneiss at Meløy with a post Caledonian disturbation age of 280 ± 12 Ma. U-Pb ages of a second generation of zircons from the Be-mineralized metaluminous metagranite from the Hogtuva window yielded variable ages between 525 ± 37 and 434 ± 14 Ma (Schilling et al., 2015). Schilling et al. (2015) also identified similar zircons that are cogenetic with phenakaite in Be-mineralized peraluminous aplites and pegmatites within the area. The youngest age of 434 ± 14 Ma is in good agreement with the oldest pegmatites in this study from the Meløy area (Figure 50). Overall, ages of the Caledonian metamorphic overprint on the North Helgeland basement gneisses overlap within error with similar metamorphic age determinations in the Høgtuva window (Skår, 2002; Schilling et al., 2015).

5.6 Genetic model for Caledonian pegmatite formation in northern Norway

In northern Scandinavia, the Caledonian orogeny involved two main types of magmatic phases consisting of an older phase of nappe stacking, and a younger phase of orogenic uplift (e.g., Larsen et al., 2002; Stelenpohl et al., 2003). In the Sjona window ~70 km southwest of Glomfjord, local migmatization and granitic gneiss formation was associated with the top-to-the east nappe stacking at ~425 Ma (Larsen et al., 2002). We can assume similar conditions in the Glomfjord window as evidenced by the onset of pegmatite formation at ~422 Ma in the Meløy area including the occurrence of migmatites in the southern parts of the study area. Around the same time, peak amphibolite facies metamorphism is recorded on Træna at 425 Ma, however with less pronounced east-directed thrusting structures (Larsen et al., 2002). Klein et al. (1999) also describe peak high-pressure metamorphism in the Lofoten-Vesterålen area at about 430 Ma, during the eastward thrusting of sheets.

During the second magmatic phase (ca. 400 – 370 Ma), the Caledonian orogen including its foreland, experienced major crustal extension (e.g., Eide et al., 2002). This extensional regime resulted in reactivation of the basal detachment zones and uplift of high- and ultrahigh-grade rocks, which formed the basement windows (Müller et al., 2022). The early Devonian pegmatites (ca. 403 to 387 Ma) in the North Helgeland area are interpreted as products of decompression melting during uplift of basement gneisses (e.g., Larsen et al., 2002). According to Bucher and Frey (1994), crustal temperatures of around 650 °C were required for partial melting. In the Tysfjord area, temperatures between 550 to 650 °C were reported at the contact between the Narvik Nappe Complex and the Tysfjord granite gneiss during the extension at 395 ± 5 Ma (Gromet & Andresen, 1993). The main foliation in the Paleoproterozoic granitic gneisses were interpreted to have developed at the 395 ± 5 Ma age by Gromet & Andresen (1993). According to Brown and Korhonen (2009), a geothermal gradient of 30 to 40 °C/km at 550 to 650 °C, would be equivalent to 3.5 to 6.5 kbar. These conditions, together with fluid availability could generate partial melts of crustal rocks along zones of weakness such as fault and shear zones to form pegmatitic melts (Sawyer et al., 2011). Based on the findings of Müller et al. (2022), the reactivation of N-S thrusts and faults during the extension phase facilitated the creation of pathways for fluids, which in turn intensified localized melting and could have led to the formation of the Tysfjord pegmatites between 400 to 379 Ma. In contrast to the Tysfjord area, the Nesna Shear Zone (NSZ) which forms the contact between the Rödingsfjället and Helgeland Nappe Complexes, was responsible for regional extensional reworking during the Caledonian orogen in areas south of the Sjona window (Osmundsen et al., 2003; Larsen et al., 2002). In the absence of coeval granites in the North Helgeland area, the pegmatites are interpreted as local partial melting products of the basement gneisses (e.g., Müller et al., 2022). The study did not find any tourmaline in the basement gneisses, which may indicate that they are poor in B (e.g., Müller et al., 2022). However, tourmaline (schorl and minor dravite) occurs in most of the pegmatite bodies and significant Li enrichment is recorded in minerals such as feldspar, mica, tourmaline and garnets. This points to a source of tourmaline derived from metasedimentary rocks. The case of rare metal enrichment in the Helgeland pegmatites could indicate that the metasedimentary rocks were pre-enriched in rare metals, whereas Li-

and B-bearing fluids were derived from evaporite-rich metasediments associated with the Paleoproterozoic basement rocks (Simmons & Webber, 2008; Romer & Kroner, 2016). According to Chorlton and Martin (1978), introduction of B to a H_2O-saturated granitic system can significantly decrease the solidus by 125 °C to about 600 °C at 1 kbar. Based on this theory, it is assumed that a similar process lowered the melting temperature of the North Helgeland granitic gneisses and metasediments to form partial melts. Furthermore, field observations indicate that pegmatite formation favored zones of weakness, such as foliation planes and shear zones, as observed in the Meløy area (Figure 17). Overall, the pegmatite emplacement ages in this study broadly conforms with other pegmatite age determinations from other tectonic windows in the central Scandinavian Caledonides. The study by Ihlen (2004) identified about 600 pegmatites solely within North Helgeland. Our research, focusing on a 20 by 50 km area, successfully identified several of these pegmatites. This goes to confirm that the partial melting event allowing for the generation of these pegmatites was not a local event.

Notably, earlier studies, have shown that coeval pegmatitic melts on Træna and in the Sjona window resulted from partial melting of the late Svecofennian granitic rocks during the Caledonian orogeny (Larsen et al., 2002). Additionally, in the Tysfjord window to the north, Müller et al., (2022) report that pegmatites formed from partial melting of the Tysfjord granitic gneisses late in the Caledonian orogeny between 400 and 379 Ma. Hence, the Scandinavian Caledonides were largely affected by partial melting on a regional scale by a combination of eastward thrusting of the nappes at peak metamorphism at 430 Ma (Klein et al., 1999), and subsequent extension by to top-to-west ductile shearing around 400 to 370 Ma (Eide et al., 2002).

5.7 Economic Implications

This study has provided further insights to enhance the current understanding of the North Helgeland pegmatites, which were previously documented by Ihlen (2004). The results of this study suggest that most of the analyzed pegmatites demonstrate relatively small dimensions, with widths ranging from 4 to 5 m and lengths extending to up to 70 m. The

pegmatites were observed to exist as isolated bodies, with no occurrence of a dense pegmatite field. The study could not identify the mineral diversity of these pegmatites as reported in earlier studies. A few of the Helgeland pegmatites are rare mineral enriched but overall show relatively poor fertility. Compared to other known fertile pegmatites from localities worldwide, the sizes and overall low rare metal concentrations render the Helgeland pegmatites uneconomic under current market conditions. However, based on the findings of this study, some recommendations are made:

- To prioritise the comprehensive investigation of additional pegmatite occurrences within the study region in order to enhance the understanding of pegmatite magmatism in the area.
- To conduct whole rock geochemical analyses to accurately characterize the pegmatites including rare-metal concentration, and further constrain their sources.
- To carry out a boron isotope study on the abundant tourmaline crystals in order to track melt and fluid evolution upon pegmatite crystallization and decipher the source rock of the pegmatites (i.e., metasedimentary versus orthogneissic units).

6 Conclusions

Based on a comprehensive application of geological and petrographic investigations, which encompassed the examination of mineral chemistry using EPMA and LA-SF-ICPMS techniques, as well as the evaluation of U-Pb and Lu-Hf isotopic data, we arrive at the following conclusions regarding the Caledonian pegmatites and the Paleoproterozoic basement rocks in North Helgeland:

- U-Pb zircon age determinations indicate that the North Helgeland granitic pegmatites represent two different generations. An older generation of pegmatites with ages between 422 ± 5 and 412 ± 5 Ma that was formed by partial melting related to collision and thrusting during the Caledonian orogenic event. The younger generation of pegmatites has ages between 403 ± 6 and 387 ± 6 Ma

and are related to decompression melting during crustal extension during the late stages of the Caledonian orogeny.

- The basement gneisses in the study area are of Paleoproterozoic age (1870 ± 12 to 1811 ± 6 Ma) and form part of the Transscandinavian Igneous Belt (TIB). In the Glomfjord window, the Paleoproterozoic basement gneisses were overprinted by the Caledonian regional high-grade metamorphism during the late extensional phase between 414 ± 17 Ma and 346 ± 28 Ma.
- The youngest identified pegmatite occurs at the Ågskardet OQ, which is also the most differentiated pegmatite body in Helgeland; micas from this pegmatite show lower K/Rb and Nb/Ta ratios and higher Li, Cs, Ta concentrations than the minerals from other Helgeland pegmatites studied. This indicates that the granitic melts that formed this rock underwent high differentiation, which is not observed for the older Helgeland pegmatites such as on Meløy.
- Hafnium isotopic data reveal subchondritic to juvenile εHf_i values between -3.3 and +5 for the Paleoproterozoic gneisses, whereas the pegmatites show a spread between -32 and -8 ε units. The higher and mostly positive εHf_i values displayed by the Paleoproterozoic gneisses suggest magma derivation from a source that included some mantle components to more evolved crustal rocks, likely in a subduction zone setting.
- Hf isotopic data reveal that the pegmatites in North Helgeland could have formed by partial melting of the Paleoproterozoic basement gneisses during Caledonian metamorphism, which included crustal anatexis. However, the largely I-type signature of the orthogneisses questions their potential as favorable source rocks to generate peraluminous pegmatites with LCT signature. Alternatively, the study has demonstrated that partial melting of a metasedimentary rock from the Neverdalen locality can generate pegmatitic melts with similar Hf isotopic compositions as the Helgeland pegmatites.

7 References

Åhäll, K. I., & Connelly, J. N. (2008). Long-term convergence along SW Fennoscandia: 330 my of Proterozoic crustal growth. Precambrian Research, 161(3-4), 452-474.

Anderson, J. L. (2012). Cold pegmatites. Elements, 8(4), 248-249.

Andersen, T., Andersson, U. B., Graham, S., Åberg, G., & Simonsen, S. L. (2009). Granitic magmatism by melting of juvenile continental crust: new constraints on the source of Palaeoproterozoic granitoids in Fennoscandia from Hf isotopes in zircon. Journal of the Geological Society, 166(2), 233-247.

Andersson, U. B. (1991). Granitoid episodes and mafic-felsic magma interaction in the Svecofennian of the Fennoscandian Shield, with main emphasis on the ~ 1.8 Ga plutonics. Precambrian Research, 51(1-4), 127-149.

Andréasson, P. G. (1994). The Baltoscandian margin in Neoproterozoic-early Palaeozoic times. Some constraints on terrane derivation and accretion in the Arctic Scandinavian Caledonides. Tectonophysics, 231(1-3), 1-32.

Andresen, A., & Tull, J. F. (1986). Age and tectonic setting of the Tysfjord gneiss granite, Efjord, North Norway. Norsk Geologisk Tidsskrift, 66, 69-80.

Baldwin, J. R., & von Knorring, O. (1983). Compositional range of Mn-garnet in zoned granitic pegmatites. The Canadian Mineralogist, 21(4), 683-688.

Barbarin, B. (1996). Genesis of the two main types of peraluminous granitoids. Geology, 24(4), 295-298.

Ballouard, C., Massuyeau, M., Elburg, M. A., Tappe, S., Viljoen, F., & Brandenburg, J. T. (2020b). The magmatic and magmatic-hydrothermal evolution of felsic igneous rocks as seen through Nb-Ta geochemical fractionation, with implications for the origins of rare-metal mineralizations. Earth-Science Reviews, 203, 103115.

Ballouard, C., Elburg, M. A., Tappe, S., Reinke, C., Ueckermann, H., & Doggart, S. (2020a). Magmatic-hydrothermal evolution of rare metal pegmatites from the Mesoproterozoic Orange River pegmatite belt (Namaqualand, South Africa). Ore Geology Reviews, 116, 103252.

Barnes, C. G., Frost, C. D., Yoshinobu, A. S., McArthur, K., Barnes, M. A., Allen, C. M., ... & Prestvik, T. (2007). Timing of sedimentation, metamorphism, and plutonism in the Helgeland Nappe Complex, north-central Norwegian Caledonides. Geosphere, 3(6), 683-703.

Belousova, E. A., Walters, S., Griffin, W. L., & O'reilly, S. Y. (2001). Trace‐element signatures of apatites in granitoids from the Mt Isa Inlier, northwestern Queensland. Australian Journal of Earth Sciences, 48(4), 603-619.

Bergh, S. G., Kullerud, K., Myhre, P. I., Corfu, F., Armitage, P. E. B., Zwaan, K. B., & Ravna, E. J. K. (2014). Archaean Elements of the Basement Outliers West of the Scandinavian Caledonides in Northern Norway: Architecture, Evolution and Possible Correlation with Fennoscandia. In Y. Dilek & H. Furnes (Eds.), *Evolution of Archean Crust and Early Life* (pp. 103–126). Springer Netherlands.

Bergh, S., Kullerud, K., Armitage, P., Zwaan, K., Corfu, F., Ravna, E., & Myhre, P. (2010). Neoarchaean to Svecofennian tectono-magmatic evolution of the West Troms Basement Complex, North Norway. *Norsk Geologisk Tidsskrift*, *90*, 21–48.

Berndt, J., & Klemme, S. (2022). Origin of carbonatites—liquid immiscibility caught in the act. Nature Communications, 13(1), 2892.

Black, L. P., Kamo, S. L., Allen, C. M., Davis, D. W., Aleinikoff, J. N., Valley, J. W., ... & Foudoulis, C. (2004). Improved 206Pb/238U microprobe geochronology by the monitoring of a trace-element-related matrix effect; SHRIMP, ID–TIMS, ELA–ICP–MS and oxygen isotope documentation for a series of zircon standards. Chemical Geology, 205(1-2), 115-140.

Blichert-Toft, J. (2008). The Hf isotopic composition of zircon reference material 91500. Chemical Geology, 253(3-4), 252-257.

Bonzi, W. M. E., Vanderhaeghe, O., Van Lichtervelde, M., Wenmenga, U., André-Mayer, A. S., Salvi, S., & Poujol, M. (2021). Petrogenetic links between rare metal-bearing pegmatites and TTG gneisses in the West African Craton: The Mangodara district of SW Burkina Faso. Precambrian Research, 364, 106359.

Bouvier, A., Vervoort, J. D., & Patchett, P. J. (2008). The Lu–Hf and Sm–Nd isotopic composition of CHUR: constraints from unequilibrated chondrites and implications for the bulk composition of terrestrial planets. Earth and Planetary Science Letters, 273(1-2), 48-57.

Bowell, R. J., Lagos, L., de los Hoyos, C. R., & Declercq, J. (2020). Classification and characteristics of natural lithium resources. Elements, 16(4), 259-264.

Bradley, D.C., Stillings, L.L., Jaskula, B.W., Munk, L., McCauley, A.D. (2017b). Lithium. In: Schulz KJ, DeYoung JH Jr, Seal RR II, Bradley DC (eds) Chapter K. Critical Mineral Resources of the United States— Economic and Environmental Geology and Prospects for Future Supply. U.S. Geological Survey, Professional Paper 1802-K, pp K1–K21.

Bradley, D. C., McCauley, A. D., & Stillings, L. L. (2017a). Mineral-deposit model for lithium-cesium-tantalum pegmatites (No. 2010-5070-O). US Geological Survey.

Brown, M., & Korhonen, F. J. (2009). Some remarks on melting and extreme metamorphism of crustal rocks. In Physics and Chemistry of the Earth's interior: Crust, Mantle and Core (pp. 67-87). New York, NY: Springer New York.

Bucher, K., & Frey, M. (1994). Petrogenesis of Metamorphic Rocks. Springer-Verlag. Berlin and Heidelberg.

Bugge, A. (1963). Norges molybdenforekomster (No. 217). Universitetsforlaget.

Cao, C., Wu, S., Shen, P., Wang, S., Guo, Z., Xiu, D., ... & Feng, H. (2022). Geochemical characteristics of apatite and amphibole within the granitic intrusions from the Suyunhe Mo deposit, Xinjiang province, NW China: Insights into petrogenesis and mineralization potential. Ore Geology Reviews, 105232.

Cameron, M., Sueno, S., Prewitt, C. T., & Papike, J. J. (1973). High-temperature crystal chemistry of acmite, diopside, hedenbergite jadeite, spodumene and ureyite. American Mineralogist: Journal of Earth and Planetary Materials, 58(7-8), 594-618.

Cameron, E. N., Jahns, R. H., McNair, A. H., & Page, L. R. (1949). Internal structure of granitic pegmatites.

Černý, P., London, D., & Novák, M. (2012). Granitic pegmatites as reflections of their sources. Elements, 8(4), 289-294.

Černý, P., & Ercit, T. S. (2005). The classification of granitic pegmatites revisited. The Canadian Mineralogist, 43(6), 2005-2026.

Černý, P. (1991b). Fertile granites of Precambrian rare-element pegmatite fields: is geochemistry controlled by tectonic setting or source lithologies? Precambrian Research, 51(1-4), 429-468.

Černý, P. (1991a). Rare-element granite pegmatites. Part I: anatomy and internal evolution of pegmatite deposits. Part II: regional to global relationships and petrogenesis. Geoscience Canada 18: 49-81.

Černý, P. (1989b). Characteristics of pegmatite deposits of tantalum. In Lanthanides, Tantalum and Niobium: Mineralogy, Geochemistry, Characteristics of Primary Ore Deposits, Prospecting, Processing and Applications Proceedings of a workshop in Berlin, November 1986 (pp. 195-239). Springer Berlin Heidelberg.

Černý, P. (1989a). Exploration strategy and methods for pegmatite deposits of tantalum. In Lanthanides, Tantalum and Niobium: Mineralogy, Geochemistry, Characteristics of Primary Ore Deposits, Prospecting, Processing and Applications Proceedings of a workshop in Berlin, November 1986 (pp. 274-302). Berlin, Heidelberg: Springer Berlin Heidelberg.

Cerny, P., & Burt, D. (1984). Paragenesis, crystallochemical characteristics, and geochemical evolution in micas in granite pegmatites. In Micas (pp. 257-297). Reviews in Mineralogy, Vol. 13, Min. Soc. America.

Chakraborty, T. (2021). Tourmaline growth and evolution in S-type granites and pegmatites: constraints from textural, chemical and B-isotopic study from the Gangpur Schist Belt granitoids, eastern India. Geological Magazine, 158(9), 1657-1670.

Chang, L. L., Deer, W. A., Howie, R. A., & Zussman, J. (1998). Rock-forming minerals. Geological Society of London.

Chappell, B. W., & White, A. J. (2001). Two contrasting granite types: 25 years later. Australian journal of earth sciences, 48(4), 489-499.

Chorlton, L. B., & Martin, R. F. (1978). The effect of boron on the granite solidus. The Canadian Mineralogist, 16(2), 239-244.

Chu, N. C., Taylor, R. N., Chavagnac, V., Nesbitt, R. W., Boella, R. M., Milton, J. A., ... & Burton, K. (2002). Hf isotope ratio analysis using multi-collector inductively coupled plasma mass spectrometry: an evaluation of isobaric interference corrections. Journal of Analytical Atomic Spectrometry, 17(12), 1567-1574.

Corfu, F. (2004). U–Pb age, setting and tectonic significance of the anorthosite–mangerite–charnockite–granite suite, Lofoten–Vesterålen, Norway. Journal of Petrology, 45(9), 1799-1819.

Corfu, F., Armitage, P. E., Kullerud, K., & Bergh, S. G. (2003). Preliminary U-Pb geochronology in the West Troms Basement Complex, North Norway: Archaean and Palaeoproterozoic events and younger overprints. Norges Geologiske Undersøkelse, 441, 61-72.

Corfu, F., & Emmett, T. (1992). U-Pb age of the Leirungsmyran gabbroic complex, Jotun Nappe, southern Norway. Norsk geologisk tidsskrift, 72, 369-374.

Cribb, S. J. (1981). Rb-Sr geochronological evidence suggesting a reinterpretation of part of the north Norwegian Caledonides.

Deer, W. A., Howie, R. A., & Zussman, J. (2013). An introduction to the rock-forming minerals. Mineralogical Society of Great Britain and Ireland.

Dill, H. G. (2015). Pegmatites and aplites: Their genetic and applied ore geology. Ore Geology Reviews, 69, 417-561.

Dutrow, B. L., & Henry, D. J. (2011). Tourmaline: a geologic DVD. Elements, 7(5), 301-306.

Eide, E. A., Osmundsen, P. T., Meyer, G. B., Kendrick, M. A., & Corfu, F. (2002). The Nesna Shear Zone, north-central Norway: an 40 Ar/39 Ar record of Early Devonian-Early Carboniferous ductile extension and unroofing. Norwegian Journal of Geology/Norsk Geologisk Forening, 82(4).

Evans, K. (2014). Lithium, Critical Metals Handbook. American Geophysical Union.

Feng, Y., Cen, J., Liang, T., Wang, M., Tan, X., Hao, Y., & Yan, S. (2022). Lithium, Phosphorus, and rare earth elements in magmatic garnets from granitic Pegmatites: Coupled substitution and petrogenetic implications. Ore Geology Reviews, 105284.

Feng, Y., Lei, R., Ju, M., Song, G., & Xu, F. (2017). Origin and petrogenetic implications of garnet from Rb‐rich pegmatites in North Qinling Orogen, China. Geological Journal, 52, 215-237.

Fisher, C. M., Vervoort, J. D., & Hanchar, J. M. (2014). Guidelines for reporting zircon Hf isotopic data by LA-MC-ICPMS and potential pitfalls in the interpretation of these data. Chemical geology, 363, 125-133.

Fisher, C. M., Hanchar, J. M., Samson, S. D., Dhuime, B., Blichert-Toft, J., Vervoort, J. D., & Lam, R. (2011). Synthetic zircon doped with hafnium and rare earth elements: A reference material for in situ hafnium isotope analysis. Chemical Geology, 286(1-2), 32-47.

Gaál, G., & Gorbatschev, R. (1987). An outline of the Precambrian evolution of the Baltic Shield. Precambrian research, 35, 15-52.

Garrett, D. E. (2004). Handbook of lithium and natural calcium chloride. Elsevier.

Gee, D. G., Fossen, H., Henriksen, N., & Higgins, A. K. (2008). From the early Paleozoic platforms of Baltica and Laurentia to the Caledonide Orogen of Scandinavia and Greenland. Episodes Journal of International Geoscience, 31(1), 44-51.

Gee, D.G., Sturt, B.A. (1985). The Caledonide Orogen-Scandinavia and related areas. Wiley, New York.

Glover, A. S., Rogers, W. Z., & Barton, J. E. (2012). Granitic pegmatites: Storehouses of industrial minerals. Elements, 8(4), 269-273.

Gorbatschev, R. (2004). The Transscandinavian Igneous Belt- Introduction and background. In Högdahl, K., Andersson, U. B., & Eklund, O. (Eds.), The Transscandinavian Igneous Belt (TIB) in Sweden: a review of its character and evolution (Vol. 37, p. 125). Espoo: Geological survey of Finland.

Gorbatschev, R. (1985). Precambrian basement of the Scandinavian Caledonides. The Caledonide Orogen—Scandinavia and Related Areas, 197-212.

Greiling, R. O., & Garfunkel, Z. (2007). An Early Ordovician (Finnmarkian?) foreland basin and related lithospheric flexure in the Scandinavian Caledonides. American Journal of Science, 307(2), 527-553.

Greiling, R. O., Gayer, R. A., & Stephens, M. B. (1993). A basement culmination in the Scandinavian Caledonides formed by antiformal stacking (Bångonåive, northern Sweden). Geological Magazine, 130(4), 471-482.

Grew, E. S. (2020). The minerals of lithium. Elements: An International Magazine of Mineralogy, Geochemistry, and Petrology, 16(4), 235-240.

Grew, E. S., Locock, A. J., Mills, S. J., Galuskina, I. O., Galuskin, E. V., & Hålenius, U. (2013). Nomenclature of the garnet supergroup. American Mineralogist, 98(4), 785-811.

Griffin, W. L., Pearson, N. J., Belousova, E. A., & Saeed, A. (2006). Comment: Hf-isotope heterogeneity in zircon 91500. Chemical Geology, 233(3-4), 358-363.

Griffin, W. L., Wang, X., Jackson, S. E., Pearson, N. J., O'Reilly, S. Y., Xu, X., & Zhou, X. (2002). Zircon chemistry and magma mixing, SE China: in-situ analysis of Hf isotopes, Tonglu and Pingtan igneous complexes. Lithos, 61(3-4), 237-269.

Griffin, W. L., Pearson, N. J., Belousova, E., Jackson, S. V., Van Achterbergh, E., O'Reilly, S. Y., & Shee, S. R. (2000). The Hf isotope composition of cratonic mantle: LAM-MC-ICPMS analysis of zircon megacrysts in kimberlites. Geochimica et Cosmochimica Acta, 64(1), 133-147.

Gromet, L. P., & Andresen, A. (1993). U-Pb age constraints on Caledonian shear strain developed at the basement-allochthon contact, Ofoten region, Norway. Eos Trans. AGU, 74(43), 123.

Gustavson, M., & Gjelle, S. T. (1991). Geological map of Norway (1: 250 000) Mo i Rana. Geological Survey of Norway.

Geological Survey of Norway. (2023). Bedrock geology of Norway (1:1 350 000). Retrieved on 26.03.2023 from: https://geo.ngu.no/kart/berggrunn_mobil/.

Geological Survey of Norway. (2023). Topographic map of Norway (1:250 000). Retrieved on 26.03.2023 from: https://geo.ngu.no/kart/berggrunn_mobil/.

Hawthorne, F. C., & Dirlam, D. M. (2011). Tourmaline the indicator mineral: From atomic arrangement to Viking navigation. Elements, 7(5), 307-312.

Hawthorne, F. C., & Henry, D. J. (1999). Classification of the minerals of the tourmaline group.

Henry, D. J., Novák, M., Hawthorne, F. C., Ertl, A., Dutrow, B. L., Uher, P., & Pezzotta, F. (2011). Nomenclature of the tourmaline-supergroup minerals. American Mineralogist, 96(5-6), 895-913.

Henry, D. J., & Dutrow, B. L. (1996). Metamorphic tourmaline and its petrologic applications. Reviews in Mineralogy and Geochemistry, 33(1), 503-557.

Hölttä, P., Balagansky, V., Garde, A. A., Mertanen, S., Peltonen, P., Slabunov, A., Sorjonen-Ward, P., & Whitehouse, M. (2008). Archean of Greenland and Fennoscandia. Episodes Journal of International Geoscience, 31(1), 13–19.

Högdahl, K., Andersson, U. B., & Eklund, O. (Eds.). (2004). The Transscandinavian Igneous Belt (TIB) in Sweden: a review of its character and evolution (Vol. 37, p. 125). Espoo: Geological survey of Finland.

Hulsbosch, N., Hertogen, J., Dewaele, S., André, L., & Muchez, P. (2014). Alkali metal and rare earth element evolution of rock-forming minerals from the Gatumba area pegmatites (Rwanda): Quantitative assessment of crystal-melt fractionation in the regional zonation of pegmatite groups. Geochimica et Cosmochimica Acta, 132, 349-374.

Husdal, T., Müller, A., Olerud, S., Thorsen, Ø. (2017). Pegmatites of the Tysfjord-Hamarøy area, northern Norway. in Müller et al. (2017) Norwegian pegmatites. Tysfjord-Hamarøy, Evje-Iveland, Langesundsfjord. Geological Society of Norway Geological Guides 6-2017: 3-47.

Ihlen, P.M. (2004). Investigation of Li pegmatites in North Helgeland. Geological Survey of Norway. NGU report No.2004.061. 42 pp (in Norwegian).

Jackson, S. E., Pearson, N. J., Griffin, W. L., & Belousova, E. A. (2004). The application of laser ablation-inductively coupled plasma-mass spectrometry to in situ U–Pb zircon geochronology. Chemical geology, 211(1-2), 47-69.

Jahns, R. H. (1982). Internal evolution of pegmatite bodies. Granitic pegmatites in science and industry, 293-328.

Jahns, R. H., & Burnham, C. W. (1969). Experimental studies of pegmatite genesis; l, A model for the derivation and crystallization of granitic pegmatites. Economic Geology, 64(8), 843-864.

Jahns, R. H. (1953). The genesis of pegmatites: I. Occurrence and origin of giant crystals. American Mineralogist: Journal of Earth and Planetary Materials, 38(7-8), 563-598.

Kaeter, D., Barros, R., Menuge, J. F., & Chew, D. M. (2018). The magmatic–hydrothermal transition in rare-element pegmatites from southeast Ireland: LA-ICP-MS chemical

mapping of muscovite and columbite–tantalite. Geochimica et Cosmochimica Acta, 240, 98-130.

King, P. L., White, A. J. R., Chappell, B. W., & Allen, C. M. (1997). Characterization and origin of aluminous A-type granites from the Lachlan Fold Belt, southeastern Australia. Journal of petrology, 38(3), 371-391.

Klein, A. C., Steltenpohl, M. G., Hames, W. E., & Andresen, A. (1999). Ductile and brittle extension in the southern Lofoten Archipelago, North Norway; implications for differences in tectonic style along an ancient collisional margin. American Journal of Science, 299(1), 69-89.

Knoll, T., Huet, B., Schuster, R., Mali, H., Ntaflos, T., & Hauzenberger, C. (2023). Lithium pegmatite of anatectic origin-A case study from the Austroalpine Unit Pegmatite Province (Eastern European Alps): geological data and geochemical model. Ore geology reviews, 105298.

Kocman, V., Gait, R. I., & Rucklidge, J. (1974). The crystal structure of bikitaite, Li $[AlSi_2O_6]\cdot H_2O$. American Mineralogist: Journal of Earth and Planetary Materials, 59(1-2), 71-78.

Korja, A., & Heikkinen, P. (2005). The accretionary Svecofennian orogen—insight from the BABEL profiles. Precambrian Research, 136(3-4), 241-268.

Kroner, U., Stephan, T., Romer, R. L., & Roscher, M. (2021). Paleozoic plate kinematics during the Pannotia–Pangaea supercontinent cycle.

Lahtinen, R., Korja, A., Nironen, M., & Heikkinen, P. (2009). Palaeoproterozoic accretionary processes in Fennoscandia. Geological Society, London, Special Publications, 318(1), 237-256.

Lahtinen, R., Garde, A. A., & Melezhik, V. A. (2008). Paleoproterozoic evolution of Fennoscandia and Greenland. Episodes Journal of International Geoscience, 31(1), 20-28.

Larsen, R. B. (2002). The distribution of rare-earth elements in K-feldspar as an indicator of petrogenetic processes in granitic pegmatites: examples from two pegmatite fields in southern Norway. The Canadian Mineralogist, 40(1), 137-152.

Larsen, Ø., Skår, Ø., & Pedersen, R.-B. (2002). U-Pb zircon and titanite geochronological constraints on the late/post-Caledonian evolution of the Scandinavian Caledonides in north-central Norway. Norwegian Journal of Geology.

Laurent, O., Vander Auwera, J., Bingen, B., Bolle, O., & Gerdes, A. (2019). Building up the first continents: Mesoarchean to Paleoproterozoic crustal evolution in West Troms, Norway, inferred from granitoid petrology, geochemistry and zircon U-Pb/Lu-Hf isotopes. Precambrian Research, 321, 303-327.

Lindahl, I. & Grauch, R.I. (1988). Be-REE-U-Sn-mineralization in Precambrian granitic gneisses, Nordland County, Norway. In Zachrisson, E. (ed.) Proceedings of the Seventh

Quadrennial IAGOD Symposium, Luleå, Sweden, E. Schweizerbart'sche Verlagsbuchhandlung, Stuttgart, pp. 583-594.

Linnen, R. L., & Keppler, H. (1997). Columbite solubility in granitic melts: consequences for the enrichment and fractionation of Nb and Ta in the Earth's crust. Contributions to Mineralogy and Petrology, 128, 213-227.

London, D. (2017). Reading pegmatites: part 3—what lithium minerals say. Rocks & Minerals 92: 144-157.

London, D. (2014). A petrologic assessment of internal zonation in granitic pegmatites. Lithos, 184, 74-104.

London, D., & Kontak, D. J. (2012). Granitic pegmatites: scientific wonders and economic bonanzas. Elements, 8(4), 257-261.

London, D., & Morgan, G. B. (2012). The pegmatite puzzle. Elements, 8(4), 263-268.

London, D. (2008). Pegmatites. Can. Mineral., 10, 347.

London, D. (2005). Geochemistry of alkali and alkaline earth elements in ore-forming granites, pegmatites, and rhyolites. In Linnen, R. L., Samson, I. M. (Eds.), Rare-element geochemistry and mineral deposits, 17, 17-43. Geological Association of Canada Short Course Notes.

London, D., & Morgan, G. B. (2005). Speciation reactions of acidic boron, phosphorous, fluorine, and of hydrogen in granitic melt as deduced from coupled diffusion experiments. In Geol. Soc. Am. Progr. Abstr. (Vol. 37, p. 307).

London, D., Wolf, M. B., Morgan, G. B., & Garrido, M. G. (1999). Experimental silicate–phosphate equilibria in peraluminous granitic magmas, with a case study of the Alburquerque batholith at Tres Arroyos, Badajoz, Spain. Journal of Petrology, 40(1), 215-240.

London, D. (1995). Geochemical features of peraluminous granites, pegmatites, and rhyolites as sources of lithophile metal deposits. In Magmas, Fluids, and Ore Deposits (J.F.H. Thompson, ed.). Mineralogical Association of Canada, Short Course Handbook 23, 175-202.

London, D., Morgan, G. B., & Hervig, R. L. (1989). Vapor-undersaturated experiments with Macusani glass + H_2O at 200 MPa, and the internal differentiation of granitic pegmatites. Contributions to Mineralogy and Petrology, 102, 1-17.

London, D. (1984). Experimental phase equilibria in the system $LiAlSiO_4$–SiO_2–H_2O: A petrogenetic grid for lithiumx-rich pegmatites. American Mineralogist, 69(11-12), 995-

1004.

Maner IV, J. L., London, D., & Icenhower, J. P. (2019). Enrichment of manganese to spessartine saturation in granite-pegmatite systems. American Mineralogist: Journal of Earth and Planetary Materials, 104(11), 1625-1637.

Marschall, H. R., Wanless, V. D., Shimizu, N., Von Strandmann, P. A. P., Elliott, T., & Monteleone, B. D. (2017). The boron and lithium isotopic composition of mid-ocean ridge basalts and the mantle. Geochimica et Cosmochimica Acta, 207, 102-138.

Marschall, H. R., & Jiang, S. Y. (2011). Tourmaline isotopes: no element left behind. Elements, 7(5), 313-319.

Martin, R. F., & De Vito, C. (2005). The patterns of enrichment in felsic pegmatites ultimately depend on tectonic setting. The Canadian Mineralogist, 43(6), 2027-2048.

Montel, J. M. (1993). A model for monazite/melt equilibrium and application to the generation of granitic magmas. Chemical geology, 110(1-3), 127-146.

Morgan VI, G. B., & London, D. (1999). Crystallization of the Little Three-layered pegmatite-aplite dike, Ramona District, California. Contributions to Mineralogy and Petrology, 136(4), 310-330.

Müller, A., Romer, R. L., Augland, L. E., Zhou, H., Rosing-Schow, N., Spratt, J., & Husdal, T. (2022). Two-stage regional rare-element pegmatite formation at Tysfjord, Norway: implications for the timing of late Svecofennian and late Caledonian high-temperature events. International Journal of Earth Sciences, 111(3), 987-1007.

Müller, A., Romer, R. L., & Pedersen, R. B. (2017). The Sveconorwegian Pegmatite Province–Thousands of pegmatites without parental granites. The Canadian Mineralogist, 55(2), 283-315.

Müller, A., Ihlen, P. M., Snook, B., Larsen, R. B., Flem, B., Bingen, B., & Williamson, B. J. (2015). The chemistry of quartz in granitic pegmatites of southern Norway: Petrogenetic and economic implications. Economic Geology, 110(7), 1737-1757.

Müller, A., Kearsley, A., Spratt, J., & Seltmann, R. (2012). Petrogenetic implications of magmatic garnet in granitic pegmatites from southern Norway. The Canadian Mineralogist, 50(4), 1095-1115.

Müller, A. (2011). Potential of rare earth element and Zr-, Be, U-, Th-, (W-) mineralisations in central and northern Nordland-Part 2.

Müller, A. (2010). Potentials of rare earth element and Zr-, Be-, U-, Th-, (W-) mineralizations in central and northern Nordland.

Nash, W. P. (1984). Phosphate minerals in terrestrial igneous and metamorphic rocks. In Phosphate minerals (pp. 215-241). Berlin, Heidelberg: Springer Berlin Heidelberg.

Neumann, H. (1985). Norge mineraler. NGU 68, 278 p.

Nironen, M. (1997). The Svecofennian Orogen: a tectonic model. Precambrian Research, 86(1-2), 21-44.

Northrup, C. J. (1997). Timing Structural Assembly, Metamorphism, and Cooling of Caledonian Nappes in the Ofoten-Efjorden Arca, North Norway: Tectonic Insights From U-Pb and 40Ar/39Ar Geochronology. The Journal of Geology, 105(5), 565-582.

Nowell, G. M., Kempton, P. D., Noble, S. R., Fitton, J. G., Saunders, A. D., Mahoney, J. J., & Taylor, R. N. (1998). High precision Hf isotope measurements of MORB and OIB by thermal ionisation mass spectrometry: insights into the depleted mantle. Chemical Geology, 149(3-4), 211-233.

Oftedal I. (1950). En litiumførende granittpegmatitt i Nordland. Norsk Geologisk Tidsskrift 28:234-237.

Orlando, A., Ruggieri, G., Chiarantini, L., Montegrossi, G., & Rimondi, V. (2017). Experimental investigation of biotite-rich schist reacting with B-bearing fluids at upper crustal conditions and correlated tourmaline formation. Minerals, 7(9), 155.

Osmundsen, P. T., Braathen, A., Nordgulen, Ø., Roberts, D., Meyer, G. B., & Eide, E. (2003). The Devonian Nesna shear zone and adjacent gneiss-cored culminations, North–Central Norwegian Caledonides. Journal of the Geological Society, 160(1), 137-150.

O'Sullivan, G., Chew, D., Kenny, G., Henrichs, I., & Mulligan, D. (2020). The trace element composition of apatite and its application to detrital provenance studies. Earth-Science Reviews, 201, 103044.

Palme, H., Jones, A. (2003). Solar system abundances of the elements, in: Carlson, R.W. (Ed.), Treatise on Geochemistry. Elsevier, Amsterdam, pp. 41-61.

Pan, L. C., Hu, R. Z., Wang, X. S., Bi, X. W., Zhu, J. J., & Li, C. (2016). Apatite trace element and halogen compositions as petrogenetic-metallogenic indicators: Examples from four granite plutons in the Sanjiang region, SW China. Lithos, 254, 118-130.

Patchett, P. J., & Tatsumoto, M. (1981). A routine high-precision method for Lu-Hf isotope geochemistry and chronology. Contributions to Mineralogy and Petrology, 75(3), 263-267.

Patchett, P. J., & Tatsumoto, M. (1980). Hafnium isotope variations in oceanic basalts. Geophysical Research Letters, 7(12), 1077-1080.

Piccoli, P. M., & Candela, P. A. (2002). Apatite in igneous systems. Reviews in Mineralogy and Geochemistry, 48(1), 255-292.

Pichavant, M., Villaros, A., Deveaud, S., Scaillet, B., & Lahlafi, M. (2016). The influence of redox state on mica crystallization in leucogranitic and pegmatitic liquids. The Canadian Mineralogist, 54(3), 559-581.

Pogge von Strandmann, P. A., Kasemann, S. A., & Wimpenny, J. B. (2020). Lithium and lithium isotopes in Earth's surface cycles. Elements: An International Magazine of

Mineralogy, Geochemistry, and Petrology, 16(4), 253-258.

Puziewicz, J., & Johannes, W. (1988). Phase equilibria and compositions of Fe-Mg-Al minerals and melts in water-saturated peraluminous granitic systems. Contributions to Mineralogy and Petrology, 100(2), 156-168.

Rieder, M., Cavazzini, G., D'yakonov, Y. S., Frank-Kamenetskii, V. A., Gottardi, G., Guggenheim, S., ... & Wones, D. R. (1998). Nomenclature of the micas. Clays and clay minerals, 46, 586-595.

Roberts, D., Nordgulen, Ø., & Melezhik, V. (2007). The Uppermost Allochthon in the Scandinavian Caledonides: From a Laurentian ancestry through Taconian orogeny to Scandian crustal growth on Baltica.

Roberts, D., Gee, D. G. (1985). An introduction to the structure of the Scandinavian Caledonides. In Gee, D. G., Sturt, B. A. (Eds.), The Caledonide orogen–Scandinavia and related areas, 1, 55-68.

Roda-Robles, E., Villaseca, C., Pesquera, A., Gil-Crespo, P. P., Vieira, R., Lima, A., & Garate-Olave, I. (2018). Petrogenetic relationships between Variscan granitoids and Li-(FP)-rich aplite-pegmatites in the Central Iberian Zone: Geological and geochemical constraints and implications for other regions from the European Variscides. Ore Geology Reviews, 95, 408-430.

Romer, R. L., & Kroner, U. (2016). Phanerozoic tin and tungsten mineralization—tectonic controls on the distribution of enriched protoliths and heat sources for crustal melting. Gondwana Research, 31, 60-95.

Romer, R. L., & Bax, G. (1992). The rhombohedral framework of the Scandinavian Caledonides and their foreland. Geologische Rundschau, 81, 391-401.

Romer, R. L., Kjøsnes, B., Korneliussen, A., Lindahl, I., Skyseth, T., Stendal, M., & Sundvoll, B. (1992). The Archaean–Proterozoic boundary beneath the Caledonides of northern Norway and Sweden: U–Pb, Rb–Sr and Nd isotopic data from the Rombak–Tysfjord area. Geological Survey of Norway, Report, 91.

Rosing-Schow, N., Müller, A., & Friis, H. (2018). A Comparison of the Mica Geochemistry of the Pegmatite Fields in Southern Norway. The Canadian Mineralogist, 56(4), 463–488.

Rudnick, R. L., & Gao, S. (2003). Vol. 3: The Crust, 3.01–The Composition of the Continental Crust. Treatise on geochemistry, 1-64.

Rutland, R. W. R., Holmes, M., & Jones, M. A. (1960). Granites of the Glomfjord area, northern Norway. In Int geol Congr (Vol. 21, No. 19, pp. 43-53).

Sauzéat, L., Rudnick, R. L., Chauvel, C., Garçon, M., & Tang, M. (2015). New perspectives on the Li isotopic composition of the upper continental crust and its weathering signature. Earth and Planetary Science Letters, 428, 181-192.

Sawyer, E. W., Cesare, B., & Brown, M. (2011). When the continental crust melts. Elements, 7(4), 229-234.

Scherer, E., Münker, C., & Mezger, K. (2001). Calibration of the lutetium-hafnium clock. Science, 293(5530), 683-687.

Schilling, J., Bingen, B., Skår, Ø., Wenzel, T., & Markl, G. (2015). Formation and evolution of the Høgtuva beryllium deposit, Norway. Contributions to Mineralogy and Petrology, 170, 1-21.

Segal, I., Halicz, L., & Platzner, I. T. (2003). Accurate isotope ratio measurements of ytterbium by multiple collection inductively coupled plasma mass spectrometry applying erbium and hafnium in an improved double external normalization procedure. Journal of Analytical Atomic Spectrometry, 18(10), 1217-1223.

Simmons, W. B. S., & Webber, K. L. (2008). Pegmatite genesis: state of the art. European Journal of Mineralogy, 20(4), 421-438.

Skår, O. (2002). U–Pb geochronology and geochemistry of early Proterozoic rocks of the tectonic basement windows in central Nordland, Caledonides of north-central Norway. Precambrian Research, 116(3–4), 265–283.

Skjerlie, K. P., & Johnston, A. D. (1992). Vapor-absent melting at 10 kbar of a biotite-and amphibole-bearing tonalitic gneiss: implications for the generation of A-type granites. Geology, 20(3), 263-266.

Slack, J. F., & Trumbull, R. B. (2011). Tourmaline as a recorder of ore-forming processes. Elements, 7(5), 321-326.

Slack, J. F., & Coad, P. R. (1989). Multiple hydrothermal and metamorphic events in the Kidd Creek volcanogenic massive sulphide deposit, Timmins, Ontario: evidence from tourmalines and chlorites. Canadian Journal of Earth Sciences, 26(4), 694-715.

Sláma, J., Košler, J., Condon, D. J., Crowley, J. L., Gerdes, A., Hanchar, J. M., ... & Schaltegger, U. (2008). Plešovice zircon—a new natural reference material for U–Pb and Hf isotopic microanalysis. Chemical Geology, 249(1-2), 1-35.

Söderlund, U., Patchett, P. J., Vervoort, J. D., & Isachsen, C. E. (2004). The ^{176}Lu decay constant determined by Lu–Hf and U–Pb isotope systematics of Precambrian mafic intrusions. Earth and Planetary Science Letters, 219(3-4), 311-324.

Søvegjarto, U., Marker, M., Graversen, O., & Gjelle, S. (1988). Berggrunnskart Mo I Rana 1927 I—M. 1: 50000. Norges Geol Unders kart.

Stacey, J. S., Kramers, J. D. (1975). Approximation of terrestrial lead isotope evolution by a two-stage model. Earth Planet. Sci. Lett. 26, 207-221.

Steffenssen, G., Müller, A., Munnik, F., Friis, H., Erambert, M., Kristoffersen, M., & Rosing-Schow, N. (2020). Unusual scandium enrichments of the Tørdal pegmatites, south Norway. Part I: Garnet as Sc exploration pathfinder. Ore Geology Reviews, 126, 103729.

Steiner, B. M. (2019). Tools and workflows for grassroots Li–Cs–Ta (LCT) pegmatite exploration. Minerals, 9(8), 499.

Steltenpohl, M. G., Andresen, A., Lindstrøm, M., Gromet, P., & Steltenpohl, L. W. (2003). The role of felsic and mafic igneous rocks in deciphering the evolution of thrust-stacked terranes: an example from the north Norwegian Caledonides. American Journal of Science, 303(2), 149-185.

Stepanov, A., A Mavrogenes, J., Meffre, S., & Davidson, P. (2014). The key role of mica during igneous concentration of tantalum. Contributions to Mineralogy and Petrology, 167, 1-8.

Stephens, M. B., Gustavson, M., Ramberg, I. B., & Zachrisson, E. (1985). The Caledonides of central-north Scandinavia–a tectonostratigraphic overview. The Caledonide orogen–Scandinavia and related areas, 135-162.

Sylvester, P. J. (1998). Post-collisional strongly peraluminous granites. lithos, 45(1-4), 29-44.

Thomas, A. V., Bray, C. J., & Spooner, E. T. (1988). A discussion of the Jahns–Burnham proposal for the formation of zoned granitic pegmatites using solid-liquid-vapour inclusions from the Tanco Pegmatite, SE Manitoba, Canada. Earth and Environmental Science Transactions of The Royal Society of Edinburgh, 79(2-3), 299-315.

Tischendorf, G., Forster, H. J., Gottesmann, B., & Rieder, M. (2007). True and brittle micas: composition and solid-solution series. Mineralogical Magazine, 71(3), 285-320.

Tischendorf, G., Förster, H. J., & Gottesmann, B. (2001). Minor-and trace-element composition of trioctahedral micas: a review. Mineralogical Magazine, 65(2), 249-276.

Tischendorf, G., Gottesmann, B., Förster, H. J., & Trumbull, R. B. (1997). On Li-bearing micas: estimating Li from electron microprobe analyses and an improved diagram for graphical representation. Mineralogical Magazine, 61(409), 809-834.

Tkachev, A. V. (2011). Evolution of metallogeny of granitic pegmatites associated with orogens throughout geological time. Geological Society, London, Special Publications, 350(1), 7-23.

Vaasjoki, M., Rämö, O. T., & Sakko, M. (1991). New U-Pb ages from the Wiborg rapakivi area: constraints on the temporal evolution of the rapakivi granite-anorthosite-diabase dyke association of southeastern Finland. Precambrian Research, 51(1-4), 227-243.

Van Hinsberg, V. J., Henry, D. J., & Dutrow, B. L. (2011). Tourmaline as a petrologic forensic mineral: A unique recorder of its geologic past. Elements, 7(5), 327-332.

Van Lichtervelde, M., Holtz, F., & Melcher, F. (2018). The effect of disequilibrium crystallization on Nb-Ta fractionation in pegmatites: Constraints from crystallization experiments of tantalite-tapiolite. American Mineralogist, 103(9), 1401-1416.

Vermeesch, P. (2018). IsoplotR: A free and open toolbox for geochronology. Geoscience Frontiers, 9(5), 1479-1493.

Villaros, A., Buick, I. S., & Stevens, G. (2012). Isotopic variations in S-type granites: an inheritance from a heterogeneous source?. Contributions to Mineralogy and Petrology, 163, 243-257.

Westrenen, W. V., Allan, N. L., Blundy, J. D., Lavrentiev, M. Y., Lucas, B. R., & Purton, J. A. (2003). Trace element incorporation into pyrope–grossular solid solutions: an atomistic simulation study. Physics and Chemistry of Minerals, 30, 217-229.

Wiedenbeck, M. A. P. C., Alle, P., Corfu, F. Y., Griffin, W. L., Meier, M., Oberli, F. V., ... & Spiegel, W. (1995). Three natural zircon standards for U‐Th‐Pb, Lu‐Hf, trace element and REE analyses. Geostandards newsletter, 19(1), 1-23.

Wilberg, R., Lindahl I. (1991). The Bordvedåga beryllium deposit, Rana, Nordland County, Norway. Summary report. Norges Geologiske Undersøkelse Rapport 91.181.

Wilberg, R. (1987). Rekognoserende Rb-Sr aldersbestemmelser av granittiske gneiser fra grunnfjellsvinduene Høgtuva og Sjona i Nordland. Norges Geologiske Undersøkelse Rapport 87.074, 21 pp. (in Norwegian).

Wilson, M. R. (1982). Magma types and the tectonic evolution of the Swedish Proterozoic. Geologische Rundschau, 71(1), 120-129.

Wilson, M. R., & Åkerblom, G. (1980). Uranium enriched granites in Sweden (No. SGU--19). Sveriges Geologiska Undersoekning.

Wilson, M. R., & Nicholson, R. (1973). The structural setting and geochronology of basal granitic gneisses in the Caledonides of part of Nordland, Norway. Journal of the Geological Society, 129(4), 365-386.

Woodhead, J. D., & Hergt, J. M. (2005). A preliminary appraisal of seven natural zircon reference materials for in situ Hf isotope determination. Geostandards and Geoanalytical Research, 29(2), 183-195.

Yavuz, F., Karakaya, N., Yıldırım, D. K., Karakaya, M. Ç., & Kumral, M. (2014). A Windows program for calculation and classification of tourmaline-supergroup (IMA-2011). Computers & Geosciences, 63, 70-87.

Zhao, H., Chen, B., Huang, C., Bao, C., Yang, Q., & Cao, R. (2022). Geochemical and Sr–Nd–Li isotopic constraints on the genesis of the Jiajika Li-rich pegmatites, eastern Tibetan Plateau: implications for Li mineralization. Contributions to Mineralogy and Petrology, 177(1), 4.

8 Appendix

8.1 Sample List

SAMPLE ID	Coordinates (UTM 33 W)		Locality	Rock type	Mineral Assemblage	Host rock	Analyses
	E	N					
RL22-01A	431085	7409524	Grønnøya	Pegmatite	Quartz, K-feldspar, plagioclase, biotite, muscovite, garnet, tourmaline,	Amphibolite	OM, EPMA, LA-SF-ICP-MS, U-Pb Geochronology, Lu-Hf isotopic composition
RL22-01B	431085	7409524	Grønnøya	Pegmatite	Quartz, K-feldspar, plagioclase, muscovite, biotite, zircon, opaque minerals	Amphibolite	OM
RL22-01C	431085	7409524	Grønnøya	Pegmatite	Quartz, K-feldspar, tourmaline, garnet, plagioclase	Amphibolite	OM, EPMA, LA-SF-ICP-MS
RL22-02	440319.33	7406335.66	Åsjord	Granitic gneiss	Quartz, K-feldspar, plagioclase, biotite, amphibole, opaque minerals, zircon		OM, SEM, BSE imaging (zircon), U-Pb Geochronology, Lu-Hf Isotopic composition
RL22-03E	440814.4	7420879.9	Kleiva Quarry, Reipa	Granitic gneiss	Quartz, K-feldspar, plagioclase biotite, garnets, pyrite, zircon		OM, SEM, BSE imaging, (zircon), U-Pb Geochronology, Lu-Hf Isotopic composition
RL22-04F	442956.24	7418429.87	Ørnes	Pegmatite	Quartz, K-feldspar, plagioclase, tourmaline, muscovite	Amphibolite	OM, LA-SF-ICP-MS
RL22-04I	442956.24	7418429.87	Ørnes	Pegmatite	Quartz, plagioclase, K-feldspar, tourmaline, garnet, apatite, zircon	Amphibolite	SEM, BSE imaging (zircon), U-Pb Geochronology, Lu-Hf isotopic composition
RL22-04J	442956.24	7418429.87	Ørnes	Pegmatite	Quartz, K-feldspar (perthite), plagioclase, muscovite, biotite, opaque minerals	Amphibolite	OM, EPMA, LA-SF-ICP-MS, SEM, BSE imaging, U-Pb Geochronology, Lu-Hf isotopic composition
RL22-05D	445717.59	7412753.23	Neverdalen	Metasedimentary rock	Quartz, K-feldspar, plagioclase, muscovite, opaque minerals, zircon		OM, SEM, BSE imaging (zircon), U-Pb Geochronology, Lu-Hf isotopic composition

RL22-05F	445717.59	7412753.23	Neverdalen	Mafic gneiss	Quartz, K-feldspar, plagioclase, amphibole, zircon		OM, SEM, BSE imaging (zircon), U-Pb Geochronology, Lu-Hf isotopic composition
RL22-05J	445717.59	7412753.23	Neverdalen	Pegmatitic dyke	Quartz, K-feldspar, plagioclase, garnet, biotite, muscovite, magnetite, ilmenite, sulphides, allanite, apatite, zircon	Mafic gneiss, Metasedimentary rock	OM, EPMA, LA-SF-ICP-MS, SEM, BSE imaging, U-Pb Geochronology, Lu-Hf isotopic composition
RL22-06A	430959.32	7400672.37	Ågskardet Upper Body	Pegmatite	Quartz, plagioclase, garnet, amphibole, garnet, zircon		OM, SEM, BSE imaging (zircon), U-Pb Geochronology, Lu-Hf isotopic composition
RL22-07E	431145.89	7401398.67	Ågskardet Old Quarry	Pegmatite	Quartz, plagioclase, K-feldspar, muscovite, tourmaline, green apatite, garnet, coltan, opaque minerals		OM, EPMA, LA-SF-ICP-MS, BSE imaging
RL22-08C	431137.54	7401857.87	Ågskardet Old Quarry	Pegmatite	Quartz, plagioclae, K-feldspar, garnet, green apatite, tourmaline, muscovite		OM, EPMA, LA-SF-ICPMS, BSE imaging
RL22-08F	431137.54	7401857.87	Ågskardet Old Quarry	Pegmatite	Quartz, plagioclase, K-feldspar, muscovite, apatite, tourmaline, cookeite, zircon, apatite		OM, SEM, BSE imaging (zircon), U-Pb Geochronology, Lu-Hf isotopic composition
RL22-12	448231.96	7410779.6	Selstad	Granitic gneiss	Quartz, K-feldspar, plagioclase, amphibole, ilmenite, biotite, zircon		OM, SEM, BSE imaging (zircon), U-Pb Geochronology, Lu-Hf isotopic composition
RL22-13	450309.6	7410688.49	Ytre holten	Granitic gneiss	Quartz, K-feldspar, amphibole, plagioclase, biotite, zircon		OM, SEM, BSE imaging (zircon), U-Pb Geochronology, Lu-Hf isotopic composition
RL22-16	430864.53	7400726.38	Ågskardet Upper Body	Pegmatite	Quartz, K-feldspar, plagioclase, garnet, tourmaline, biotite, muscovite, zircon, monazite		OM, EPMA, LA-SF-ICP-MS, SEM, BSE imaging, U-Pb Geochronology, Lu-Hf isotopic composition
RL22-18	436323	7414287	Meløy	Granitic gneiss	Quartz, K-feldspar, biotite, amphibole, opaque minerals, zircon		OM, SEM, BSE imaging (zircon), U-Pb Geochronology, Lu-Hf isotopic composition

RL22-21	431933	7412873	Meløy	Pegmatite	Quartz, K-feldspar, biotite, apatite, zircon	Mafic gneiss	OM, SEM, BSE imaging (zircon), U-Pb Geochronology, Lu-Hf isotopic composition
RL22-22	430350	7414829	Meløy	Pegmatite	Quartz, K-feldspar, plagioclase, muscovite, biotite, garnet, tourmaline, zircon	Metasedimentary rock	OM, LA-SF-ICPMS, SEM, BSE imaging (zircon), U-Pb Geochronology, Lu-Hf isotopic composition
RL22-23C	430539	7414752	Meløy	Pegmatite	Quartz, K-feldspar (perthite), tourmaline, muscovite	Metasedimentary rock	OM, EPMA, LA-SF-ICP-MS, BSE imaging
RL22-24	431785	7412865	Meløy	Mafic gneiss	Quartz, plagioclase, K-feldspar, biotite, amphibole, garnet, zircon, apatite		OM, BSE imaging (zircon)
RL22-25A	429811	7413165	Meløy	Pegmatite	Quartz, K-feldspar, plagioclase, muscovite, zircon, monazite	Banded gneiss	SEM, BSE imaging (zircon), U-Pb Geochronology, Lu-Hf isotopic composition
RL22-25B	429811	7413165	Meløy	Pegmatite	Quartz, K-feldspar, plagioclase, muscovite, biotite, opaque minerals, chlorite, zircon	Banded gneiss	OM
2904R	431011	7397201	Ågskardet-South	Pegmatite	Quartz, plagioclase, K-feldspar (perthite), biotite, tourmaline, muscovite, zircon, monazite		OM, EPMA, SEM, BSE imaging, LA-SF-ICP-MS,
2906R	433940	7397169	Rismålstinden	Pegmatite	Quartz, plagioclase, K-feldspar (perthite), biotite, muscovite, apatite, zircon		OM, SEM, BSE imaging (zircon), U-Pb Geochronology, Lu-Hf isotopic composition

8.2 Thin Sections

8.2.1 Thin Section Scans

RL22-01A

RL22-01B

RL22-04J1

RL22-04F

RL22-05J

RL22-06A1

RL22-06A2

RL22-07E

RL22-08C

RL22-08F2

2904R

2906R

RL22-16

RL22-23C

RL22-25A

RL22-25B

RL22-02

RL22-03E

RL22-05D

RL22-05F

RL22-12

RL22-24

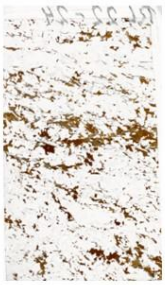

8.2.2 Summary of mineral assemblages of other North Helgeland rocks in thin section.

Thin Section	Location	Mineral assemblage	Mode (%)	Grain size (mm)	Comments
RL22-4F Pegmatite	Ørnes	Quartz	45	0.2-5	Sample is K-feldspar rich with ~25% of K-feldspar altered into sericite. Tourmaline is brown with lighter core and darker rim. Muscovite forms as tiny flakes in plagioclase cracks.
		K-feldspar	30	0.3-4.5	
		Plagioclase	10	0.5-20	
		Tourmaline	10	0.7-5	
		Muscovite	5	< 0.2	

Thin Section	Location	Mineral assemblage	Mode (%)	Grain size (mm)	Comments
RL22-01B Pegmatite	Grønnøya	K-feldspar	40	1-10	Subgrains in quartz with undulose extinction. Myrmekite development in plagioclase. Plagioclase is altered into sericite and has diffuse boundary with K-feldspar. Secondary muscovitization of K-feldspars. Biotite is tabular, contains zircon inclusions, and has reaction rims with K-feldspar that form secondary muscovites. Zircons are prismatic with high relief.
		Quartz	15	0.4-5	
		Plagioclase	15	1.2-6.5	
		Biotite	15	1-14	
		Muscovite	10	0.2-1	
		Opaque minerals	5	0.5-1	
		Zircon	<1	<0.15	

Thin Section	Location	Mineral assemblage	Mode (%)	Grain size (mm)	Comments
RL22-7E Pegmatite	Ågskardet Old Quarry	Plagioclase	23	0.3 - 5	Feldspar is entirely plagioclase. Plagioclase reacts to form tiny muscovite flakes with sericitization along boundary with quartz and in cracks. Garnet contains fractures and inclusions of quartz and apatite. Most tourmalines are zoned, with dark blue cores and lighter rims. Apatite is late and often grows into garnet fractures.
		Quartz	23	< 0.1 - 4	
		Muscovite	5	0.1 - 2	
		Tourmaline	20	3 - 15	
		Garnet	25	1 - 18	
		Apatite	3	0.2 - 2	
		Opaque minerals	1	< 0.1	
		Zircon	< 1	< 0.08	
		Coltan	< 1	0.8	
RL22- 8F	Ågskardet Old Quarry	Plagioclase	40	0.5 - 10	
		K-feldspar	15	0.2 - 0.1	

		Quartz	20	0.1- 8	Cracks in feldspars filled by tiny mica flakes. Recrystallization in quartz. Lots of blue to green tourmalines. Two tourmaline generations: 1. Forms euhedral crystals. 2. may be hydrothermal and fills cracks and interstices between quartz and feldspar. Both types display dark green core and light to purple rims.
		Muscovite	7	< 0.1- 0.7	
		Cookeite	3	< 0.1	
		Tourmaline	14	1 - 15	
		Zircon	1	0.1 - 0.2	

Thin Section	Location	Mineral assemblage	Mode (%)	Grain size (mm)	Comments
RL22-16	Ågskardet Upper Body	K-feldspar	40	0.4 - 15	Plagioclase is grainy and highly altered to sericite. Myrmekite up to 2.4 mm present in plagioclase. Garnet is anhedral and stretched, hosts quartz and muscovite inclusions and has magmatic contact with quartz and K-feldspar. Muscovite formed from secondary muscovitization of K-feldspar. Biotite is patchy and forms reaction rims with K-feldspar. Tourmaline is elongated with dark brown core and transparent rim. It forms in interstices of large quartz and K-feldspar crystals.
		Quartz	35	0.4 - 11	
		Plagioclase	10	1.3 - 7	
		Garnet	6	3 - 4.5	
		Tourmaline	4	1.2 - 1.5	
		Biotite	2	0.6-1.4	
		Muscovite	1	3	
		Zircon	< 1	0.1	

Thin Section	Location	Mineral assemblage	Mode (%)	Grain size (mm)	Comments
RL22-25B Pegmatite	Meløy	K-feldspar	40	0.4 - 10	Early stage subgrain development in quartz. Interfingering and recrystallization in quartz and feldspars. Myrmekite development is common in plagioclase. Secondary muscovitization of K-feldspar.
		Quartz	30	< 0.1 - 5	
		Plagioclase	10	0.2 - 10	
		Biotite	15	0.1 4	
		Muscovite	3	< 0.1 - 0.4	
		Chlorite	1	0.4 - 1.2	
		Opaque minerals	1	< 0.1	

Thin Section	Location	Mineral assemblage	Mode (%)	Grain size (mm)	Comments
RL22-12 Granitic Gneiss	Selstad	K-feldspar	35	0.3 - 2	Weak alteration of K-feldspars and plagioclase into sericite. Twinning clear in most feldspars. K- feldspars and quartz show diffuse boundaries
		Plagioclase	20	0.42	
		Quartz	20	0.1 - 1.1	
		Biotite	5	0.1 1	
		Amphibole	14	0.2 - 0.8	

		Ilmenite	6	0.2 1	indicative of incipient deformation. Quartz and plagioclase host biotite inclusions. Myrmekite occurs in K-feldspar and plagioclase crystal boundary.
		Zircon	< 1	0.1	

Thin Section	Location	Mineral assemblage	Mode (%)	Grain size (mm)	Comments
RL22-05J Pegmatite	Neverdalen	Quartz	30	0.3 1.5	Ilmenite is very common in sample. Some K-feldspar grains altered to perthite. Several zircon crystals. Garnets host quartz inclusions. Biotite is greenish with brown specks. EPMA confirmed allanite in sample.
		K-feldspar	25	0.5 - 2	
		biotite	10	0.4 0.8	
		plagioclase	12	0.5 - 2	
		ilmenite	15	0.1 - 0.5	
		Muscovite	3	0.2 - 0.8	
		Garnet	2	0.70	
		Allanite	< 1	0.15	
		Zircon	< 1	0.12 - 0.2	

8.3 BSE images of zircons used in U-Pb Geochronology and Hf isotopic measurements.

The blue and yellow spots on zircon crystals represents 15 and 40 µm spot sizes used for U-Pb and Lu-Hf measurements respectively.

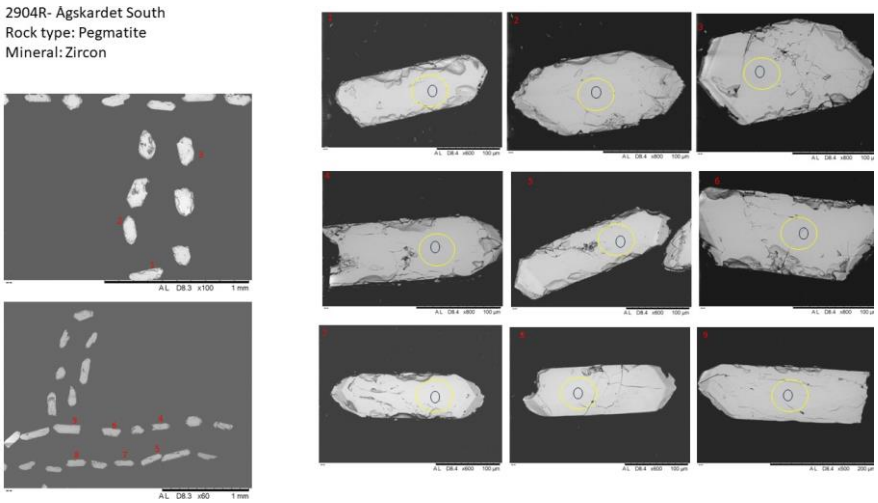

2904R- Ågskardet South
Rock type: Pegmatite
Mineral: Zircon

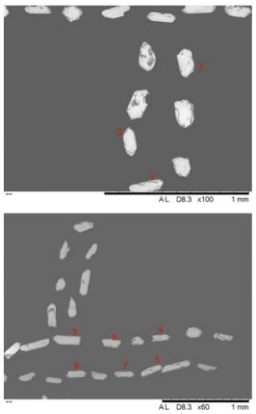

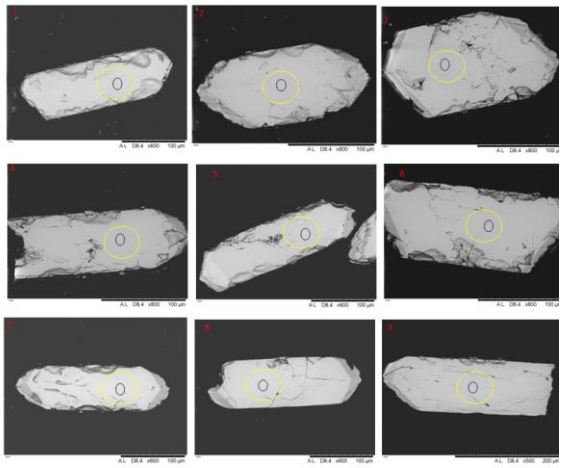

RL22-25A – Meløy
Rock type : Pegmatite
Mineral: Zircon

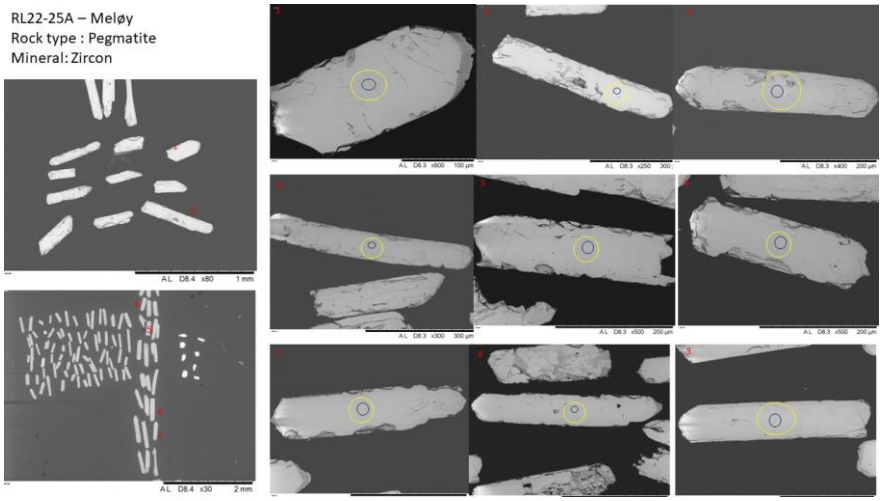

RL22-25A – Meløy
Rock type : Pegmatite
Mineral: Zircon

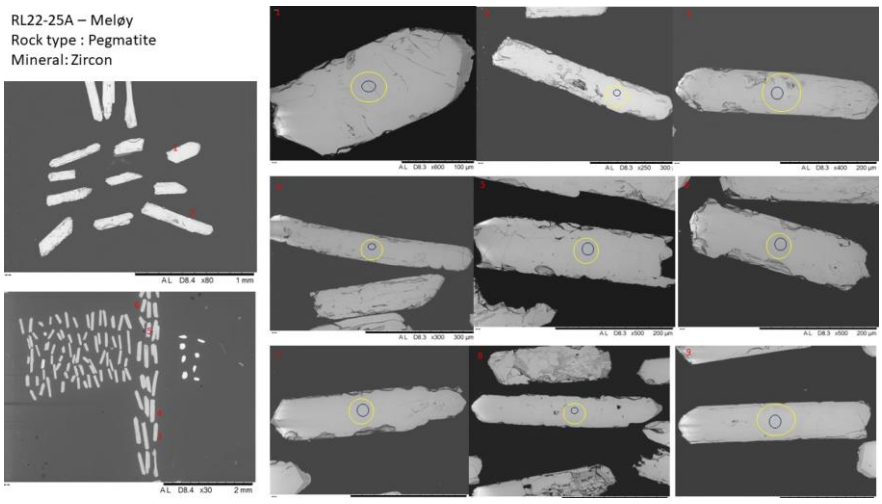

RL22-06A – Ågskardet Upper body
Rock type: Pegmatite
Mineral: Zircon

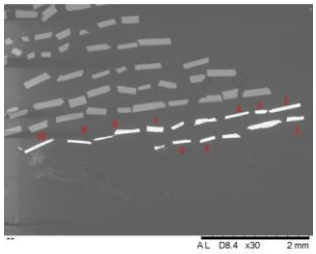

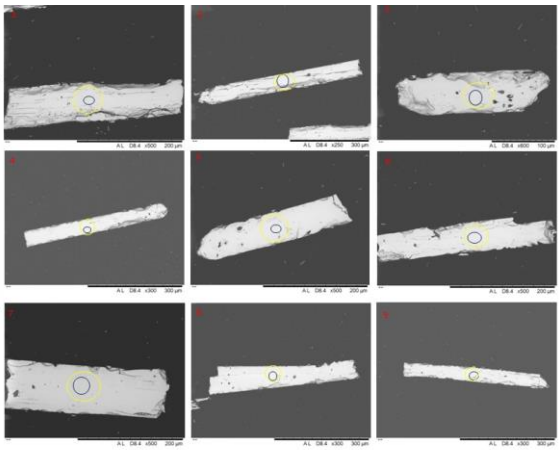

RL22-16 – Ågskardet upper body
Rock type: Pegmatite
Mineral: Zircon

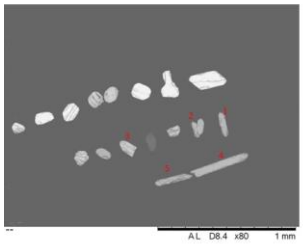

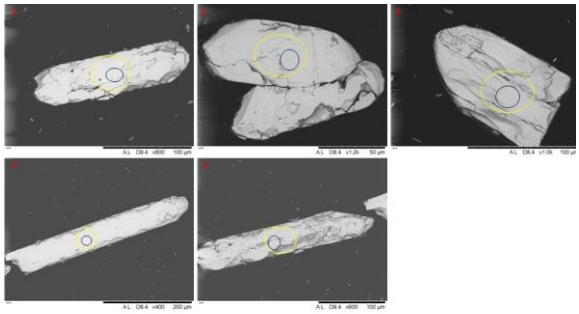

RL22-22 – Meløy
Rock type: Pegmatite
Mineral : Zircon

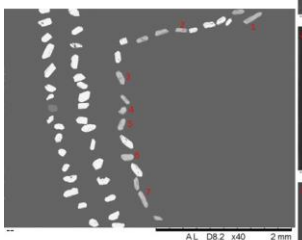

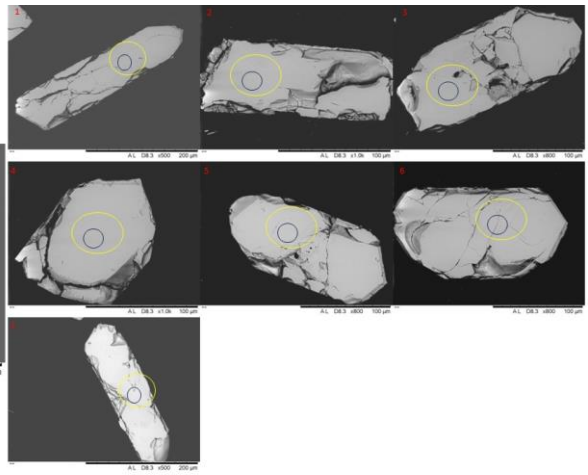

2906R – Rismålstinden
Rock type: Pegmatite
Mineral: Zircon

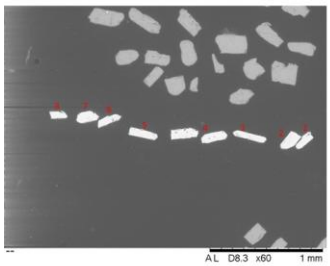

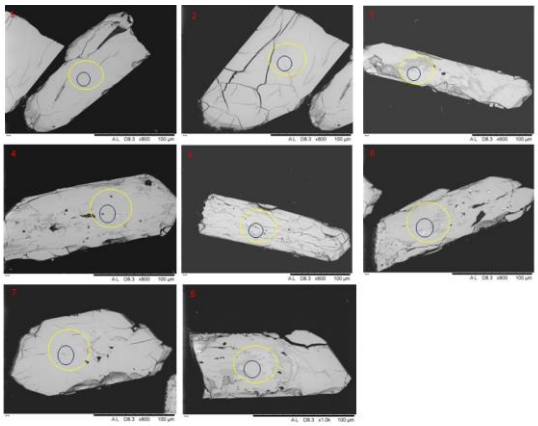

RL22-04I – Ørnes
Rock type: Pegmatite
Mineral : Zircon

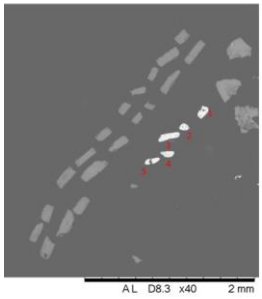

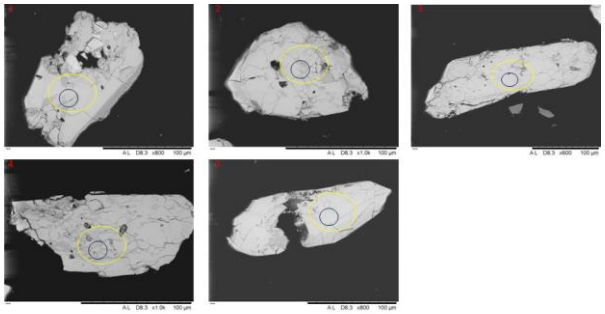

RL22-05J – Neverdalen road section
Rock type: Pegmatite
Mineral: Zircon

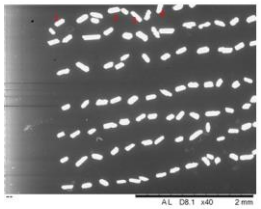

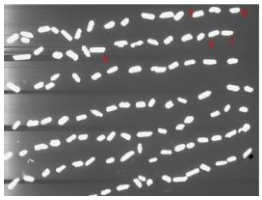

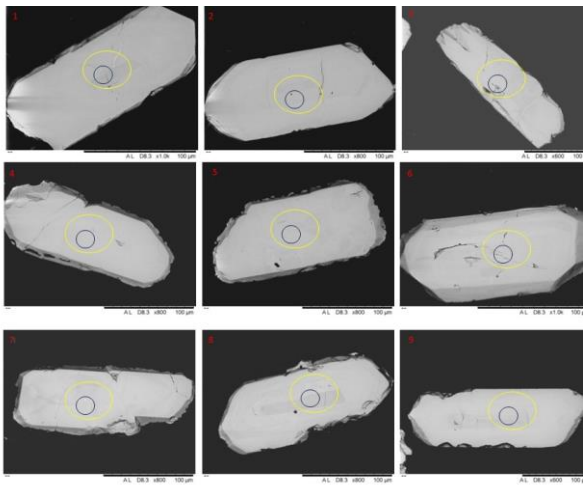

RL22-05J – Neverdalen road section
Rock type: Pegmatite
Mineral: Zircon

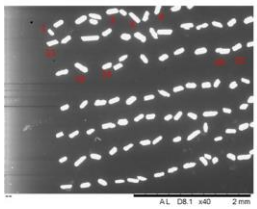

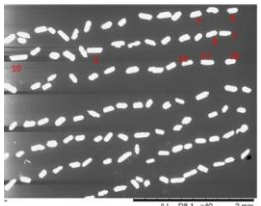

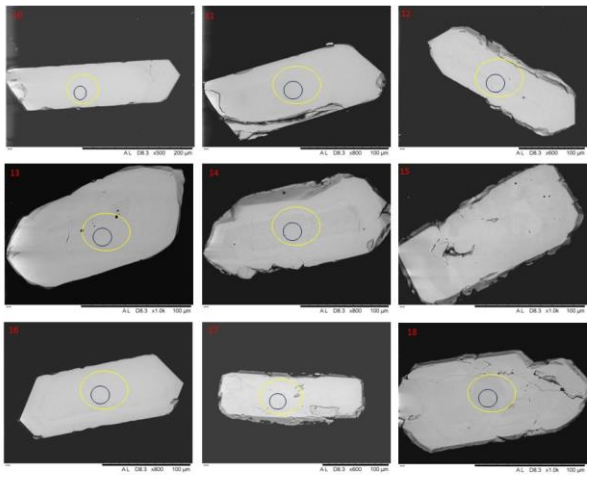

RL22-08F – Ågskardet Old Quarry
Rock type: Pegmatite
Mineral: Zircon

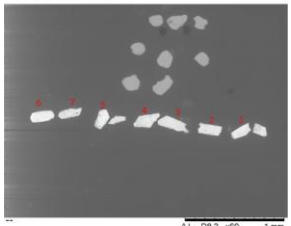

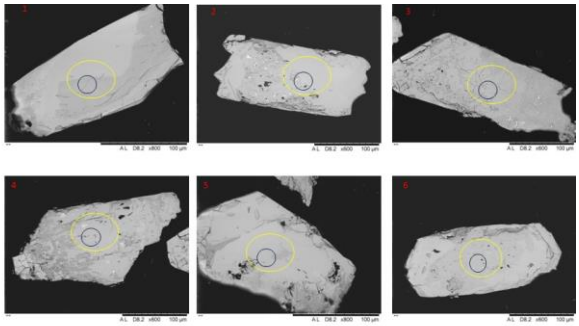

RL22-21 – Meløy
Rock type: Pegmatite
Mineral: Zircon

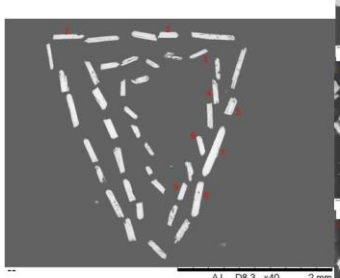

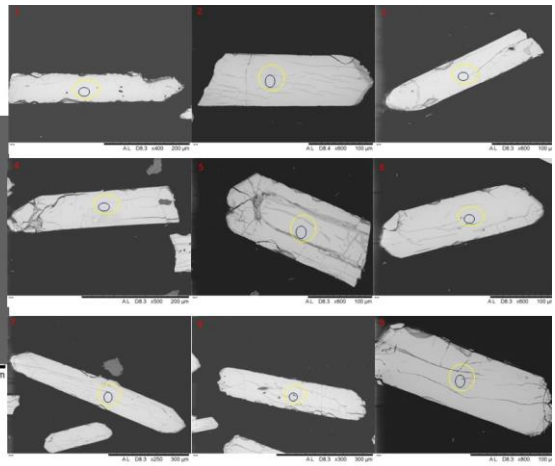

RL22-21 – Meløy
Rock type: Pegmatite
Mineral: Zircon

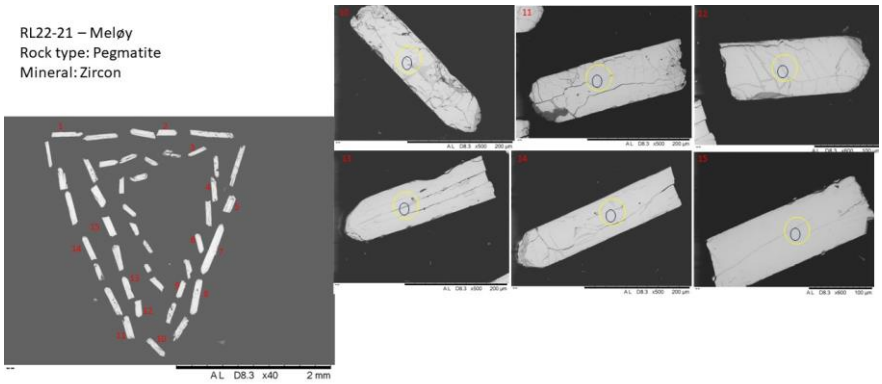

RL22-02 – Åsjord road section
Rock type: Granitic gneiss
Mineral : Zircon

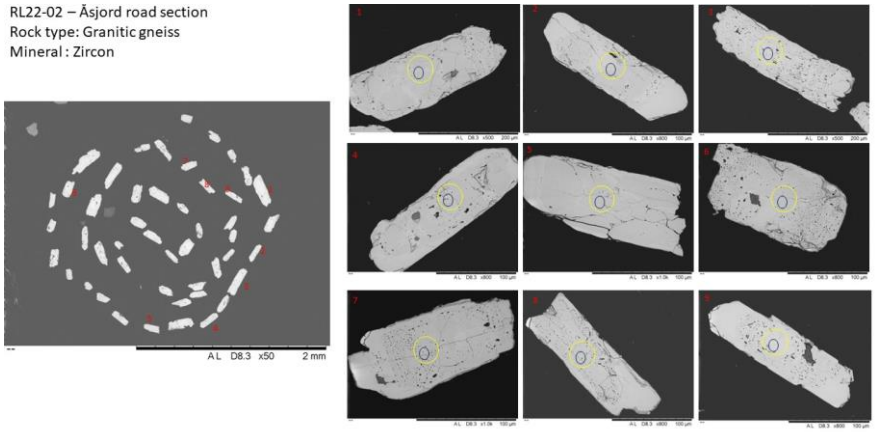

RL22-02 – Åsjord road section
Rock type: Granitic gneiss
Mineral : Zircon

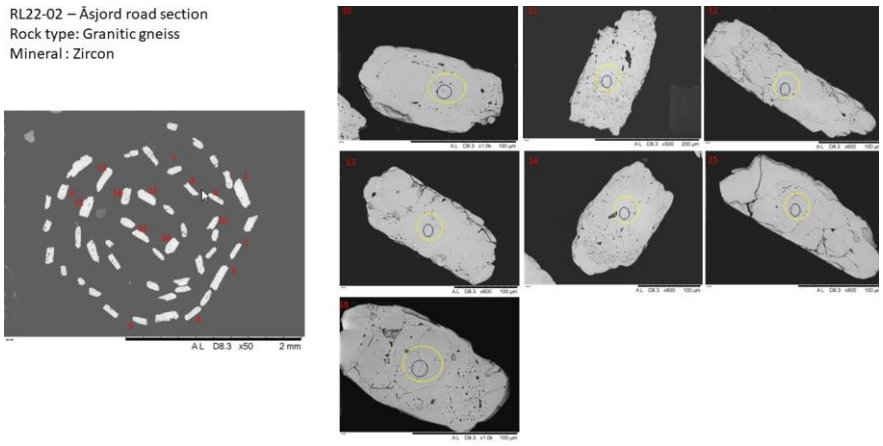

RL22-12 – Selstad road section
Rock type: Granitic gneiss
Mineral: Zircon

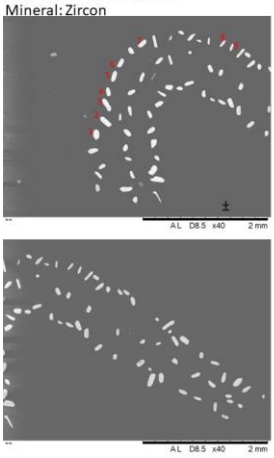

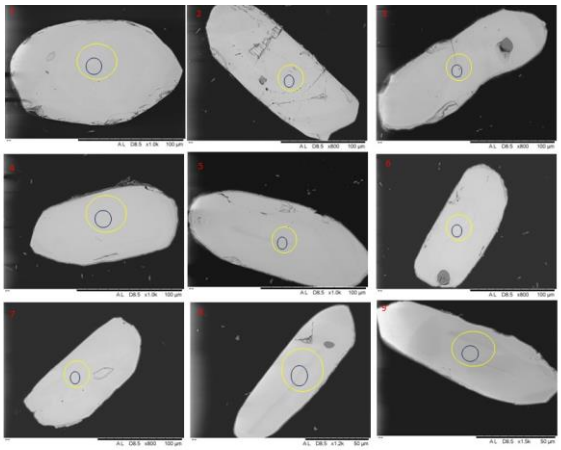

RL22-12 – Selstad road section
Rock type: Granitic gneiss
Mineral: Zircon

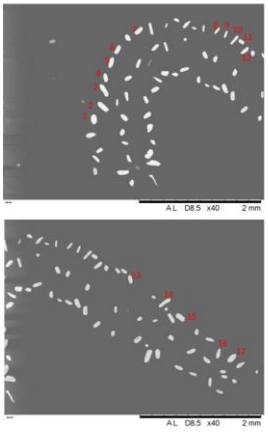

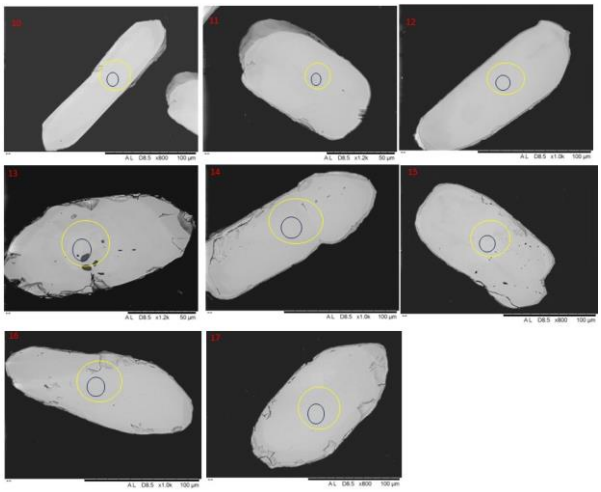

RL22-05D – Neverdalen road section
Rock type: Metasediment
Mineral: Zircon

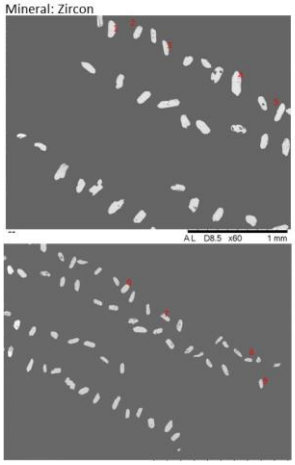

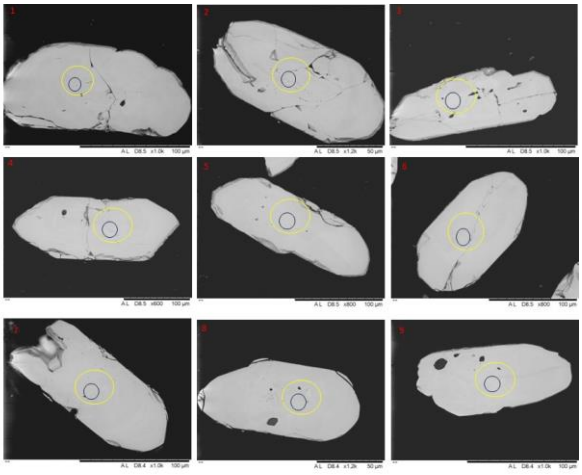

RL22-05D – Neverdalen road section
Rock type: Metasediment
Mineral: Zircon

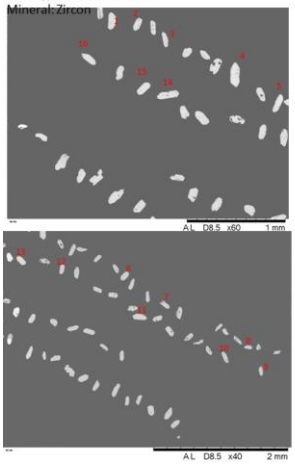

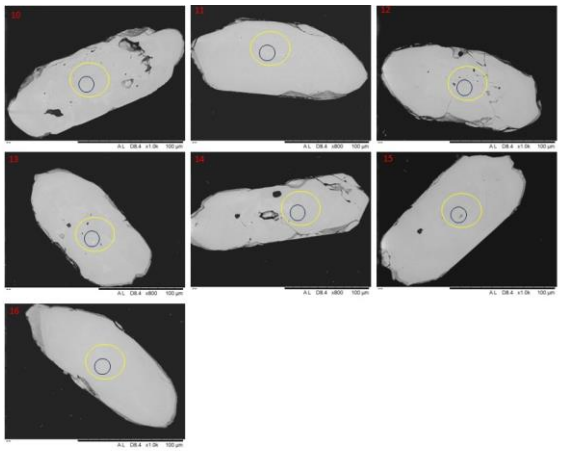

RL22-05F – Neverdalen road section
Rock type: Mafic gneiss
Mineral: Zircon

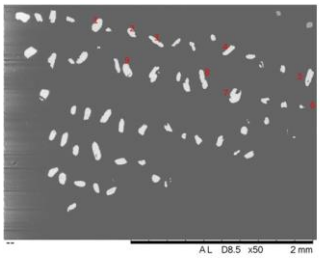

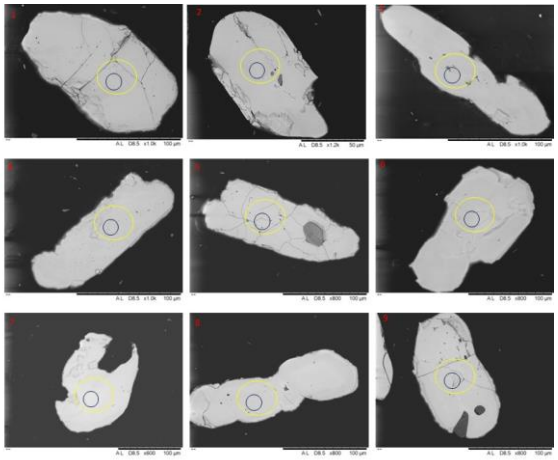

RL22-05F –Neverdalen road section
Rock type: Mafic gneiss
Mineral: Zircon

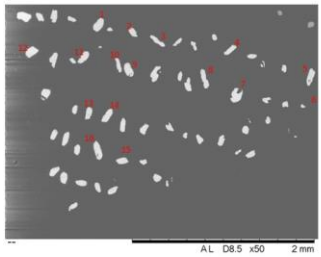

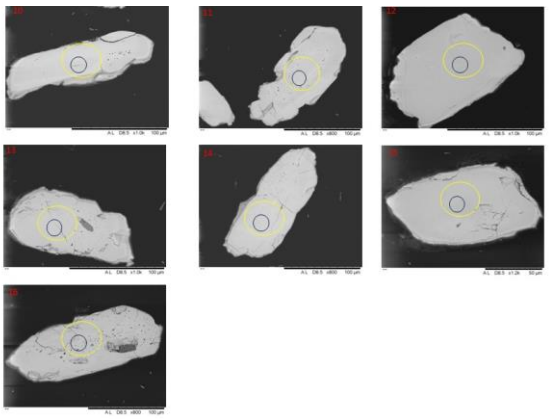

RL22-03E – Kleiva Quarry-Reipå
Rock type: Granitic gneiss
Mineral : Zircon

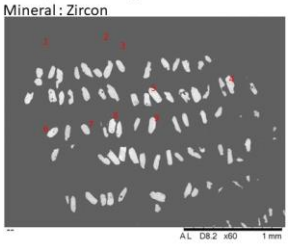

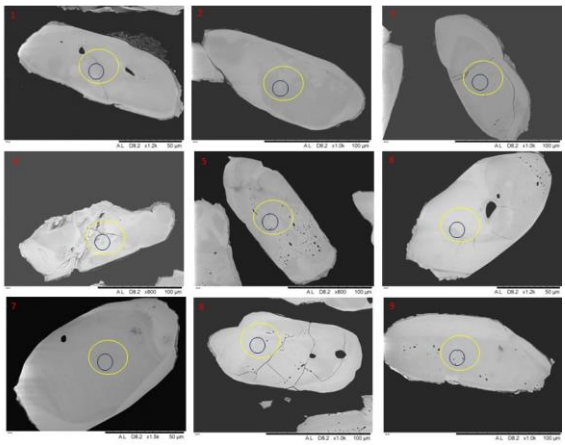

RL22-03E – Kleiva Quarry-Reipå
Rock type: Granitic gneiss
Mineral : Zircon

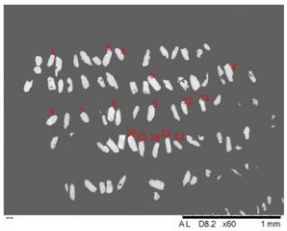

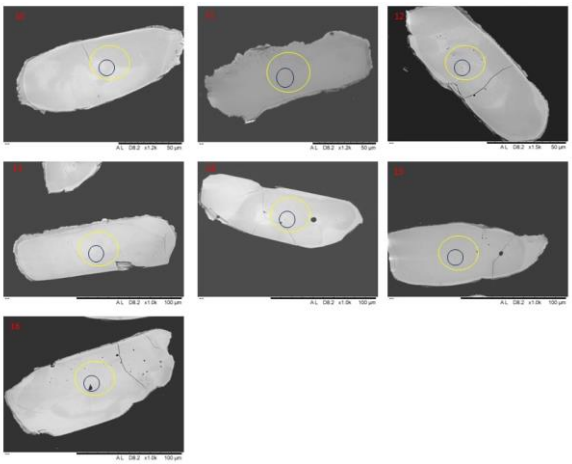

RL22-18 – Meløy
Rock type: Granitic gneiss
Mineral: Zircon

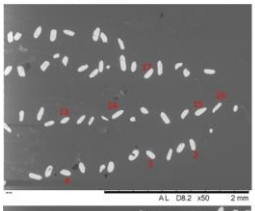

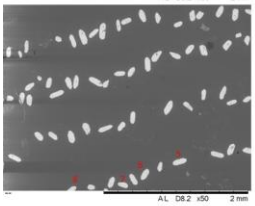

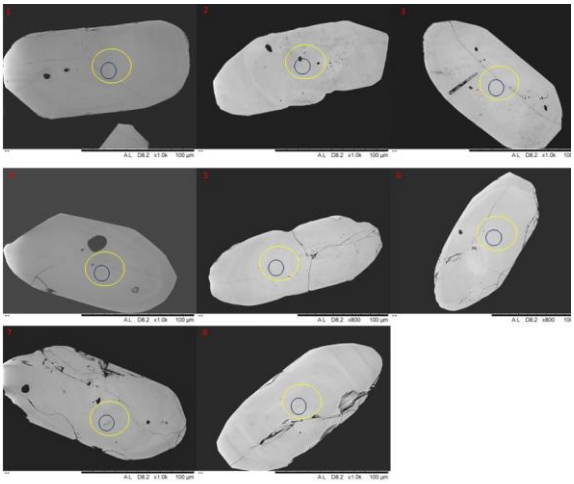

RL22-18 – Meløy
Rock type: Granitic gneiss
Mineral: Zircon

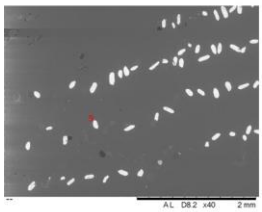

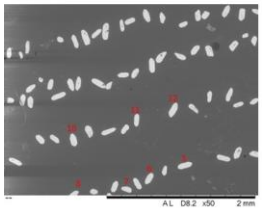

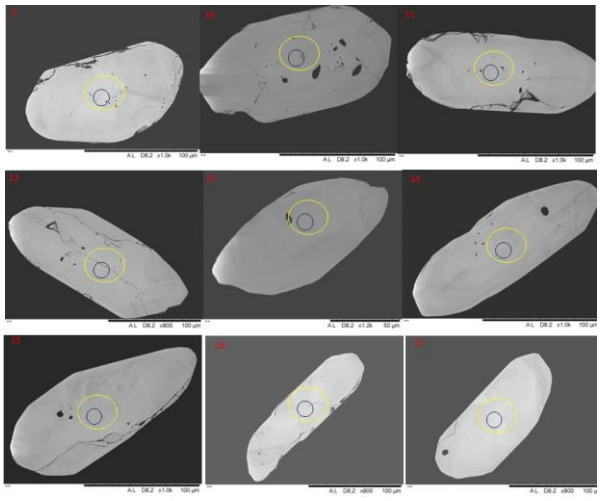

RL22-13 – Ytre holten road section
Rock type: Granitic gneiss
Mineral: Zircon

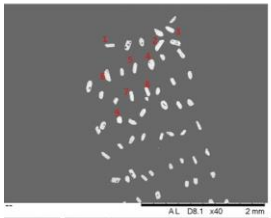

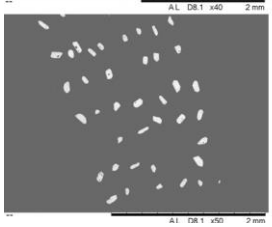

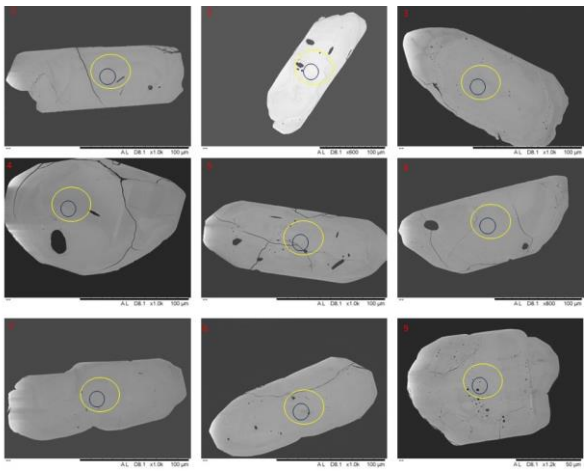

RL22-13 – Ytre holten road section
Rock type: Granitic gneiss
Mineral: Zircon

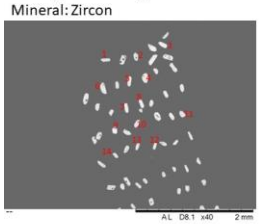

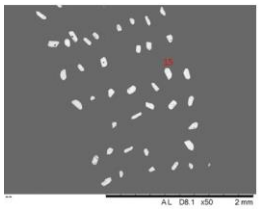

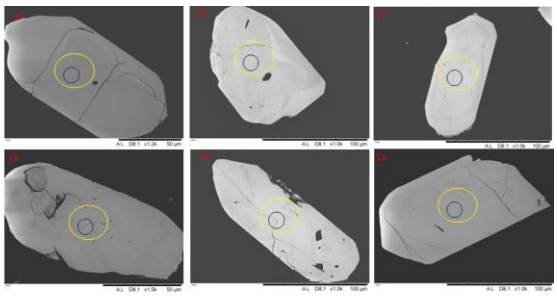

Appendices 8.4 to 8.7 are attached as excel supplementary sheets.

8.4 Major element analyses by EPMA

8.4.1 Major element data of feldspars

8.4.2 Major element data of micas

8.4.3 Major element data of garnets

8.4.4 Major element data of tourmalines

8.4.5 Major element data of apatites

8.5 Trace element analyses by LA-SF-ICP-MS

8.5.1 Trace element data of feldspars

8.5.2 Trace element data of micas

8.5.3 Trace element data of garnets

8.5.4 Trace element data of tourmalines

8.5.5 Accuracy and Precision of Trace element concentration data

8.6 U-Pb zircon isotopic composition

8.6.1 Secondary Standards

8.7 Lu-Hf isotopic compositio